

NASA Contractor Report 4215

Deformation Modeling and Constitutive Modeling for Anisotropic Superalloys

Walter W. Milligan and Stephen D. Antolovich
Georgia Institute of Technology
Atlanta, Georgia

**Prepared for
Lewis Research Center
under Grant NAG3-503**



National Aeronautics and
Space Administration
Office of Management
Scientific and Technical
Information Division

1989

TABLE OF CONTENTS

	Page
LIST OF SYMBOLS	vii
SUMMARY	xi
I. INTRODUCTION	1
Project Goals	3
II. BACKGROUND: MECHANICAL METALLURGY	4
PWA 1480 Microstructure	4
Strength and Deformation Behavior: <001> Crystals of PWA 1480	5
Superalloy Anisotropy	9
Extension to Complex Loading	19
III. BACKGROUND: CONSTITUTIVE MODELING	24
Pure Microstructural Approach	25
Continuum Mechanics Approach	35
Phenomological Approach	42
Walker-Jordan Anisotropic Model	48
Dame-Stouffer Anisotropic Model	50
IV. EXPERIMENTAL PROCEDURES	54
Material	54
Tensile Testing	55
LCF Testing	56
Microstructural Evaluation	57

(Continued)

V. RESULTS: MECHANICAL BEHAVIOR	59
Tensile Deformation of $\langle 001 \rangle$ Crystals	59
Orientation Effects and Tension-Compression Asymmetry	62
Cyclic Deformation	67
Summary	73
VI. RESULTS: DEFORMATION BEHAVIOR	75
High Temperatures	76
Low Temperatures	78
The Nature of the Faults and Partials	85
Summary	97
VII. DISCUSSION: THE TEMPERATURE DEPENDENCE OF THE γ' SHEARING MECHANISM	98
The Nature of the Transformation	98
Modeling the $a\langle 110 \rangle$ Dissociation	101
The High Temperature Faults	105
Summary	106
VIII. DISCUSSION: ON THE PHYSICAL MECHANISM OF CROSS-SLIP	107
Slip Reversibility	108
The Cross-Slip Mechanism	110
Total Cross-Slip Model	111
Limited Cross-Slip Model	117
Summary	127

(Continued)

IX. DISCUSSION: IMPLICATIONS FOR CONSTITUTIVE MODELING	128
Sources of Anisotropy	129
Selection of the Model	136
The Walker-Jordan Constitutive Model: Form and Physical Consistency	137
Regimes of Similar Behavior	149
General Evaluation and Summary	154
X. SUMMARY AND CONCLUSIONS	156
General Observations	156
The CRSS Minimum at 400°C	158
Cross-Slip Models	159
Constitutive Modeling	160
XI. RECOMMENDATIONS	162
The Temperature Dependence of Fault Energies .	162
Constitutive Modeling	163
Primary Cube Slip	163
TABLE I - ALLOY COMPOSITION	164
FIGURES	165
APPENDIX A - DETERMINATION OF CRYSTAL ORIENTATION IN THE TEM	230
APPENDIX B - DISLOCATION AND STACKING FAULT ANALYSIS	234
APPENDIX C - CRSS DATA TABLE	239
APPENDIX D - CYCLIC DEFORMATION DATA	242
APPENDIX E - ADDITIONAL CYCLIC DEFORMATION DATA . . .	256
REFERENCES	273

LIST OF SYMBOLS

Note: The subscripts "i" and "j" are variable subscripts (i.e. $n_i = n_1, n_2, n_3, \text{etc.}$)

a	Lattice parameter
A	Constant
b	Dislocation Burgers vector
C_i	Constants
d	Dislocation pair spacing; Also lattice d-spacing
d_c	Dislocation spacing on {001} (Cube)
d_e	Equilibrium (stress-free) dislocation spacing
d_o	Dislocation spacing on {111} (octahedral)
D	$\mu b^2/2\pi$; Also Diffusivity
D_o	Diffusion coefficient
E	Energy
F	Force on a dislocation
g	Diffraction vector
h	Hardening parameter
h_1	Hardening parameter
h_{ij}	Hardening matrix
ΔH	Activation energy
ΔH_{sd}	Activation energy for self-diffusion
i	Imaginary operator
k	Boltzmann's constant
K	Drag stress. Also Drag stress state variable
K_i	Drag stress state variable on i^{th} octahedral system
$l_i^{\alpha\beta}$	Unit vector in the β direction

L	TEM camera length
M	Schmid factor, $= \cos\phi\cos\theta$
n	Constant
n_i^α	Unit vector normal to the α plane
N	Schmid factor ratio, $= \tau_{(010)[101]} / \tau_{(111)[101]}$
N'	Schmid factor ratio, $= \tau_{(001)[110]} / \tau_{(111)[101]}$
N_C	Number of active cube slip systems
N_O	Number of active octahedral slip systems
q	Latent hardening constant
Q	Schmid factor ratio, $= \tau_{(111)[121]} / \tau_{(111)[101]}$
r	A distance in PPV model
r_O	Dislocation core radius
r_S	Average particle radius in slip plane
R	TEM spot spacing; Also dislocation cut-off radius
R_f	Stacking fault displacement vector
s_{ij}	Deviatoric stress
t	Time
t_C	Thickness of a crystal
T	Temperature
T_O	Dislocation line tension
v	Dislocation velocity
v_t	Dislocation terminal velocity
V_i	Constants
w	Cross-slip distance in PPV model
z	A distance in PPV model

Z	Bodner-Partom-Stouffer state variable
α	Wave phase factor
α_i	Inelastic shear strain on the i^{th} cube system
β_i	Temperature dependent material constants
γ	Inelastic shear strain
γ_i	Inelastic shear strain on the i^{th} octahedral system
Γ_a	APB energy (APBE)
Γ_c	APBE on $\{001\}a/2\langle 110 \rangle$
Γ_o	APBE on $\{111\}a/2\langle 110 \rangle$
Γ_s	Superlattice intrinsic stacking fault energy
δ_{ij}	Kronecker delta, $\delta = 1$ if $i = j$, $\delta = 0$ if $i \neq j$
ϵ_{ij}	Strain
$\epsilon_{ij}^{\text{in}}$	Inelastic strain
ϵ_{ij}^{p}	Plastic strain
ϵ_{ij}^{c}	Creep strain
ϵ_{p}	Uniaxial plastic strain
ζ	Dummy integration variable
η_i	Temperature dependent material constants
θ	Angle between σ and slip plane normal
κ_i	Drag stress state variable on i^{th} cube system
κ_1	Latent drag stress
λ	Dislocation mean free path
λ_e	Electron wavelength
μ	Shear modulus

ν	Lattice vibrational frequency
ν_0	Constant
ξ_i	Geometric (dislocation character) terms
ξ_g	Extinction distance
π_i	Shear stress on the i^{th} cube system
ρ	Dislocation density
ρ_m	Mobile dislocation density
σ	Uniaxial stress
σ_{ij}	Stress
τ	Shear stress
τ_b	A measure of back stress
τ_B	A measure of back stress (Normalized)
τ_c	Constriction stress, $\tau_{(111)[\bar{1}\bar{2}1]}$.
τ_i	Shear stress on i^{th} octahedral system
τ_m	Peierls stress of the matrix
τ_p	Peierls stress of the γ'
τ_s	Cross-slip stress, $\tau_{(010)[\bar{1}01]}$
τ_y	Shear yield strength (CRSS)
ϕ	Angle between σ and b
ϕ_i	Model-dependent functions.
ϕ_g	Amplitude of diffracted wave
ψ_i	Model-dependent functions
ω_i	Back stress state variable on i^{th} cube system
Ω	Back stress
Ω_i	Back stress state variable on i^{th} octahedral system
Ω_{ij}	Back stress state variable

SUMMARY

A study of deformation mechanisms in the single crystal superalloy PWA 1480 has been conducted. Monotonic and cyclic tests were conducted from 20 to 1093°C. Both $\langle 001 \rangle$ and near- $\langle 123 \rangle$ crystals were tested, at strain rates of 0.5 and 50%/minute.

The deformation behavior could be grouped into two temperature regimes: low temperatures, below 760°C; and high temperatures, above 820-950°C depending on the strain rate. At low temperatures, the mechanical behavior was very anisotropic. An orientation dependent CRSS, a tension-compression asymmetry, and anisotropic strain hardening were all observed. The material deformed by planar octahedral slip. The anisotropic properties were correlated with the ease of cube cross-slip, as well as the number of active slip systems. At high temperatures, the material was isotropic, and deformed by homogeneous γ' by-pass.

It was found that the temperature dependence of the formation of superlattice-intrinsic stacking faults was responsible for the local minimum in the CRSS of this alloy at 400°C. It was proposed that the cube cross-slip process must be reversible. This was used to explain the reversible tension-compression asymmetry, and was used to study models of cross-slip. As a result of this study, the cross-slip model proposed by Paidar, Pope and Vitek was found to be

consistent with the proposed slip reversibility.

The results of this study were related to anisotropic viscoplastic constitutive models. The model proposed by Walker and Jordan was found to be capable of modeling all aspects of the material anisotropy. Temperature and strain rate boundaries for the model were proposed, and guidelines for numerical experiments were proposed.

CHAPTER I

INTRODUCTION

Nickel-base superalloys are used extensively in aircraft engines and rocket engines, where excellent oxidation resistance and high temperature strength are required. Several good reviews of superalloy design are available [1,2]. A very brief introduction is presented below.

Most superalloys are based on a highly oxidation resistant solid solution of 5-20% chromium in nickel. For strength, aluminum and titanium are added. These elements form the ordered $\text{Ni}_3(\text{Al},\text{Ti})$ γ' phase by an ageing reaction. The γ' phase, which has the L1_2 structure, exhibits an fivefold increase in strength with temperature from 20 to 650°C. The γ' precipitate is responsible for the excellent high temperature strength of superalloys.

By controlling the amount of Al and Ti, the γ' volume fraction (V_f) can be varied over a wide range; most commercial superalloys contain 20-60% γ' . By controlling the thermomechanical treatment, the size and shape of the γ' precipitate can also be closely controlled. These factors (γ' shape, size, and volume fraction) are manipulated by alloy designers to yield a wide range of mechanical

properties. For example, the Waspalloy alloy (25% γ') is used at relatively low temperatures (below 650°C) when moderate strength, high ductility and high fracture toughness are required; the PWA 1480 alloy (60% γ') is used at very high temperatures (1100°C) where excellent strength and creep resistance are necessary, and limited ductility is tolerable.

Many superalloys contain several elements in addition to Ni, Cr, Al, and Ti. These elements are added to solid solution strengthen the γ and γ' , to control the γ/γ' lattice parameter mismatch, and to control the γ' anti-phase boundary energy (APBE). They include Fe, Co, Mo, W, Ta, and Nb. Additionally, polycrystalline superalloys may contain elements which improve grain boundary properties and creep strength. These include C, B, Zr, and Hf [1,2].

In applications where very high temperatures and essentially uniaxial stresses are encountered, the creep and fatigue lives of components can be markedly improved by the elimination of transverse grain boundaries. Thus, directionally solidified (DS) and single crystalline superalloys are used in jet engine turbine blades. PWA 1480, which is the subject of this study, is such a single crystal alloy. In addition to its present use in jet engines, it is being considered for use in the turbopump blades of the space shuttle main engine.

The use of single crystal blades presents an analytical problem, because these alloys exhibit complex plastic anisotropy. This anisotropy is discussed in Chapter II. In Chapter III, advanced constitutive models which have been developed for structural analysis of these materials are reviewed. These models require detailed knowledge of the physical mechanisms of deformation over the entire range of operating conditions. This requirement is the driving force behind the present study.

Project Goals

In broad terms, this project had three goals:

1. To improve the understanding of the deformation behavior of PWA 1480 (Chapters V and VI);
2. To model this behavior when possible at the microstructural level (Chapters VII and VIII);
3. To interpret the results from the perspective of the constitutive modelers (Chapter IX).

The study includes both monotonic and cyclic deformation studies at several strain rates in the temperature range from 20-1093°C. This is representative of the service conditions of components made of the PWA 1480 alloy.

CHAPTER II

BACKGROUND: MECHANICAL METALLURGY

PWA 1480 Microstructure

The specific class of superalloys which is of interest to this study contains alloys which have high volume fractions of γ' , typically 45-60%. These alloys have excellent strength and oxidation resistance at high temperatures, and are used structurally up to 1100°C. A typical alloy in this class is Mar-M 200, which has a well-documented microstructure [3]. More modern alloys in this class include Rene' N4, CMSX-2, and PWA 1480, which is the subject of this study. The microstructure of PWA 1480 was studied in an earlier phase of this work (the author's M.S. Thesis) [4,5], and is summarized below.

PWA 1480 contains a fine dispersion of coherent, cuboidal γ' , Figure 1(a). The γ' size is fairly uniform, ranging from 0.25 μm to 1 μm , with an average size of 0.5 μm . As shown in Figure 1(b), the alloy contains a residual dendritic structure, with micropores and interdendritic eutectic pools. The initial dislocation density is very low, about $10^8/\text{cm}^2$. The lattice parameter mismatch is also very low, less than 0.2%. Due to a low carbon content of 42 ppm, there are very few carbides in the structure.

Strength and Deformation Behavior:

<001> Crystals of PWA 1480 [4,5]

In a two phase alloy, deformation is controlled by interactions between mobile dislocations and the precipitates. The plastic shear strain introduced into a crystal by slip can be calculated by [6]:

$$\gamma = b\rho_m\lambda \quad (2-1)$$

where γ = Plastic shear strain,
 b = Dislocation Burgers vector,
 ρ_m = Mobile dislocation density,
 λ = Dislocation mean free path.

Using microstructural parameters measured for PWA 1480, the plastic strain which can occur without dislocations "overcoming" the γ' precipitates is a negligible 0.006% [5]. Therefore, for measurable yielding to occur, the dislocations which are present in the material must "overcome" the γ' by one of three possible mechanisms:

1. Since the γ' is coherent, the dislocations may shear (cut) through the γ' (Figure 2(a)).
2. Assisted by climb or cross-slip, dislocations may by-pass the γ' (Figure 2(b)).
3. The γ' may be by-passed by Orowan looping. Due to the large γ' size and high V_f , this mechanism is negligible.

The behavior of <001> PWA 1480 crystals is described below.

Yield Strength

As shown in Figure 3, the strength was the same at 20 and 705°C. Other studies have shown slight variations in strength over this temperature regime [7-9]. Above 760°C, the strength dropped off rapidly and became a strong function of strain rate. This flow stress vs. temperature behavior is typical for this class of alloys [5].

An Arrhenius-type analysis (Figure 4) of the strength-temperature data revealed two distinct temperature regimes: low temperatures, where the activation energy (ΔH) was independent of temperature; and high temperatures, where a constant activation energy was found that was independent of strain rate. (There was a strain rate-dependent transition range between these two regimes). The activation energy observed at high temperatures was indicative of a diffusion-controlled process.

Deformation Behavior

Analysis of the deformation microstructures showed that there were two distinct temperature regimes, and the boundaries were exactly the same as in the Arrhenius analysis. At low temperatures ($\Delta H = 0$), plastic deformation occurred via γ' shearing by pairs of $a/2\langle 110 \rangle$ dislocations on $\{111\}$ slip planes. A typical structure in this temperature regime is shown in Figure 5. At high

temperatures, deformation was dominated by climb-assisted by-pass. A typical structure in this regime is shown in Figure 6. Since the deformation process at high temperatures was thermally activated, the temperature at which the transition occurred was a function of strain rate. High temperature behavior began to dominate at 815°C at a strain rate of 0.5%/min, while the boundary was 927°C at 50%/min.

Modeling of the Yield Process

To model the yield process over the entire temperature regime, two models are necessary: a low temperature model based on shearing, and a high temperature model based on by-pass.

The most widely accepted shearing model for high V_f superalloys is that of Copley and Kear [10]. Assuming that dislocation penetration into the precipitate is the rate-limiting step, a static force balance results in their expression for the Critical Resolved Shear Stress (CRSS):

$$\tau_y = \Gamma_a/2b - T_o/br_s + (\tau_m + \tau_p)/2 \quad (2-2)$$

where $\tau_y = \text{CRSS}$,

$\Gamma_a = \text{Antiphase boundary energy (APBE)}$,

$T_o = \text{Line tension}$,

$r_s = \text{Average particle radius in slip plane}$,

$\tau_m = \text{Peierls stress of the matrix}$,

$\tau_p = \text{Peierls stress of the } \gamma'.$

However, in the earlier phase of this study [4,5], it was found that the CRSS was not controlled solely by the penetration step; dislocation drag within the γ' particle was also very important. Additionally, the discussion of anisotropy which follows indicates that the model is too simple to capture the complicated behavior of these alloys. Therefore, there is not a model available which fully describes the yield process for PWA 1480 in the low temperature regime.

At high temperatures, it was found that a model exists which is both physically relevant and functionally correct with respect to temperature. The model was developed by Brown and Ham [11]. The model assumes that climb-assisted by-pass controls plastic flow. An analysis of vacancy diffusion in the vicinity of a climbing dislocation results in their expression for the CRSS:

$$\tau_y = \tau_0 + C_1 \Delta H - C_2 T |(\ln[C_3 \dot{\epsilon}])| \quad (2-3)$$

where τ_0 = Threshold stress,

ΔH = Activation energy of the rate-limiting
diffusion process,

T = Absolute temperature,

$\dot{\epsilon}$ = Strain rate,

C 's = Constants which include microstructural
parameters.

The foundation of the model appears to be very sound for PWA

1480 [5].

Superalloy Anisotropy

In an annealed, disordered FCC crystal, plastic flow commences when the shear stress resolved on the slip plane in the direction of the mobile dislocation's Burgers vector reaches a critical value (a material parameter):

$$\tau_y = \sigma \cos \theta \cos \phi \quad (2-4)$$

where σ = Uniaxial normal stress,

ϕ, θ = Angles between the tensile axis and the slip plane normal, slip direction.

This is referred to as Schmid's Law, and of course implies that any anisotropy is simply geometrical.

In single crystals of γ' , however, there is additional anisotropy which cannot be explained by Schmid's Law. When the γ' precipitates are sheared in PWA 1480, as they are at low temperatures, this inherent γ' anisotropy becomes very important. Pope and Ezz [12] have recently written an excellent review article covering this area of research. Pertinent aspects of their article and related works are summarized and discussed below.

Behavior of Pure γ' Crystals

When the $L1_2$ lattice is sheared by an $a/2\langle 110 \rangle$ dislocation, an antiphase boundary (APB) is left behind.

The energy of this APB depends strongly on the slip plane [13]. An $a/2\langle 110 \rangle$ shear on a $\{111\}$ (octahedral) plane results in a very high APBE due to nearest-neighbor bond violations across the APB plane. However, the same $a/2\langle 110 \rangle$ shear on an $\{001\}$ (cube) plane results in a much lower APBE, due to only second nearest-neighbor bond violations across the APB plane. The result is that it is energetically favorable for dislocation pairs to lie on $\{001\}$ planes instead of $\{111\}$ planes. Since the $\{111\}$ planes are the normal slip planes in FCC crystals, this can result in deformation behavior which is unique to $L1_2$ compounds. Two types of distinct mechanisms can occur, both of which can directly affect the properties of a superalloy:

1. $a/2\langle 110 \rangle$ dislocations can sometimes shear the γ' on $\{001\}$ planes instead of $\{111\}$ planes. This phenomenon is called primary cube slip.
2. Screw portions of $a/2\langle 110 \rangle$ dislocations which are gliding on $\{111\}$ planes can sometimes cross-slip to $\{001\}$ planes, thus reducing their APBE. These cross-slipped segments act as pinning points, thus strain hardening the materials. This phenomenon is called cube cross-slip.

Based on Schmid factor considerations, the primary cube slip Burgers vector and slip plane are different from the cube cross-slip Burgers vector and slip plane. For crystals with stress axes in the standard $[001] - [011] - [\bar{1}11]$

stereographic triangle, the primary cube slip system is $(001)a/2[\bar{1}10]$, while the cube cross-slip system is $(010)a/2[\bar{1}01]$.

Copley and Kear were the first to study single crystals of $\text{Ni}_3\text{Al } \gamma'$ [14]. Among their important findings were:

1. The CRSS increased five-fold from room temperature to an orientation-dependent peak temperature in the range from 650 to 750°C. There is now a reasonable consensus [12] that the increase is due to cube cross-slip, which is thermally activated.
2. The peak strength temperature was lowest for $\langle 111 \rangle$ crystals, and much higher for $\langle 001 \rangle$ and $\langle 011 \rangle$ crystals. They attributed the reduction in strength of the $\langle 111 \rangle$ crystals above 650°C to the onset of primary cube slip. The $\langle 111 \rangle$ crystal has a Schmid factor of 0.47 for primary cube slip, but only 0.28 for octahedral slip. However, cube slip was not proven in this study.

Later studies [12] have confirmed the occurrence of primary cube slip in near- $\langle 111 \rangle \gamma'$ crystals. However, Copley and Kear postulated that since reduction in strength in $\langle 111 \rangle$ crystals occurred due to cube slip, then the peak in strength in all orientations was due to the onset of cube slip. This is clearly not the case, since $\langle 001 \rangle$ crystals exhibit a peak in strength, even though the shear stress on

the cube planes is zero in this orientation. More recent studies have revealed an additional source of anisotropy in pure γ' , which occurs when only octahedral slip operates. Takeuchi and Kuramoto [15], based on studies of the $L1_2$ compound Ni_3Ga , found that the $(111)[\bar{1}01]$ CRSS was a function of the resolved shear stress on the cube cross-slip plane in the direction of cross-slip. This implied that the CRSS was controlled by cube cross-slip, and that the rate of cube cross-slip was a function of the stress state. Later, Pope and co-workers [12,16,17] found that in Ni_3Al the rate of cube cross-slip was also affected by the shear stress which tends to constrict or extend the Shockley partial dislocations. This leads to complex orientation-dependent behavior and a significant tension-compression asymmetry in the CRSS. They have developed and refined a model which explains these trends in the CRSS. It is described and discussed below.

Cross-Slip Model [12,16,17]

Screw segments of gliding $\{111\}a/2\langle 110 \rangle$ dislocations can cross-slip to cube planes, thus strengthening and strain hardening the material. The physical mechanism of cross-slip and pinning are still very uncertain, as discussed in detail in Chapter VIII. For the purposes of the present discussion, it is assumed (as it was by Takeuchi and Kuramoto [15] and Lall, Chin and Pope [16]) that cube cross-slip does pin the glissile octahedral dislocations, and that

the rate of cross-slip controls the CRSS.

If the leading $a/2\langle 110 \rangle$ screw superpartial dislocation is dissociated into two $a/6\langle 112 \rangle$ partials (as is energetically favorable), then the partials must constrict and recombine for cross-slip to occur. Two factors can increase the probability of recombination:

1. Increasing temperature, which increases the amplitude of lattice fluctuations;
2. A stress state which constricts the partials, thus decreasing the mean partial separation distance.

Consider the screw portions of a primary octahedral superpartial, $(111)a/2[\bar{1}01]$, which lies in a uniaxial test specimen that has a stress axis inside the standard stereographic triangle. As illustrated by the Burgers vector diagram in Figure 7, the resulting Shockley partials have identical screw components, but their edge components are of opposite sign ($\pm a/12[1\bar{2}1]$). The force on a dislocation is given by:

$$F = \tau b \quad (2-5)$$

where F = Force per unit length,

τ = Shear stress resolved on the slip
plane in the direction of b .

Therefore, the only component of stress which will affect constriction is the shear stress $\tau_{(111)[1\bar{2}1]}$, since this

stress is the only one which tends to move the partials either towards each other (resulting in easier cross-slip) or away from each other (resulting in more difficult cross-slip). Figure 8(b) shows how this "constriction stress" varies with orientation. For tensile loading, there is a great circle of zero stress which cuts the triangle. As the stress axis deviates from this line towards $\langle 001 \rangle$, the partials tend to become more and more constricted, thus aiding cross-slip. As the stress axis deviates towards $\langle 011 \rangle$ and $\langle 111 \rangle$, the partials tend to become more and more extended, thus hindering cross-slip. Note that these trends are reversed if compressive loading is used.

These qualitative trends were quantified by Pope et. al. [16,17] in a manner similar to the approach of Takeuchi and Kuramoto [15]. It was assumed that the rate of cross-slip is increased with temperature because of the increasing amplitude of lattice fluctuations, and is therefore a thermally activated process which can be described by an Arrhenius rate equation. It was further assumed that the activation energy for cross-slip is influenced by the constriction stress and the cross-slip stress. Therefore, the CRSS may be written as [16,17]:

$$\tau_y = A \exp(-\Delta H/3kT) \quad (2-6)$$

where $A = A$ constant,

ΔH = The activation energy for cube cross-slip,

k = Boltzmann's constant,

T = Absolute temperature.

The activation energy may be broken into its stress-dependent and stress-independent components:

$$\tau_y = A \exp(-[\Delta H_0 + V_1 \tau_c + V_2 \tau_s]/3kT) \quad (2-7)$$

where ΔH_0 = Stress independent portion of H,

τ_c = Constriction stress,

τ_s = Cross-slip stress,

V's = Activation volumes.

The constriction stress term in the activation energy has been shown to dominate the stress dependence [16,17].

The model correlates the temperature dependence, orientation dependence, and stress direction dependence of the data extremely well. The temperature dependence is described through the thermally activated form of the CRSS equation; the orientation dependence and stress direction dependence of the CRSS are described through the constriction stress term in the activation energy. It explains, for example, why the $\langle 001 \rangle$ orientation has a higher CRSS than the $\langle 011 \rangle$ orientation in tension, while the opposite is true in compression (the sign of the constriction stress changes). It also describes the increasing CRSS with increasing temperature.

In addition to the correlation of anisotropic mechanical properties, deformation studies have supported the physical basis of the model. $L1_2$ crystals tested at low temperatures typically contain many straight screw dislocations in the deformation substructures [12], implying a lower mobility for screw dislocations. (The faster moving edge and mixed components glide out of the crystal). Also, weak beam TEM studies of these trapped screw segments have found evidence of superdislocation dissociation on cube planes [18-20].

Although most of the data are consistent with the cross-slip model, there is a serious inconsistency which the proponents of the cross-slip model have not been able to explain. It lies in the observation that the CRSS of Ni_3Al γ' is independent of strain rate in the temperature regime where the CRSS is a strong function of temperature. This is inconsistent with every known example of thermally activated processes. Tien et. al. [21] have proposed that this invalidates the cross-slip model, and they have proposed that the increase in CRSS with temperature is due to changes in the APBE with temperature. However, their model cannot explain the tension-compression asymmetry or orientation dependence of the CRSS. It appears that most investigators believe that the cross-slip model is more physically valid, even though the strain rate insensitivity cannot be justified.

Behavior of High Volume Fraction Superalloys

Since superalloys are composite structures composed of γ' and a matrix, the behavior is much more complex than that of pure γ' . However, one generalization can be made: if the γ' is sheared during deformation, then the anisotropy associated with γ' will have some effect on the superalloy behavior.

The first type of anisotropy which was observed in single crystal superalloys was seen during the pioneering work conducted at Pratt & Whitney on Mar-M 200 [22,23]. Similar to the behavior of pure γ' , they found an orientation-dependent peak strength temperature in the range from 650 to 800°C. The $\langle 111 \rangle$ orientation obtained its peak strength at a temperature lower than $\langle 001 \rangle$ and $\langle 011 \rangle$ crystals, consistent with the pure γ' studies. This lead Copley et. al. [23] to propose that primary cube slip occurred in $\langle 111 \rangle$ crystals at temperatures greater than about 700°C, thus reducing the apparent octahedral CRSS. However, it must be noted that no physical evidence of cube slip was observed in these studies.

The occurrence of primary cube slip in orientations near $\langle 111 \rangle$ has been proposed for a number of alloys which display gross violations of Schmid's Law for $\{111\}\langle 110 \rangle$ slip. In a study of an alloy similar to Mar-M 200, Giamei [24] found that the measured $\{111\}a/2\langle 110 \rangle$ CRSS for $\langle 111 \rangle$ crystals was up to a factor of two lower than the CRSS for

$\langle 001 \rangle$ and $\langle 011 \rangle$ crystals, even at temperatures as low as 20°C . As already mentioned, a slightly reduced octahedral CRSS was found in the Mar-M 200 tensile tests [22]. Miner and co-workers [25-27] have proposed that primary cube slip occurs in Rene' N4 crystals near $\langle 111 \rangle$ at temperatures from 20 to 980°C . They support this not only with CRSS data, but also by analyses of slip traces, dislocation Burgers vectors, and lattice rotations. Their experimental results are extremely important evidence in support of the primary cube slip proposed by other investigators. In related work, Gabb and Welsh [28] found primary cube slip traces in near- $\langle 111 \rangle$ PWA 1480 crystals fatigued at 650°C . Finally, PWA 1480 data [7-9] and slip trace analysis [7] indicate the likelihood of primary cube slip in near $\langle 111 \rangle$ crystals even at temperatures below the peak strength temperature.

In addition to primary cube slip in $\langle 111 \rangle$ superalloy crystals, there is a growing body of evidence showing the importance of cube cross-slip in all orientations in which octahedral slip occurs. Pope and Ezz [12] pointed out in their review article that the orientation dependence of the CRSS for Mar-M 200 could be qualitatively explained by their cube cross-slip model. Duhal and Shah [7] qualitatively correlated the tension-compression asymmetry and the orientation-dependent octahedral CRSS for PWA 1480 with the cube cross-slip model. (For PWA 1480, the magnitude of the tension-compression asymmetry is as high as 30%). Finally,

Miner et. al. [27] quantitatively used the model (Equation 2-7) to substantially improve the Schmid's law predictions of the CRSS. Similar to the studies of Ni_3Al γ' , they found that the cross-slip stress term was negligible compared to the constriction stress term, so they modified the Pope et. al. model to:

$$\tau_y = A \exp(-[\Delta H_0 + V_1 \tau_c]/kT) \quad (2-8)$$

where τ_c is the constriction stress. Equation 2-8 is simply an extension of Schmid's Law, considering both temperature effects and constriction (cross-slip) effects. Heredia and Pope [29] found similar qualitative trends in PWA 1480.

In review, the work of Miner and co-workers was extremely important, for two reasons: first, they were the first to actually show primary cube slip experimentally in superalloy crystals (although others speculated that it occurred); second, they were able to quantitatively use the cross-slip model to substantially improve CRSS predictions as a function of orientation and stress direction.

Extension to Complex Loading

The above discussion shows that our understanding of the yielding behavior of single crystal superalloys is reasonably complete. However, our understanding of deformation mechanisms and their relationships with properties beyond the yield point is very limited. In this

regime, we must consider strain hardening or softening, changing deformation mechanisms, creep, cyclic deformation, microstructural changes, and history effects (path dependence).

Tensile Deformation

At temperatures below the peak strength temperature, slip in this class of alloys is very planar. Due to the high degree of slip planarity, the number of active slip systems greatly influences post-yield tensile behavior, just as in disordered FCC metals. Single slip crystals exhibit maximum ductility and minimum work hardening, while multiple slip crystals exhibit minimum ductility and maximum work hardening [22,25]. Above the peak strength temperature, slip is much more homogeneous, and as a result the tensile behavior is much more isotropic.

It must be emphasized that deformation and properties above 700°C are strain rate-dependent. Additionally, it was shown earlier in this study [4,5] that with accumulating strain the rate-limiting deformation process changes from by-pass to shearing in PWA 1480 during a tensile test at intermediate temperatures and strain rates (800-950°C, 0.5%/min). This severely complicates deformation modeling and analysis in the high strain regime.

Creep Deformation

In general, the same deformation mechanisms occur

during creep as during tensile deformation [12,22,30], due in part to the lack of grain boundaries (and therefore grain boundary creep mechanisms). The temperature and stress regimes in which each type of mechanism is dominant may of course be different during creep. However, there are several deformation mechanisms which can occur during creep or slow strain rate deformation which are not normally observed in tensile loading. The first is the activation of a $\{111\}\langle 112 \rangle$ type slip system, and the second is a dynamic change in precipitate morphology and size during deformation.

Leverant and Kear [31] and later MacKay and Maier [32] showed that γ' shearing by $\{111\}\langle 112 \rangle$ slip systems is the dominant deformation mechanism during primary creep of Mar-M 200-type alloys in the range from 760 to 800°C. Also, it was shown earlier in this study [4,5] that PWA 1480 undergoes γ' shearing by $\{111\}a/3\langle 112 \rangle$ dislocations at 760°C and a slow strain rate of 0.5%/min. This type of mechanism must therefore be considered if the material is to be used under static or slow loading at 750 to 800°C.

An additional concern under creep conditions is microstructural stability. At very high temperatures, γ' coarsening and directional coarsening (rafting) can occur under load [33-35]. Not only can this changing precipitate structure greatly affect dislocation motion, but the coarsening itself can dominate plastic flow: Nathal and

Ebert [36] showed that the activation energy for steady-state creep of NASAIR 100 at 925 and 1000°C was equal to the activation energy for Ostwald ripening of the precipitates.

Cyclic Deformation

Under cyclic loading, all factors mentioned above are important for single crystal superalloys, and at least three others gain importance: elastic modulus (during strain controlled fatigue); slip reversibility; and cyclic hardening or softening.

When two different crystal orientations are tested under strain control to the same strain limits, differing elastic moduli produce vastly differing stress ranges and plastic strain ranges. This simple concept has been used to explain fatigue properties and lives in several single crystal alloys [37,38]. A much more fundamental representation of cyclic constitutive behavior and crack initiation behavior would be based on a comparison of constant inelastic strain range. Milligan et. al. [39] conducted such a study on Mar-M 200 single crystals. At 760°C, where planar octahedral slip dominated, cyclic properties could be understood on the basis of the number of active slip systems, fully consistent with Kear and Pearcey's monotonic work [22]. Multiple slip crystals exhibited rapid strain hardening, high stress ranges, and low cyclic lives, while single slip crystals with the same plastic strain range resulted in easy glide, low stress

ranges, and high cyclic lives. These trends are easily explained based on slip reversibility and its influence on strain hardening. Also consistent with the monotonic work, cyclic mechanical properties and deformation behavior at 870°C were much more isotropic (based on constant plastic strain range).

Gabb et. al. [26] studied the cyclic behavior of Rene' N4 crystals at 760 and 980°C. Among other findings, their results showed that the initial tension-compression asymmetry at yield extends to fatigue. In a related study, Gabb and Welsch [28] showed that in PWA 1480 fatigued at 650°C, the stress direction which had the higher initial flow stress (tension or compression) also cyclically strain hardened to a much higher degree. Clearly, the cube cross-slip mechanism plays an extended role in cyclic as well as monotonic deformation.

CHAPTER III

BACKGROUND: CONSTITUTIVE MODELING

Chapter II summarizes our current knowledge of the fundamental relationships between microstructural deformation mechanisms and structural properties for single crystal superalloys. It has been shown that our ability to quantitatively predict a property as simple as the yield strength from first principles is limited. Although our fundamental knowledge is incomplete, these alloys are still used structurally under very severe operating conditions. Therefore, designers and engineers need analytical relationships between stress, strain, temperature, and time in order to do structural analysis and life prediction. Such relationships are known as constitutive equations. To be useful for structural analysis, they must be three-dimensional, time-dependent, and accurate over the entire range of interest.

If the loads or displacements are small enough that the stresses at all points of the body are below the yield strength, the constitutive relation is simply the generalized Hooke's Law [40]. In this case, the current state of the material is path-independent, and structural analysis problems are generally solvable.

If the stresses at any point in the body exceed the elastic limit, plastic deformation will occur, and Hooke's Law will no longer describe the behavior. In this regime, constitutive relations are difficult to develop, for several reasons:

1. In general, the current state of the body is dependent on the path taken.
2. In the viscoplastic temperature regime, strain rate enters the constitutive relations.
3. In general, the relations are nonlinear.

Historically, the problem of developing constitutive relations has been attacked in three different ways. Although some connections do exist between the three, the approaches are fairly distinct. These are:

1. Materials science (pure microstructural).
2. Continuum mechanics.
3. Phenomological (hybrid).

Each will now be considered in detail.

Pure Microstructural Approach

Although the rate limiting step is temperature and rate dependent, dislocation glide is in most cases the primary mechanism of plastic flow in single crystal superalloys. Naturally, materials scientists have tried to model macroscopic behavior based on dislocation dynamics.

Most of this work has been done on single phase metals, either pure elements or solid solutions. Single crystals are studied to gain fundamental information, then a statistical approach can be used to model polycrystalline behavior. Some important results are now considered.

Dislocation Motion in the Absence of Strain Hardening

The plastic strain introduced into the crystal is calculated by the Orowan equation, Equation 2-1. Differentiating with respect to time and assuming a constant mobile dislocation density,

$$\dot{\gamma} = b\rho_m v(\tau) \quad (3-1)$$

where $v(\tau)$ is the average dislocation velocity as a function of stress. Assuming ρ_m and v can be measured, the plastic strain rate on any slip plane can be measured. Substituting the relationship between dislocation velocity and stress, Equation 3-1 would then be a valid constitutive equation. However, this approach is not useful in an engineering framework, for several reasons:

1. The dislocation density does not generally remain constant during deformation.
2. Measuring dislocation velocities and determining stress/velocity relationships is very difficult, especially when dealing with complex microstructures.
3. Except in the case of single slip, interactions

between gliding dislocations are very important, and these interactions are very difficult to handle in this type of model.

However, this is the most widely used approach, so it is now considered in detail.

The relationship between dislocation velocity and stress can be divided into two regimes, with a critical stress τ^* separating the two [41-43]. Below τ^* , dislocation motion is impeded by local barriers which the dislocations cannot penetrate by virtue of stress alone. Each barrier has a characteristic activation energy, Figure 9. Due to thermal vibration, these local obstacles can be overcome at a frequency of:

$$\nu = \nu_0 \exp(-\Delta H/kT) \quad (3-2)$$

where ν_0 = Attempt frequency,

ΔH = Local barrier activation energy.

Since long range slip will be limited by the slowest of these processes (i.e. the strongest barrier), the constitutive relation will be of the type:

$$\dot{\gamma} = C\nu \exp(-\Delta H^*/kT) \quad (3-3)$$

where ΔH^* is the activation energy associated with the strongest barriers, and C is a constant between 0 and 1. Specific forms of this equation are important in creep

analysis, and are treated later.

At stresses above τ^* , a significant number of dislocations are able to overcome all short-range barriers without thermal activation. In this regime, the theoretical terminal velocity is the shear wave velocity in the crystal [41-44]. However, viscous damping forces (phonon drag, "bond breaking" forces, etc.) reduce the terminal velocity. As Gilman [45] first pointed out, in many materials at low temperatures the flow rate below τ^* is almost negligible, then yielding occurs at τ^* . A simple analytical form which represents this behavior is [45]:

$$v = v_t \exp(-K/\tau) \quad (3-4)$$

where v_t = The terminal velocity,

K = "Drag stress", a material constant,

τ = Applied stress.

This form is consistent with data for many single phase materials at low temperatures [46]. However, as already mentioned, materials with complex microstructures are very difficult to treat with this approach, if for no other reason than the measurement of dislocation velocity is no easy task.

As summarized by Figure 10, below τ^* dislocation velocity is controlled by the Boltzmann statistics associated with overcoming short range barriers, while above τ^* the velocity is limited by viscous drag. As a result,

deformation processes will be rate-dependent below τ^* , but relatively rate-independent above τ^* .

Strain Hardening

The previous models make no provision for interactions between gliding dislocations, which is an obvious shortcoming. Unfortunately, the analytical description of strain hardening from a fundamental point of view is only well-developed for single phase alloys with high stacking fault energies. These alloys tend to develop well defined cells (subgrains) as deformation proceeds. Kuhlmann-Wilsdorf's "mesh-length" theory [47] for single crystals in the Stage II hardening regime relates flow stress to dislocation density, and predicts the hardening coefficient. The flow stress is given by:

$$\tau_y = \tau_0 + C_1 \mu b \rho^{1/2} \quad (3-5)$$

where τ_0 = Friction stress due to factors other than interacting dislocations,

C_1 = A constant,

μ = Shear modulus,

ρ = Total dislocation density.

The strain hardening coefficient is given by:

$$\partial \tau / \partial \gamma = (\partial \tau / \partial \rho) (\partial \rho / \partial \gamma) = C_1 \mu \rho / 2 C_2 C_3 \quad (3-6)$$

where C_2 and C_3 are also constants. The model successfully

correlates the behavior of this class of single phase metals, but again is not useful for engineering alloys due to the high degree of complexity of both the microstructures and dislocation interactions [43,47].

One Application - Creep Theory

At homologous temperatures (i.e. T/T_m in $^{\circ}K$) greater than about 0.5, thermally activated slip at stresses below τ^* becomes important. The result is a strain rate-dependent flow stress, and the occurrence of creep strains at stresses well below the flow stress. Since there are no grain boundaries in single crystal superalloys, the only creep mechanism which is important is dislocation motion (assuming stable precipitates).

Dislocation creep of most metals can be divided into primary and secondary (steady state) stages. Primary creep occurs first, upon loading. Analytically, it suffers from the same complications as the theory of strain hardening: rapidly changing dislocation densities and velocities. For this reason, models of primary creep are not well developed. A good review of the available models is given by Garafalo [48].

During steady-state creep, two mechanisms compete to govern the strain rate: hardening and recovery. At steady state:

$$d\tau = (\partial\tau/\partial\gamma)d\gamma + (\partial\tau/\partial t)dt = 0 \quad (3-7)$$

where the first term represents hardening and the second term represents recovery [47]. Under steady state in most metals, the dislocation density and structure remain relatively constant.

At intermediate stresses, almost all metals obey the semi-empirical Dorn Equation [49]:

$$\dot{\epsilon}_s = A(\sigma/E)^n \exp(-\Delta H/kT) \quad (3-8)$$

where $\dot{\epsilon}_s$ = Steady state creep rate,

σ = Applied stress,

E = Young's modulus,

ΔH = Activation energy.

Note the similarities between Equations 3-8 and 3-3. For pure metals, ΔH is found to be equal to the activation energy for self diffusion, indicating that diffusion is the rate-limiting step [48-50]. This leads to the formulation of several purely microstructural models based on the mechanisms of climb and jog dragging, both of which are limited by self diffusion [48-50]. Specific forms of the models are not considered here.

Equation 3-8 is often expressed in a slightly different, less empirical form [49,51]. Substituting the diffusion coefficient,

$$D = D_0 \exp(-\Delta H_{sd}/kT) \quad (3-9)$$

and introducing microstructural parameters to keep dimensional consistency, Equation 3-8 becomes:

$$\dot{\epsilon}_s kT/D\mu b = A(\sigma/E)^n \quad (3-10)$$

For pure metals and solid solutions, n is between 3 and 5. The constant A is strongly dependent on stacking fault energy and grain size [49,51]. Therefore, for pure metals the problem of modelling steady state creep is reduced to one of determining the diffusion characteristics and one structure-dependent constant.

Anelastic Strain and Back Stresses

When in the process of deformation the load level is reduced or the loading direction is reversed, the strain which is recoverable can have elastic as well as inelastic components. The recoverable inelastic strain is referred to as anelastic strain, and is usually attributed to the action of long range internal stresses which develop during deformation [48,51]. One obvious manifestation of anelastic strain recovery is the Bauschinger effect. The Bauschinger effect, which is caused by reversible dislocation motion, occurs during reversed cyclic deformation. For instance, the tensile CRSS can be reduced by the reversed motion of dislocation pile-ups which are formed during the compressive portion of the cycle. Two other effects also occur which

are very relevant to engineering alloys like superalloys: The first is the transient behavior which results after a stress dip in a creep test, and the second is the observation of apparently high stress exponents in creep of precipitation-hardened systems. Both of these phenomena can be treated and understood very well by introducing the concept of a back stress into the constitutive equation, as described below.

When an alloy is creeping under steady-state, constant stress conditions, it is generally believed that a stable structure exists. If the stress is suddenly reduced and the instantaneous strain rate is measured, one of the following occurs [51-54]:

1. If $\Delta\sigma$ is small, forward creep will re-commence at a rate slower than the steady-state value for virgin material;
2. If $\Delta\sigma$ is some critical value (Say $\Delta\sigma_c$), the strain rate will be zero;
3. If $\Delta\sigma > \Delta\sigma_c$, backwards creep occurs as the dislocation substructure readjusts to an equilibrium configuration.

In any case, after the transient period the material will resume steady-state creep at a rate equal to that of the virgin material. This retardation of the creep rate after the stress dip is attributed to back stress: the dislocation structures developed at high stresses cause long range

elastic stresses in the negative creep direction. Several fundamental models based on recovery kinetics [54,56-58] or viscous slip (through the Orowan Equation) [52,53,55] have been proposed.

When creep data from dispersion or precipitation hardened systems are fit to the Dorn Equation, high values of activation energy and stress exponent result. Stress exponents as high as 40 have been observed [58], as well as activation energies which are much higher than that for self diffusion [58]. Based on this observation, early investigators concluded that diffusion did not control the steady-state creep of these alloys [59]. However, introduction of the back stress concept changed this conclusion. High back stresses can be present in these alloys due to several factors. Differing elastic constants between matrix and precipitate can cause long range internal back stresses (see Eshelby [60] for a typical exact solution). Also, compatibility requirements around hard particles may necessitate cross slip and dislocation tangle formation in the region around the precipitate [61]. Finally, attractive forces at a particle interface may oppose climb, or forces which resist particle shearing can lead to back stresses. This has lead investigators to modify the Dorn Equation, using an "effective stress" [51-58,62-65]. The effective stress is the difference between the applied stress and the back stress, and the resulting

creep equation becomes:

$$\dot{\epsilon}_s = A'([\sigma - \Omega]/E)^{n'} \exp(-\Delta H/kT) \quad (3-11)$$

where Ω is the back stress. This type of model brings the stress exponent down into the range observed for pure metals, and yields activation energies equal to those for self diffusion. The result is satisfying, because all evidence indicates that creep deformation in these alloys is indeed controlled by diffusional processes, just as in pure metals.

Critique

The pure microstructural approach has had limited success in correlating constitutive behavior under very simple loading situations in simple materials. It is useful from the fundamental perspective, for it allows us to understand the effects of microstructural features on deformation more fully. However, the models are not useful for bulk deformation under general loading, due to the relative simplicity of the models, and the lack of a mechanism to account for transients, three dimensional stresses, and history. These shortcomings are best dealt with in a mechanics formulation.

Continuum Mechanics Approach

While materials science is concerned with microstructural deformation mechanisms, continuum mechanics

is concerned with modeling macroscopic behavior. Since microstructural effects are generally not considered, the development of powerful analytic relations is greatly simplified. However, the models are 3-Dimensional, rate dependent, and incorporate transient as well as steady-state behavior. These factors result in enormously complex models which are often far removed from the physical deformation mechanisms.

Classical Theory

The stress state at a point in a body generally depend on the current values and histories of strain, strain rate, and temperature. This can be formalized by the mathematical tool of functional analysis [66-68]. In one such framework, stress may be a functional of strain, strain rate, and temperature:

$$\sigma_{ij}[t] = \mathcal{F}_{t_0}^t (\epsilon_{ij}[\zeta], \dot{\epsilon}_{ij}[\zeta], T[\zeta]) \quad (3-12)$$

where σ_{ij} = Stress tensor,

ϵ_{ij} = Strain tensor,

t = Time,

T = Temperature,

ζ = Dummy (time) integration variable.

The functional must fulfill the requirements of rotation invariance and any material symmetry constraints. If the

functional is linear and continuous, it can be expressed as an integral. For example, if stress is a linear functional of strain only, the constitutive relation may be expressed as [68]:

$$\sigma_{ij}[t] = k_{ijpq}[t_0]\epsilon_{pq}[t_0] + \int_{t_0}^t k_{ijpq}[\zeta](\partial\epsilon_{pq}[\zeta]/\partial\zeta)d\zeta \quad (3-13)$$

(Here and throughout this dissertation, repeated indices imply summation over those indices). Any material symmetry which is present restricts the form and reduces the number of independent terms in the coefficient tensor \underline{k} . Equation 3-13 is a general linear constitutive relation for a material with memory, such as a linearly strain hardening metal. Obviously, the case of a rate independent linearly strain hardening metal is a very simple one, yet the constitutive relation is fairly complex, and the coefficient tensor can contain a large number of independent constants. This serves to show the difficulty in developing general constitutive relations for real materials. Although the classical theory has been successful in the areas of viscoelasticity and fluid dynamics, its application to viscoplastic metals has been hindered by the complexity of the relations and experimental difficulties in determining the form of the models and the constants.

Plasticity Theory

The theory of incremental plasticity is a constitutive theory for rate-independent plastic deformation of ductile metals [69,70]. As outlined below, it introduces several ideas which are important for most advanced theories, including the concepts of a yield surface and flow rule, as well as an analytical treatment of strain hardening.

If a material has some degree of symmetry, its yield strength values under different stress states may be related. For isotropic metals, Schmid's Law can be generalized to three dimensions in the form of the Tresca yield condition:

$$f[\sigma_{ij}] = \max\{|\sigma_i - \sigma_j|\}/2 \geq \tau_y \quad (3-14)$$

where σ_i = Principal stresses,

τ_y = Yield stress in pure shear.

The von Mises yield condition closely approximates the Tresca condition, and is more convenient mathematically:

$$f[\sigma_{ij}] = (s_{ij}s_{ij}/2)^{1/2} \geq \tau_y \quad (3-15)$$

where s_{ij} is the deviatoric stress tensor:

$$s_{ij} = \sigma_{ij} - \sigma_{kk}\delta_{ij}/3 \quad (3-16)$$

and δ_{ij} is the Kronecker delta. Note that the determination of the yield condition is reduced to a scalar equation, even under general 3-D loading.

The yield surface is a graphical representation of the yield condition in 3-D principal stress space. For isotropic metals which obey the von Mises condition, the yield surface is a cylinder whose axis coincides with the hydrostatic axis ($\sigma_1 = \sigma_2 = \sigma_3$). Inside the surface, the yield condition is not satisfied, so the stresses are elastic. Yielding occurs when the stress state reaches the surface. The intersection of the von Mises cylinder and the plane normal to the hydrostatic axis (the so-called π -plane) is a circle (Figure 11). By definition, the stress state cannot exceed the yield surface. If the stress state lies on the yield surface and $\dot{s}_{ij}(\partial f / \partial s_{ij}) > 0$, the material will strain harden. As a result, the yield surface will expand and/or translate. If the yield surface expands uniformly, the material is said to have undergone isotropic hardening, Figure 11(b). If the yield surface translates without changing shape, the material is said to have undergone kinematic hardening, Figure 11(c).

To simplify the constitutive relations under isotropic hardening, a scalar measure of strain hardening is adopted. Two commonly used parameters are:

$$dh = s_{ij} d\epsilon_{ij}^p \quad (3-17)$$

and

$$dh = (d\epsilon_{ij}^P d\epsilon_{ij}^P)^{1/2} \quad (3-18)$$

where $d\epsilon^P$ is the incremental plastic strain and h is the hardening parameter. The current value of h is an indication of the accumulated inelastic strain.

Under kinematic hardening, the current yield surface is fully defined by the original diameter and the current axis. The current axis in stress space is a tensor quantity, and it has traditionally been referred to as the "back stress", α_{ij} .

It has been experimentally determined that for small incremental plastic strains accumulated under proportional loading, the principal ratios of the plastic strain increment are equal to the principal ratios of the current stress deviator. (In other words, the direction of the incremental plastic strain is fully determined by the current stress state). For a material which undergoes both isotropic and kinematic hardening, the resulting flow rule is:

$$d\epsilon_{ij}^P = (s_{ij} - \alpha_{ij})d\lambda \quad (3-19)$$

where λ is a scalar multiplier. If the shape of the yield surface does not change during hardening, it is easy to derive the specific form of $d\lambda$, which will depend on the choice of the yield condition and hardening parameter. If kinematic hardening is introduced, a differential equation

governing the back stress evolution must also be determined. Under all these constraints, Equation 3-19, along with Hooke's Law, is a valid path-dependent constitutive model.

For time-dependent deformation, classical plasticity theory partitions the plastic strain rate tensor into rate-dependent and rate-independent components:

$$\dot{\epsilon}_{ij}^{in} = \dot{\epsilon}_{ij}^p + \dot{\epsilon}_{ij}^c \quad (3-20)$$

where $\dot{\epsilon}_{ij}^{in}$ = Total inelastic strain rate,

$\dot{\epsilon}_{ij}^p$ = Rate-independent "plasticity",

$\dot{\epsilon}_{ij}^c$ = Rate-dependent "creep".

The creep rate is determined empirically by previously mentioned methods. This treatment of time-dependent deformation is one of the limitations of plasticity theory in the area of high temperature materials. As already discussed, for superalloys "creep" and "plasticity" occur by the same mechanism, so this artificial division of the two mechanisms is neither justified nor wise.

Critique

The methods of classical mechanics have been very useful in developing a framework for analyzing general 3-D loading. This framework is the basis for all the advanced models. In addition, the simplification of the relations

(by using scalar quantities to replace tensors) has been very useful. The only major drawbacks are the inherent complexity of the relations, and the artificial separation of "creep" and "plasticity". Additionally, the models tend to become so far removed from the fundamentals of deformation that it is easy to lose sight of the true essence of the material behavior.

Phenomological Approach

The preceding discussion shows that the pure approaches (materials or mechanics) are highly developed and useful only in simple cases. In response to this, a new type of hybrid model has been developed which combines aspects of mechanics, curve fitting, and insight into materials science. This "unified viscoplastic" approach, which is based on mechanical state variables, is described below.

State Variables

The objective of state variable theory is to identify measurable phenomological parameters which fully characterize the current "state" of the material, independent of path. Obviously, the accumulated inelastic strain is not a state variable, because material parameters do not change during steady-state creep. Hart [71,72] proposed that a meaningful state variable for polycrystalline pure metals would be a "hardness parameter", which could be a room temperature hardness value or a yield

strength at constant strain rate. If the "hardness" is known, then all important mechanical properties of this simple class of materials can be determined without knowledge of prior history. Intuitively, this idea is appealing for simple pure FCC metals, because the hardness is directly related to the dislocation substructure, which is relatively path-independent in many cases for metals with high stacking fault energies.

Unified Viscoplastic Models

Modern constitutive theories are based on state variables, and do not partition "creep" and "plasticity". Since they often occur by the same mechanism, a single analytical expression (flow rule) is used. Two good reviews of the unified viscoplastic models are available [73,74]. As Walker summarizes [73], of the dozen or so current models, ten are of the same general form. These are referred to as "back stress / drag stress models" in reference to their two state variables. The first state variable is a tensor quantity referred to as the "equilibrium stress", or "back stress". This state variable allows the models to handle anelasticity, texture, the Bauschinger effect, and kinematic hardening. This state variable is qualitatively and physically similar to the back stress in the uniaxial steady-state creep models, Equation 3-11, and to the back stress in the classical plasticity flow rule, Equation 3-19. The second state variable is the

scalar "drag stress", which allows the models to handle isotropic hardening. Physically, the drag stress is similar to the scalar hardening parameter, q , in the classical plasticity model. The form of the flow rule is:

$$\dot{\epsilon}_{ij}^{in} = \psi \{ (s_{ij} - \Omega_{ij}) / K \} \quad (3-21)$$

where Ω_{ij} = Back stress state variable,

K = Drag stress state variable,

ψ = Model-dependent function.

Note the similarity in form between this flow rule and the classical plasticity flow rule. One significant difference, however, is that the unified models generally do not employ a yield surface. Instead, the form of ψ must be such that the plastic strain rate approaches zero as the "overstress", $(s_{ij} - \Omega_{ij})$, approaches zero.

The constitutive models respond to changes in the material through evolution of the state variables. In the most general case, the rate of change of the state variables will depend on a hardening term and recovery terms (static and dynamic). Again, the specific forms of the evolution equations are mathematically complex. The general forms are:

$$\dot{\epsilon}_{ij} = \psi_1 \{\dot{\epsilon}_{ij}^{in}\} - \psi_2 \{\epsilon_{ij} |\dot{\epsilon}_{ij}^{in}|\} - \psi_3 \{\epsilon_{ij}\} \quad (3-22)$$

and

$$\dot{K} = \phi_1 \{\dot{\epsilon}_{ij}^{in}\} - \phi_2 \{K |\dot{\epsilon}_{ij}^{in}|\} - \phi_3 \{K\} \quad (3-23)$$

The ψ 's and ϕ 's are model-dependent functions. The ψ_1 and ϕ_1 terms describe direct hardening. The ψ_2 and ϕ_2 terms describe dynamic recovery, as they are activated only in the presence of inelastic strain. The ψ_3 and ϕ_3 terms describe static recovery, as they are time activated even in the absence of inelastic strain.

These models have been successful in correlating complex deformation behavior in isotropic materials [75,76]. However, as discussed later, the models need to be substantially modified for application to superalloy single crystals.

A second class of unified viscoplastic model which relies on only one state variable has been developed by Bodner and co-workers [73,77,78]. The use of a single state variable simplifies the model, but also limits it: anelasticity and static recovery cannot be accurately modeled. The form of the flow rule is:

$$\dot{\epsilon}_{ij}^{in} = \psi \{s_{ij} \exp(\phi[Z])\} \quad (3-24)$$

where Z = The state variable,

ψ, ϕ = Functions of the second invariant of the stress deviator.

The state variable Z is considered a measure of the material's resistance to inelastic flow. It is not a tensor quantity, but its value depends on the sign of the ij^{th} component of the stress rate. Note the similarity between the flow rule and the Gilman dislocation velocity expression, Equation 3-4, on which the model was based. Z is analogous to Gilman's drag stress. Again, the evolution of the state variable is used to handle hardening and softening during deformation.

Anisotropic Models

Both types of models do a reasonable job of correlating isothermal constitutive behavior of isotropic materials. However, when the investigators tried to apply the models to single crystal superalloys, they could not correlate constitutive behavior as a function of orientation. As an example, consider the schematic shown in Figure 12 (from Reference 79). The isotropic Walker model which was fit to the $\langle 001 \rangle$ crystal data during cyclic loading at 870°C cannot correlate $\langle 111 \rangle$ crystal data at the same temperature. In Chapter II, it was shown that many investigators believe that primary cube slip occurs in $\langle 111 \rangle$ crystals at this temperature, but not in $\langle 001 \rangle$ crystals. Recognizing this, Walker and co-workers [80] and Stouffer and co-workers [81]

have both proposed anisotropic modifications of their viscoplastic models, with cube slip incorporated to handle the anisotropy. Additionally, both models incorporate a cube cross-slip term in the octahedral flow rule to model the anisotropy which occurs when octahedral slip dominates. Both models are based on classical crystal plasticity [82], which partitions the global inelastic strain rate into its components on each active slip system:

$$\dot{\epsilon}_{ij}^{in} = \sum_{\alpha, \beta} \{ \dot{\gamma}^{\alpha\beta} (l_i^{\alpha\beta} n_j^{\alpha} + l_j^{\alpha\beta} n_i^{\alpha}) / 2 \} \quad (3-25)$$

where $\dot{\gamma}^{\alpha\beta}$ = Crystallographic shear strain rate
on the α plane in the β direction,

$l_i^{\alpha\beta}$ = Unit vector in the β direction,

n_i^{α} = Unit normal to the α plane.

In the anisotropic models, a unified viscoplastic formulation is specified for each slip system, then each system's contribution to the total strain rate is added per Equation 3-25. Cube slip and octahedral slip are included:

$$\dot{\epsilon}_{ij}^{in} = \sum \dot{\epsilon}_{ij}^{in}(\text{Octahedral}) + \sum \dot{\epsilon}_{ij}^{in}(\text{Cube}) \quad (3-26)$$

The summations are taken over the number of active slip

planes, which must be determined experimentally. The tension-compression asymmetry and orientation dependence are modeled by the form and evolution of the state variables. Specific forms are detailed below.

Walker-Jordan Anisotropic Model [80]

The anisotropic Walker-Jordan constitutive model was developed for use in structural analysis of single crystal superalloys. Below is a summary of the functional form of the model in the isothermal case.

Assume that each of the twelve octahedral and six cube slip systems obey a unified viscoplastic flow rule in shear:

$$\dot{\gamma}_i = (\text{sign}[\tau_i - \Omega_i])(|\tau_i - \Omega_i|/K_i)^{\eta_1} \quad (3-27)$$

where $\dot{\gamma}_i$ = Inelastic strain rate on the i^{th} slip system,
 τ_i = Shear stress on the i^{th} slip system,
 Ω_i = Back stress state variable,
 K_i = Drag stress state variable
 η_1 = Constant.

As before, the evolution of Ω and K describes strain hardening, the Bauschinger effect, and stress relaxation. In this model, the octahedral drag stress state variable is used to handle all of the anisotropy associated with single crystal superalloys. It contains:

1. A "latent hardening" term, which attempts to capture

the effect of the number of active slip systems on strain hardening. (Discussed in Chapter IX).

2. A cube cross-slip term due to constriction stress.
3. A cube cross-slip term due to cross-slip stress.

The form of the evolution equation is:

$$\dot{K}_i = \left\{ \sum_{j=1}^{12} (h_{ji} - C_1 [K_i - K_i^O]) |\dot{\gamma}_j| \right\} - C_2 (K_i - K_i^O)^{\eta_2} \quad (3-28)$$

where h_{ji} = A "hardening modulus", which depends on the number of active slip systems. (Discussed in Chapter IX).

C_i, η_i = Temperature dependent material constants.

Additionally,

$$K_r^O = C_3 + C_4 \exp(C_5 \tau_c + C_6 \tau_s) \quad (3-29)$$

where τ_c = The constriction stress,

τ_s = The cross-slip stress.

Note the similarity between Equation 3-29 and the Lall, Chin and Pope model, Equation 2-7. (In fact, Equation 3-29 was based on Equation 2-7). The above equations illustrate that the drag stress contains a term which describes each important source of anisotropy that operates during

octahedral slip, and so theoretically the model should be capable of describing true material behavior. Of course, the structure of the model must be consistent with the deformation mechanisms.

The back stress state variable evolution is much more simple:

$$\dot{\Omega}_i = C_7 \dot{\gamma}_i - C_8 |\dot{\gamma}_i| \Omega_i - C_9 (\text{sign}[\Omega_i]) |\Omega_i|^{\eta_3} \quad (3-30)$$

As in the isotropic models, the three terms in the back stress evolution equation describe hardening, dynamic recovery, and static recovery, respectively.

For primary cube slip, an identical set of equations is developed, except there are no cube cross slip or latent hardening terms in the drag stress. The global strain rate is calculated per Equation 3-25.

Dame-Stouffer Anisotropic Model [81]

As above, the following is a summary of the functional form of the model in the isothermal case. The model is quite similar to the Walker-Jordan model, in that it sums the crystallographic shear strain rate on individual slip systems (including cube systems) to calculate the global strain rate. This model partitions the octahedral inelastic strain rate into two components, one for γ' shearing and another for creep-type deformation which is limited by

interstitial or vacancy diffusion:

$$\dot{\gamma}_{\{111\}}^{\alpha\beta} = (\dot{\gamma}_{\{111\}}^{\alpha\beta})_1 + (\dot{\gamma}_{\{111\}}^{\alpha\beta})_2 \quad (3-31)$$

Assume that a Bodner-Stouffer type flow rule describes each type of deformation for each slip system in shear. As an example, the flow rule for γ' shearing would be:

$$(\dot{\gamma}_{\{111\}}^{\alpha\beta})_1 = (C_1 \text{sign}[\tau^{\alpha\beta}]) \exp([-Z_1^{\alpha\beta} / |\tau^{\alpha\beta}|]^{\eta_1}) \quad (3-32)$$

where Z_1 is the state variable which describes the resistance to inelastic deformation by γ' shearing. (No sum is taken over α and β). Similarly, the flow rule for diffusion-limited deformation

is:

$$(\dot{\gamma}_{\{111\}}^{\alpha\beta})_2 = (C_2 \text{sign}[\tau^{\alpha\beta}]) \exp([-Z_2^{\alpha\beta} / |\tau^{\alpha\beta}|]^{\eta_2}) \quad (3-33)$$

The total octahedral strain rate is calculated per Equation 3-31.

As in the Walker-Jordan model, anisotropy due to cube cross-slip is accounted for by the expression for the state variable:

$$Z_1^{\alpha\beta} = C_3 + Z^{\alpha\beta} + C_4 \tau_c + C_5 \tau_s \quad (3-34)$$

where τ_c = The constriction stress,

τ_s = The cross-slip stress.

Z = Strain hardening term.

The strain hardening term evolves as follows:

$$\dot{Z}^{\alpha\beta} = C_6 (C_7 - Z^{\alpha\beta}) \tau^{\alpha\beta} \dot{\gamma}^{\alpha\beta} \quad (3-35)$$

Again, no sum is taken over α and β . A similar expression is developed for Z_2 . Although they acknowledge that it is probably necessary, the authors do not include a latent hardening term or a recovery term. However, the additional degree of complexity introduced by the bi-modal deformation mechanism and flow rule can probably do an adequate job of modeling dynamic recovery effects.

Similar to the Walker-Jordan model, a set of equations governing cube slip which are virtually identical to the octahedral equation, with the exception of the lack of cube cross-slip terms in the state variable evolution. The octahedral shear strain rates are then added to the cube shear strain rates in a linear fashion (with the appropriate geometric constants).

Critique: The models appear to be a major step forward in the effort to link microstructural deformation mechanisms with macroscopic constitutive behavior. They are based on

state-of-the-art descriptions of microstructural behavior, and they are able to overcome the orientation-dependent breakdown of the isotropic models in limited testing programs. The physical basis of the models will be discussed in light of our experimental results in Chapter IX.

CHAPTER IV

EXPERIMENTAL PROCEDURES

Material

The composition of the PWA 1480 alloy is given in Table 1. Single crystal rods and slabs were cast by the withdrawal method and heat treated by TRW, Inc. The heat treatment procedure consisted of:

1. Solutionize @ 1285°C, 4 hrs, rapid cool.
2. Age @ 1080°C, 4 hrs, rapid cool.
3. Age @ 870°C, 32 hrs, air cool.

The orientations of the crystals were determined by the Laue back-reflection X-ray technique. The baseline $\langle 001 \rangle$ specimens had tensile axes within 10° of $\langle 001 \rangle$. The off- $\langle 001 \rangle$ specimens had orientations near $\langle 123 \rangle$. The actual tensile axis orientations of the $\langle 123 \rangle$ specimens are plotted in Figure 13. Throughout this dissertation, these specimens are referred to as " $\langle 123 \rangle$ crystals" even though the orientations deviated slightly from $\langle 123 \rangle$.

The $\langle 001 \rangle$ specimens were machined from $\langle 001 \rangle$ oriented slabs and rods. The specimen configurations are shown in Figure 14. The $\langle 123 \rangle$ specimens were cut at an angle from the $\langle 001 \rangle$ slabs. Since this did not yield a sufficiently long crystal to fabricate the LCF specimens, In 718 rods

were inertia welded to both ends of the <123> crystals by Manufacturing Technology Inc (Mishawaka, Indiana). LCF specimens were machined from these composites such that the inertia weld was in the thick portion of the specimen, away from the gage length. Only one specimen out of 17 failed in the inertia weld.

Tensile Testing

Tensile tests were conducted in a computer controlled SATEC CATS servohydraulic testing system. The high temperature extensometer was fabricated by attaching alumina probes to an MTS clip-on gage. The specimens were heated by a 2.5 kW Lepel induction heater which was controlled by an Omega PID controller. The temperature was measured by chromel-alumel thermocouples which were welded to the gage length. A temperature gradient of $\pm 3^{\circ}\text{C}$ was maintained over the gage length.

Interrupted tensile tests were conducted in strain control to pre-determined plastic strain levels. The SATEC computer controller had the capability of controlling the test in strain control, while monitoring the real-time calculated value of plastic strain. Plastic strain was calculated and monitored as "combinatorial feedback" via the following equation:

$$\epsilon_p = \epsilon_t - \sigma/E \quad (4-1)$$

where ϵ_p is the plastic strain and ϵ_t is the total strain. The computer ended the test (returned to zero load) after the desired plastic strain level was obtained. The actual test conditions are given in Chapter V.

LCF Testing

Low cycle fatigue tests were conducted on the same testing system. The only difference between the tensile tests and the fatigue tests was that the thermocouples were welded to the specimen shoulders (in the thick section) instead of the gage length to avoid crack initiation. A calibration specimen was used to determine the temperature profile and the relationship between the shoulder temperature and the gage length temperature. One measure of the repeatability of temperature control from specimen to specimen was the relative temperature measured at the top and bottom shoulder thermocouples. Based on this criterion, the repeatability was excellent for <001> specimens. However, the <123> specimens (which were inertia welded) sometimes exhibited significant deviations from the calibration specimen ($\sim 20^\circ\text{C}$). This was due to variations in the quality of the inertia welds, which directly affects heat conduction out the ends of the specimen.

Fully reversed (tension-compression) tests were conducted under total strain control. A triangular strain waveform was used. The total strainrange was kept at a constant level throughout the test. Stress-strain data was acquired by computer and conventional analog means. Again, specific test conditions are given in Chapter V.

Microstructural Evaluation

Metallography

Samples were sectioned, mounted, polished and etched for microstructural evaluation. The etchant consisted of 33% nitric acid (70% concentration, reagent grade), 33% acetic acid (98% concentration, reagent grade), 33% distilled water, and 1% hydrofluoric acid (52% concentration, reagent grade).. Photomicrographs were taken on a Leitz metallograph and Cambridge SEM.

Acetate surface replicas were used to study slip band behavior at low temperatures. The acetate film was saturated with a solution of methyl acetate, then allowed to conform to the specimen surface. After drying, the film was removed and mounted on a glass slide. Replicas were examined under reflected lighting conditions on the Leitz metallograph at 100X.

Transmission Electron Microscopy

Thin foils were prepared for TEM from the as-heat treated material and the tested specimens. It was found

that the use of conventional disk punching equipment deformed the material, so this technique was not used. Instead, a 3 mm rod was obtained from the center of the specimens by electric discharge machining (EDM). A copper tube with a 1/8 inch inside diameter was used as the EDM tool. The rod was then sliced to 0.2 mm thickness on a high speed sectioning saw using a SiC blade. These disks were then electropolished until perforation in a Struers Tenupol unit, using a solution of 5% perchloric acid (70% concentration, reagent grade) and 35% butyl cellusolve (Purified grade ethylene glycol monobutyl ether) in methanol. Polishing temperature was -25°C , and the voltage was 8.5 to 12 volts, depending on the condition of the solution and the size of the holder. See reference 5 for further details.

Foils were studied with a JEOL 100C TEM operating at 100 kV. Appendix A describes the methods used to determine crystal orientations, and Appendix B describes methods used for dislocation and stacking fault analyses.

CHAPTER V

RESULTS: MECHANICAL BEHAVIOR

Tensile Deformation of $\langle 001 \rangle$ Crystals

As summarized in Chapter II, the tensile deformation behavior of $\langle 001 \rangle$ crystals was studied in detail in an earlier phase of this work. In that study, however, the low temperature regime (from 20-705°C) was not fully characterized. This temperature regime is now considered.

Figure 15 shows average values (taken from three studies) [7-9] of the CRSS of $\langle 001 \rangle$ PWA 1480 crystals as a function of temperature. It shows that the CRSS decreases from 20 to 400°C, and then rises to a maximum at about 750°C. The mechanism responsible for this local minimum at about 400°C has been neither understood nor explained. In order to study this phenomenon, interrupted tensile tests were conducted at 20, 200, 400, 600, 705, and 760°C. The strain rate was 0.5%/minute. Average values are shown in Figure 16, and the data are contained in Appendix C. In some cases, only one test was conducted, to the statistical significance of the strength values is not known.

Figure 16 shows the local maxima at 20 and 760°C, in agreement with the published data. The local minimum at 400°C is not as distinct in our data. Duplicate testing was

not possible in the intermediate temperature regime due to a limited number of specimens. These tests were conducted primarily to generate specimens for the TEM studies which are presented in the next chapter.

It should be noted that Heredia and Pope [29] did not observe the local minimum at 400°C in their study of PWA 1480. However, they used a single specimen for a sequence of tests over the entire temperature range, so prior history effects may have influenced their results. A very recently published study of PWA 1480 [83] yielded trends very similar to those seen in Figure 15, thus further supporting the proposal that Heredia and Pope's data are not representative of virgin material behavior.

In addition to the temperature dependence of the CRSS, the initial strain hardening behavior was strongly temperature-dependent. The stress/strain curves of the interrupted tensile tests are shown in Figure 17. It is clear that the degree of strain hardening increased with temperature from 20 to 760°C (Although the degree of strain hardening at 20°C was slightly higher than at 200°C). This is easily quantified. Inspection of Figure 17 shows that the stress/strain curves in this strain regime may be approximated very well by a bi-linear (elastic - linear plastic) model. (This ignores the transition region, which is non-linear up to no more than 0.1% plastic strain). The degree of strain hardening can be estimated by calculating

the slope, $d\sigma/d\epsilon$, in the linear plastic regime. As an objective (but arbitrary) measure, consider the slope between the limits of 0.1 and 0.2% plastic strain. This slope is plotted vs. temperature in Figure 18, which reinforces the conclusions that can be drawn from the curves in Figure 17: The behavior changed from that of a perfectly plastic material (no strain hardening, $d\sigma/d\epsilon = 0$) at 20°C to that of an intensely strain hardening material at higher temperatures. Additionally, the degree of strain hardening at 705 and 760°C increased as the strain rate decreased (Figure 18). Both of these trends are indicative of a thermally activated process. However, the magnitude of the strain rate effect may not be statistically significant, as seen in Figure 18.

In order to study strain hardening in the regime of higher plastic strains, tests were conducted to 2.5% plastic strain at 20 and 705°C. The stress/strain curves are shown in Figure 19, which shows that the perfectly plastic behavior at 20°C extended from the yield point to at least 2.5% ϵ_p . Also consistent with the initial yield behavior, strain hardening at 705°C continued until a "saturation stress" was reached, at a stress level about 40% above the yield stress.

Orientation Effects and Tension/Compression Asymmetry

As described in Chapter II, previous investigators [7,12,27-29] who have studied PWA 1480 and similar alloys have found that the γ' cube cross-slip model correlated orientation-dependent and stress direction-dependent mechanical properties very well. In this study, a limited set of tests was conducted, for two reasons: First, to further study the problem, especially as related to thermally activated strain hardening; and second, to generate specimens for TEM studies. The TEM studies are particularly relevant, since the deformation mechanisms which have been proposed to this point have not been documented on a scale finer than slip-trace analysis.

In addition to the $\langle 001 \rangle$, crystals near $\langle 123 \rangle$ were studied. These crystals are ideal for isolating variables related to cube cross-slip: They are oriented for single slip when octahedral slip operates, thus eliminating the effects of intersecting slip systems. Additionally, they are oriented such that the constriction stress $\tau_{(111)[121]}$ has the opposite sense than the constriction stress in $\langle 001 \rangle$ crystals. (Figure 13).

Orientation Effects

Interrupted tensile tests were conducted on $\langle 001 \rangle$ and $\langle 123 \rangle$ crystals from 20 to 927°C. CRSS results are shown in Figure 20, using two different definitions of the CRSS:

0.05 and 0.2% plastic offset. This proves to be necessary to separate early strain hardening effects from initial yielding effects.

Figure 20 and Appendix C show that the highest degree of anisotropy was observed at 705°C. $\langle 001 \rangle$ crystals were about 30% stronger than $\langle 123 \rangle$ crystals at this temperature, and the degree of anisotropy was larger at the slower strain rate. Additionally, the apparent CRSS anisotropy increases as the offset strain definition of yield increases from 0.05% to 0.2%. All four observations (the sense of the anisotropy, the increasing amount of anisotropy from 20 to 705°C, the increasing amount of anisotropy at slower strain rates, and the increasing amount of anisotropy at larger plastic strains) are fully consistent with the proposed thermally activated cross-slip strain hardening mechanism.

At 20°C, the degree of anisotropy was significantly smaller than at 705°C. (The CRSS values for $\langle 001 \rangle$ and $\langle 123 \rangle$ crystals differed by only about 10%). Again, $\langle 001 \rangle$ crystals were stronger, in agreement with the cross-slip model.

Consistent with the CRSS results, the stress/strain behavior of $\langle 001 \rangle$ and $\langle 123 \rangle$ crystals in the low strain regime (below 0.25% ϵ_p) was independent of orientation at 20 and 927°C. At 20°C, the $\langle 123 \rangle$ crystals behaved in a nearly perfectly plastic manner (Figure 21), just as the $\langle 001 \rangle$ crystals did. One significant difference, however, was that deformation in the $\langle 123 \rangle$ crystals was extremely

heterogeneous. A localized zone of intense deformation formed and grew (as observed on the specimen surface), similar to the behavior of Luder's bands in low carbon steels. This band, which is shown in Figure 22, corresponded exactly to the primary octahedral slip plane, indicating localized shearing on $\{111\}$ slip planes.

At 927°C, the CRSS anisotropy was also smaller than at 705°C. At a strain rate of 0.5%/minute, the CRSS was essentially the same for $\langle 001 \rangle$ and $\langle 123 \rangle$ crystals. At 50%/minute, there was about a 10-15% difference in CRSS, and the sense of the anisotropy was again consistent with the cube cross-slip model. It will be shown later that the anisotropy seen at 927°C and 50%/minute was due to a difference in deformation mechanism between the two orientations; $\langle 001 \rangle$ crystals deformed exclusively by γ' bypass, while some γ' shearing occurred in $\langle 123 \rangle$ crystals.

As expected, at 705°C where the degree of anisotropy in the CRSS depended on the definition of yield, the stress/strain behavior was orientation-dependent. As already mentioned, $\langle 001 \rangle$ crystals strain hardened rapidly after yield. $\langle 123 \rangle$ crystals behaved in a more complicated manner (Figure 21). At the slow strain rate, a sharp yield point occurred followed by rapid unloading. (This unloading was a direct result of the test being conducted at a constant (slow) strain rate. The fast moving dislocations created a high plastic strain rate, so the computer

controller reduced the load in order to try to maintain its desired total strain rate). The crystals then strain hardened to a stress at or slightly above the original yield stress, upon which another instantaneous load drop occurred, and so on. Each load drop was accompanied by the appearance of a discreet slip trace on the specimen surface (Figure 23). It appears from the width of the slip traces that shearing probably occurred on several closely spaced parallel slip planes. Although each "slip burst" strain hardened, the macroscopic stress/strain curve (ignoring unloading) appeared almost perfectly plastic. This was probably due to the continuing activation of fresh dislocation sources on parallel slip planes, followed by a short period of relatively easy glide.

At the higher strain rate at 705°C, the crosshead velocity was high enough to maintain constant load, and as a result the macroscopic stress/strain behavior was almost perfectly plastic (Figure 21). Many fine slip traces were observed, even at low plastic strains.

<123> crystals were also tested to 2.5% plastic strain at 20 and 705°C. Again consistent with a thermally activated strain hardening mechanism, the crystals remained nearly perfectly plastic at 20°C, but hardened at 705°C (Figure 24). However, the magnitude of the "saturation stress" was only 15% above the yield stress, which is much lower than the 40% value observed in the <001> crystals.

Tension-Compression Asymmetry

Interrupted compression tests were conducted on $\langle 001 \rangle$ and $\langle 123 \rangle$ crystals at 20 and 705°C, at a strain rate of 0.5%/minute. Duplicate tests were conducted. Average results are shown in Figure 25. This figure shows that there was a significant (10-25%) tension-compression asymmetry in both orientations at 705°C, independent of the definition of CRSS. At 20°C, there was no significant anisotropy in the $\langle 123 \rangle$ orientation, and the anisotropy observed in the $\langle 001 \rangle$ orientation was not as great as at 705°C.

The sense of the anisotropy was fully consistent with Miner's modification of the cube cross-slip model (Equation 2-8): The tensile CRSS was higher than the compressive CRSS in $\langle 001 \rangle$ crystals, while the compressive CRSS was higher than the tensile CRSS in $\langle 123 \rangle$ crystals.

Figure 26 shows the stress/strain curves in both tension and compression at 20 and 705°C. Again, the behavior was much more orientation-dependent at 705°C than at 20°C. At 20°C, both orientations behaved close to perfectly plastic in tension and compression. At 705°C, there was a strong effect of stress direction in both the $\langle 001 \rangle$ and $\langle 123 \rangle$ crystals. The behavior of the $\langle 123 \rangle$ crystals was again complicated by the "slip burst" behavior. $\langle 001 \rangle$ crystals strain hardened much more in tension ($d\sigma/d\epsilon = 46$ GPa) than in compression ($d\sigma/d\epsilon = 9$ GPa). Since both

tensile and compressive loading activate the same number of slip systems (four {111} planes for $\langle 001 \rangle$ crystals), this indicates that early strain hardening of $\langle 001 \rangle$ crystals was dominated by cube cross-slip, not by intersecting slip systems.

As before, the macroscopic stress/strain behavior of $\langle 123 \rangle$ crystals at 705°C was complicated by the heterogeneous "slip burst" behavior, Figure 26(b). However, two points can still be made. First, the compression tests did harden slightly more than the tensile tests, in agreement with the cube cross-slip model. Second, and more importantly, the mechanical behavior was not completely independent of the number of active slip systems: The easy glide seen after each slip burst occurred in tension as well as compression in the $\langle 123 \rangle$ crystals. If the behavior was completely controlled by cube cross-slip, there should have been a big difference in behavior in tension vs. compression, as there was in the $\langle 001 \rangle$ crystals.

Cyclic Deformation

Fully reversed, strain controlled low cycle fatigue tests were conducted to study cyclic deformation. The baseline study was conducted on $\langle 001 \rangle$ crystals at a strain rate of 50%/minute. In order to fully characterize deformation behavior, the following variables were studied:

Temperature: Tests were conducted at 20, 200, 400, 600, 705, 927, and 1093°C.

Strain Rate: Tests were conducted at 0.5 and 50%/min. at 705, 927, and 1093°C.

Strain Level: Tests were conducted at two different strain levels at 20, 705, 927 and 1093°C, 50%/min.

Number of Cycles: Tests were run to failure and to steady-state stress response. In some cases, a test was interrupted prior to steady-state.

Orientation: Tests were conducted to failure on <123> crystals at 20, 705, and 927°C at both strain rates.

Due to the widely varying elastic moduli and strengths as a function of temperature, orientation and strain rate, it is virtually impossible to keep a meaningful variable constant throughout such a large test matrix. Within a given test, the total strain range, $\Delta\epsilon_t$ was kept constant. When studying plastic deformation, it would be much more meaningful to compare tests conducted under different conditions which had the same plastic shear strain range, $\Delta\gamma_p$. By using projections based on the monotonic yield strengths (and limited trial and error), it was possible to generate a complete set of tests (one at each condition outlined above) which had substantially similar $\Delta\gamma_p$'s. With the exception of two tests with slightly different $\Delta\gamma_p$'s, each of these tests had a saturated $\Delta\gamma_p$ between 0.03% and 0.08%. For completeness, Appendix D contains plots of the

cyclic data for this entire set of tests. Major conclusions from this data set are summarized below.

General Observations

The cyclic mechanical behavior can be separated into the same two temperature regimes as the monotonic behavior: Low temperatures, 705°C and below; and high temperatures, 927°C and above. Low temperature behavior was characterized by high strengths, cyclic strain hardening, orientation dependence, stress direction dependence, and a relatively low degree of strain rate sensitivity. Conversely, high temperature behavior was characterized by low strengths, cyclic stability or slight strain softening, isotropic behavior, and a relatively high degree of strain rate sensitivity.

Tension-Compression Asymmetry

At low temperatures, the tension-compression asymmetry seen in the CRSS of virgin crystals extended to the cyclic yield strength. Figure 27 shows a plot of τ_{\max} in tension and compression vs cycle for typical $\langle 001 \rangle$ and $\langle 123 \rangle$ crystals tested in fully reversed, strain controlled fatigue. The tension-compression asymmetry was about 10% of τ_{\max} , and the asymmetry persisted during cycling. The asymmetry was consistent with the cross-slip model: $\langle 001 \rangle$ crystals were stronger in tension, $\langle 123 \rangle$ crystals were stronger in compression. The data in Appendix D show that

these trends were followed in every low temperature test. Additionally, duplicate tests and tests at higher strain ranges (whose data are contained in Appendix E) were fully consistent.

At high temperatures, where the CRSS was isotropic, no tension-compression asymmetry occurred. Figure 28 and Appendix D demonstrate that the values of τ_{\max} in tension and compression were identical at 927°C, 0.5%/minute, and at 1093°C, both strain rates.

One significant orientation effect was observed which was related to the tension-compression asymmetry. Figure 29 shows that at 927°C and 50%/minute, the $\langle 001 \rangle$ crystal exhibited no asymmetry, while the $\langle 123 \rangle$ crystal exhibited asymmetry which was comparable to the low temperature tests. From this result, it appears that the transition temperature at constant strain rate may be a function of orientation. This is consistent with the CRSS results discussed earlier, and will be shown to be consistent with the deformation behavior in the next Chapter.

Cyclic Strain Hardening

At constant $\Delta\epsilon_t$, cyclic strain hardening manifests itself in the form of increasing $\Delta\sigma$ and/or decreasing $\Delta\epsilon_p$. At low temperatures, $\langle 001 \rangle$ and $\langle 123 \rangle$ crystals cyclically strain hardened, as would be expected from the monotonic stress-strain curves. Figure 30 shows the response of a typical $\langle 001 \rangle$ crystal tested at low temperature. During the

first five cycles, $\Delta\tau$ increased and $\Delta\gamma_p$ decreased in response to the plastic deformation. Of course, the degree of strain hardening was a function of the plastic strain range.

The macroscopic behavior of $\langle 123 \rangle$ crystals was again complicated by the "slip burst" mechanism. Figure 31 shows the response of a typical $\langle 123 \rangle$ crystal tested at low temperature. During the first ten cycles, $\Delta\tau$ increased. Unlike the $\langle 001 \rangle$ crystals, $\Delta\gamma_p$ first increased, then decreased. This apparent strain softening after the first cycle was probably due to the easy glide seen after the activation of the first dislocation sources. After a relatively short easy glide period, the active slip planes hardened, and $\Delta\gamma_p$ decreased. This sequence of easy glide followed by hardening can be seen clearly in the evolution of the stress-strain hysteresis loops, Figure 32. The first few loops were shaped like parallelograms as a result of elastic-perfectly plastic behavior. The loops seen at steady-state were narrow, and did not exhibit the sharp yield point, which is typical of a high strength, strain hardening material. Although there are not enough test results at identical $\Delta\gamma_p$'s to do a quantitative study, inspection of the data in Appendix D indicates that the $\langle 001 \rangle$ crystals strain hardened more than the $\langle 123 \rangle$ crystals. For the same initial $\Delta\gamma_p$, the reduction in $\Delta\gamma_p$ during cycling appears to have been about a factor of two greater

in $\langle 001 \rangle$ crystals. This may indicate another effect of the number of active slip systems. $\langle 123 \rangle$ crystals are expected to exhibit a higher degree of slip reversibility. This is supported by slip trace analysis. Figure 33 shows replicas of the specimen surfaces of both $\langle 001 \rangle$ and $\langle 123 \rangle$ crystals fatigued at 20°C . The $\langle 123 \rangle$ crystal exhibited very parallel, planar offsets, Figure 33(a). Conversely, the $\langle 001 \rangle$ crystal exhibited wavy slip traces indicative of the operation of intersecting slip systems or cross-slip, Figure 33(b).

At high temperatures, the strain hardening behavior was isotropic. The cyclic stress-strain behavior was relatively stable, showing slight strain softening, especially at 1093°C , 0.5%/minute strain rate.

Back Stress

The Bauschinger effect can be quantified to give an objective measure of deformation induced back stress. Define the back stress as:

$$\tau_b = \tau_0 - \tau \quad (5-1)$$

where τ_b = Back stress,

τ_0 = CRSS (at 0.05% offset) of the virgin material,

τ = CRSS (at 0.05% offset) measured during cycling.

Define the normalized back stress as:

$$\tau_B = (\tau_0 - \tau) / \tau_0 \quad (5-2)$$

The steady-state values of τ_b and τ_B for similar $\Delta\gamma_p$'s are shown in Figures 34 and 35. These figures show that high normalized back stresses (0.6 to 0.95) developed in both orientations over the entire temperature range. There is a large amount of scatter in the data, so comparisons between testing conditions are not meaningful. This scatter is probably due to the fact that the plastic strain ranges were small, on the order of the plastic offset used to define the CRSS.

Even though the scatter in the data is extensive, there is one clear difference in back stress which is easily seen in Figures 34 and 35. At 705°C, <123> crystals developed relatively small back stresses at both strain rates. The values of the normalized back stresses were between 0.08 and 0.2, which is a factor of at least four lower than the average, and well outside the scatter band of the rest of the data.

Summary

As postulated earlier, the mechanical behavior of PWA 1480 can be divided into low temperature and high temperature regimes. At low temperatures, the material is highly anisotropic, exhibits a tension/compression asymmetry, strain hardens, and deforms very heterogeneously. At high temperatures, the material is isotropic and highly

rate sensitive.

The low temperature behavior was fully consistent with the cube cross-slip model. The model qualitatively explains the orientation dependence of the CRSS and the tension-compression asymmetry, as well as the increased amount of strain hardening at higher temperatures.

CHAPTER VI

RESULTS: DEFORMATION BEHAVIOR

As described in Chapter II, it was found earlier in this study [4,5] that the deformation behavior of $\langle 001 \rangle$ crystals subjected to interrupted tensile tests and creep tests fell into two temperature regimes. At low temperatures, the dominant mechanism was planar γ' shearing. At high temperatures, the dominant mechanism was γ' by-pass. In this phase of the project, the study has been expanded to include the effects of orientation and cyclic deformation. Also, a more thorough study of low temperature deformation has been conducted to try to determine the mechanism responsible for the shape of the CRSS vs Temperature curve.

In general, the trends found earlier are applicable to cyclic deformation and deformation of $\langle 123 \rangle$ crystals. High temperature deformation occurred by γ' by-pass, and low temperature deformation occurred by γ' shearing. However, two new effects were discovered. First, the low temperature shearing mechanism was found to be much more complicated than originally believed. By fully understanding this mechanism, it now appears possible to explain the shape of the CRSS curve. Second, in agreement with the apparent orientation dependence of the high temperature boundary at

high strain rate, γ' shearing was observed at 927°C, 50%/minute strain rate in $\langle 123 \rangle$ crystals. Since the high temperature behavior was the least complicated, it is discussed first.

High Temperatures

Both $\langle 001 \rangle$ and $\langle 123 \rangle$ crystals subjected to interrupted tensile tests and LCF tests at high temperatures (927°C and above) deformed by γ' by-pass. Figure 36 shows typical deformation structures in cyclically strained $\langle 001 \rangle$ crystals. In Figure 36(a), the structure which developed during an LCF test at 927°C, 0.5%/minute is shown. All the dislocations are either in the γ matrix or on the γ/γ' interface. Figure 36(b) shows the structure which developed during LCF at 1093°C, 50%/minute. Under these conditions, the interfacial dislocations formed a regular array. These structures are nearly identical to those which developed during monotonic tensile and creep tests conducted earlier [4,5].

$\langle 123 \rangle$ crystals tested under similar conditions contained similar structures. Figure 37 shows typical by-pass structures which developed at 927°C. Again, all the dislocations in this area are in the matrix or interface. The parallel dislocations, which look like a low temperature slip band, are actually not. They are simply a parallel array of interfacial dislocations.

Recall from Chapter IV that the $\langle 123 \rangle$ crystal tested at 927°C , 50%/minute exhibited anisotropy similar to the low temperature tests. Deformation structures observed after this test and the interrupted tensile test at the same rate contained several dislocation within the γ' precipitates, as shown in Figure 38. Although the majority of dislocations are interfacial (Figure 37), these few dislocations trapped in the γ' (which is never observed in the virgin material) indicate that some shearing did occur during the test.

It was found earlier that at 760°C and slow strain rates, extensive γ' shearing by $a/3\langle 112 \rangle$ dislocations occurred, leaving superlattice intrinsic stacking faults (S-ISF's) behind [4,5]. This mechanism was also observed infrequently at higher temperatures. In the present study, occasional faults have been observed in $\langle 123 \rangle$ crystals tested at 927°C , as shown in Figure 39. As discussed later in this chapter, these faults were identified as S-ISF's also.

The correlation between deformation substructures and mechanical behavior is exact. At high temperatures, isotropic behavior was observed when γ' by-pass was observed. Since the γ' is not sheared during by-pass, it's intrinsic properties cannot affect deformation, and so isotropic behavior is to be expected. The only testing condition at 927°C or above which resulted in a tension-compression asymmetry was the $\langle 123 \rangle$, 50%/minute test. This

condition was also the only one which contained any evidence of γ' shearing, in both tension and LCF.

Low Temperatures

In the temperature range from 20-760°C, it was reported earlier that deformation occurred by γ' shearing by the $\{111\}a/2\langle 110 \rangle$ system [4,5]. In the current study, it has been found that this is an incomplete description. At 600°C and above, it is completely valid. At 400°C and below, however, it has been found that extensive γ' shearing also occurs by the $\{111\}a/3\langle 112 \rangle$ system. This mechanism profoundly affects the mechanical properties of the material.

705 and 760°C

In this temperature range, at both strain rates and orientations, the dominant deformation mechanism in tension and LCF was γ' shearing by $\{111\}a/2\langle 110 \rangle$ dislocations. (Recall that the dislocation analysis procedures are reported in Appendix B). Figure 23 shows the octahedral slip traces generated by shearing in the early stages of a tensile test on a $\langle 123 \rangle$ crystal at 705°C. Figure 40 shows a typical deformation substructure developed in a $\langle 123 \rangle$ crystal tested at 705°C. There were clearly many dislocations trapped within the γ' when the test was interrupted. Most of these dislocations have Burgers vectors parallel to $[\bar{1}01]$, the primary octahedral slip

direction.

Figure 41 shows a typical substructure developed at 705°C in $\langle 001 \rangle$ crystals. In addition to several areas of interfacial dislocation tangles, there are a large number of straight dislocation segments within the γ' . This structure was very common in crystals tested in this temperature regime. Dislocation analysis revealed that the majority of these straight dislocations are nearly pure screw in character. In Figure 41, for instance, dislocations of three different $\langle 110 \rangle$ Burgers vectors are indicated, and they all have line directions which are indistinguishable from their Burgers vector directions (within experimental error). Since $\langle 001 \rangle$ is a multiple slip orientation, it is not surprising to find glissile dislocations of more than one Burgers vector.

This type of structure, which contains large numbers of screw segments trapped within the γ' , is very similar to the structures which have been reported in $L1_2$ crystals deformed at low temperatures (Chapter II). This trapping of screw segments suggests a lower mobility for screw dislocations, in agreement with the cross-slip model. Therefore, the cross-slip model is consistent with both the anisotropic properties described in Chapter V and the deformation substructures described above.

20°C

It has been demonstrated that deformation at 20°C is

heterogeneous, as seen in Figure 22. In the $\langle 001 \rangle$ interrupted tensile specimens studied earlier [4,5], the foils made from the 20°C tests contained a very low density of dislocations, and the few dislocations found within the γ' were of the type $\{111\}a/2\langle 110 \rangle$. It is now clear that these foils were taken from areas of the crystal which had not been extensively plastically deformed. In order to obtain foils in the deformed regions, three techniques were employed: First, more foils were prepared from the low ϵ_p specimens with the hope of finding a deformed region; second, the crystals strained to 2.5% ϵ_p were examined; and third, cyclically deformed crystals were studied.

The high ϵ_p specimens did not yield much information, due to an extremely high defect density. The additional foils cut from the low ϵ_p tests did yield several deformed areas, but the areas were unfortunately in regions of the foils which were too thick to do high resolution work. The LCF specimens, however, proved to be very useful for deformation studies.

Analysis of these specimens revealed that deformation at 20°C was accomplished by γ' shearing on $\{111\}$ planes, by a mixture of $a/2\langle 110 \rangle$ and $a/3\langle 112 \rangle$ dislocations. (The dislocation and fault analysis is presented later in this chapter.) Figure 42(a) shows the structure which developed in one of the low ϵ_p tensile tests. The foil contains several slip bands, and the bands contain unit dislocations,

partial dislocations, and partial dislocation loops. The partials are identified by the stacking fault fringe contrast between two partials or within a partial loop. Figure 42(b) shows the structure which developed during cyclic deformation. Fortunately, it appears to be very similar to the structure which developed during the interrupted tensile test. Therefore, the LCF structures will be assumed to be representative of cyclic as well as monotonic deformation.

Figure 43 shows additional micrographs of the LCF structures. There are many unit dislocations pushed against the precipitate, in the interface. Some of these dislocations have penetrated the precipitate as unit dislocations, while others have reacted or decomposed into partials which have left stacking faults.

Figure 44 shows another typical substructure. Again, both partial and unit dislocations have penetrated the γ' . Figure 44(b) clearly shows that the dislocations and faults are confined to parallel planar slip bands on the (111) plane. The photo in Figure 44(a) shows the same area under different diffraction conditions. It shows that each slip band contains unit dislocation pairs (marked by arrows) in the matrix areas, between the γ' precipitates. The unit dislocations in this area were identified as $a/2\langle 110 \rangle$, and nearly screw in character. These matrix unit dislocations lie in slip bands which contain stacking faults on either

side. The implications of this structure are discussed later in this chapter.

200 to 600°C

At 20°C, a mixture of partial and unit dislocations sheared the precipitates. At 705°C, only unit dislocations were found. It would be reasonable to suspect some sort of transition behavior between the two temperatures. This is exactly what was observed.

Figure 45 shows the substructures which developed during LCF of $\langle 001 \rangle$ crystals at 200, 400, and 600°C. The 200°C test resulted in a structure very similar to the 20°C test, as shown in Figure 45(a). A mixture of partial and unit dislocation shearing has occurred. The 400°C test resulted in shearing by only unit dislocations, as seen in Figure 45(b). Only one stacking fault was found in this entire foil. Deformation substructures observed after LCF at 600°C closely resembled those seen after deformation at 705°C, as shown in Figure 45(c). Many straight screw dislocation segments were trapped within the γ' , and no stacking faults were observed.

The Form of the CRSS vs Temperature Curve

Recall from Chapter V that the CRSS falls from 20°C to a local minimum at 400°C. This trend follows the reduction in density of stacking faults seen in the deformation substructures. 400°C corresponds to both the minimum in

strength and the disappearance of the partial dislocation shearing mechanism. This indicates that the partial shearing mechanism or residual stacking faults acted to strengthen the material.

There are two possible strengthening mechanisms which may be due to partial shearing. First, the residual stacking faults and faulted loops can act as obstacles to further dislocation motion. Also, the $a/3\langle 112 \rangle$ partial dislocations probably have a larger lattice friction stress than the unit dislocations. The reason behind this is described later in this chapter.

The increase in strength from 400 to 760°C follows an increase in the density of straight screw segments trapped within the γ' . This increase, therefore, appears to be due to increased cross-slip strengthening with temperature. The form of the curve in this temperature range mimics the CRSS vs Temperature curve for pure γ' crystals.

It must be noted that strengthening from 20 to 400°C was not solely due to the partial dislocation mechanism. This is clear for two reasons. First, there was a tension-compression asymmetry at 20 and 200°C that was presumably caused by cube cross-slip of unit dislocations. Second, these unit dislocations have been observed (along with the partials) inside the γ' after deformation. In cases like this, when more than one strengthening mechanism is active at the same time, the relative effects of the two mechanisms

on the CRSS are unclear. If the mechanisms act purely in parallel, the weakest of the two obstacles will control the strength. If the mechanisms act purely in series, the strongest of the two obstacles will control the strength. However, in real materials neither of these two idealizations is generally the case. In studies of solution strengthened and precipitation strengthened metals, it is found that the most accurate models are based on some type of addition of the effects of different mechanisms [11,84,85]. The addition rule is model-dependent; some models use linear addition, some use pythagorean addition, some use a rule of mixtures based on the relative frequency of obstacles [85]. In the present case, it appears that some type of addition rule is appropriate at temperatures below 400°C. The effect of the stacking fault strengthening is clearly seen via the reduction in CRSS as the mechanism disappears, while the effect of cross-slip is clearly seen via the tension-compression asymmetry. Therefore, the CRSS seems to be influenced by both at temperatures below 400°C.

Figure 46 shows a schematic plot of the dominant strengthening mechanism as a function of temperature in the low temperature regime. The stacking fault mechanism is at a maximum at 20°C and decreases to zero at about 400°C. Based on the behavior of pure γ' , the cross-slip mechanism should result in a low value of the CRSS at 20°C, then the CRSS should continuously rises to a maximum at 760°C. The

alloy behavior is a composite of the two, with the highest resisting stress controlling the shape of the curve. Using this model, the shape of the CRSS vs Temperature curve (Figure 15) is accurately correlated.

The Nature of the Faults and Partial Dislocations

Theory

Figure 47(a) is a drawing of the {111} plane in the $L1_2$ structure, using the hard sphere model. The three possible lattice positions for close packing are indicated. Define the positions in the plane shown as "C" positions. Then the atoms in the plane below the paper are in "B" positions, and the atoms in the plane above the paper are in "A" positions. The result is the FCC stacking sequence (ABCABC). The nickel and aluminum sites are indicated. The $L1_2$ structure requires that each aluminum atom is completely surrounded by nickel atoms. Therefore, the only possible sites for aluminum atoms in the plane above the paper are the "A" sites indicated in Figure 47(b). Of course, the periodic structure shown in the "C" plane is identical in the "A" plane.

Consider the possible slip vectors which can shear the "A" plane with respect to the "C" plane, and the resultant atomic arrangements. There are four unique possibilities, and each is indicated in the vector diagram in Figure 47(c). The possible slip vectors are:

- 1) $a/6\langle 112 \rangle$. The aluminum atom in the "A" site in the plane above the paper is translated to the nearest "B" site. An intrinsic fault is created (ABC BCA). This aluminum atom is now in direct contact with an aluminum atom in the "C" plane, so an APB is also created. This is called a complex fault (CF).
- 2) $a/2\langle 110 \rangle$. Translates the "A" aluminum atom to the nearest "A" site, so no stacking fault is created. Aluminum atoms are now in contact, so an APB is created.
- 3) $a/3\langle 112 \rangle$. Translates the "A" aluminum atom to one of the "B" sites which are completely surrounded by nickel atoms. Thus, no APB is created, but an intrinsic stacking fault is (ABC BCA). This is the S-ISF. Note from Figure 47(c) that the glide of this dislocation should be very difficult, since it must move directly over an atomic "peak", not through the "valleys" that Shockley partials travel. For this reason, it is possible that the $a/3\langle 112 \rangle$ partials may dissociate into three Shockleys; this arrangement has been predicted by computer simulations [86,87].
- 4) $a\langle 110 \rangle$. This is the superlattice unit translation vector. No faults or APB's are created.

Extrinsic stacking faults can be created by slip on parallel planes. If two $a/3\langle 112 \rangle$ partials shear the crystal

on adjacent {111} planes, a superlattice extrinsic stacking fault (S-ESF) is created (ABCA C BCA). The two $a/3\langle 112 \rangle$ partials may have collinear Burgers vectors, but an S-ESF is created whether the partials have collinear Burgers vectors or not.

The creation of an S-ISF or an S-ESF requires glissile $a/3\langle 112 \rangle$ dislocations. Since this type of dislocation is rarely found in the virgin material, dislocation reactions during deformation are necessary. Two possible reactions have been proposed. The first has been found during TEM weak-beam studies of deformed Ni_3Al [18]. The reaction is of the type:

$$a/2[\bar{1}01] = a/3[\bar{2}11] + a/6[1\bar{2}1] \quad (6-1)$$

If this reaction occurs in the γ/γ' interface, the $a/3\langle 211 \rangle$ partial can shear the precipitate, leaving an S-ISF behind. Now, the $a/6\langle 121 \rangle$ partial could follow, thus eliminating the S-ISF. However, this would leave behind the same high energy APB that would have been created by the glide of the $a/2\langle 011 \rangle$ superpartial. Therefore, this $a/6\langle 211 \rangle$ partial is expected to be trapped in the interface, and will completely surround the precipitate after the shearing event. (This assumes that the APBE is higher than the sum of the S-ISF energy and the glide force on the dislocation. As discussed in the next chapter, it is believed that the S-ISF energy is about an order of magnitude lower than the APBE.)

The second type of reaction requires two $a/2\langle 110 \rangle$ dislocations with the same Burgers vector on the same plane. This is easily found during low temperature deformation, due to the operation of Frank-Read dislocation sources and the extreme planarity of glide. The two $a/2\langle 110 \rangle$ dislocations may be thought of as a single $a\langle 110 \rangle$ dislocation, and the reaction is of the type:

$$a[\bar{1}01] = a/3[\bar{2}11] + a/3[\bar{1}\bar{1}2] \quad (6-2)$$

If this reaction occurs in the interface, both partial dislocations are glissile, because the net slip vector is a unit superlattice translation vector. An S-ISF is present between the two partials, but neither a stacking fault nor an APB is left behind after both partials shear the crystal.

Results

As already mentioned, there were two temperature regimes which contained stacking faults in the deformation substructures. At 200°C and below, the substructure was heavily faulted. At 760°C and above, occasional faults were observed, with the highest density occurring during slow strain rate deformation at 760°C [4,5]. The high temperature faults were the easiest to analyze, due to their relatively low density. The low temperature faults were difficult to analyze, due to high fault densities, overlapping faults, and the resulting heavily faulted and bent crystals.

Single faults in relatively thick FCC crystals are easy to identify. Due to anomalous absorption, the dark field image of the fault is asymmetric [88]. In FCC crystals, a simple rule has been determined to identify the faults as intrinsic or extrinsic [88]. Place the origin of the g -vector at the center of the dark field image of the fault. If the g -vector is $\langle 200 \rangle$, $\langle 222 \rangle$, or $\langle 440 \rangle$, and the g -vector points toward the light fringe on a positive print, the fault is intrinsic. If it points toward the dark fringe, it is extrinsic. If the g -vector is $\langle 111 \rangle$, $\langle 220 \rangle$ or $\langle 400 \rangle$ and points toward the light fringe, it is extrinsic. If it points toward the dark fringe, it is intrinsic. (Please note that a mistake was made in the earlier report [5], and these rules were stated exactly backwards).

The stacking faults and partials observed after high temperature deformation (above 700°C) have been identified with a high degree of certainty. The faults were caused by the glide of partials whose Burgers vectors were parallel to $\langle 112 \rangle$, and the faults are intrinsic in nature. Figure 48 shows several partials which were moving through the γ' precipitates when the test was interrupted. Dislocation analysis (Appendix B) of this area clearly established that the partial's Burgers vectors were parallel to $[112]$, and that the fault translation vectors were parallel to $[111]$. Every "single" stacking fault observed after high temperature deformation was found to be intrinsic. Since

the faults were intrinsic and the partials were of the type $a/x\langle 112 \rangle$, the earlier discussion would indicate that the exact Burgers vectors of the partials were $a/3\langle 112 \rangle$.

Having established the nature of the faults and the Burgers vector of the leading partials, only the dislocation reaction and the trailing partial need to be identified. Figure 49 shows a typical high temperature substructure. This photo, along with Figures 39, 48 and 50, shows that all the high temperature stacking faults are attached to the γ/γ' interface on at least one side. This indicates that one edge of the fault is bounded by an interfacial partial dislocation which is not glissile. This implies that the dislocation reaction which took place at high temperatures was that given in Equation 6-1:

$$a/2[\bar{1}01] = a/3[\bar{2}11] + a/6[1\bar{2}1] \quad (6-1)$$

Ideally, one would like to identify the $a/6\langle 211 \rangle$ partial by TEM diffraction experiments. This was not possible, because the trailing partials were "masked" by both the interfacial elastic strain field and the fault fringe contrast.

In the absence of direct proof, circumstantial evidence supporting the reaction in Equation 6-1 is available. Figure 48 shows a group of dislocations and a related stacking fault on the (111) plane after deformation at 760°C. Only the interfacial dislocation could not be identified by diffraction experiments. Inspection of Figure 48(b) reveals

that the observed arrangement is perfectly compatible with a reaction equivalent to Equation 6-1; the necessary $a/2[101]$ precursor that would lead to the proposed reaction in Figure 48(b) is exactly the same as the $a/2[101]$ dislocation seen next to the fault in Figure 48(a). During planar shearing which results from dislocations generated by a Frank-Read source, parallel $a/2\langle 110 \rangle$ dislocations with the same Burgers vector are readily available.

As further evidence, Figure 49(a) shows a micrograph of a $\langle 123 \rangle$ crystal deformed at 927°C . There are a number of parallel $a/2\langle 110 \rangle$ dislocations (about 8-10) in the γ/γ' interface, on either side of the precipitate. In the middle of this array are four parallel stacking faults that each appear to have been formed by the dissociation and glide of a single $a/2\langle 110 \rangle$ interfacial dislocation.

In contrast to the easily identified single faults seen after high temperature deformation, the substructures which developed during low temperature deformation are very complicated. These structures are characterized by high fault densities, overlapping faults on parallel planes, and a large number of faulted dislocation loops. In order to understand these substructures, some background material concerning diffraction theory in the presence of overlapping faults must be introduced.

The two-beam kinematical theory of electron diffraction [88] predicts that the amplitude of a scattered wave

travelling through a crystal containing a planar fault is:

$$\phi_g = (i\pi/\xi_g) \int_0^{t_c} \exp(-2\pi isz) \exp(-2\pi i \underline{g} \cdot \underline{R}) dz \quad (6-3)$$

where ϕ_g = Diffracted wave amplitude,

ξ_g = Extinction distance,

t_c = Crystal thickness,

s = Deviation parameter,

z = Position in crystal,

\underline{g} = Diffraction vector,

\underline{R} = Fault translation vector.

The phase factor, α , is defined as

$$\alpha = 2\pi \underline{g} \cdot \underline{R} \quad (6-4)$$

Stacking faults in the FCC lattice have R values of $1/3\langle 111 \rangle$ and $-1/3\langle 111 \rangle$, so the phase factor α can have values of $2n\pi/3$, where n is an integer. α is periodic in 2π . From Equation 6-3, if α has a value of $0 + 2n\pi$, the fault will not be imaged. If α has a value of $\pi/3 + 2n\pi$ or $2\pi/3 + 2n\pi$, then the term $e^{-i\alpha}$ in Equation 6-3 yields the familiar periodic fringe contrast. For a given g , if $\alpha = \pi/3$ corresponds to an intrinsic fault, then $\alpha = 2\pi/3$ corresponds to an extrinsic fault. This is the basis for the fault identification rules stated earlier.

Closely spaced stacking faults on parallel planes can appear to be single faults with a displacement vector equal

to the sum of the individual displacement vectors. For instance, adjacent intrinsic faults with individual characteristics $R = -1/3\langle 111 \rangle$ and $\alpha = \pi/3$ are imaged as an extrinsic fault with $R = -2/3\langle 111 \rangle$ and $\alpha = 2\pi/3 = -\pi/3$. An example of this is shown in Figure 50. Two $a/3\langle 112 \rangle$ partials were shearing the γ' on parallel planes. Between the "leading" and "trailing" partials, where there is no fault overlap, intrinsic contrast is observed. Behind the "trailing" partial, where the two faults overlap, extrinsic contrast is observed. If three closely spaced intrinsic faults overlap, the phase factor $\alpha = 2\pi = 0$, so no contrast is expected. With this background, a description of the low temperature substructures is possible.

The most obvious feature which differentiates the faulted structures at low and high temperatures is the extremely high density of faults on parallel planes after low temperature deformation. Figures 42-44 and 51 demonstrate this very clearly. As a direct result, the additive contrast described above is often observed. Intrinsic contrast, extrinsic contrast, and no contrast are routinely present in the same micrograph. For instance, Figure 52 shows several areas where overlapping faults lead to residual fault contrast between partials and imaged faults. This problem, coupled with the high dislocation density and relatively poor quality of the heavily faulted crystals, rendered the foils inappropriate for high

resolution diffraction experiments. Therefore, the deformation mechanisms operative at temperatures below 200°C are not known to the same level of confidence as at higher temperatures. However, several facts are known, and further information can be obtained when these facts are coupled with the theory discussed earlier.

The most useful observation concerns the mobility of the trailing partials. In contrast to the high temperature faults, the low temperature faults are generally not attached to the γ/γ' interface. In areas where the fault density is low enough to resolve individual faults, it can be seen that two types of structures developed which were not seen after high temperature deformation. The first type of structure consists of an S-ISF completely within the interior of a γ' particle, bounded by a pair of partial dislocations. The second type of structure consists of faulted dislocation loops.

Figure 53 shows a good example of several partial pairs bounding S-ISF's. The partials have no contact with the γ/γ' interface. This implies that the trailing partial is glissile, and is fully consistent with the dislocation reaction proposed in Equation 6-2:

$$a[\bar{1}01] = a/3[\bar{2}11] + a/3[\bar{1}\bar{1}2] \quad (6-2)$$

Recall that both of the resultant partials should be glissile, in agreement with the structure shown in Figures

52 and 53. This dislocation arrangement was fairly common after deformation at 20 and 200°C. Pairs bounding S-ISF's are clearly seen in Figures 43, 44, 52 and 53.

Figures 42-44 and 51 also contain many examples of the faulted dislocation loops which were mentioned above. These loops are potent strengthening obstacles, because the applied shear stress will either expand or contract the loops, but will not translate the loops out of the γ' precipitate. Thus, the loops are essentially trapped. The mechanism responsible for the formation of the faulted loops is not clear. One possibility would be an Orowan-type looping event. This could occur during the glide of the trailing $a/3\langle 112 \rangle$ partial, and could occur completely within the precipitate, as shown in the model in Figure 54. The exact same structure can also be formed by the collapse of an interfacial $a/3\langle 112 \rangle$ loop. This interfacial loop may easily be formed during the shearing process, as shown in Figure 55. Both of these mechanisms are consistent with the observed structures, Figure 44. These micrographs clearly show faulted loops in the γ' parallel to and in the same slip band as unit matrix dislocations. This is the exact same arrangement as in the schematics of Figures 54(e) and 55(e).

One observation can be made which is unexplainable at present. After an $a/3\langle 112 \rangle$ S-ISF loop is formed, a driving force to collapse the loop is present. If the loop

collapses, both the S-ISF and the dislocation line will be annihilated, so the process is energetically favorable. However, many loops are observed which did not collapse. This may indicate that the $a/3\langle 112 \rangle$ partials have a very large Peierls stress. Further research is necessary.

In addition to these faulted loops, unfaulted loops which were bounded by pairs of unit dislocations were sometimes observed. An example of this is shown in Figure 56. This indicates that the looping process seen within the precipitates was not limited to the $a/3\langle 112 \rangle$ partials, although the partial loops were certainly more common.

From the above discussion, it appears probable that the γ' precipitates are sheared by two different mechanisms at temperatures below 400°C : pairs of $a/2\langle 110 \rangle$ superpartials, and pairs of $a/3\langle 112 \rangle$ superpartials. Additionally, the $\langle 112 \rangle$ shearing mechanism can leave a trail of faulted S-ISF loops in its wake.

It is certain from the deformation substructures that shearing occurred on many closely spaced, parallel slip planes. This is in good agreement with the observation that each slip burst contained many finely-spaced slip planes, as seen in the surface replicas in Figures 22, 23 and 33. Recall that the $\langle 123 \rangle$ crystal deformed at 20°C exhibited slip trace behavior similar to Luders Band growth. Apparently, the easy glide period enjoyed by the dislocations generated in the first Frank-Read source did

not last long. Partial dislocation shearing by the first few dislocations littered the slip plane with faults and faulted loops. In order for deformation to continue, screw portions of gliding $a/2\langle 110 \rangle$ dislocations cross-slipped up or down a few atomic planes, thus by-passing the loops. By the continuation of this process, the width of the surface slip band continued to grow.

Summary

New observations, and new interpretations of established observations have been used successfully to correlate the mechanical behavior observed in Chapter V. In the low temperature regime, where $\{111\}$ plane shearing operates, it has been shown that two temperature-dependent strengthening mechanisms operate. "Fault strengthening" is important below 400°C , and its temperature dependence is negative. "Cross-slip strengthening" is important over the entire low temperature regime, and its temperature dependence is positive. A superposition of these mechanisms can successfully correlate the form of the CRSS vs temperature curve in the low temperature regime. At high temperatures, γ' by-pass dominates deformation, consistent with the observed isotropic properties.

Primary cube slip was never observed in these experiments on $\langle 001 \rangle$ and $\langle 123 \rangle$ crystals.

CHAPTER VII
DISCUSSION: THE TEMPERATURE DEPENDENCE
OF THE γ' SHEARING MECHANISM

As discussed in Chapter VI, the density of S-ISF's was very high after deformation at 20°C, and the density gradually fell to zero as the deformation temperature was raised to 400°C (Figure 45). This reduction in fault density corresponded to a decrease in the CRSS, implying that the faults strengthened the material. In this chapter, a discussion of the mechanisms responsible for this behavior will be presented. First, it will be shown that the change in shearing mechanism was due solely to changes in intrinsic superlattice properties. Next, a model which describes such transformations in $L1_2$ superlattices will be critically reviewed. Finally, the model will be related to the observed behavior of PWA 1480.

The Nature of the Transformation

At temperatures between 20 and 705°C, two γ' shearing mechanisms were observed. At all temperatures in this range, shearing occurred by pairs of $a/2\langle 110 \rangle$ dislocations on $\{111\}$ planes. This will be referred to as "APB shearing", because the pairs are connected by a ribbon of

APB. At 20 and 200°C, deformation occurred by APB shearing and by shearing by two $a/3\langle 112 \rangle$ dislocations on $\{111\}$ planes. The latter will be referred to as "S-ISF shearing", because the $a/3\langle 112 \rangle$ dislocations are connected by a ribbon of S-ISF. Both mechanisms rely on the same $a\langle 110 \rangle$ dislocation precursor (or equivalently two $a/2\langle 110 \rangle$ dislocations with the same Burgers vector on the same plane):

$$a[\bar{1}01] = a/2[\bar{1}01] + a/2[\bar{1}01] \quad (7-1)$$

and

$$a[\bar{1}01] = a/3[\bar{2}11] + a/3[\bar{1}\bar{1}2] \quad (7-2)$$

Therefore, the central issue is the temperature dependence of the dissociation of the $a\langle 110 \rangle$ dislocation.

In general, the dissociation which results in the lowest free energy will be favored. Since the superalloy is a two phase material, and the dissociation occurs at or near the γ/γ' interface, both interfacial properties and intrinsic γ' properties are capable of affecting the dissociation. Temperature dependent interfacial properties include the lattice parameter mismatch and the elastic constant mismatch. Temperature dependent intrinsic properties include the shear modulus (μ), the APBE (Γ_a), the S-ISF energy (Γ_s), and the diffusion and clustering characteristics of the alloy. The most direct method to discriminate between interfacial effects and intrinsic

effects would be to conduct identical tests on single phase γ' of the same composition as the γ' in PWA 1480. Lacking this information, results from previous investigations of single phase γ' and other $L1_2$ compounds must be used. As discussed below, such studies have found behavior which was very similar to the behavior of PWA 1480, thus supporting the proposition that the temperature dependence of the shearing mechanism is due to the temperature dependence of intrinsic γ' properties.

S-ISF Dissociation in $L1_2$ Alloys

S-ISF loops and widely extended $a/3\langle 112 \rangle$ pairs have been observed in Ni_3Al deformed at low temperatures [18,89,90]. In one of these studies, Veyssiere et. al. [18] found large loops at $20^\circ C$, but as the deformation temperature reached $350^\circ C$ S-ISF loops were not found. This is in complete agreement with the present study. However, it must be noted that Ni_3Al does not exhibit an inverse CRSS dependence on temperature. Therefore, although the $a\langle 110 \rangle$ S-ISF dissociation and its temperature dependence appear to be common to γ' and PWA 1480, the strengthening effect is not. S-ISF dissociation at low temperatures has also been observed in the $L1_2$ compounds Ni_3Ga [91,92], Pt_3Al [93], and Zr_3Al [94,95]. Similar to the behavior of Ni_3Al and PWA 1480, the fault density was found to decrease with increasing deformation temperature in Ni_3Ga [91] and Zr_3Al alloys [95]. Also consistent with the present study (but

inconsistent with the Ni_3Al studies), Pt_3Al and Zr_3Al both exhibit an inverse CRSS dependence on temperature in the regime where the S-ISF mechanism occurs [93].

These results from single phase L1_2 alloys indicate that the temperature-dependent superdislocation dissociation behavior is the same in monolithic γ' and the γ' in PWA 1480. Therefore, it appears that the temperature dependence of the dissociation is due to the temperature dependence of intrinsic γ' properties, not interfacial properties. In order to describe the observed temperature dependence of the dissociation, a model is necessary which predicts the conditions under which S-ISF dissociation, APB dissociation, or both will occur. Such a model is described below.

Modeling the $a\langle 110 \rangle$ Dissociation

Suzuki et. al. [96] have calculated the total energies of the APB and S-ISF dissociations, based on isotropic linear elasticity theory. The model assumes that the $a\langle 110 \rangle$ superdislocation dissociates according to Equations 7-1 and 7-2. It is further assumed that the $a/2\langle 110 \rangle$ and $a/3\langle 112 \rangle$ superpartials do not dissociate into $a/6\langle 112 \rangle$ Shockleys. The total energy of the dissociated system includes three terms: One due to the APB (or S-ISF), one due to the sum of the partial dislocations self energies, and one due to the interactions of the dislocations strain fields. Let E_a and

E_s be the total energies of the APB and S-ISF dissociations per unit length. Then:

$$E_a = \Gamma_a d_a + (\xi_1 \mu b_a^2 / 2\pi) \ln(R/r_a) - (\xi_1 \mu b_a^2 / 2\pi) \ln(d_a/R) \quad (7-3)$$

and

$$E_s = \Gamma_s d_s + (\xi_2 \mu b_s^2 / 2\pi) \ln(R/r_s) - (\xi_3 \mu b_s^2 / 2\pi) \ln(d_s/R) \quad (7-4)$$

where Γ = Fault energy,
 d = Equilibrium dislocation spacing,
 μ = Shear modulus,
 b = Burgers vector,
 r = Dislocation core radius,
 R = Outer cut-off radius,
 ξ_1 = Geometric (dislocation character) terms.

Equation 7-3 may be subtracted from Equation 7-4 to determine which dissociation scheme is energetically favorable. After substituting reasonable values for the microstructural parameters and simplifying, the following boundary conditions for the dissociation of screw and edge $a\langle 110 \rangle$ dislocations are determined:

$$E_s < E_a \quad \text{if} \quad \Gamma_a/\Gamma_s \geq 20 \quad (\text{Screw}) \quad (7-5)$$

and

$$E_s < E_a \quad \text{if} \quad \Gamma_a/\Gamma_s \geq 3 \quad (\text{Edge}) \quad (7-6)$$

It is readily seen that the dissociation is controlled solely by the ratios of the APB and S-ISF energies. Additionally, there are three regimes of behavior: When $\Gamma_a/\Gamma_s < 3$, the APB dissociation is favored; when $\Gamma_a/\Gamma_s > 20$, the S-ISF dissociation is favored; Between these limits, both dissociations are possible, depending on the character of the $\langle 110 \rangle$ precursor dislocation.

Experimental Observations

In this study, both APB and S-ISF dissociations were observed after deformation at 20°C (Figures 42-44, 51-53). According to the model, this implies that the ratio Γ_a/Γ_s is in the transition region, between 3 and 20 at 20°C. Theoretically, these parameters can be measured by weak-beam microscopy, but these experiments were not conducted as part of this study. Lacking this data, results from the literature indicate that the fault energy ratio for Ni₃Al at 20°C is indeed between 3 and 20: the currently accepted values for Ni₃Al are $\Gamma_a = 110 \text{ mJm}^{-2}$ and $\Gamma_s = 10 \text{ mJm}^{-2}$ [97-100], yielding a ratio of 11. However, it should be noted that the γ' in PWA 1480 is alloyed with Ti and Ta, so the fault energies could be substantially different from those of Ni₃Al. For example, Holdway and Staton-Bevan [95] found

that the addition of Ti or Nb to Zr_3Al substantially reduced the density of S-ISF's observed after low temperature deformation. The relative effects of Ti and Ta on Γ_a and Γ_s are not known.

The Temperature Dependence of the Model

In this study, the fault density decreased substantially with temperature over a range of about 400°C. The decrease in shear modulus over this temperature range is small, about 10%. Therefore, only two terms in Equations 7-3 and 7-4 could be strongly temperature dependent within this range: The fault energies and the equilibrium dislocation spacings. In fact, the dislocation spacings are only strongly temperature dependent through the fault energies [96]:

$$d_a = \xi_1 \mu b_a^2 / 2\pi \Gamma_a \quad (7-7)$$

and

$$d_s = \xi_3 \mu b_s^2 / 2\pi \Gamma_s \quad (7-8)$$

Therefore, the only intrinsic properties which can vary strongly with temperature are the fault energies, Γ_a and Γ_s . In order to apply the model to PWA 1480, it is necessary to determine the temperature dependence of the ratio Γ_a/Γ_s .

Based on the observation that the fault density decreased significantly with temperature, it appears likely that the ratio Γ_a/Γ_s also decreased significantly with

temperature between 20 and 400°C. The same conclusion was drawn by Holdway and Staton-Bevan in their study of Zr_3Al [95]. Ideally, one would like to measure the fault energies as a function of temperature. However, this information is neither available nor easily generated. It is known that the stacking fault energy (SFE) of most FCC alloys increases by about a factor of two from zero to 350°C [101,102]. It is also frequently assumed (although this topic is still the subject of debate [21,103]) that the APB energy (Γ_a) is about constant in this temperature range [10,13,18,21,90,97,103]. Therefore, if the S-ISF energy in ordered alloys exhibits a temperature dependence similar to the SFE of disordered alloys, then the ratio Γ_a/Γ_s could be decreased by about a factor of two from 20 to 400°C, due solely to an increase in the S-ISF energy. Although speculative, this trend corresponds very well with the disappearance of S-ISF's and the assumed decrease in the fault ratio from 20 to 400°C. In-situ measurements of Γ_a and Γ_s as functions of temperature are necessary to confirm this speculation.

The High Temperature Faults

Recall that there were two temperature regimes in which the γ' was sheared by partials which left S-ISF's behind. Extensive faulting was observed at 200°C and below, while occasional faulting was observed at 760°C and above. The low

temperature faults were bounded by pairs of $a/3\langle 112 \rangle$ partials which formed from an $a\langle 110 \rangle$ dislocation, while the high temperature faults were bounded by an $a/3\langle 112 \rangle$ partial and an $a/6\langle 112 \rangle$ partial which formed from an $a/2\langle 110 \rangle$ dislocation. Since the high temperature faults did not form via the dissociation of an $a\langle 110 \rangle$ dislocation, the theory described in this chapter is not applicable to these faults. Since the density of faults was low, and the faults occurred in the temperature range where γ' by-pass controlled deformation and strength, an in-depth analysis was not conducted.

Summary

It has been shown that an analytical framework for studying the formation of APB's or S-ISF's from an $a\langle 110 \rangle$ superdislocation exists. The only parameter that influences the reaction is the ratio of APB energy to S-ISF energy. This framework is consistent with the observations made in this study. With several assumptions based on studies of random FCC alloys, the temperature dependence of the dislocation reaction (which was observed in this and other studies) can be successfully predicted by the model.

CHAPTER VIII

DISCUSSION: ON THE PHYSICAL MECHANISM OF CROSS-SLIP

It was demonstrated in Chapter V that the anisotropy observed in this study at low temperatures was fully compatible with the cross-slip model. As proposed by Miner et. al. [27], the constriction stress is the dominant factor, so the cross-slip stress can be ignored. During plastic deformation, the orientation dependence of the constriction stress leads to orientation dependent cube cross-slip rates. This difference in the rate of cube cross-slip results in the following trends which are observed in γ' and PWA 1480:

1. $\langle 001 \rangle$ crystals are stronger than $\langle 123 \rangle$ crystals in tension, while the opposite is true in compression.
2. The $\langle 001 \rangle$ CRSS is higher in tension than in compression, while the $\langle 123 \rangle$ CRSS is higher in compression than in tension.
3. Under fully reversed, strain controlled cyclic loading $\langle 001 \rangle$ crystals produce maximum shear stresses which are higher in tension than in compression, while $\langle 123 \rangle$ crystals produce maximum shear stresses which are higher in compression than

in tension.

The cyclic trends are stable throughout the lives of the tests. This observed cyclic stability of the tension-compression asymmetry, although not new, can be used to study the cross-slip mechanism.

Slip Reversibility

The cyclic tension-compression asymmetry has been observed in Ni_3Al [104-106] and high V_f superalloys [26,28]. Bonda, Pope and Laird [104] have discussed the cyclic stability of the tension-compression asymmetry in Ni_3Al . They proposed that the reversible plastic strains which occur during steady-state cycling are carried by one of the following two mechanisms:

1. A "flip-flop" motion of edge dislocation dipoles.
2. Bowing or gliding of unpinned segments of screw dislocations or screw dislocation dipoles.

The first mechanism is inconsistent with the reversible tension-compression asymmetry. Although it is certainly possible that much of the strain is carried by edge or mixed dislocations, screw dislocation motion must control the CRSS; otherwise, no tension-compression asymmetry is to be expected. The second mechanism is inconsistent with the attainment of steady-state. If unpinned screw segments are responsible for plastic strain, then with each cycle more

and more of these free screws must become pinned, and the flow stress should increase continuously with cycling. Therefore, neither mechanism proposed above can explain the observed behavior.

In a given crystal under uniaxial loading, all screw dislocations have the same value of the constriction stress. Therefore, it is unlikely that different dislocations are responsible for deformation in tension and compression. Since screw dislocation motion controls the CRSS in both tension and compression, and since a cyclically stable tension-compression asymmetry develops during reversed loading, it appears that cube cross-slip must be a dynamic, process that is effectively reversible. Screw dislocations which become pinned by cube cross-slip during the tensile portion of the cycle must become unpinned during stress reversal, and can become pinned again during compressive yielding. The process can repeat itself indefinitely. In this way, the completely reversible plastic strains which are observed in γ' and PWA 1480 (without constantly increasing values of shear stress) can be explained.

Let us assume for the sake of argument that the cross-slip event is not reversible. Then, under tensile straining, portions of the leading screw dislocations will become pinned, as shown schematically in Figure 57(a). Now, when the stress is reversed, these pinning points are being assumed to remain. Since the number of pinning points per

unit length is the same in tension and compression, then the force to move the dislocation is the same, and no tension-compression asymmetry is expected. Since the asymmetry is observed, the cross-slip mechanism must be reversible. The mechanism of this reversibility, as well as a thermodynamic derivation which supports its feasibility, are both discussed in greater detail later in the chapter.

This observation has important implications for understanding the physical cross-slip event, and can be used as a new critical test of the available cross-slip models. The remainder of this chapter addresses these two points.

The Cross-Slip Mechanism

Although the CRSS data are in excellent agreement with the cross-slip model, the details of the cross-slip event and the subsequent cross-slipped configuration are not known with certainty [17]. Prior to cross-slip, the $a\langle 110 \rangle$ superdislocations which are within the γ' are dissociated into two $a/2\langle 110 \rangle$ superpartials on the (111) plane, Figure 58(a). Two cross-slip mechanisms have been proposed. The first is a cross-slip of both superpartials to (010), after which the APB is completely contained on the (010) plane, Figure 58(b). This is equivalent to a cube plane dissociation of the $a\langle 110 \rangle$ superdislocation. The second is a limited cross-slip, which results in a bi-planar APB, Figure 58(c). This configuration can result if the leading

superpartial cross slips to the cube plane, then becomes immediately pinned. The goal of the following discussion is to determine which of these two mechanisms, if either, is consistent with the observed slip reversibility.

As already stated, the details of the cross-slip event and subsequent configuration are not known for certain. The present study has not clarified this matter. Therefore, a discussion of the kinetics of cross-slip would be speculative. Instead, the problem will be studied by calculating the equilibrium energy of a unit length of screw superdislocation prior to cross-slip, after cross-slip, and after cross-slip under an applied stress. These thermodynamic calculations will indicate whether or not a driving force for cross-slip exists, and whether or not an applied stress stabilizes or de-stabilizes each configuration. Unfortunately, the calculations cannot yield the rate of cross-slip in forward and reverse, so the problem will not be completely solved. This is an area that requires further research. However, the results will be somewhat useful for the present study, and will at least show that one of the models can probably be eliminated from consideration.

Total Cube Cross-Slip Model

Until very recently, skeptics who questioned the validity of the cross-slip model have pointed to the fact that no physical evidence of cube cross-slip had been found

in the TEM or the Field Ion Microscope. However, using the weak beam TEM technique, Veyssiere et. al. [19,20,107] have recently shown examples of screw superdislocation dissociation on {001} planes in deformed Ni_3Al . It was not known for certain whether these structures evolved during deformation, or were produced by relaxation after deformation in the bulk or thin foil form [107]. Assuming that this mechanism can occur during deformation, it must be determined whether or not it could be the dominant strengthening mechanism. The reversibility constraint can help answer this question.

The Energy Prior to Cross-Slip: The total energy per unit length of a dissociated screw superdislocation is:

$$E = \Gamma_a d + D \cdot \ln(R/r_o) - D \cdot \ln(d/R) \quad (8-1)$$

where Γ_a = APBE,
 d = Equilibrium superpartial spacing,
 $D = \mu b^2 / 2\pi$,
 R = Cut-off radius,
 r_o = Core radius.

The first term is due to the APB, the second is the self energy of the superpartial pair, and the third is the superpartial interaction energy. Combining constants,

$$E = \Gamma_a d - D \cdot \ln(d) + C \quad (8-2)$$

This is a general expression. Inserting the specific planar

APBE yields the energy on the desired plane.

The Driving Force for Cross-Slip: The difference in energy between the reference (octahedral) state and the cross-slipped (cube) state is the driving force for cross-slip. Applying Equation 8-2 yields the driving force per unit length:

$$\Delta E = E_O - E_C = \Gamma_O d_O - \Gamma_C d_C + D \cdot \ln(d_C/d_O) \quad (8-3)$$

where the "o" subscript means octahedral and the "c" subscript means cube. Substituting the equilibrium dislocation spacing,

$$d = D/\Gamma_a \quad (8-4)$$

the difference in energy between the cube plane dissociation and the octahedral plane dissociation is found:

$$\Delta E = D \cdot \ln(\Gamma_O/\Gamma_C) \quad (8-5)$$

If ΔE is positive (i.e. $\Gamma_O/\Gamma_C > 1$), the cube plane configuration is energetically favorable, so cube cross-slip will reduce the energy of the system. Assuming that the cross-slip event is thermodynamically reversible, this means that cross-slip will occur at a higher rate in forward than in reverse, and so at equilibrium all screw segments will lie on {001} planes. (Of course, equilibrium is not necessarily obtained during deformation processes). Since Γ_O/Γ_C is about 1.2 for Ni_3Al [97,99], the cross-slipped

configuration always has a lower energy than the reference octahedral dissociation. Therefore, according to Equation 8-5, cube cross-slip will occur in Ni_3Al , and so to this point the model is consistent with experimental observations.

The Effect of Stress: It was proposed earlier in this chapter that cross-slip is reversible under a change in loading direction. Therefore, a valid model of the cross-slip event must yield a driving force for reverse cross-slip under a change in stress direction. The following discussion shows that the total cube cross-slip model cannot generally predict a driving force for reverse cross-slip, and thus eliminates the model from consideration as the rate limiting step during deformation.

The difference in energy between the reference state and the cross-slipped state is given by Equation 8-5. It is valid under any stress state, as long as both superpartials are glissile. Inspection of Equation 8-5 reveals that there is always a driving force for cross-slip in the forward direction, independent of the stress state. Unpinning (reverse cross-slip) is not predicted. For this reason, the model is inconsistent with the observed reversibility of the cross-slip event.

Equation 8-5 is not a valid description if one of the cross-slipped superpartials is sessile while the other is glissile, because then the dislocation spacing is a function

of stress. Ignoring the fact that such a configuration is difficult to support physically, the following derivation will show that the model cannot predict reversible cross-slip even under these (hypothetical) conditions.

Assume that the leading superpartial becomes pinned after a total cross-slip event by an unspecified mechanism. The difference in energy between the reference state and the cross-slipped state (under stress) is still given by Equation 8-3, but the spacings need to be modified. Equilibrium of the glide forces on the glissile dislocation yields the superpartial spacing on the cube plane:

$$d_c = D/(\Gamma_c + \tau b) \quad (8-6)$$

where τ is the cube plane glide stress, $\tau_{(010)[101]}$. Substituting Equations 8-6 and 8-4 into Equation 8-3, the difference in energy between the glissile octahedral state and the sessile cube cross-slipped state is found as a function of stress:

$$\Delta E = D\{1 - \Gamma_c/(\Gamma_c + \tau b) + \ln(\Gamma_o/\Gamma_c + \tau b)\} \quad (8-7)$$

Again, $\tau = \tau_{(010)[\bar{1}01]}$. After cross-slip has occurred, this difference in energy either stabilizes the cross-slipped configuration or promotes reverse cross-slip, depending on the sign. If ΔE is negative, reverse cross-slip is predicted. Therefore, this difference in energy can be considered to be the driving force for reverse cross-slip

(unpinning). This driving force is plotted vs cube plane glide stress in Figure 59, using the following material constants which are representative for Ni_3Al :

$$\mu = 90 \text{ GPa (Vogt average of elastic constants [108])},$$

$$b = 2.5 \times 10^{-10} \text{ m},$$

$$\Gamma_o = 110 \text{ mJ}\cdot\text{m}^{-2} [99],$$

$$\Gamma_c = 90 \text{ mJ}\cdot\text{m}^{-2} [99].$$

Figure 59 shows that both tensile and compressive applied stresses tend to de-stabilize this hypothetical cross-slipped configuration. This is easy to visualize physically. Tensile stresses push the superpartials closer together, thus increasing the interaction energy; compressive stresses push the superpartials farther apart, thus increasing the energy via increases in the APB area. Of course, when one term in Equation 8-7 increases the energy, the other term decreases the energy. Figure 59 shows that the increase overwhelms the decrease, both in tension and compression.

Figure 59 also predicts the reversibility of cross-slip. Under a stress reversal, a cube plane glide stress of only 150 MPa results in a driving force for unpinning, and this driving force approaches infinity as $\tau_{(010)[\bar{1}01]}$ approaches $-\Gamma_c/b$. This stress is a very attainable -360 MPa. Thus, the model predicts that as the cube plane glide stress approaches -360 MPa after a stress reversal, the dislocations which have cross-slipped will experience an

effectively infinite driving force for reverse cross-slip. Thus, unpinning after a stress reversal is predicted, in agreement with our experimental observation. However, one critical experiment eliminates the model. Uniaxially loaded $\langle 001 \rangle$ crystals have a cube plane glide stress $\tau_{(010)[101]}$ equal to zero. Therefore, Equation 8-7 predicts that there is no driving force for unpinning in $\langle 001 \rangle$ crystals. However, $\langle 001 \rangle$ crystals do exhibit a cyclically stable tension-compression asymmetry. This asymmetry was seen in the PWA 1480 crystals with tensile axes between 3° and 10° from $\langle 001 \rangle$ in this study, as well as in Ni_3Al crystals with tensile axes within 4° of $\langle 001 \rangle$ [104]. Although the Schmid factors for cube glide are not zero except exactly at the $\langle 001 \rangle$ orientation, crystals within 4° of $\langle 001 \rangle$ have negligibly small cube glide Schmid factors of 0.04. Also, there is no evidence that the asymmetry decreases as the deviation from $\langle 001 \rangle$ decreases. Since the total cube cross-slip model described above does not satisfy this reversibility constraint, it is not consistent with experimental observations, and can therefore be discarded.

Limited Cross-Slip Model [17]

The second model for cube cross-slip was proposed by Paidar, Pope and Vitek [17], and is based on an immediate pinning of the leading superpartial after cross-slip. It will be demonstrated that this model, when slightly modified, is consistent with both the CRSS data and the

reversibility constraint.

In reviewing the work of Takeuchi and Kuromoto [15] and Lall, Chin and Pope [16], Paidar, Pope and Vitek (PPV) [17] noted that the cross-slip models were incomplete, for two reasons:

1. The models provided no detailed mechanism for cross-slip.
2. The models provided no reason why screw dislocations which cross-slip to cube planes should be immobile.

Using the results of pair-potential based computer simulations of superpartial dislocation cores [86,87], PPV proposed a cross-slip mechanism which eliminates these shortcomings. The results from these studies which are pertinent to the present discussion of cube cross-slip in Ni_3Al may be summarized as follows [17]:

1. It is always energetically favorable for $a/2\langle 110 \rangle$ superpartials to dissociate into $a/6\langle 112 \rangle$ Shockley partials. The Shockley separation distance is very small (about $2b - 3b$ for Ni_3Al [100]), so the dissociation may be treated as a "core-width effect".
2. If the APB is contained on the (111) plane, the Shockley dissociation is also on the (111) plane, so the superpartial is glissile.
3. If the APB is contained on the (010) plane, the Shockley dissociation occurs on either the (111) or

($\bar{1}\bar{1}1$) plane. In this case, the glide plane of the superpartial is not the same as the plane of the APB, so the superpartial is assumed to be sessile.

Based on these results, the following cross-slip sequence was proposed by PPV:

1. Plastic flow begins by gliding of dissociated $a\langle 110 \rangle$ superdislocations on the (111) plane.
2. Screw segments of the leading dissociated superpartial become constricted and cross-slip to (010). This is a "double kink" configuration, which is shown in Figure 60.
3. Immediately after cross-slip, the leading superpartial re-dissociates into Shockleys on the (111) or ($\bar{1}\bar{1}1$) plane. Thus, the double kink acts as a pinning point for the entire superpartial.

The resulting configuration is shown in detail in Figure 60. There is an APB of length w on the (010) plane, and an APB of length $(r - w/\sqrt{3})$ on the (111) plane. The length of the (010) APB is a very small distance, either b or $b/2$.

It is not clear what the length of the double kink is after cross-slip. PPV calculated a critical activation length for the formation of the double kink, but once the double kink forms it can substantially reduce its energy by increasing its length [17]. This is only one of the details of the cross-slip event that is not known for certain. As

another example, it is not clear that the rate limiting step (and therefore the activation energy) is the same in forward and reverse: in the forward direction, the rate limiting step is almost certainly the thermally activated formation of the critical length of constriction on the leading superpartial [17]; in reverse, the rate limiting step must depend on the (unknown) length of the double kink. Therefore, in the following calculations the details of the cross-slip event and the length of the double kink are not considered. Instead, the driving forces for cross-slip in forward and reverse are calculated for a unit length of screw superdislocation. This calculation will show that the PPV cross-slip mechanism is consistent with the reversibility constraint.

The Energy Prior to Cross-Slip: Since the reference state is the same as in the earlier derivation, the energy per unit length prior to cross-slip for this configuration is also given by Equation 8-2.

The Driving Force for Cross-Slip: Inspection of Figure 60 results in the expression similar to Equation 8-2 for the energy per unit length after the PPV cross-slip event. After combining constants, the expression is [17]:

$$E = \Gamma_O(r - w/\sqrt{3}) + \Gamma_C w - D \cdot \ln(z) + C \quad (8-8)$$

where r , w , and z are defined in Figure 60. The driving force for cross-slip is the difference between Equations 8-2

and 8-8 [17]:

$$\Delta E = \Gamma_o(d_e - r - w/\sqrt{3}) - \Gamma_c w + D \cdot \ln(z/d_e) \quad (8-9)$$

The equilibrium {111} superpartial spacing, d_e , is given by Equation 8-4. The distances z and r are related geometrically (Figure 60):

$$z^2 = r^2 + 2w^2/3 \quad (8-10)$$

Applying Equation 8-6 to the specific case of Ni_3Al with the material constants stated earlier, the calculated value of r is greater than $14b$ when the octahedral glide stress is 400 MPa or less. Since the model assumes that $b/2 < w < b$, then $w/r \ll 1$, and terms in w/r of quadratic order or higher may be safely ignored. This results in $z = r$. Under zero applied stress, z also equals d_e . Thus, the difference in energy between the reference state and the cross-slipped state, which is the driving force for cross-slip is [17]:

$$\Delta E = \{(\Gamma_o/\sqrt{3}) - \Gamma_c\}w \quad (8-11)$$

Again, if ΔE is positive, the cross-slip event is energetically favorable. This is the case if

$$\Gamma_o/\Gamma_c > \sqrt{3} \quad (8-12)$$

Yoo [97,108] has pointed out that weak-beam TEM studies have yielded values of Γ_o/Γ_c in the range from 1.1 to 1.3. Using Equation 8-11 with this range of APB ratios, the

cross-slip mechanism proposed by PPV is not energetically favorable. However, since the available data are consistent with some type of cube cross-slip mechanism, and since it has been demonstrated that the total cube cross-slip mechanism discussed earlier is inconsistent with the reversibility of cross-slip, then let us assume for the purposes of argument that the PPV mechanism does occur. This would be consistent with the above derivation if one of the following is true:

1. The experimentally determined values of Γ_O/Γ_C are in error, and the true ratio is greater than $\sqrt{3}$.
2. The boundary condition specified by Equation 8-12 is in error. As one possible alternative, Yoo [108] has repeated the derivation of Equation 8-11 using anisotropic elasticity. His boundary condition is:

$$1.9 \cdot \Gamma_O/\Gamma_C > \sqrt{3} \quad (8-13)$$

The reported APB ratios of Ni_3Al satisfy this constraint.

3. The cross-slip event is not completely reversible (in the thermodynamic sense), and so the event may occur at a higher rate in forward than in reverse even though the driving force is not favorable.

For the purposes of the present discussion, let us simply assume that one of the above is true, and so the PPV mechanism can occur. Next, we will show that this mechanism

is consistent with the observed reversibility of cross-slip.

The Effect of Stress: After a PPV cross-slip event occurs, the driving force for reverse cross-slip must be calculated, in a manner similar to the earlier derivation in the case of total cube cross-slip. PPV added a term to Equation 8-8 to include the effects of stress on the cross-slip energy. However, their approach is inadequate for the present discussion. Because they used a high reported value of $\Gamma_0 = 300 \text{ mJ}\cdot\text{m}^{-2}$ and restricted their discussion to low stresses, they assumed that terms on the order of $(\tau b/\Gamma_0)^3$ and higher would be negligible. However, using a more commonly accepted value of $\Gamma_0 = 110 \text{ mJ}\cdot\text{m}^{-2}$, and realizing that $\tau_{(111)[101]}$ can easily reach 400 MPa at yield in Ni_3Al and PWA 1480, $(\tau b/\Gamma_0)^3$ is on the order of unity. Therefore, a more rigorous derivation is necessary.

Consider the cross-slip event proposed by PPV, in which the leading superpartial cross-slips a distance b onto the (010) plane and becomes locked (Figure 60). Immediately after cross-slip (before the dislocation spacing has changed due to the applied stress), the energy of the system is given by Equation 8-8, with $z = r = d_e$. Since the leading superpartial is assumed to be pinned, the applied stress will change the separation of the superpartials, thus changing the energy of the system. As before, the driving force for reverse cross-slip is the difference in energy between the cross-slipped configuration (under stress) and

the reference configuration (under stress). Subtracting Equation 8-8 from Equation 8-2,

$$\Delta E = \Gamma_o \{d_e - (r - [w/\sqrt{3}])\} - \Gamma_c w + D \cdot \ln(z/d_e) \quad (8-14)$$

As in the previous derivation, $w/r \ll 1$, so $z = r$. Substituting Equation 8-4 (for d_e) and Equation 8-6 (for z), the difference in energy per unit length between the cross-slipped configuration and the reference configuration is found as a function of stress:

$$\begin{aligned} \Delta E = \{(\Gamma_o/\sqrt{3}) - \Gamma_c\}w \\ + D\{\tau b/(\Gamma_o + \tau b) + \ln(\Gamma_o/[\Gamma_o + \tau b])\} \end{aligned} \quad (8-15)$$

where τ is the octahedral glide stress, $\tau_{(111)[\bar{1}01]}$. As is required, Equation 8-15 degenerates to Equation 8-11 under zero stress. Assuming a PPV cross-slip event has already occurred, this difference in energy of the previously cross-slipped segment can be considered as a driving force for reverse cross-slip. High negative values of ΔE should result in extensive unpinning. This driving force is plotted in Figure 61, using the same material parameters as before, and assuming $w = b$ [17]. This figure shows that both tensile and compressive stresses tend to de-stabilize the cross-slipped configuration. Similar to the previous case, the driving force for unpinning approaches infinity as the stress approaches $-\Gamma_o/b$ (400 MPa) under reversed loading. Thus, unpinning must occur as this asymptotic

stress is approached. The physical argument is exactly the same as for the case of total cube cross-slip, except that the stress responsible for the driving force is the octahedral glide stress, not the cube glide stress. Since all orientations in uniaxially stressed FCC crystals exhibit octahedral glide stresses of $0.275 \cdot \sigma$ to $0.5 \cdot \sigma$, the model is general.

Let us specify in detail the sequence of events during reversible cross-slip. Consider a superpartial pair in which superpartial "A" is leading under tensile loading while superpartial "B" is trailing (Figure 62). A portion of "A" becomes pinned by the PPV mechanism during the tensile portion of the cycle. Under a stress reversal, the octahedral glide stress approaches -400 MPa (Figures 25,27), thus yielding a very large driving force for unpinning. (The physical source of this driving force is the ever increasing APB area which is created as "B" is driven away from "A" by the negative shear stress). Therefore, "A" becomes unpinned. Now, "B" is the leading superpartial, so it can now become pinned by a PPV mechanism. Since the constriction stress for "A" under tensile loading is of the opposite sign as the constriction stress for "B" under compressive loading, a fully reversible tension-compression asymmetry results. These events are shown in Figure 62. Obviously, Figure 62 is an oversimplification of the actual situation, because it is likely that different points along

the screw dislocation line would be pinned in tension and compression. However, the essence of reversible cross-slip is captured by the model in Figure 62.

General Evaluation: Pope and co-workers have used the PPV model to quantitatively predict the orientation dependence of the CRSS and the orientation dependence of the tension-compression asymmetry in Ni_3Al single crystals [106]. The above discussion has shown that the PPV model is also consistent with the observed reversibility of cross-slip in Ni_3Al and superalloy single crystals. Additionally, the PPV model specifies the physical mechanism of pinning. Therefore, it appears to be consistent with most of the experimental observations.

Two possible inconsistencies still remain. First, it is not certain that a positive driving force for cross-slip is predicted by the model (Equation 8-11). Second, the model still cannot explain the strain rate insensitivity which was discussed in Chapter II. Yoo's anisotropic elasticity argument can probably eliminate the first inconsistency, but further research is needed to determine why these alloys can exhibit such a large temperature dependence without any hint of a corresponding strain rate dependence.

Summary

Experimental evidence indicated that the cube cross-slip event must be fully reversible under reversed cyclic loading. This observation can be used as a critical test of the cross-slip models. Using simple thermodynamic calculations of energy differences between different configurations, it was shown that the total cube cross-slip mechanism is not consistent with the observed reversibility. On the other hand, the limited cross-slip event proposed by Paidar, Pope and Vitek is consistent with the reversibility constraint. This observation lends support to the proposal that the PPV mechanism is the rate limiting step during deformation of Ni_3Al and high V_f superalloys.

CHAPTER IX
DISCUSSION: IMPLICATIONS
FOR CONSTITUTIVE MODELING

The previous two chapters were concerned with mathematical modeling of deformation mechanisms from the perspective of an alloy designer or physicist. However useful or instructive these models may be, they cannot be used for structural analysis. This is the realm of constitutive modeling. A major goal of this research is to integrate the understanding of physical deformation mechanisms into the constitutive models which are intended to describe macroscopic behavior. This will be attempted in a sequential manner. First, the material anisotropy will be reviewed, including anisotropic behavior which was not studied explicitly in this investigation. Next, a candidate model to be used as an example will be chosen. This model will be reviewed in detail in light of the results of the present study, and modifications will be suggested. Finally, temperature and strain rate boundaries which separate different types of behavior will be prescribed, and several specific isothermal examples will be considered.

Sources of Anisotropy

As discussed in Chapters V and VI, significant material anisotropy is present in PWA 1480 at temperatures below 800-950°C (depending on strain rate). It has been demonstrated in this study that the anisotropy observed in $\langle 001 \rangle$ and $\langle 123 \rangle$ crystals is caused by variations in the rate of cube cross-slip and variations in the number of active slip planes. In addition, as described below it appears that primary cube γ' shearing occurs in near- $\langle 111 \rangle$ crystals of some alloys even at temperatures above 950°C (where γ' bypass operates in crystals of other orientation). The phenomenon of cube cross-slip has been thoroughly discussed in Chapter VIII. In this section, primary cube slip and hardening effects due to intersecting slip will be discussed as background for the constitutive model evaluation.

Primary Cube Slip

As discussed in Chapter II, primary cube slip is known to control deformation at elevated temperatures in Ni_3Al single crystals with tensile axes near to $\langle 111 \rangle$. Also, direct evidence for primary cube slip has been found in PWA 1480 and Rene N4 single crystals by Miner and co-workers [25]; in $\langle 111 \rangle$ and $\langle 112 \rangle$ crystals tensile tested at 760 and 980°C, they found:

1. Cube plane slip traces;
2. Dislocations with $[\bar{1}10]$ Burgers vectors, which are in the primary cube slip system but not in the

- primary octahedral slip system;
3. Tensile axis rotations toward $[\bar{1}10]$;
 4. A tension-compression asymmetry with the opposite sense than predicted by the cross-slip model.

All of these observations support the occurrence of primary cube slip in crystals near $\langle 111 \rangle$. Gabb and Welsch [28] also found evidence of primary cube slip in near- $\langle 111 \rangle$ PWA 1480 single crystals fatigued at 650°C.

Indirect evidence for primary cube slip is readily available, in that the $(111)[\bar{1}01]$ CRSS in $\langle 111 \rangle$ crystals is about 30% lower than other crystals (even at temperatures above 900°C) in PWA 1480 [7,8], Mar-M 200 [22-24], and Rene N4 [25]. This reduction in CRSS can be attributed to the operation of primary cube slip, and implies that γ' shearing on $\{001\}$ planes occurs in $\langle 111 \rangle$ crystals of these alloys even at temperatures where by-pass occurs in other orientations. However, the data from this study shows that a significant (about 30%) reduction in the CRSS occurred in PWA 1480 $\langle 123 \rangle$ crystals as compared to $\langle 001 \rangle$ crystals even when only octahedral slip was active. This implies that CRSS data alone cannot be used to infer the occurrence of primary cube slip.

To implement a constitutive model, temperature and orientation boundaries for primary cube slip must be specified. Since primary cube slip is known to occur in $\langle 111 \rangle$ crystals of Ni_3Al γ' at 600°C and above, let us

postulate that primary cube slip can also occur in PWA 1480 at 600°C and above. This is consistent with studies of Rene N4 [25], in which cube slip was observed in $\langle 111 \rangle$ and $\langle 112 \rangle$ crystals at 760 and 980°C, but not at 20°C. However, Giamei's data [24] indicate that cube slip can occur in some alloys at temperatures as low as 20°C; Caron et. al. [109] have shown that cube slip does not occur in $\langle 111 \rangle$ crystals of CMSX alloys at any temperature. Therefore, the phenomenon of cube slip and the boundary conditions under which it is observed appear to be dependent on the material. This is not unexpected, because the octahedral CRSS and cube CRSS are functions of APB energies, which are strongly influenced by composition.

Approximate orientation boundaries for cube slip in PWA 1480 and Rene N4 can be specified based on experimental data. Miner et. al. [25] proposed that the octahedral CRSS and the cube CRSS were approximately equal in Rene N4 at 760°C and above. The Schmid factor contours for the two slip systems are shown in Figure 63(a). The great circle on which the resolved shear stresses on both systems are equal is shown in Figure 63(b). It is seen that this boundary condition predicts cube slip in orientations within about 25° of $\langle 111 \rangle$. However, the data from the present study indicate that the boundary is closer to $\langle 111 \rangle$, at least for PWA 1480. Figure 64 is a summary of PWA 1480 and Rene N4 crystals which displayed octahedral slip or cube slip at

700°C and above. It is clear that the near- $\langle 123 \rangle$ crystals tested in the present study, which displayed only octahedral slip, are contained well within the area in which cube slip would be predicted. Therefore, Miner's boundary condition must be modified.

To specify a new boundary condition, define the Schmid factor ratio, N' , as the ratio of the primary cube Schmid factor to the primary octahedral Schmid factor. Thus, Miner's condition is $N' = 1$. Now, specify a new condition such that $N' = 1.15$. This condition is also plotted vs orientation in Figure 64. It is seen that the great circle representing this condition intersects one orientation that displayed cube slip ($\langle 112 \rangle$) and one orientation that displayed octahedral slip (near- $\langle 123 \rangle$). Thus, assuming similitude between crystals with the same Schmid factors, it is probable that the great circle representing $N' = 1.15$ is on or very near to the transition between octahedral and cube slip. Therefore, Figure 64 can be used to specify the boundary between octahedral slip and cube slip in PWA 1480 and Rene N4. This may not be the case for other alloys.

Thus, it is proposed that primary cube slip occurs in PWA 1480 and Rene N4 crystals at temperatures greater than 600°C when $\tau_{(001)[\bar{1}10]} \geq 1.15 \cdot \tau_{(111)[\bar{1}01]}$. Under uniaxial loading conditions, this boundary is specified by Figure 64, which shows that orientations within about 20° of $\langle 111 \rangle$ have been found to exhibit primary cube slip.

Multiple Slip

In a single crystal, the degree of strain hardening depends on the number of slip systems which are active during deformation. Also, strain hardening on a given slip system depends on the prior histories of deformation on all other slip systems. For instance, consider a crystal which is deforming by single slip. If the crystal is unloaded after some time, then loaded under a different stress state, the "yield strengths" of previously inactive slip systems will have been increased. This interactive hardening between slip systems is referred to as "latent hardening", and its quantification is essential for constitutive modeling. Physically, latent hardening is due to elastic interactions between dislocations on different slip systems. A classical rate-independent approach to quantifying latent hardening is described below.

Let the current shear yield strength of the i^{th} slip system be given by τ_i . It is postulated that the rate of change of τ_i is linearly related to the sum of the plastic shear strain rates on all the active slip planes [111,112]:

$$\dot{\tau}_i = \sum_j h_{ij} \dot{\gamma}_j \quad (9-1)$$

where h_{ij} is a matrix of hardening coefficients, sometimes called a hardening modulus. If $h_{ij} = 0$, the material is perfectly plastic. If h_{ij} contains only diagonal non-zero

terms, there is no latent hardening. Otherwise, the diagonal terms describe the self-hardening of each slip system, and the off-diagonal terms describe latent hardening. In general, the current values of h_{ij} depend on the complete deformation history.

Two simple forms of the hardening modulus which are not history dependent have gained acceptance [110,111]. The simplest possible model which includes latent hardening is a linear isotropic model, in which all slip systems (active or latent) harden equally. Thus, Equation 9-1 becomes

$$\dot{\tau}_i = h \sum_j \dot{\gamma}_j \quad (9-2)$$

where h is a scalar constant and the summation is taken over the number of active slip systems. However, this model is inadequate for describing the orientation dependence of hardening in metal crystals [112]. The second type of model is only slightly more complicated [110,111]. The form of the hardening modulus is:

$$h_{ij} = h_m + (h_s - h_m) \delta_{ij} \quad (9-3)$$

where h_m characterizes the hardening rate for multiple slip and h_s characterizes the hardening rate for single slip. The use of this hardening modulus along with Equation 9-1 will not generally result in a unique relationship between stress rate and strain rate [110]. However, the hardening matrix may be used as a measure of strain hardening in a

more complex flow rule. Equation 9-3 does have the ability to capture the essence of intersecting slip behavior. Kocks [112] has shown that the ratio h_m/h_s is between 1.0 and 1.4 in FCC crystals, so Equation 9-3 can be written as:

$$h_{ij} = qh + (h-qh)\delta_{ij} \quad (9-4)$$

with $1.0 < q < 1.4$, and q determined experimentally. If $q = 1$, the isotropic law given in Equation 9-2 results.

Slip Bursts

Macroscopic models based on microscopic behavior almost always assume homogeneous deformation. However, it was demonstrated earlier in this work that plastic deformation was far from homogeneous in single slip crystals which were deformed at 20 and 705°C; shearing occurred in discreet, widely-spaced slip bursts. This causes a huge problem for constitutive modeling. If two extensometers of different gage length were placed on the same uniaxial specimen, the two extensometers would have reported different values of plastic strain. Although this is obviously a problem, it almost has to be ignored to preserve a tractable structural analysis model. Therefore, in the remainder of this chapter it will be assumed that inaccuracies due to inhomogeneous deformation behavior are small enough to be ignored. The only other possible approach would be to formulate a statistical model of discreet slip behavior. That type of approach is beyond the scope of the present work.

Selection of the Model

As discussed in Chapter III, there were two anisotropic models available (when the majority of this research was conducted) which are intended for use with single crystal superalloys. Additionally, Stouffer's group has substantially modified their model recently, but the results are not yet generally available [113]. A group of French workers is also currently working on model development [114]. No attempt will be made here to compare the models or to decide which is better. Instead, one model will be used to demonstrate the advantages of introducing knowledge of deformation behavior into the formulation of the model.

There are two major differences between the two models in their current formulations. First, the Walker-Jordan (WJ) model [80] contains two state variables, while the Dame-Stouffer (DS) model [81] only contains one. This is a severe limitation on the DS model, as it cannot accurately model the Bauschinger effect which is clearly seen in Figure 35. (The new versions of Stouffer's model include a back stress, which should correct the problem [113]). The second major difference is that the WJ model explicitly includes a latent hardening term, while the DS model does not, even in its current form [113]. As seen in Figure 26(b), and as discussed in Chapters V and VI, the number of active slip systems has a major effect on constitutive behavior.

Therefore, it appears that the WJ model is more general in its present form, and a detailed discussion of this model will be presented in the remainder of this chapter.

The Walker-Jordan Constitutive Model:

Form and Physical Consistency

Overview

The model assumes that each slip system obeys a unified viscoplastic flow rule in shear. The flow rule for each slip system contains two state variables: a back stress and a drag stress. The drag stress state variable is used to model anisotropy due to cube cross-slip and latent hardening, as well as conventional isotropic hardening. The back stress state variable is used to model kinematic hardening and the Bauschinger effect.

Anisotropy due to primary cube slip is modeled by specifying a unified viscoplastic flow rule for cube slip, then adding the contributions of cube slip and octahedral slip to form the global strain rate. In practice, a scaling function is determined by curve fitting to determine the relative amount of each slip mechanism as a function of temperature and orientation.

Symbol Convention

The following symbol definitions will be used throughout this chapter:

σ : Applied uniaxial stress
 τ_i : Octahedral Schmid stress on the i^{th} system ($i=1,12$)
 π_i : Cube Schmid stress on the i^{th} system ($i=1,6$)
 τ_C : Constriction stress, $\tau_{(111)[121]}$
 τ_S : Cross-slip stress, $\tau_{(010)[101]}$
 ϵ^{in} : Uniaxial inelastic strain
 γ_i : Inelastic shear strain on i^{th} octahedral system
 α_i : Inelastic shear strain on i^{th} cube system
 N_O : Number of active octahedral slip systems
 N_C : Number of active cube slip systems
 Ω_i : Back stress state variable on i^{th} octahedral system
 K_i : Drag stress state variable on i^{th} octahedral system
 ω_i : Back stress state variable on i^{th} cube system
 κ_i : Drag stress state variable on i^{th} cube system
 β_i : Temperature dependent material constants
 η_i : Temperature dependent material constants (exponents)
 \underline{l} : Unit vector in slip direction
 \underline{n} : Slip plane unit normal vector

The model is presented in a sequential manner, with a discussion following each major section. A general discussion is presented at the end.

The Octahedral Flow Rule

Each of the 12 octahedral slip systems is assumed to obey a viscoplastic flow rule:

$$\dot{\gamma}_i = (\text{sign}[\tau_i - \Omega_i]) (|\tau_i - \Omega_i| / K_i)^{\eta_1} \quad (9-5)$$

Note the dissimilarity between the state variables in this model and the isotropic model. In the isotropic model (Equation 3-21), Ω_{ij} is a 3x3 tensor and K is a scalar. Here, they are both 12-row column vectors. The evolution of the state variables is discussed later in the chapter.

Discussion: This type of flow rule has been found to be useful and accurate over a wide temperature range for isotropic materials. The only question to be addressed concerning the form of the flow rule is whether or not a single flow rule can be used over the entire temperature range of interest. In fact, after observing the earlier results of this study concerning the transition from γ' shearing to γ' by-pass, Jordan [115] suggested that two different flow rules may be necessary for the two mechanisms. In their model, Dame and Stouffer do employ two different, uncoupled flow rules. One describes diffusion-limited high temperature flow, while the other describes cross-slip limited low temperature shearing. However, Jordan found that a single flow rule did an adequate job of correlating the data over an extended temperature regime [115]. This is physically reasonable, as discussed below.

The crystallographic flow rule is formulated in shear, consistent with the shear strain rate which is produced by dislocation glide. The glide force on a dislocation in its

slip plane is given by Equation 2-5, irrespective of whether the dislocation is gliding through the γ' (shearing) or gliding in the matrix between the γ' (by-pass). Since the glide force is due to the octahedral Schmid glide stress, $\tau_{(111)[\bar{1}01]}$, a single flow rule based on this stress should be valid over the entire temperature range.

Of course, the rate limiting step changes as a function of temperature and strain rate. At low temperatures, deformation is controlled by stacking fault strengthening and cube cross-slip of dislocations which are shearing the γ' (Chapters VI - VIII); at high temperatures, deformation is controlled by the ease of octahedral cross-slip and diffusion during by-pass [4,5]. These differences are modeled in the state variables. If Ω and K accurately describe the resistance to plastic deformation as a function of temperature, then a single flow rule will suffice.

The Octahedral Drag Stress

Since the drag stress is used to model all the anisotropy which is observed when octahedral slip operates, it is crucial that its form be consistent with physical deformation mechanisms. The WJ model utilizes a drag stress evolution equation which includes both latent hardening and cube cross-slip. The form of the evolution equation is

$$K_i = \sum_{j=1}^{N_o} \{ (\beta_1[q + [1-q]\delta_{ij}] - \beta_2[K_i - K^O]) |\dot{\gamma}_j| \} - \beta_3(K_i - K^O)^{\eta_2} \quad (9-6)$$

where

$$K^O = \beta_4 + \beta_5 \exp(\beta_6 \tau_c + \beta_7 |\tau_s|) \quad (9-7)$$

N_o is the number of active octahedral slip systems and q is the previously mentioned latent hardening factor. The term $\beta_1[q + [1-q]\delta_{ij}]$ in the summation is a hardening modulus which is identical to Equation 9-4, with $\beta_1 = h$. The second term in the summation is a dynamic recovery term which includes cube cross-slip terms. The final term in the evolution equation is a static recovery term which also includes cube cross-slip terms. For isothermal, uniaxial loading of single crystals during which the number of active slip systems does not change, the summation can be evaluated explicitly. Doing this, and assuming that the shear strain rate on each equally stressed active system is the same during multiple slip, Equation 9-6 becomes:

$$\dot{K} = \{ \beta_1(1 + [N_o - 1]q) - \beta_2 N_o (K - K^O) \} |\dot{\gamma}| - \beta_3 (K - K^O)^{\eta_2} \quad (9-8)$$

with K^O as in Equation 9-7. Therefore, each (equally stressed) active octahedral system has the same value of γ and K during multiple slip.

Discussion: First, the relationship may be simplified to exclude the effects of the cross-slip stress, τ_s , since its effect on properties is negligible [27]. Eliminating τ_s and substituting Equation 9-7 into Equation 9-8,

$$\dot{K} = \{\beta_1(1 + [N_O-1]q) - \beta_2 N_O(K - \beta_4 - \beta_5 \exp[\beta_6 \tau_C])\} |\dot{\gamma}| - \beta_3 (K - \beta_4 - \beta_5 \exp(\beta_6 \tau_C))^{\eta_2} \quad (9-9)$$

The functional form of Equation 9-9 is identical to the general form specified in Equation 3-23:

$$\dot{K} = \phi_1 \{\dot{\gamma}\} - \phi_2 \{K |\dot{\gamma}|\} - \phi_3 \{K\} \quad (9-10)$$

where

$$\phi_1 = \{\beta_1(1 + [N_O-1]q) + \beta_2 \beta_4 N_O + \beta_5 \exp(\beta_6 \tau_C)\} |\dot{\gamma}| \quad (9-11)$$

is the direct hardening term,

$$\phi_2 = \beta_2 N_O K |\dot{\gamma}| \quad (9-12)$$

is the dynamic recovery term, and

$$\phi_3 = \beta_3 (K - \beta_4 - \beta_5 \exp[\beta_6 \tau_C])^{\eta_2} \quad (9-13)$$

is the static recovery term. The evolution equation appears to be capable of handling all the sources of material anisotropy. It has a non-linear dependence on the number of

active slip systems, and can model the tension-compression asymmetry and orientation dependent CRSS through its dependence on the constriction stress, τ_c . However, the model has not been tested at a temperature where the effects are significant, so it is not known if the true behavior can be correlated by the model.

One minor point can be made concerning the consistency of the evolution equation. Equation 9-13 shows that the static recovery term includes the constriction stress, τ_c . Although the contribution of the constriction stress goes to zero as the applied stress goes to zero, the constriction stress should have little or no effect on thermal recovery, so it should not appear in this term. Thus, Equation 9-8 should be of the form

$$\dot{K} = \{\beta_1(1 + [N_0 - 1]q) - \beta_2 N_0 (K - K^0)\} |\dot{\gamma}| - \beta_3 (K - \beta_8)^{\eta_2} \quad (9-14)$$

with

$$K^0 = \beta_4 + \beta_5 \exp(\beta_6 \tau_c) \quad (9-15)$$

The Octahedral Back Stress

Since the material anisotropy which occurs during octahedral slip is modeled by the drag stress, the back stress evolution equation is simple. The isotropic form given in Equation 3-22 is used, with the ψ 's being

temperature dependent constants. The model also assumes an isotropic back stress which is independent of the number of active slip systems. Thus,

$$\dot{\Omega} = \beta_9 \dot{\gamma} - \beta_{10} |\dot{\gamma}| \Omega - \beta_{11} \text{sign}(\Omega) |\Omega|^{\eta_3} \quad (9-16)$$

Discussion: Since this type of equation works well for isotropic materials, it is expected to work here if the drag stress state variable normalizes out all the anisotropy. However, it appears from our results that the Bauschinger effect (and therefore the back stress) is not isotropic at 705°C. As shown in Figure 35, the normalized back stress which developed during fatigue at 705°C was 300% lower in <123> crystals than <001> crystals. At 20°C and 927°C, this anisotropy was not present. Although this result implies that an anisotropic back stress state variable is desirable, there is not enough data to suggest an analytical expression for the anisotropy. This may indicate that some of the anisotropy should be modeled in the back stress, instead of including all anisotropic terms in the drag stress. More research is necessary.

Cube Slip Formulation

Cube slip is also assumed to obey a unified viscoplastic flow rule in shear. Latent hardening is ignored, so the cube equations are simpler than the octahedral equations. The flow rule for each active cube

slip system is:

$$\dot{\alpha}_i = (\text{sign}[\pi_i - \omega_i]) (|\pi_i - \omega_i| / \kappa_i)^{\eta_4} \quad (9-17)$$

As before, the back stress is assumed to be isotropic, and equal shear rates are assumed on equally stressed slip systems during multiple slip. Therefore, the drag stress on active and latent cube slip systems evolves as:

$$\dot{\kappa} = N_C (\beta_{12} - \beta_{13}[\kappa - \beta_{14}]|\dot{\alpha}|) - \beta_{15}(\kappa - \beta_{14})^{\eta_5} \quad (9-18)$$

where N_C is the number of active cube slip systems. The back stress evolves as:

$$\dot{\omega} = \beta_{16}\dot{\alpha} - \beta_{17}|\dot{\alpha}|\omega - \beta_{18}\text{sign}(\omega)|\omega|^{\eta_6} \quad (9-19)$$

Discussion: The inclusion of primary cube slip is absolutely necessary in order to model the anisotropy which occurs in uniaxial loading of near- $\langle 111 \rangle$ PWA 1480 and Rene N4 crystals. It is also likely that primary cube slip will occur under multiaxial loading when the cube Schmid stress is high enough. (For instance, in pure torsion of crystals in which the twist axis coincides with $\langle 001 \rangle$). To be physically consistent, the constants and evolution equations must be structured such that the cube strain rate is negligibly small in uniaxial loading except in crystals near

$\langle 111 \rangle$ (See Figure 64). This indicates that the exact forms of the equations may need to be modified if the current forms predict cube slip in orientations such as $\langle 011 \rangle$. Any anisotropy observed in $\langle 011 \rangle$ crystals, for instance, must be modeled with the octahedral formulation only. Numerical experiments must be conducted to clarify this point.

One question remains unanswered with respect to the process of cube slip in these two-phase materials. It is the question of the slip plane in the matrix when the precipitate is sheared on $\{001\}$. The occurrence of cube slip in the matrix has not been documented, and so it remains possible that the screw dislocations which shear the γ' on cube planes cross-slip to octahedral planes after exiting the precipitate. Also, it is not clear whether or not $\langle 111 \rangle$ crystals deform by single cube slip with $b = a/2[\bar{1}10]$, or if primary octahedral dislocations ($b = a/2[\bar{1}01]$) also participate during some phase of the deformation process. These questions are relevant to the present discussion, because independent determination of the cube constants requires that no octahedral slip be active during the measurements. This cannot be addressed unambiguously at this point, since $\langle 111 \rangle$ crystals were not studied as part of this investigation.

The problem of determining the cube constants can be avoided by curve fitting. It is known that cube slip does not occur in $\langle 001 \rangle$ or $\langle 011 \rangle$ crystals. Therefore, the

octahedral constants and orientation dependence can be determined by testing these two orientations. The octahedral formulation can then be fit to the $\langle 111 \rangle$ data, and any deviation can be attributed to primary cube slip.

A more serious problem arises when primary cube slip and primary octahedral slip both occur, either simultaneously or in sequence. The problem is that the cube and octahedral equations are uncoupled; that is, there are no common terms, so plastic deformation on one type of system cannot effect the constitutive behavior of the other type of system. This is a significant problem. For example, consider a $\langle 001 \rangle$ crystal which is being uniaxially deformed at 700°C . If the test is interrupted, the deformation substructure will contain many trapped dislocations within the γ' , as seen in Figures 5 and 41. Now, if this deformed crystal is strained in torsion, the model would predict cube slip at a rate equal to a virgin crystal. Since these trapped dislocations strengthen the material (latent hardening), virgin behavior is highly unlikely, so the model cannot handle this history effect.

Although coupling of the evolution equations would certainly carry a steep computational price, this is necessary to completely characterize such prior history effects. This is especially relevant to real structural analysis problems, in which complex thermomechanical deformation histories are often encountered.

A simple method for introducing uncoupled latent hardening is described below. To capture some of the effects of prior history without resorting to a full coupling of the evolution equations, a scalar hardening parameter similar to that in the rate-independent plasticity theory (Equation 3-17) could be introduced. As an example, define an incremental octahedral hardening parameter as follows:

$$dh_1 = \sum_{i=1}^{12} \tau_i d\gamma_i \quad (9-20)$$

Similar to isotropic hardening, it is likely that the latent hardening effect of octahedral slip on the cube slip systems would saturate to a steady-state value. To model this, define a "latent drag stress" as

$$\kappa_1 = \beta_{19} - \beta_{20} \exp(-\beta_{21} h_1) \quad (9-21)$$

where the constants are temperature dependent. The constants could be determined experimentally by sequential deformation experiments. Now, this latent hardening drag stress could be simply added to the drag stress in the cube slip flow rule:

$$\dot{\alpha}_i = (\text{sign}[\pi_i - \omega_i]) (|\pi_i - \omega_i| / [\kappa_i + \kappa_1])^{\eta_4} \quad (9-22)$$

A similar expression could be developed to model the latent

effects of cube slip on the octahedral formulation. This simple, linear approach may be sufficient to describe some important history effects.

The Global Plastic Strain Rate

Since the shear strain rates on each slip system are determined by Equations 9-5 and 9-17, it is a simple matter to calculate the global strain rates. By linear superposition,

$$\dot{\epsilon}_{ij}^{in} = \sum_{r=1}^{12} (a_{ij}^{(r)}) \dot{\gamma}^{(r)} + \sum_{s=1}^6 (a_{ij}^{(s)}) \dot{\alpha}^{(s)} \quad (9-23)$$

where $a_{ij} = [n_i l_j + n_j l_i]/2$. The isothermal stress rate tensor is determined by

$$\dot{\sigma}_{ij} = D_{ijkl} (\dot{\epsilon}_{kl} - \dot{\epsilon}_{kl}^{in}) \quad (9-24)$$

where the D's are the elastic constants. Structural analysis problems are solved numerically.

Regimes of Similar Behavior

In its most general form, the WJ model is capable of describing the effects of all important mechanisms: Cube slip, cube cross-slip, multiple slip, latent hardening, isotropic hardening, kinematic hardening, and rate dependency. At a given temperature, however, all these mechanisms are not necessarily activated. When this is the

case, the model can be simplified and the number of constants which need to be determined can be reduced. With this goal in mind, regimes of similar behavior can be deduced from the results of the present study. These regimes are listed below in the order of increasing temperature, and a brief description of the dominant deformation mechanisms are given:

- I : Rate independent octahedral γ' shearing. (Below 600°C).
- II : Rate independent octahedral γ' shearing and rate independent cube γ' shearing. (600 to 760°C).
- III: Rate dependent octahedral γ' shearing, rate dependent cube γ' shearing, and rate dependent γ' by-pass. (760 to 820-950°C, depending on strain rate).
- IV : Rate dependent cube γ' shearing and rate dependent γ' by-pass. (Above 820-950°C, depending on strain rate).

Figure 65 summarizes the orientation and temperature boundaries for each of these regimes. Each regime will now be discussed in terms of temperature limits and model requirements for uniaxial, isothermal deformation.

Regime I

This is the low temperature regime, which includes temperatures up to about 600°C. Only octahedral slip occurs

in PWA 1480 and Rene N4, so the cube formulation may be ignored. Diffusion is slow, so thermal recovery and creep may be ignored. However, strain hardening and cube cross-slip are important, and the number of active slip systems has a strong effect on constitutive behavior, so latent hardening must be considered. If the number of active slip systems does not change during deformation, the behavior can be modeled as follows:

$$\dot{\epsilon}_{ij}^{in} = \sum_{r=1}^{N_0} (a_{ij}^{(r)}) \dot{\gamma}^{(r)} \quad (9-25)$$

$$\dot{\gamma}^{(r)} = (\text{sign}[\tau_r - \Omega]) (|\tau_r - \Omega|/K)^{\eta_1} \quad (9-26)$$

$$\begin{aligned} \dot{K} = & \{\beta_1(1 + [N_0 - 1]q) \\ & - \beta_2 N_0 (K - b_4 - \beta_5 \exp[\beta_6 \tau_c])\} |\dot{\gamma}| \end{aligned} \quad (9-27)$$

$$\dot{\Omega} = \beta_9 \dot{\gamma} - \beta_{10} |\dot{\gamma}| \Omega \quad (9-28)$$

This is a substantial simplification over the general model. Only one shear flow rule is used instead of two, and only 11 material constants need to be determined at each temperature instead of 28.

The model does not have an explicit term to describe the occurrence of the $a/3\langle 112 \rangle$ hardening mechanism seen at

200°C and below (Chapter VI). However, this is not completely necessary. The effects of the mechanism will be captured by the temperature dependence of the constants in the state variable evolution equations.

Regimes II and III

This is the intermediate temperature regime, the start of which is defined by the onset of primary cube slip in near- $\langle 111 \rangle$ crystals at about 600°C. The boundary between Regimes II and III is defined by the onset of rate dependence, at about 750°C. (Although the materials are fairly rate independent at tensile or LCF strain rates, significant creep strains can occur at temperatures above about 700°C). The upper bound of Regime III is defined as the temperature where γ' by-pass controls the deformation instead of octahedral γ' shearing in crystals not near $\langle 111 \rangle$. Since by-pass is thermally activated, the upper bound is a function of strain rate. It occurs at about 820°C at a strain rate of 0.5%/min, and at about 930°C at a strain rate of 50%/min. Unfortunately, as described earlier the boundary may be a function of orientation: Shearing was observed at 50%/min in $\langle 123 \rangle$ crystals at 927°C, while by-pass was observed in $\langle 001 \rangle$ crystals tested at the same rate and temperature. More research is necessary to clarify this orientation dependence.

This temperature regime displays the most complex behavior, and thus takes full advantage of the generality of

the anisotropic model. Octahedral γ' shearing, cube γ' shearing, cube cross-slip, strain hardening, γ' by-pass, and rate dependence are all observed. Therefore, the full form of the model must be used.

Regime IV

This is the highest temperature regime. Its description is also substantially simplified, because only γ' by-pass and primary cube slip (in crystals within 20° of $\langle 111 \rangle$) occur. Due to easy climb and cross-slip, deformation structures are non-planar (Figures 6, 36 and 37). Because of this lack of strong planarity, the number of active slip systems does not have a strong effect on strength or ductility [8,9]. Also, as shown in Figure 28 and Appendices D and E, the cyclic yield strengths and plastic strain ranges are essentially stable, so isotropic hardening can be ignored. Walker and Jordan [80] have published an example application of their model, using data from this temperature regime (870°C , less than 6%/min strain rate). The constants that they fit to the model describe the above mentioned behavior exactly. In the notation of the present study, the model has the following form for use at these high temperatures:

$$\dot{\epsilon}_{ij}^{in} = \sum_{r=1}^{12} (a_{ij}^{(r)}) \dot{\gamma} + \sum_{s=1}^6 (a_{ij}^{(s)}) \dot{\alpha}^{(s)} \quad (9-29)$$

$$\dot{\gamma}^{(r)} = (\text{sign}[\tau_r - \Omega]) (|\tau_r - \Omega|/K)^{\eta_1} \quad (9-30)$$

$$\dot{K} = \beta_3 (K - \beta_8) \quad (9-31)$$

$$\dot{\Omega} = \beta_9 \dot{\gamma} - \beta_{10} |\dot{\gamma}| \Omega - \beta_{11} \text{sign}(\Omega) |\Omega|^{\eta_3} \quad (9-32)$$

$$\dot{\alpha}^{(s)} = (\text{sign}[\pi_s - \omega]) (|\pi_s - \omega|/[\kappa + \kappa_1])^{\eta_4} \quad (9-33)$$

$$\dot{\kappa} = 0 \quad (9-34)$$

$$\dot{\omega} = \beta_{16} \dot{\alpha} - \beta_{17} |\dot{\alpha}| \omega - \beta_{18} \text{sign}(\omega) |\omega|^{\eta_6} \quad (9-35)$$

This form is also much simpler than the general form. 15 temperature dependent constants are necessary instead of 28. Again, Equation 9-33 must be structured such that the cube strain rate is negligible when $\pi_{\max} < 1.15 \cdot \tau_{\max}$.

General Evaluation and Summary

It has been found that the Walker-Jordan constitutive

model is capable of describing the constitutive behavior of PWA 1480 and while still maintaining consistency with the observed deformation mechanisms. However, the following points (which have already been made) should be addressed to assure that the model is consistent with the material deformation behavior:

1. Primary cube slip (although not seen in this study) has been reported to occur in PWA 1480 and Rene N4 at temperatures above 600°C, but only when $\tau_{(001)[\bar{1}10]}$ is greater than $1.15 \cdot \tau_{(111)[\bar{1}01]}$. Therefore, anisotropy which occurs in crystals not within 20° of $\langle 111 \rangle$ must be modeled via the octahedral formulation only. Also, it appears that cube slip is alloy dependent.
2. Latent hardening between cube and octahedral slip should be included, especially at 600-800°C, where strain hardening is extensive. A simple model was proposed in Equations 9-20 to 9-22.
3. It appears that the back stress state variable should not be isotropic in the γ' shearing temperature regime. However, more data is needed to clarify the form of the anisotropy.

The orientation and temperature boundaries proposed for the constitutive model are summarized in Figure 65.

CHAPTER X

SUMMARY AND CONCLUSIONS

In this study, experiments were carefully designed to answer specific questions regarding the relationships between mechanical properties and deformation mechanisms in the single crystal superalloy PWA 1480. These results were interpreted analytically, both from the perspective of a materials scientist and a mechanical engineer. This approach has lead to several new results, most notably the ability to explain the unique minimum in the CRSS of PWA 1480 at 400°C. Additionally, results from the current study that were not new were subjected to new interpretations and related to fundamental models. In this way, it was possible to discriminate between two models of the cube cross-slip event, lending support to one and suggesting the elimination of the other. The data from the present study has also been used (in conjunction with data from previous studies) to suggest guidelines for advanced anisotropic constitutive models. These points are summarized in more detail below.

General Observations

It was shown earlier in this study [4,5] that the monotonic mechanical properties and deformation behavior of

<001> crystals of PWA 1480 could be grouped into two temperature regimes. At low temperatures (760°C and below), the strength was independent of strain rate and the material deformed by octahedral γ' shearing; at high temperatures (above 820-950°C depending on strain rate), the rate dependent strength could be characterized by a constant activation energy, and the material deformed by γ' by-pass; a transition occurred between these two regimes. The present study has been expanded to include cyclic deformation, orientation effects, and stress direction effects. It has been found that the behavior of the alloy under these conditions can be characterized by the same two temperature regimes. In summary, <001> and <123> PWA 1480 crystals exhibited the following behavior:

Low Temperatures¹

Anisotropic CRSS

T-C CRSS Asymmetric

Anisotropic Strain Hardening
(Monotonic and Cyclic)

Latent Hardening

Inhomogeneous, Planar
Octahedral Slip

γ' Shearing

High Temperatures²

Isotropic CRSS

T-C CRSS Symmetric

Little Strain Hardening,
Cyclic Stability

No Latent Hardening

Homogeneous, Wavy
Slip

γ' By-Pass

¹Below 760°C.

²Above 820-950°C, depending on strain rate.

No cube slip was observed at any temperature in either crystal orientation.

Consistent with studies by previous investigators [7,25-27,29], it was found that the asymmetric behavior observed at low temperatures could be explained qualitatively by the application of the cube cross-slip model. Orientation dependent and stress direction dependent variations in the Shockley partial constriction stress lead to variations in the rate of cube cross-slip; this variation in cross-slip rate leads to variations in the CRSS, as well as variations in the monotonic and cyclic strain hardening behavior.

Strain hardening behavior at low temperatures was also affected by the number of active slip systems. $\langle 123 \rangle$ crystals exhibited very heterogeneous, discrete slip bursts on parallel slip planes. $\langle 001 \rangle$ crystals exhibited more homogeneous slip on intersecting slip planes. Consequently, $\langle 001 \rangle$ crystals strain hardened more than $\langle 123 \rangle$ crystals, both in tension and fatigue. At high temperatures, non-planar γ' by-pass was observed, and there was no apparent difference between $\langle 001 \rangle$ and $\langle 123 \rangle$ crystals.

The CRSS Minimum at 400°C

As proposed earlier, it was found that PWA 1480 deformed by planar γ' shearing on $\{111\}$ planes at temperatures below 760°C. In the present study, it was

found that the details of the shearing mechanism were strongly temperature dependent. At all temperatures below 760°C, γ' shearing by pairs of $a/2\langle 110 \rangle$ dislocations on $\{111\}$ planes was observed. Below 400°C, an additional mechanism was activated: The octahedral planes within the γ' were littered with S-ISF strips and loops which were formed by the glide of $a/3\langle 112 \rangle$ partials. The density of these defects was high at 20°C, and decreased to zero at 400°C. This corresponded exactly to the decrease in CRSS from 20 to 400°C, suggesting that the faults strengthened the material. At temperatures between 400 and 760°C, the CRSS exhibited an increase with temperature. This increase corresponded with the observation of an increasing density of trapped screw dislocations within the γ' , implying that the CRSS rise in this regime was caused by the classical thermally activated cube cross-slip mechanism.

Thus, it was proposed that the stacking fault mechanism was responsible for the shape of the curve below 400°C, while the cross-slip mechanism was responsible for the shape of the curve from 400 to 760°C. The minimum at 400°C marked the transition point. However the cross-slip mechanism also affected the strength at 400°C and below, as evidenced by the tension-compression asymmetry in the CRSS.

Cross-Slip Models

Similar to previous investigators, a cyclically stable

tension-compression asymmetry was observed during fully reversed cyclic deformation below 760°C. In the present study, it was proposed that this stable asymmetry implied that the cross-slip event must be reversible. This proposal was supported with thermodynamic calculations of the energy of the cross-slipped configuration relative to the reference configuration as a function of stress.

This reversibility constraint was used as a critical test of the available models for cube cross-slip. It was shown that the model proposed by Paidar, Pope and Vitek is the only available model which satisfied the reversibility constraint. Thus, the present study on PWA 1480 resulted in support for a fundamental model of deformation in single crystal γ' .

Constitutive Modeling

The results of the present study and other pertinent studies were used to specify boundaries of regimes of similar deformation behavior. For the purpose of example, these boundary conditions were introduced specifically into the Walker-Jordan anisotropic constitutive model.

Simplifications of the model were proposed for use at low temperatures (below 600°C) and at high temperatures (above 820-950°C depending on strain rate). These simplifications were based on observed deformation mechanisms and mechanical behavior. A modification was also

proposed to model latent hardening between octahedral slip systems and cube slip systems at temperatures where both operate. It was proposed that the use of an isotropic back stress was not consistent with the results of the present study. However, there was not sufficient data available to suggest an analytical form for an anisotropic back-stress state variable.

In general, it was found that foundation of the WJ model should be able to model most of the observed deformation behavior of the alloy. However, numerical experiments were not conducted, so it is not known if the actual form of the model is consistent with the guidelines established in the present study. It is known that the model contains explicit terms to handle most major sources of material anisotropy, and has resulted in a good fit between theory and experiment in limited testing. Future numerical experiments should be able to determine if the model is consistent with the deformation behavior, by comparing numerical results with the guidelines established in this study.

CHAPTER XI

RECOMMENDATIONS

There are three recommended areas of research that should yield useful, usable results within a reasonable time period. The first concerns the measurement of the temperature dependence of fault energies, the second concerns a study of primary cube slip, and the third concerns numerical experimentation designed to test the physical consistency of the advanced constitutive models.

The Temperature Dependence of Fault Energies

The discussions in Chapters VII and VIII were concerned with modeling of deformation behavior as a function of temperature. It is obvious from those chapters that more information about the temperature dependence of the superlattice stacking fault energies and APB energies was needed. These experiments are not easy to conduct; they require in-situ heating stages, and very careful weak-beam TEM measurements at temperature. However, they are not impossible, as evidenced by the availability of the temperature dependence of the stacking fault energies in FCC metals [101,102]. For example, a good study of the {111} APB energy as a function of temperature would be extremely valuable for deformation modeling.

Primary Cube Slip

A thorough experimental study of primary cube slip is necessary. The important variables are chemistry, temperature, strain rate, orientation, and deformation history. The mechanism of primary cube slip is too important to be ignored or speculated on any longer.

Constitutive Modeling

The present study has resulted in specific guidelines for the anisotropic constitutive models. For example, it has been determined that cube slip should only be active at temperatures above 600°C, and only in orientations within 20° of $\langle 111 \rangle$. This means that any anisotropy observed in other orientations must be modeled by the octahedral formulation only; otherwise, the constitutive model is just fancy curve-fitting. Numerical experiments must be conducted to test the models against these guidelines, then suggest changes if necessary. This is the logical next step for a project such as this one.

Additionally, the matter of the anisotropic back stress should be addressed. It may turn out, for example, that some of the anisotropy which is currently contained in the drag stress would be better handled in the back stress. More experimental data concerning back stress is necessary, and so is additional numerical experimentation.

Table 1
Alloy Composition

Element	Weight Percent
Al	4.8
Ti	1.3
Ta	11.9
Cr	10.4
Co	5.3
W	4.1
C	(42 ppm)
Ni	Bal.

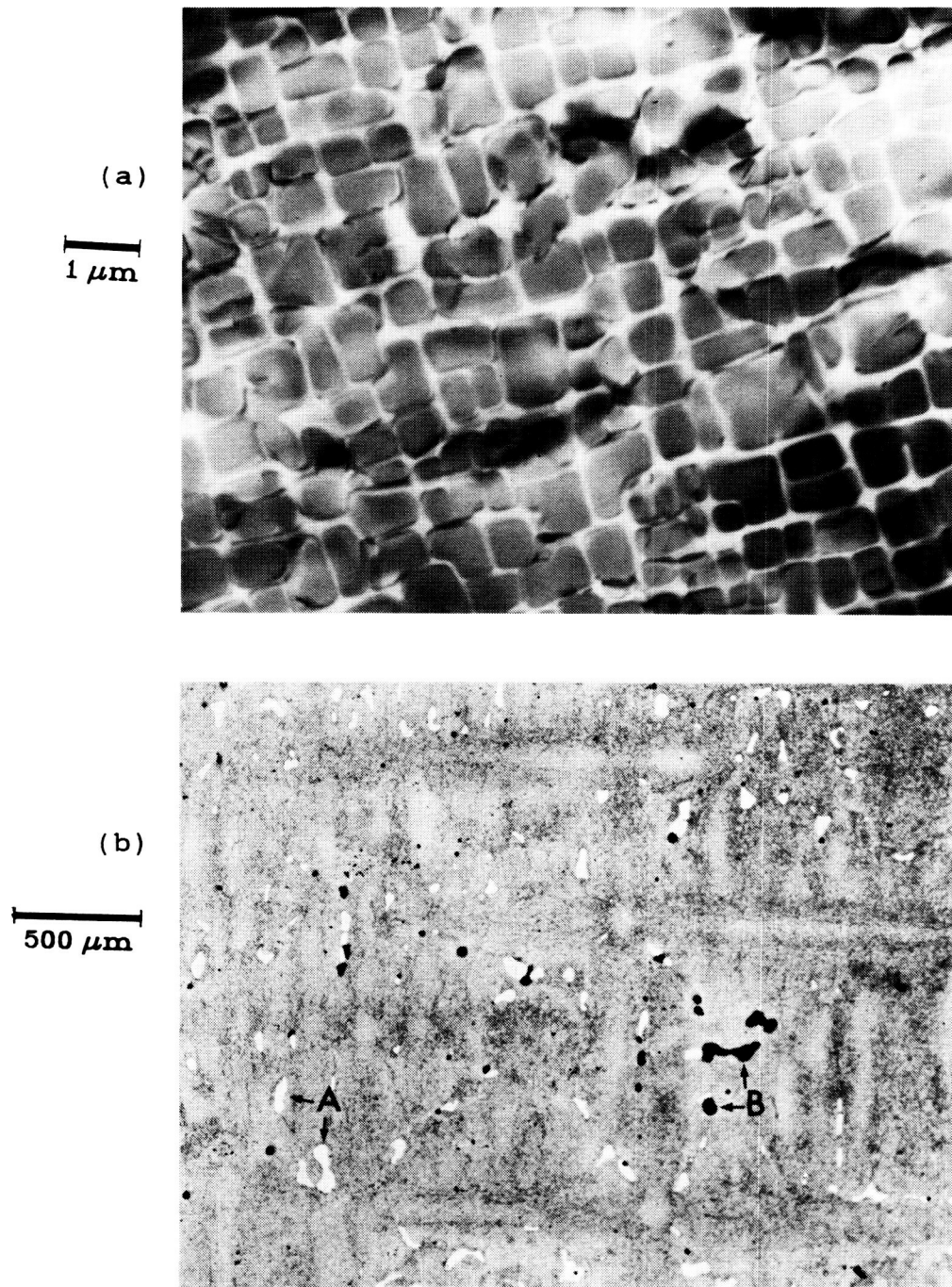
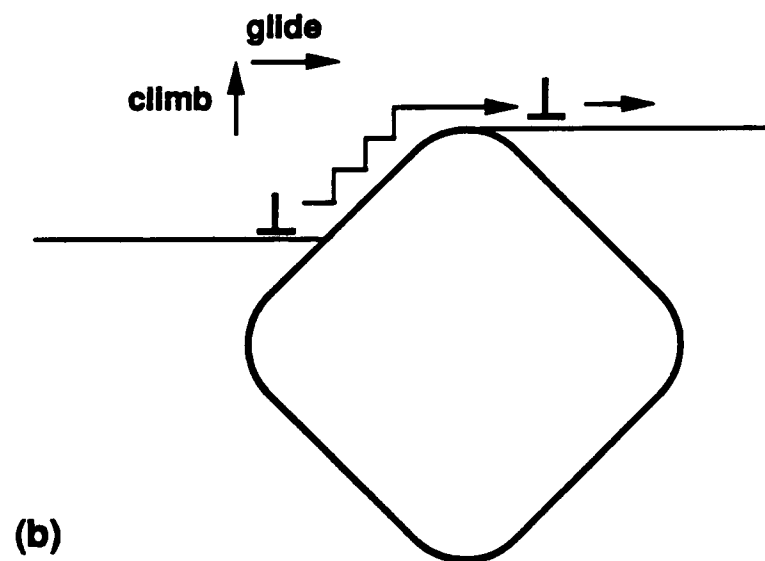
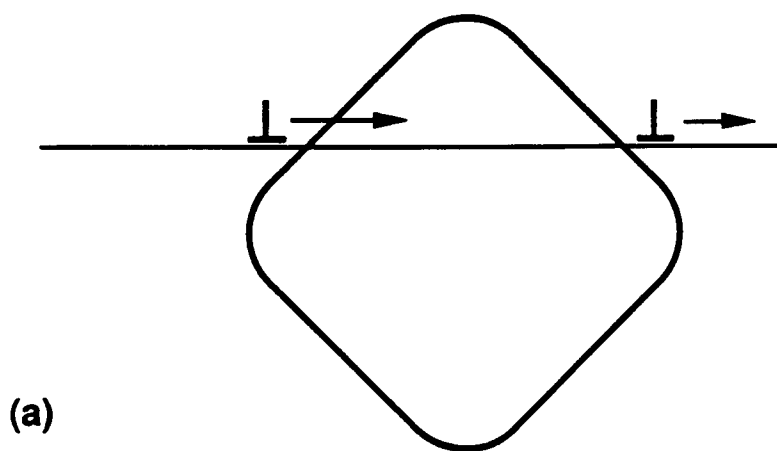


Fig 1. Initial microstructure. (a) Brightfield TEM micrograph of the γ/γ' structure, $g = \langle 200 \rangle$. (b) Optical micrograph showing residual dendritic structure, eutectic areas (A), and micropores (B).



**Fig 2. Dislocation/precipitate interactions (a) Shearing
(b) By-pass**

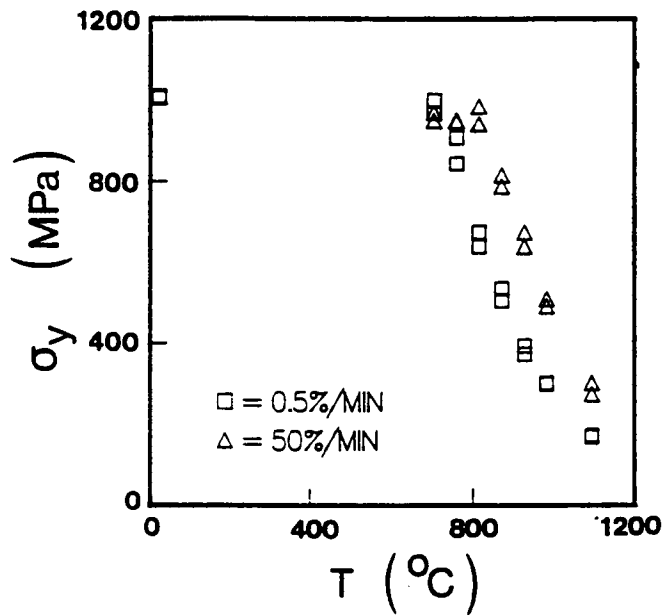


Fig 3. Yield strength (at 0.05% offset) vs Temperature for <001> crystals of PWA 1480 [4,5].

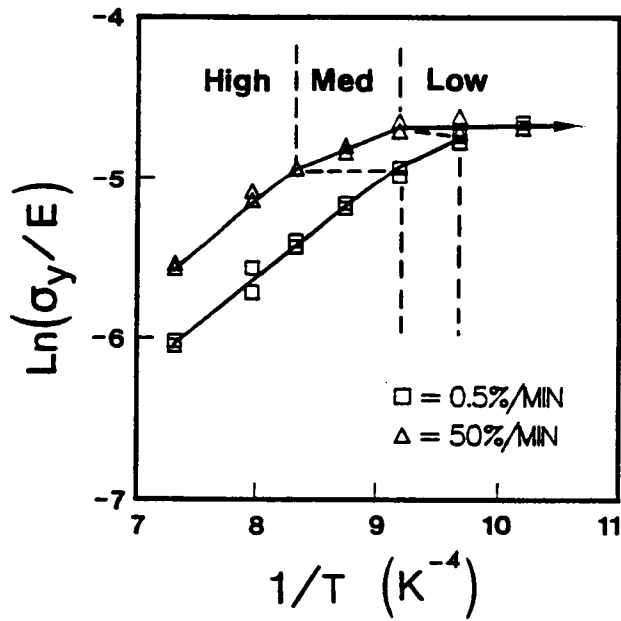


Fig 4. Arrhenius representation of the 0.05% yield strength data.

ORIGINAL PAGE IS
OF POOR QUALITY

0.2 μm



Fig 5. Typical low temperature shearing-type deformation structure. T70-2, $\langle 001 \rangle$, 705°C , $\gamma_p = 0.05\%$, $\langle 001 \rangle$ zone axis multi-beam condition.

0.5 μm

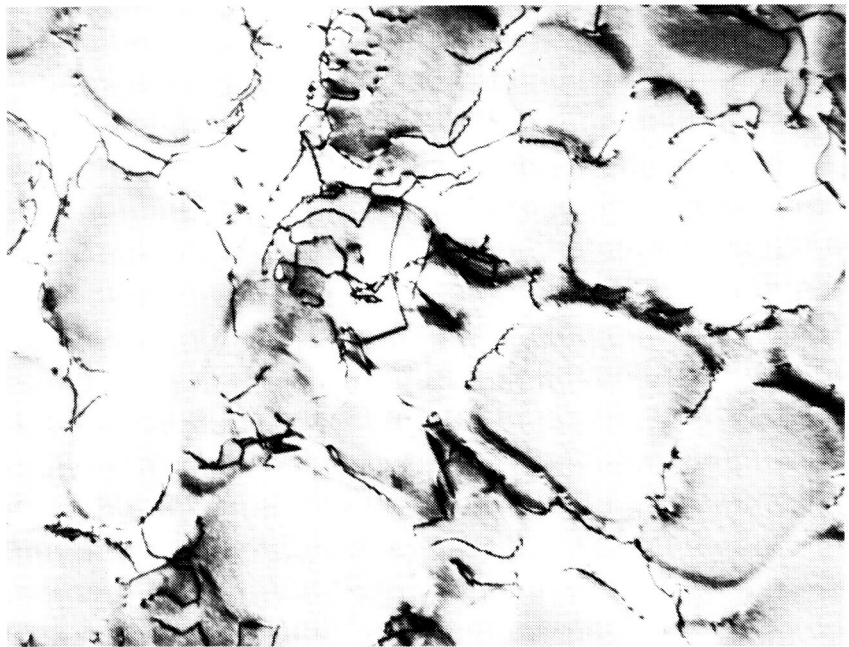


Fig 6. Typical high temperature by-pass type deformation structure. #63-1, $\langle 001 \rangle$, 982°C , $\gamma_p = 0.1\%$, $g = \langle 200 \rangle$.

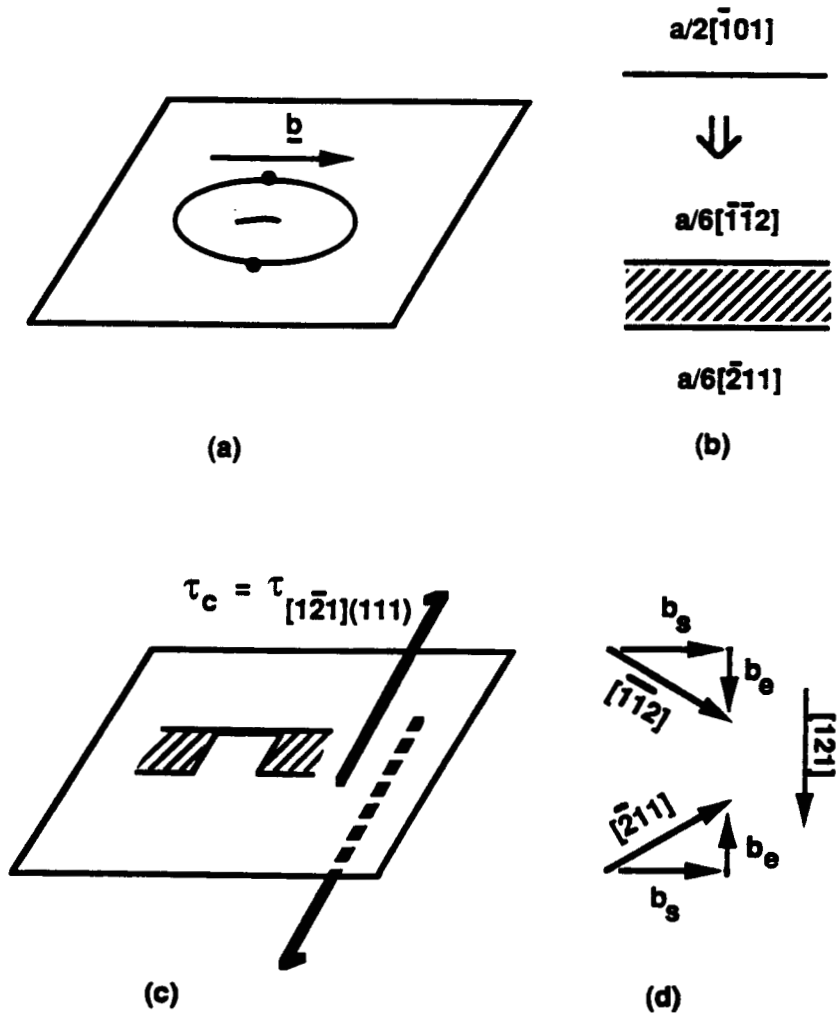
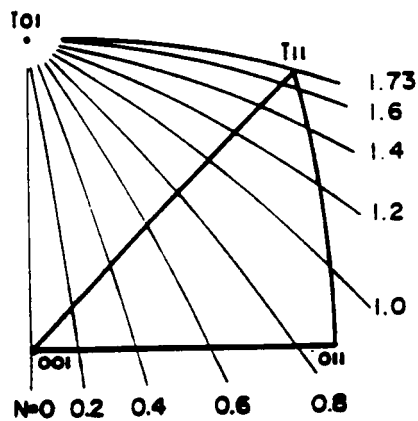
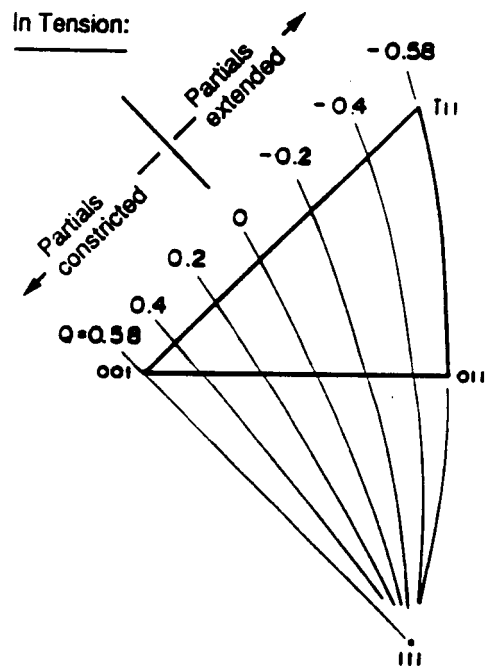


Fig 7. Mechanism of constriction. (a) $a/2\langle 110 \rangle$ loops being emitted from a Frank-Read source. (b) $a/2\langle 110 \rangle$ unit dislocations are dissociated into Shockley partials. (c) Constriction, which must preclude cross-slip. (d) Burgers vector diagram showing that τ_c , in the direction of $[\bar{1}21]$ is the only component of stress that can move the partials in different directions.



$$N = \frac{\text{Schmid factor on } (010)[\bar{1}01]}{\text{Schmid factor on } (111)[\bar{1}01]}$$

(a)



$$Q = \frac{\text{Schmid factor on } (111)[\bar{1}\bar{2}1]}{\text{Schmid factor on } (111)[\bar{1}01]}$$

(b)

Fig 8. Schmid factor ratios, from Reference 12.

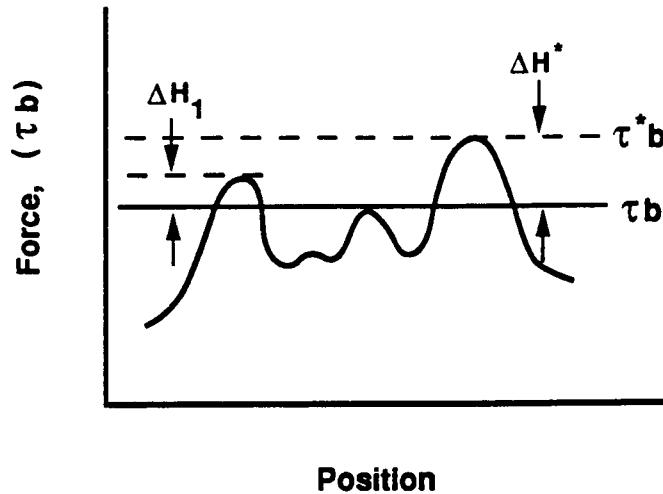


Fig 9. Schematic representation of barriers to dislocation motion along a slip plane. At the applied stress level indicated, two barriers must be overcome for further motion, and their activation energies per unit length of dislocation are indicated. If the second barrier is the strongest in the slip plane, it will control the CRSS.

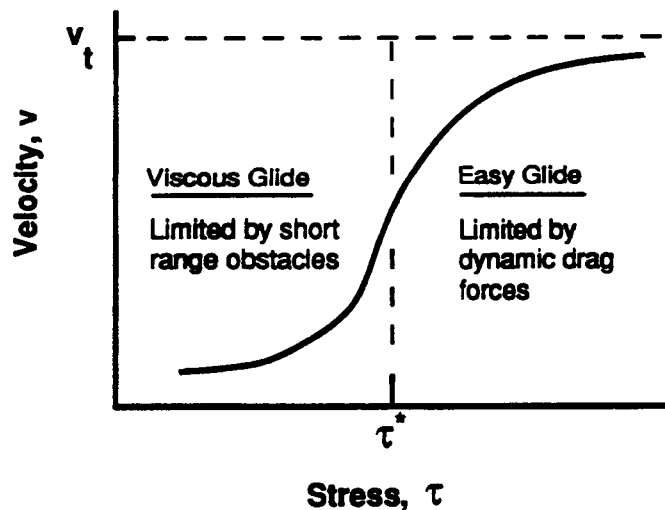


Fig 10. Schematic representation of dislocation velocity versus stress in a single phase material. At low stresses, the velocity is determined by the rate of overcoming local barriers, as in Fig 9. At high stresses, the velocity is limited by dynamic dislocation drag forces, such as phonon drag.

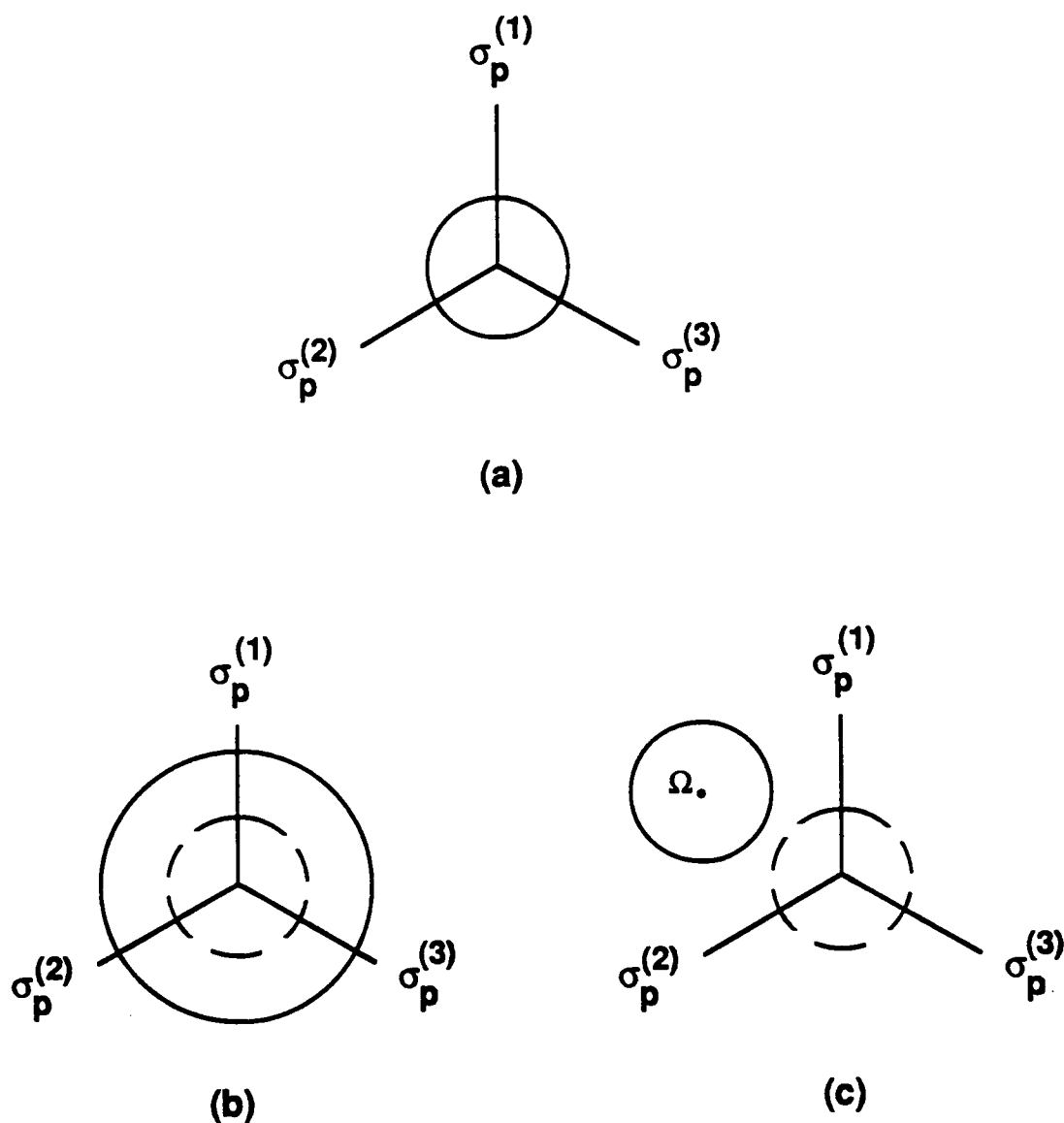
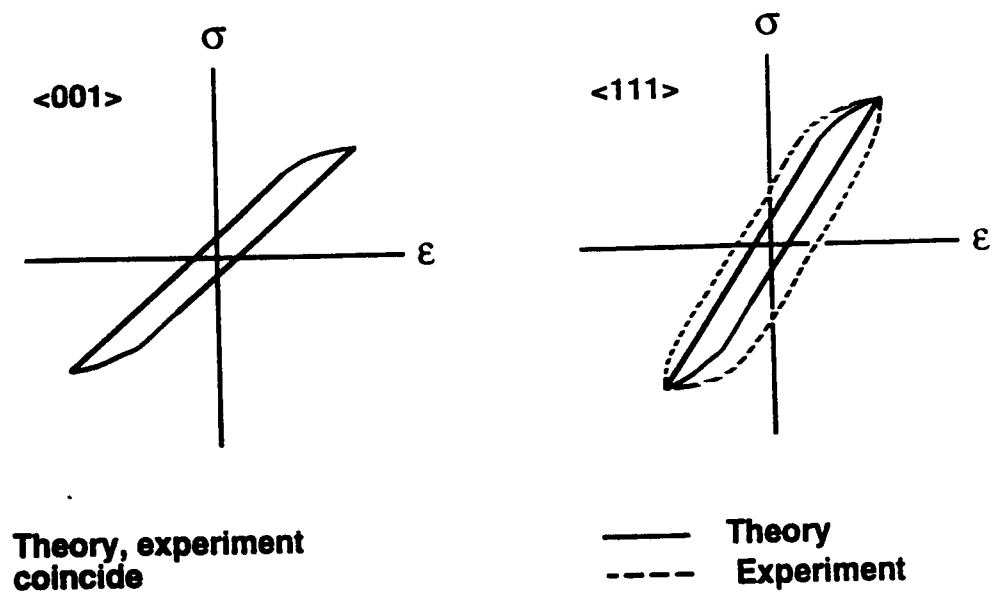


Fig 11. Von-Mises yield surface intersection with π -plane. (a) Initially isotropic yield surface. (b) Pure isotropic hardening, seen as a uniform increase in the radius of the yield surface. (c) Pure kinematic hardening, seen as a translation of the yield surface. The origin of the yield surface after kinematic hardening corresponds to the principal values of the back-stress, Ω .



$$\dot{\epsilon}_{ij}^p = \psi \left[\frac{s_{ij} - \Omega_{ij}}{\kappa} \right] \quad (\text{Unified viscoplastic flow rule})$$

Fig 12. Discrepancy between theory and experiment in single crystal PWA 1480. After Reference 79.

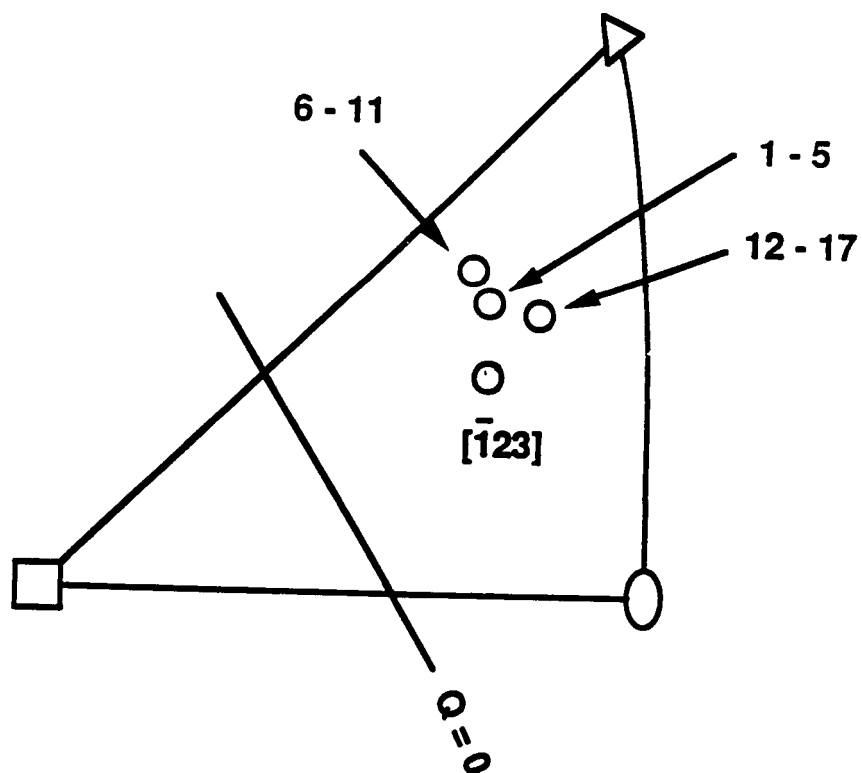


Fig 13. Tensile axis orientations of the nominally $\langle 123 \rangle$ crystals, also showing the $Q = 0$ great circle.

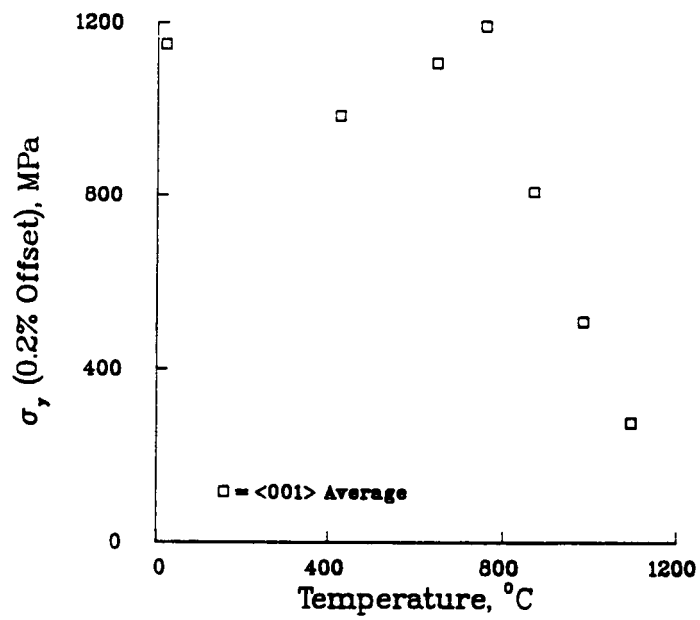


Fig 15. Average yield strength values for <001> PWA 1480 taken from the literature [7-9]. 0.5%/minute strain rate.

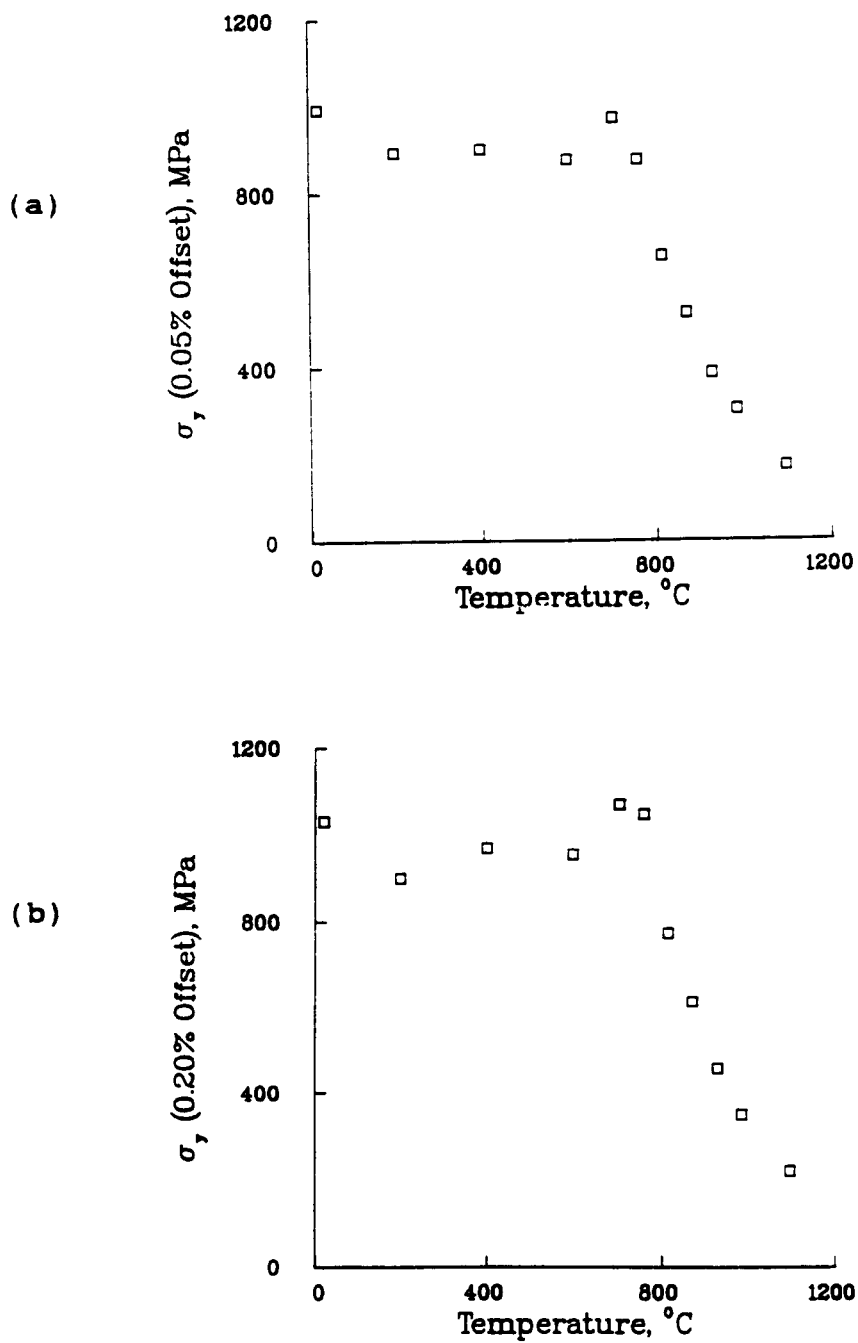


Fig 16. Average yield strength values from current study.
<001>, 0.5%/min. Data is in Appendix C.
(a) 0.05% offset (b) 0.2% offset

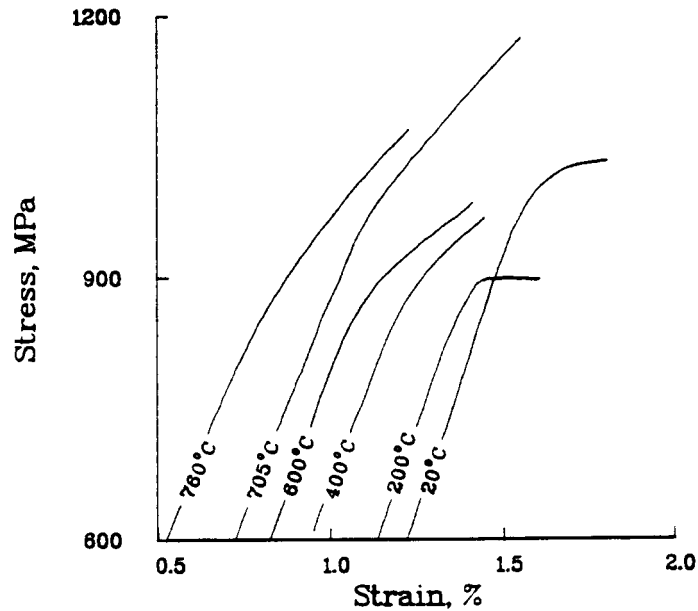


Fig 17. Stress-strain curves of the low temperature $\langle 001 \rangle$ interrupted tensile tests, showing increasing strain hardening with temperature. Strain zero is offset for clarity. 0.5%/min strain rate.

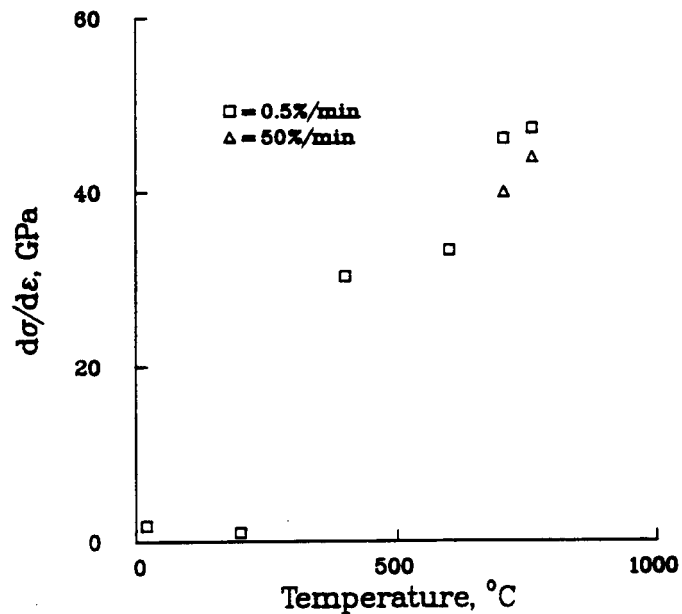


Fig 18. $d\sigma/d\epsilon$ vs Temperature, $\langle 001 \rangle$ crystals. Slope was measured between 0.1 and 0.2% plastic strain.

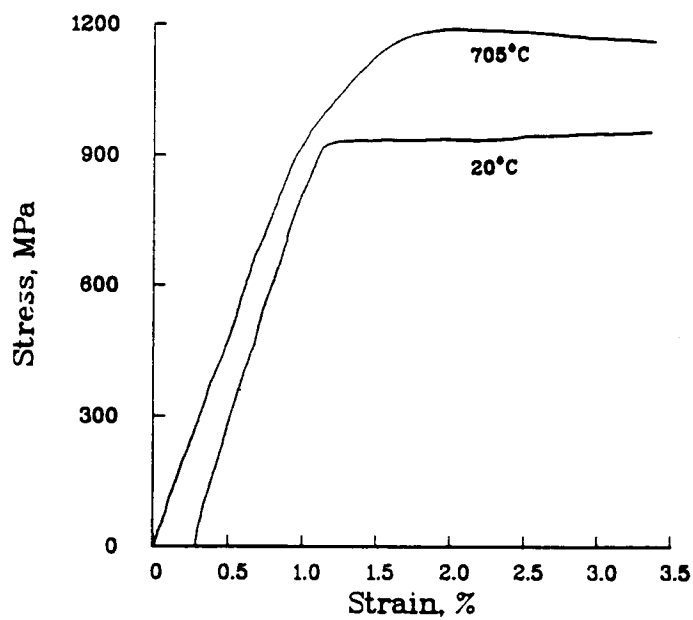


Fig 19. Large strain tensile curves, $\langle 001 \rangle$, 0.5%/min. Crystals were deformed plastically 0.25% in compression prior to test, so initial yielding data is suspect. Strain zero is offset for clarity.

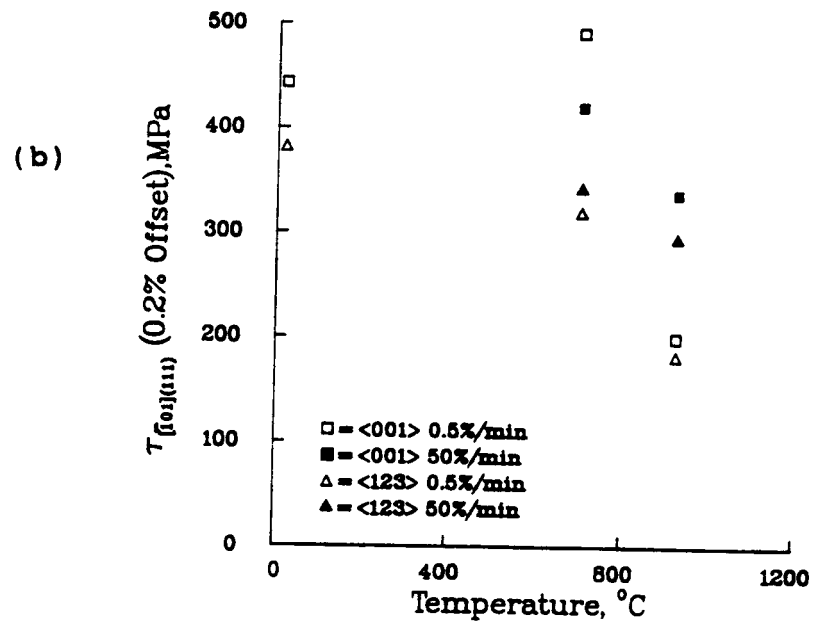
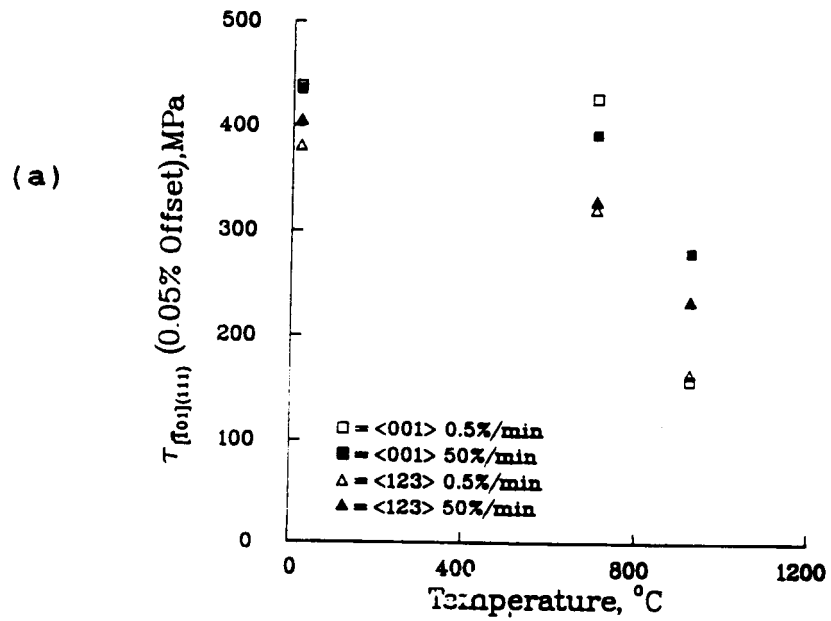


Fig 20. Average tensile CRSS values for $\overline{[101]}(111)$ system.
 (a) 0.05% offset. (b) 0.2% offset.

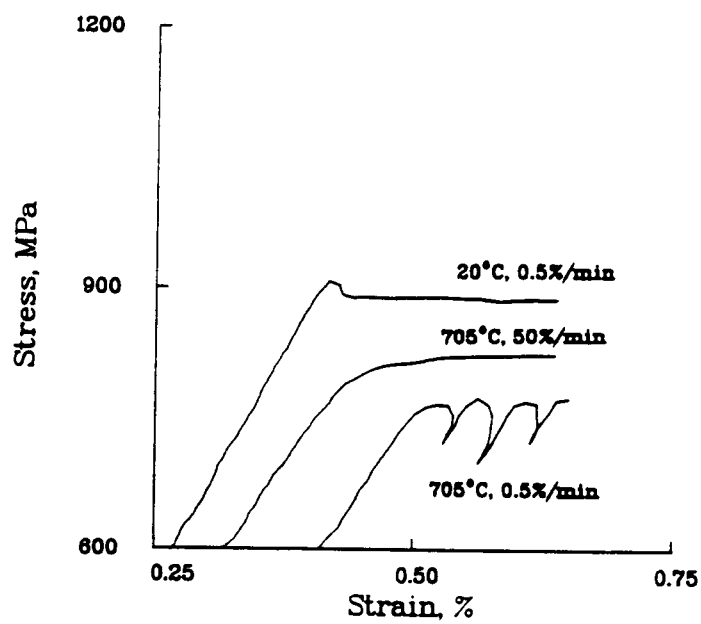


Fig 21. Stress-strain curves of the low temperature <123> interrupted tensile tests. 0.5%/min. Strain zero is offset for clarity.

ORIGINAL PAGE IS
OF POOR QUALITY

100 μm

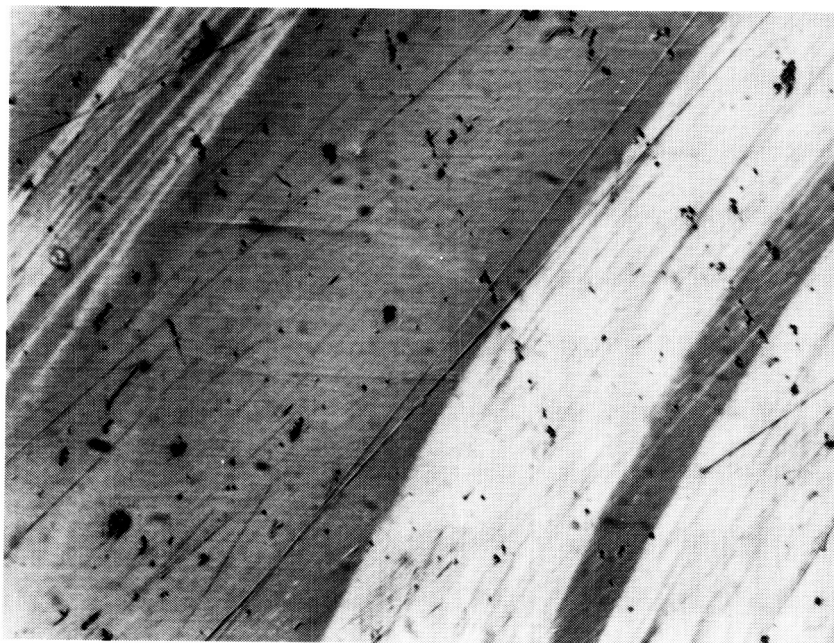


Fig 22. Surface replica showing slip traces. T1, $\langle 123 \rangle$, 20°C , $0.5\%/ \text{min}$, $\gamma_p = 0.12\%$, interrupted tensile test. Stress axis is horizontal.

100 μm

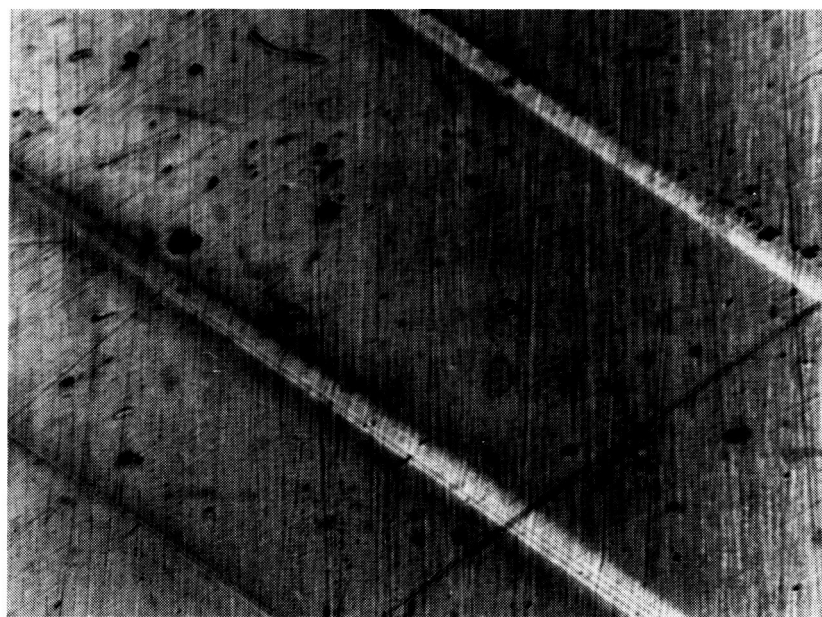


Fig 23. Surface replica showing slip traces. T6, $\langle 123 \rangle$, 705°C , $0.5\%/ \text{min}$, $\gamma_p = 0.09\%$, interrupted tensile test. Stress axis is horizontal.

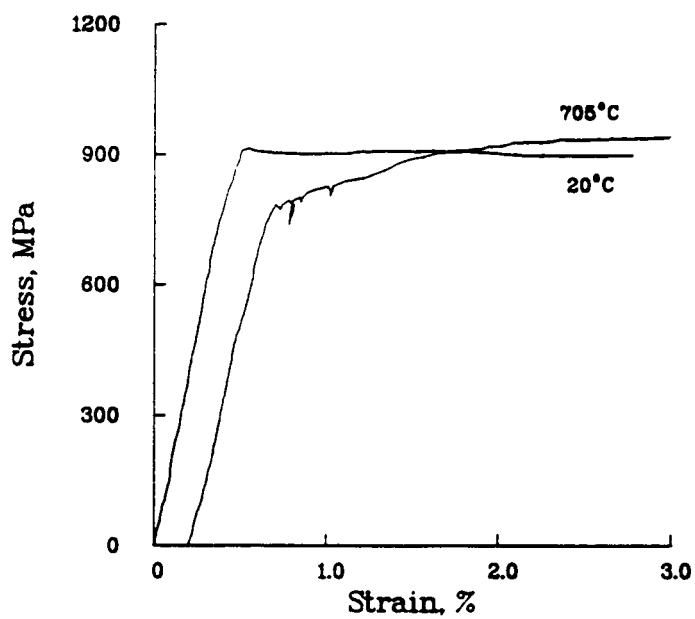


Fig 24. Large strain tensile curves, $\langle 123 \rangle$, 0.5%/min. Crystals were deformed plastically 0.25% in compression prior to test, so initial yield data in suspect. Strain zero is offset for clarity.

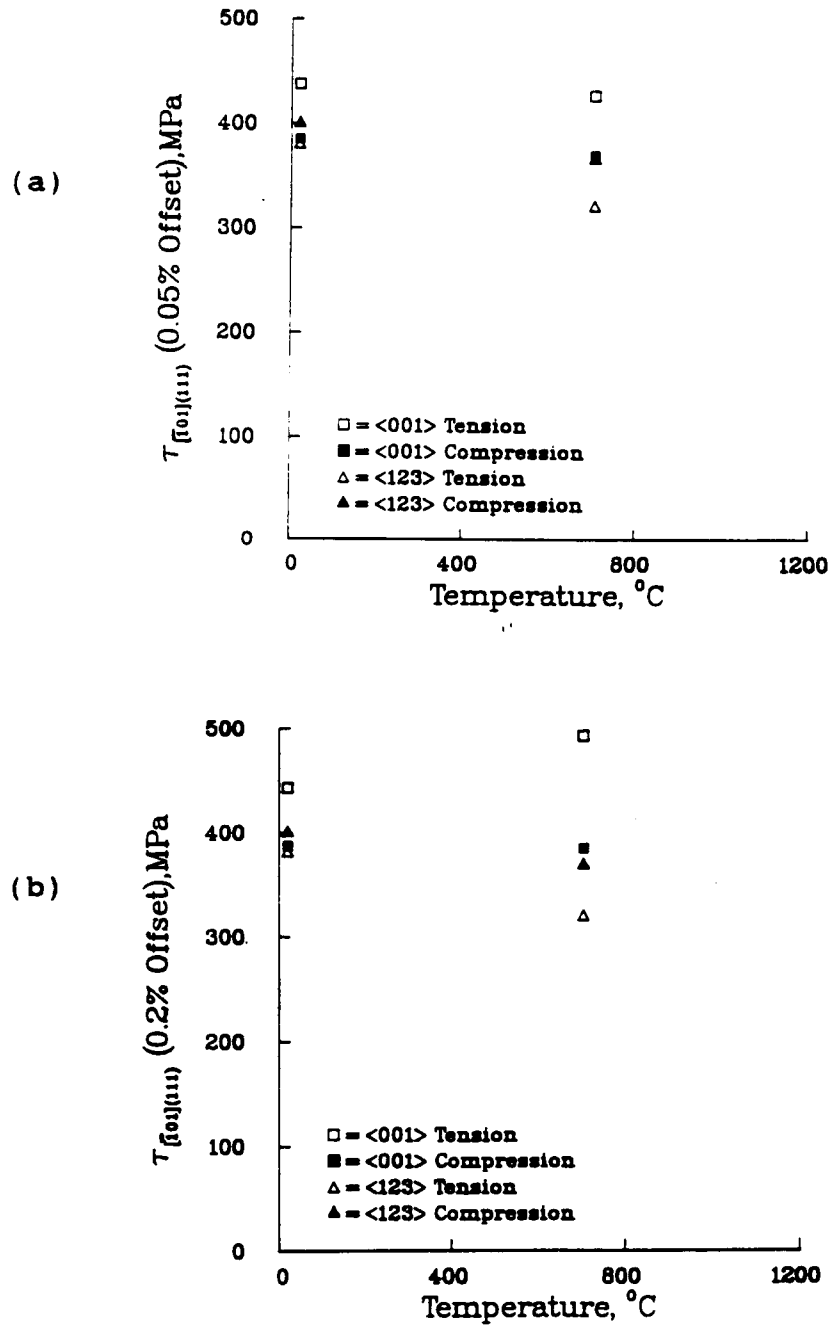


Fig 25. Average tensile and compressive CRSS values for the $[\bar{1}01](111)$ system. 0.5%/min. (a) 0.05% offset. (b) 0.2% offset.

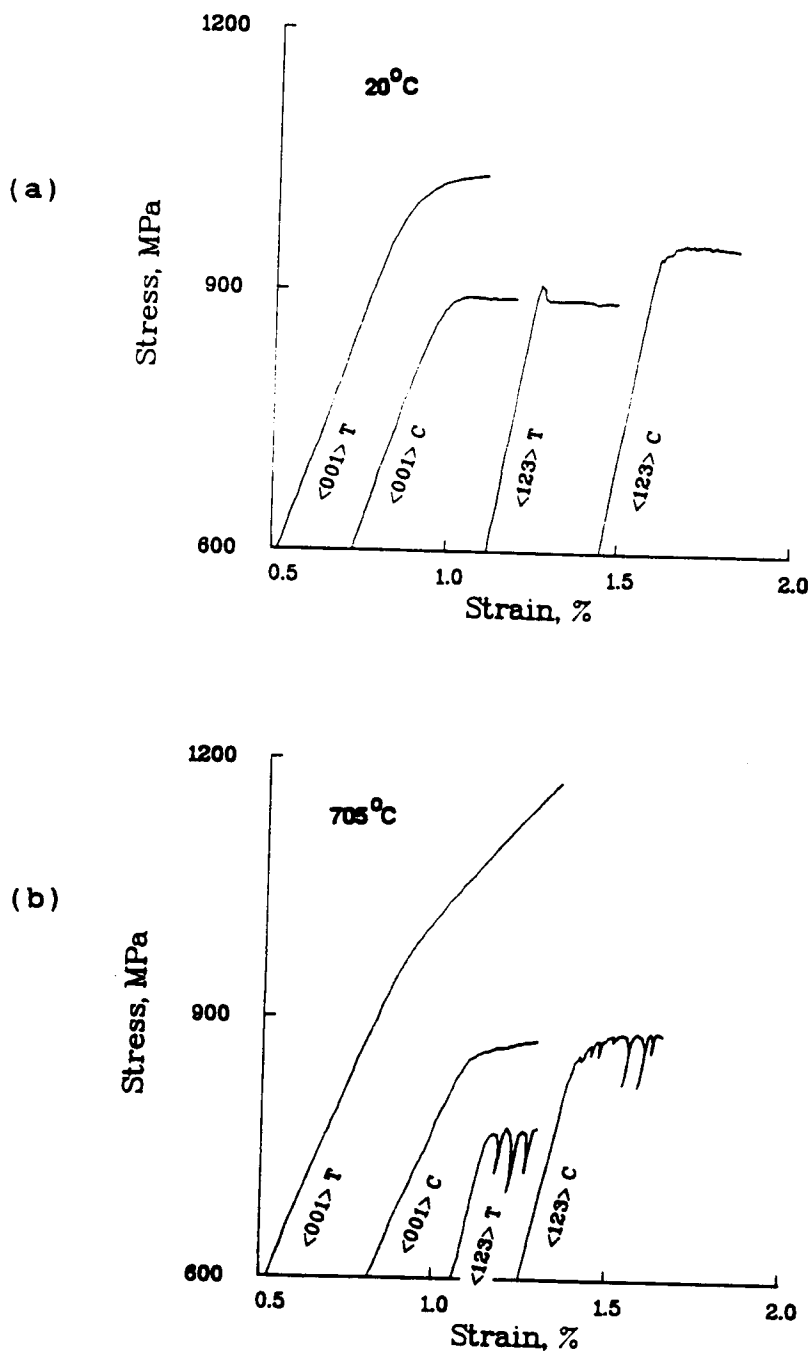


Fig 26. Stress-strain curves in tension and compression for interrupted tensile tests. Compressive curves have been inverted, and the strain zero is offset for clarity. 0.5%/min. (a) 20°C. (b) 705°C.

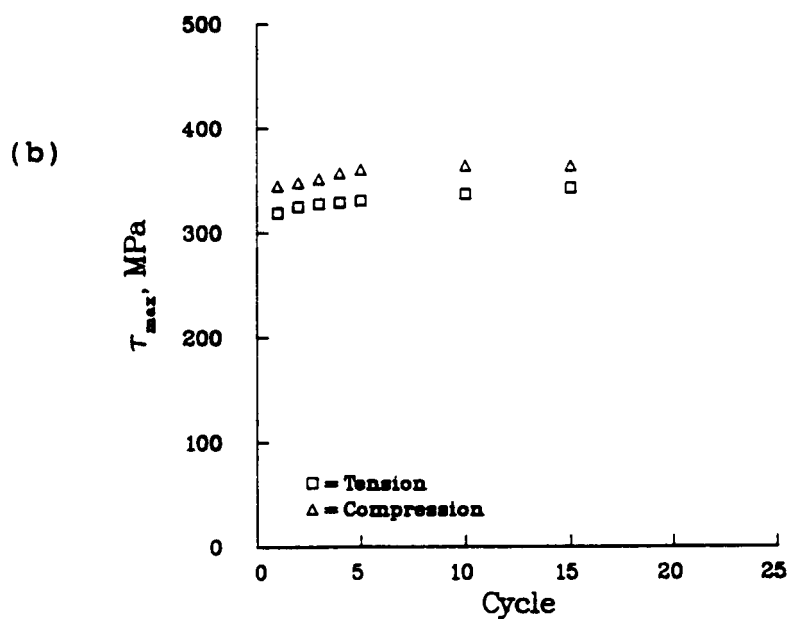
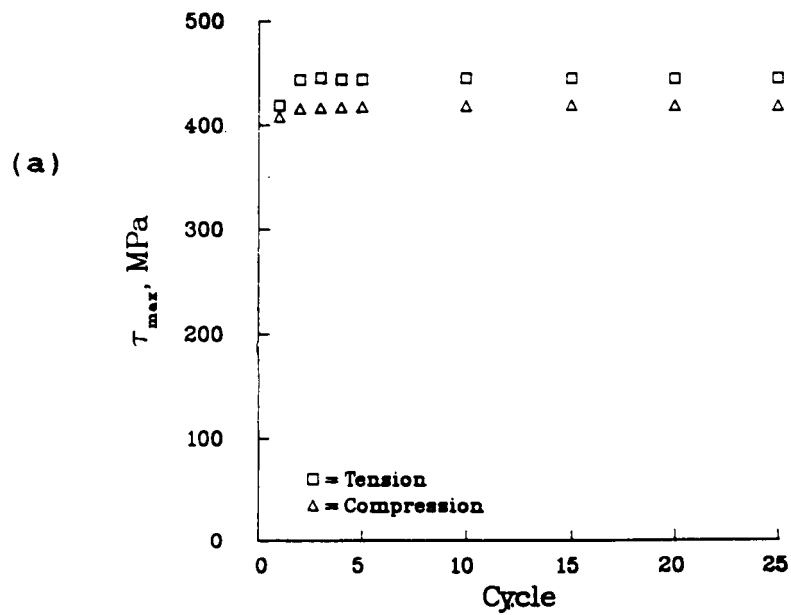


Fig 27. Octahedral τ_{max} vs cycle. 705°C, 50%/min. (a) F40-1, $\langle 001 \rangle$, $\Delta\gamma_p = 0.04\%$. (b) F11, $\langle 123 \rangle$, $\Delta\gamma_p = 0.04\%$.

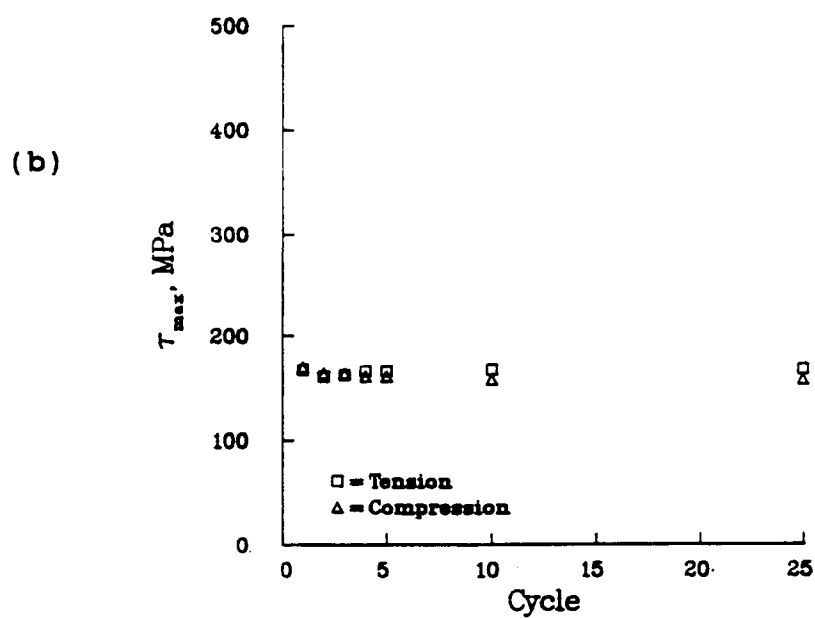
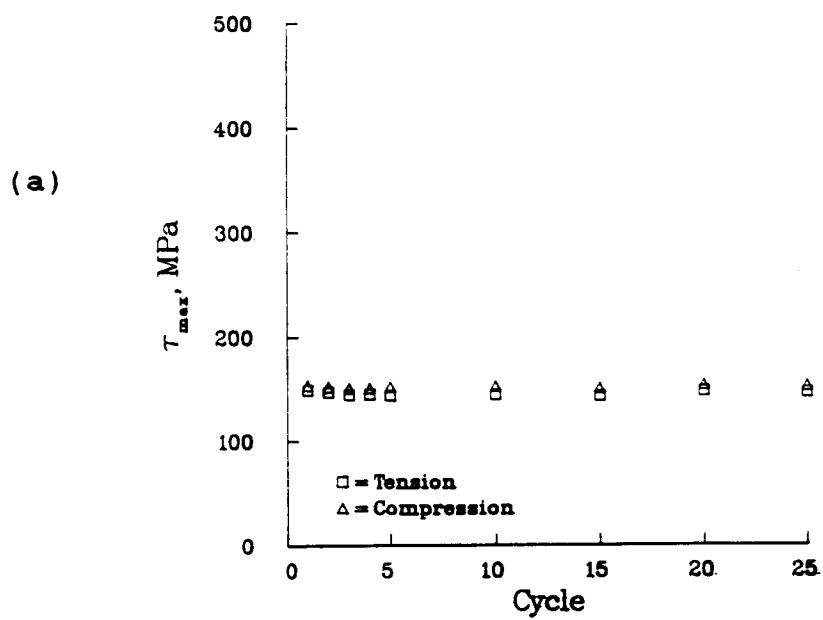


Fig 28. Octahedral τ_{\max} vs cycle. 927°C , $0.5\%/ \text{min}$.
 (a) F104-1, $\langle 001 \rangle$, $\Delta\gamma_p = 0.04\%$. (b) F13, $\langle 123 \rangle$,
 $\Delta\gamma_p = 0.05\%$.

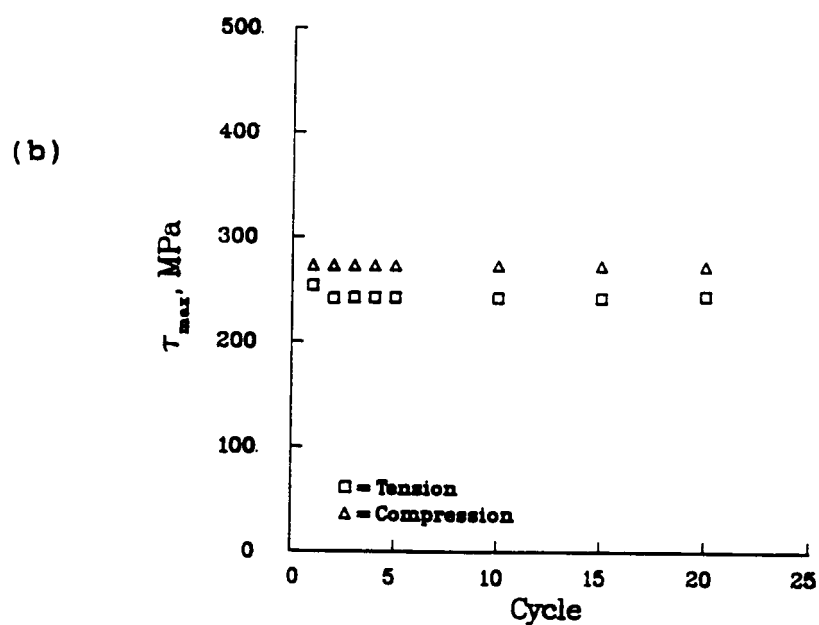
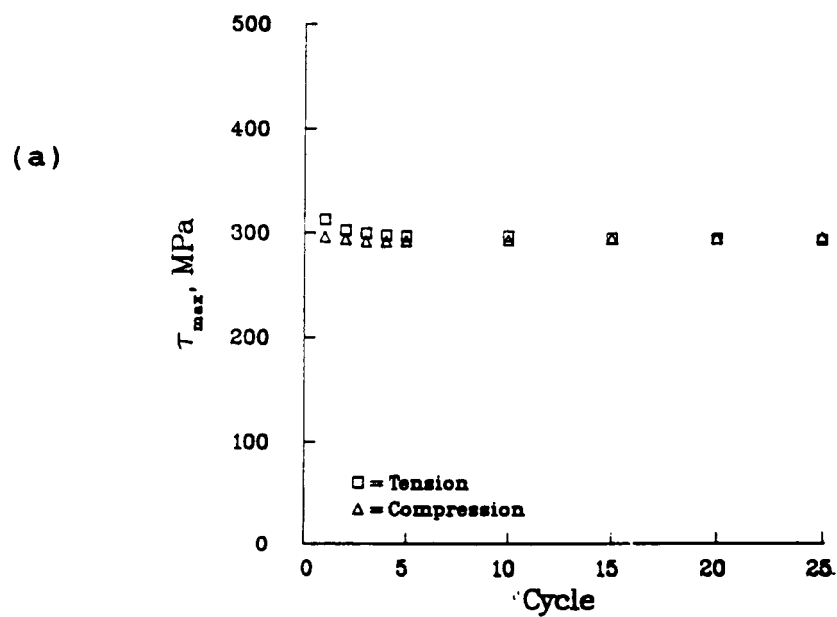


Fig 29. Octahedral τ_{max} vs cycle. 927°C, 50%/min. (a) F12-2, $\langle 001 \rangle$, $\Delta\gamma_p = 0.09\%$. (b) F17, $\langle 123 \rangle$, $\Delta\gamma_p = 0.08\%$.

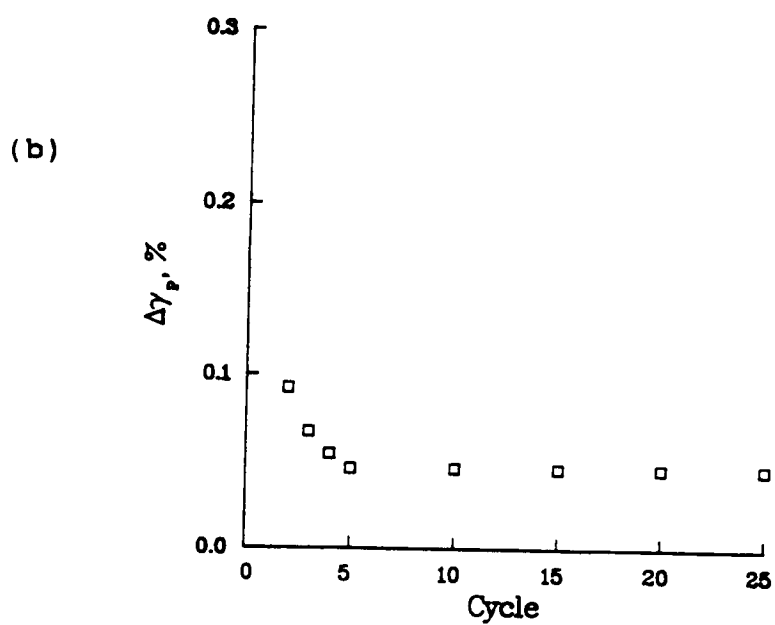
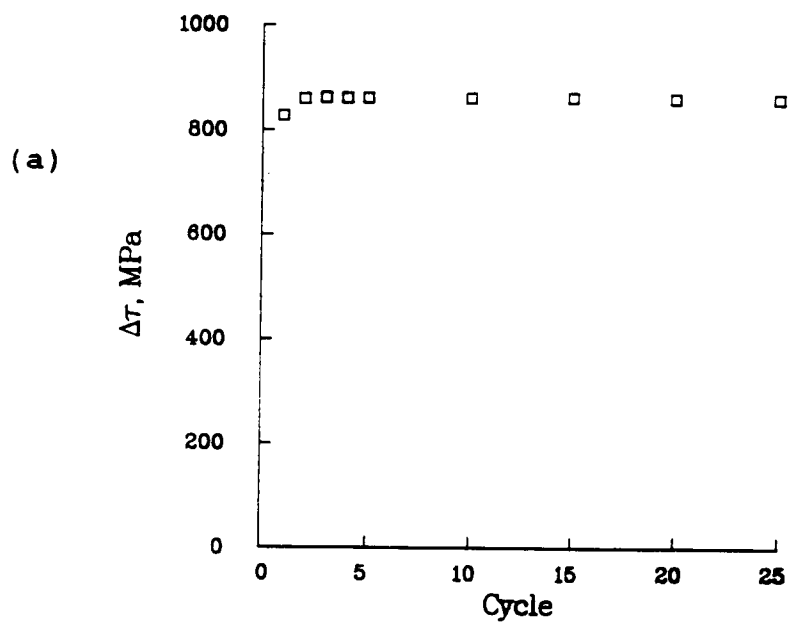


Fig 30. Cyclic strain hardening at low temperature. F40-1, $\langle 001 \rangle$, 705°C, 50%.min, $\Delta\epsilon_t = 2.4\%$

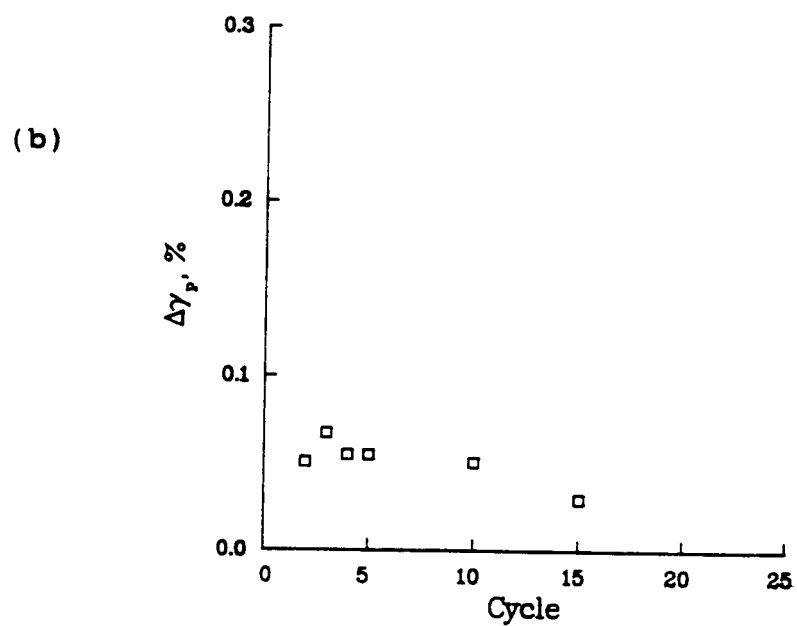
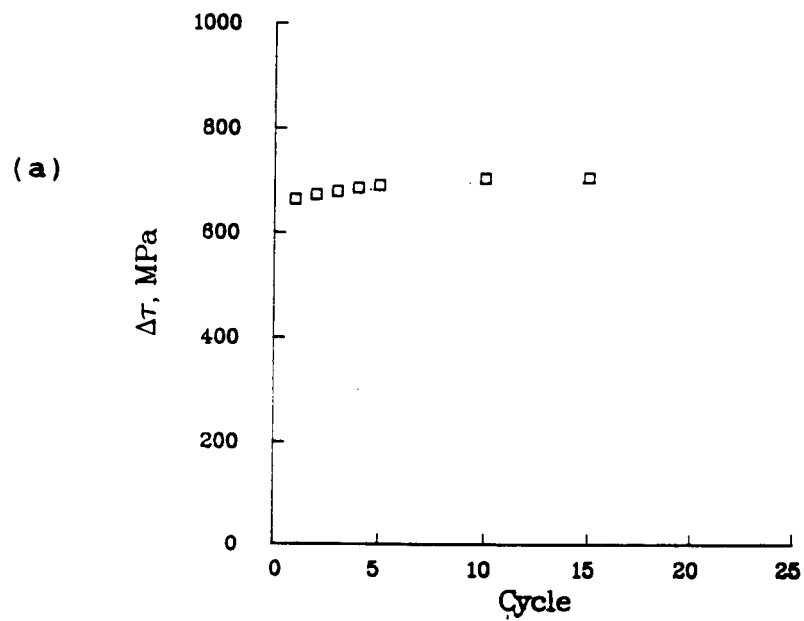


Fig 31. Cyclic strain hardening at low temperature. F11, $\langle 123 \rangle$, 705°C, 50%/min, $\Delta\epsilon_t = 0.9\%$

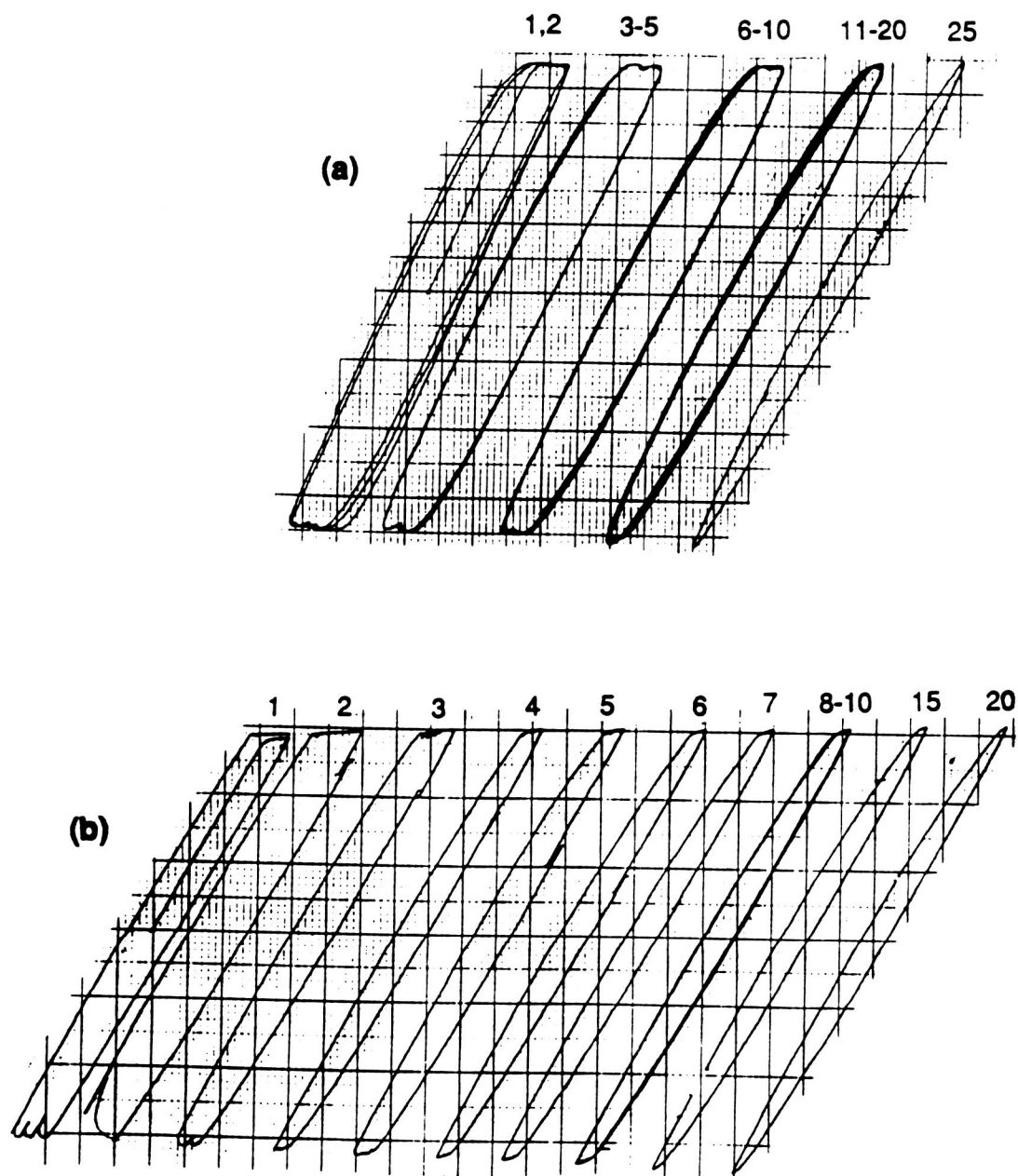
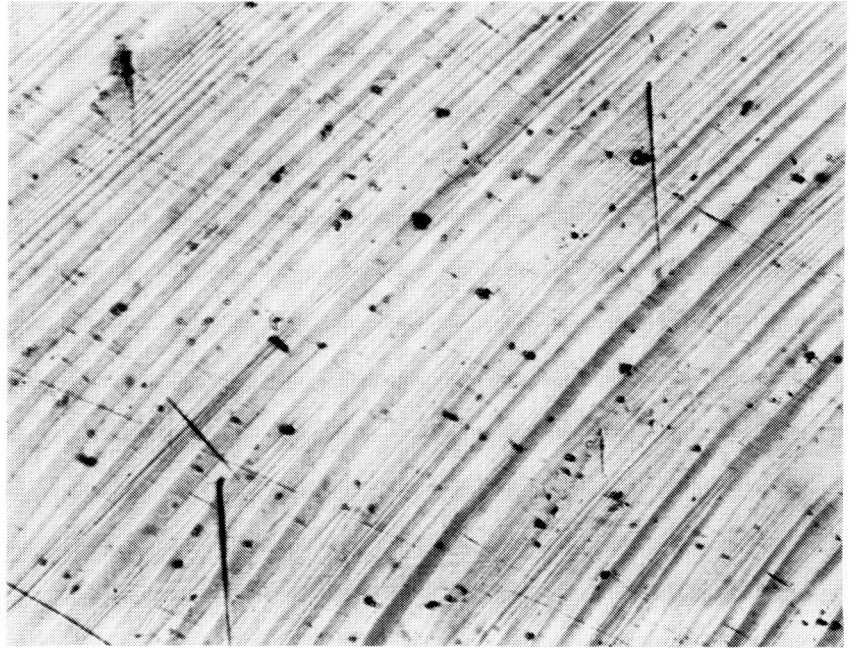


Fig 32. Evolution of LCF hysteresis loops in $\langle 123 \rangle$ crystals.
 (a) F4, 20°C, 50%/min, $\Delta\epsilon_t = 1.05\%$ (b) F8, 705°C,
 0.5%/min, $\Delta\epsilon_t = 1.05\%$

(a)
100 μm



(b)
100 μm

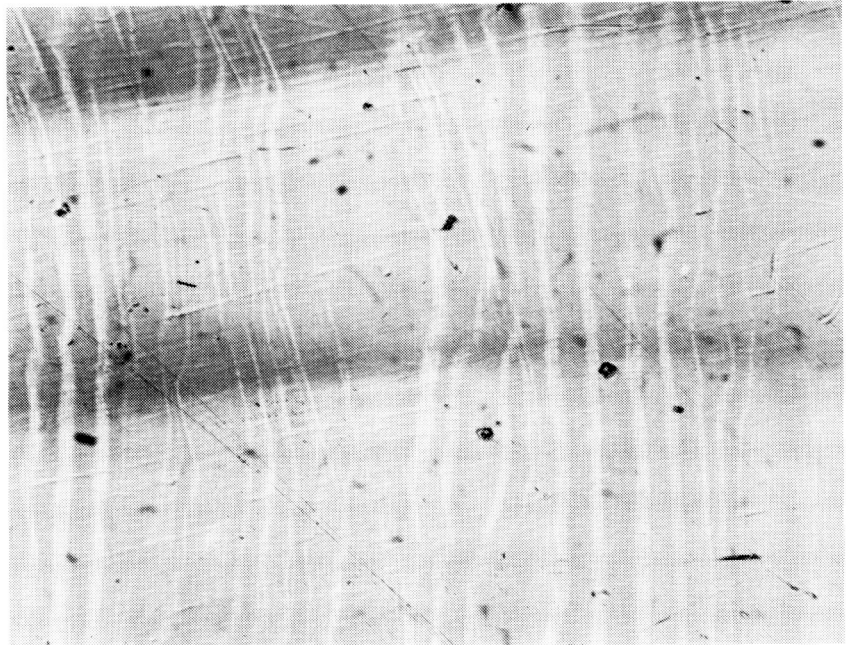


Fig 33. Surface replicas showing slip traces after LCF at 20°C. (a) F4, $\langle 123 \rangle$, 50%/min, $\Delta\gamma_p = 0.08\%$, $N = 300$. (b) F108-3, $\langle 001 \rangle$, 50%/min, $\Delta\gamma_p \approx 0.03\%$, $N = 500$. Tensile axis is horizontal.

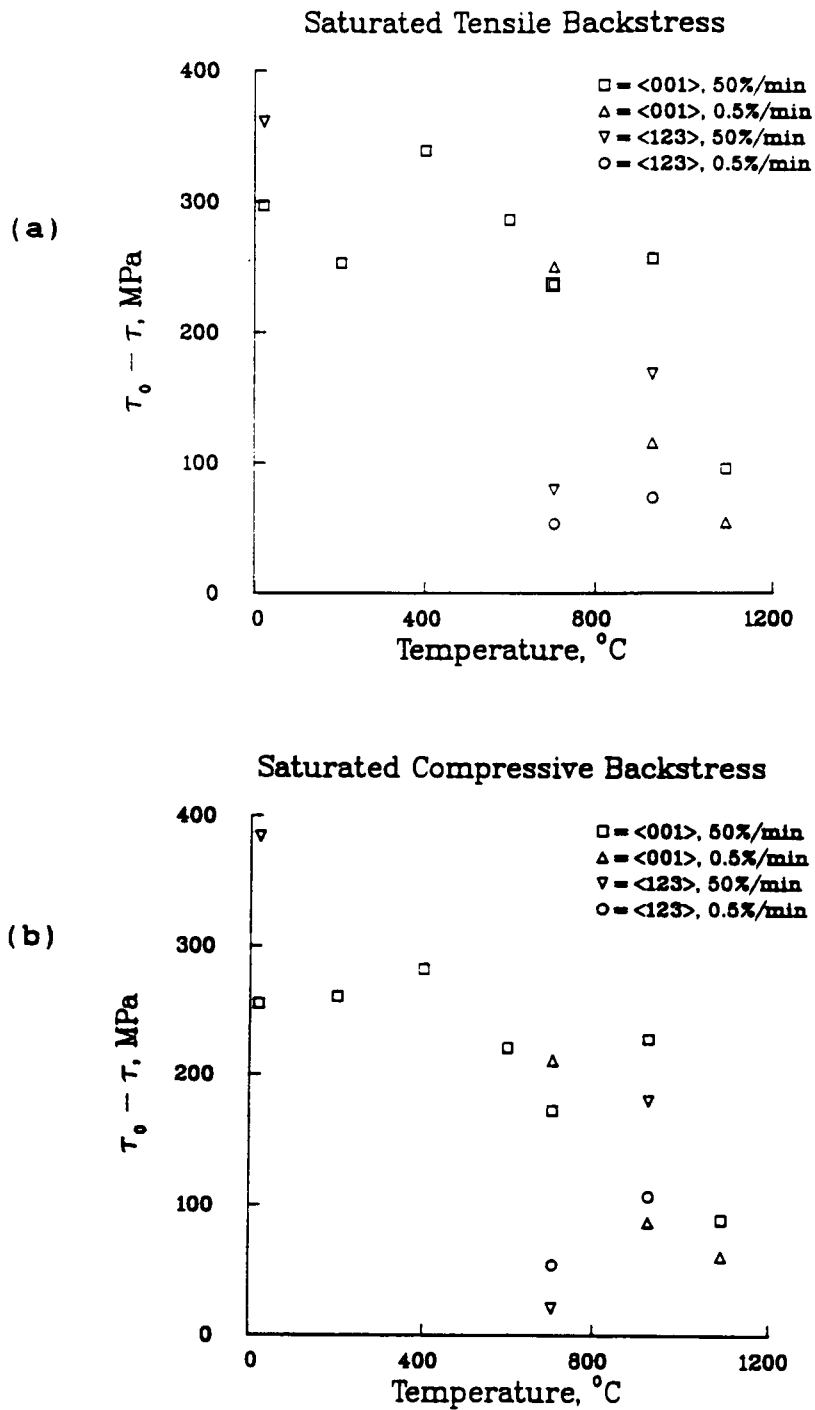


Fig 34. The Bauschinger effect. τ_0 is the CRSS at 0.05% offset for the virgin material. τ is the CRSS at 0.05% offset at steady state during LCF. Data from tests in Appendix D.

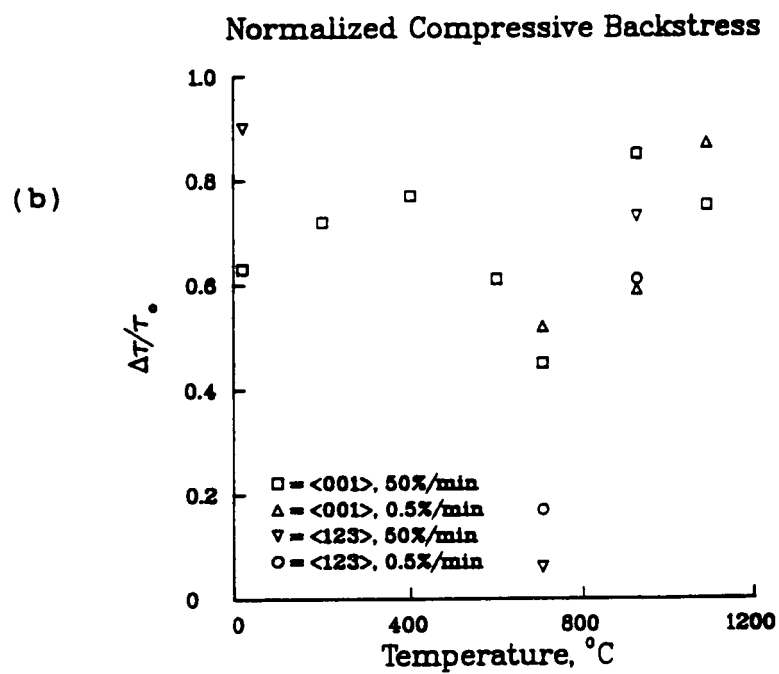
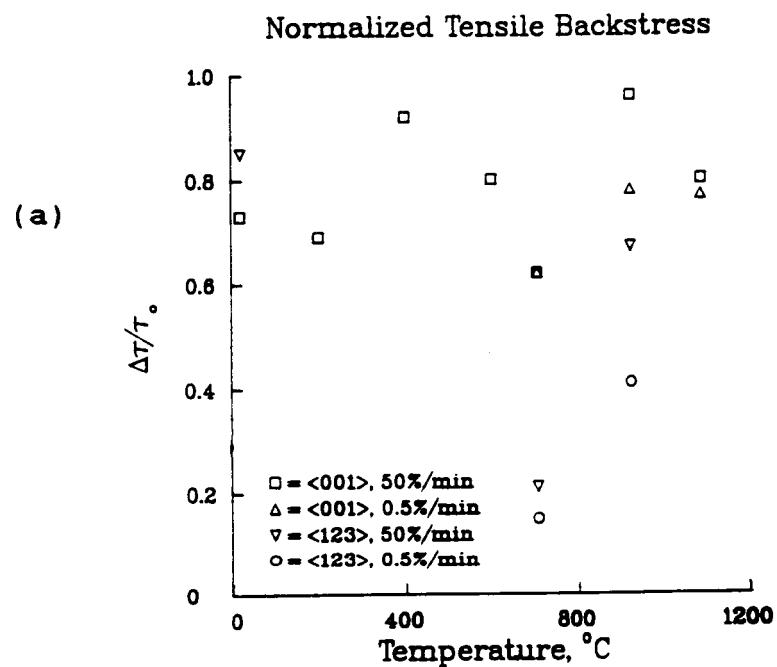


Fig 35. Data from Fig 34 normalized with respect to τ_0 .

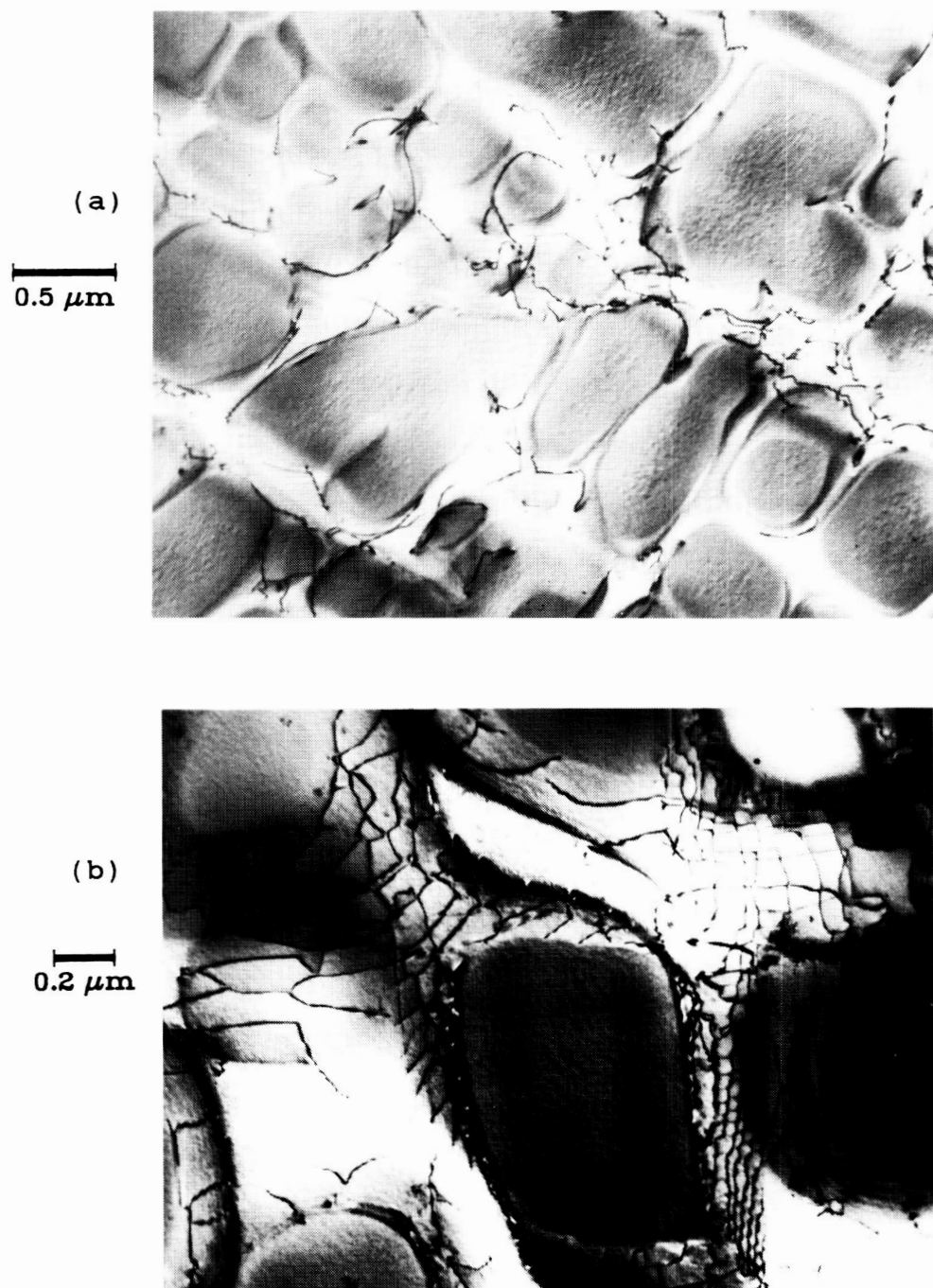


Fig 36. γ' by-pass structures which developed during LCF of $\langle 001 \rangle$ crystals. (a) F24-1, 927°C, 50%/min, $\Delta\gamma_p = 0.05\%$, $N = 2$, $g = \langle 200 \rangle$. (b) F29-2, 1093°C, 0.5%/min, $\Delta\gamma_p = 0.23\%$, $N = 765$, $g = \langle 200 \rangle$.

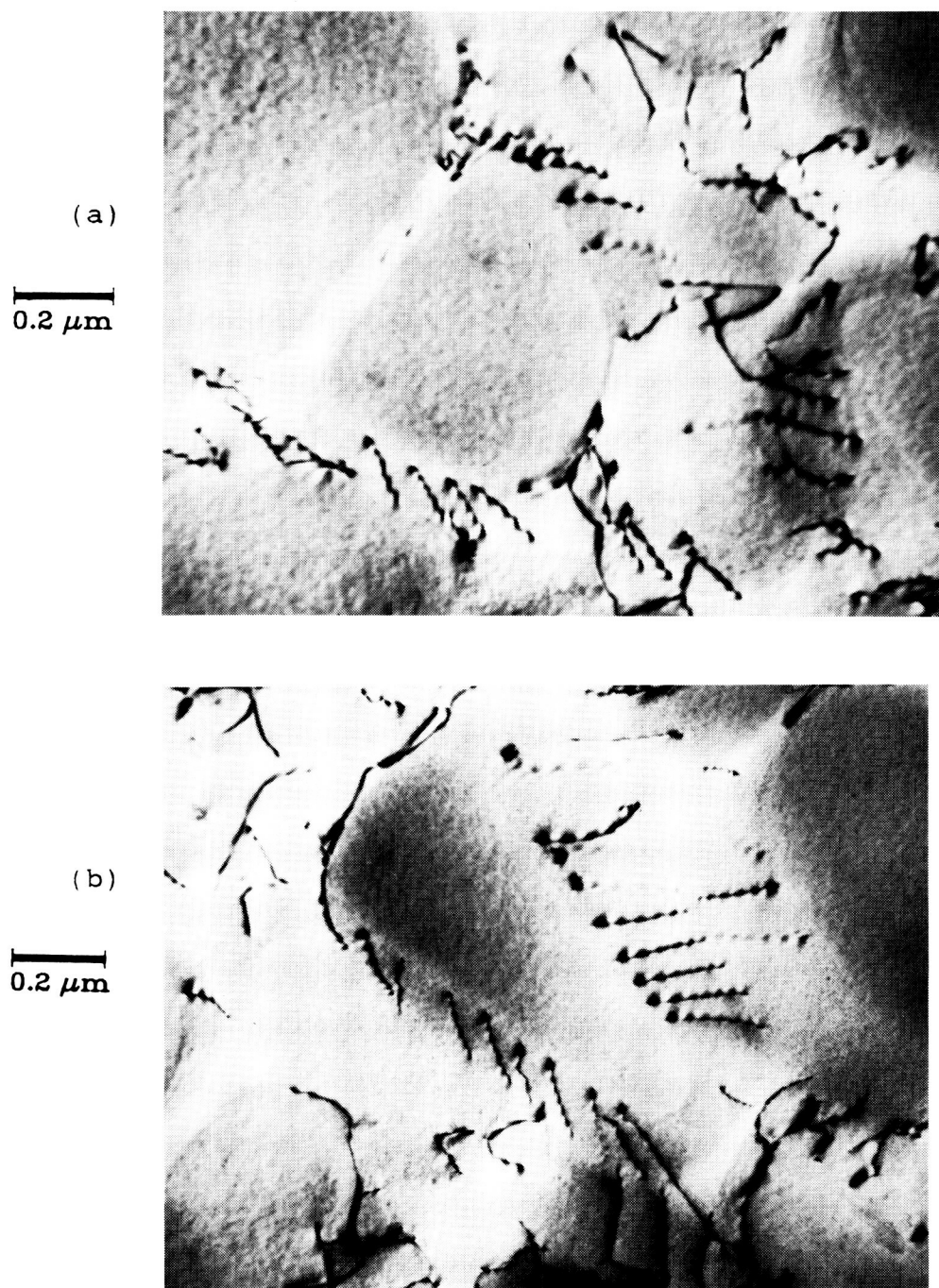


Fig 37. γ' by-pass seen in a $\langle 123 \rangle$ crystal tested at high temperature. T14, 50%/min, $\gamma_p = 0.12\%$, interrupted tensile test, $g = \langle 200 \rangle$. The parallel dislocations, which look like a low temperature slip band, are actually not. They are in the γ/γ' interface.

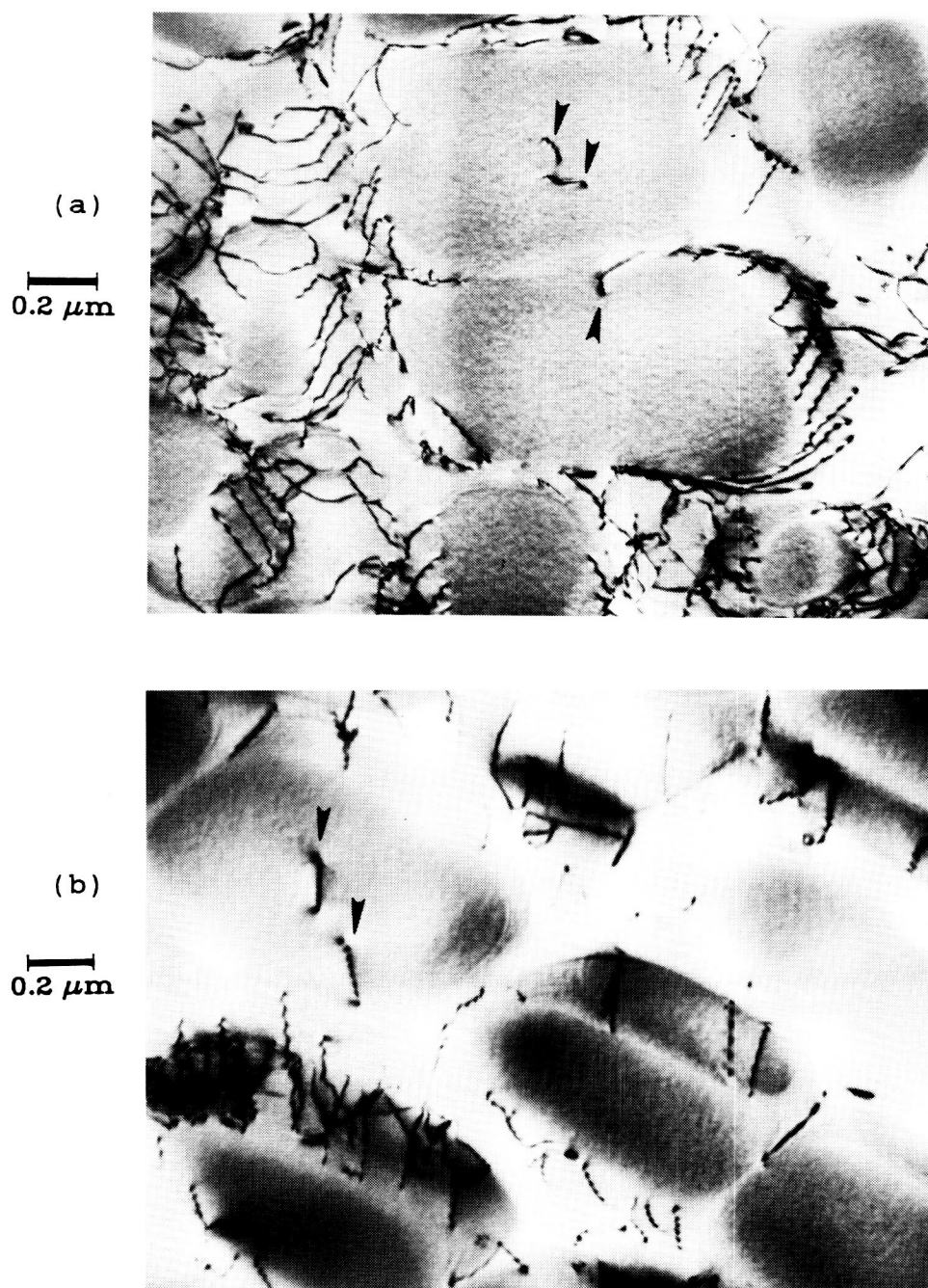


Fig 38. Evidence of γ' shearing in $\langle 123 \rangle$ crystals both LCF tested and tensile tested at 927°C at 50%/min. Dislocations marked by arrows are within the γ' . (a) T14, $\gamma = 0.12\%$, interrupted tensile test, $g = \langle 200 \rangle$. (b) F17, $\Delta\gamma_p = 0.1\%$, $N = 465$, $g = \langle 200 \rangle$.

0.2 μm

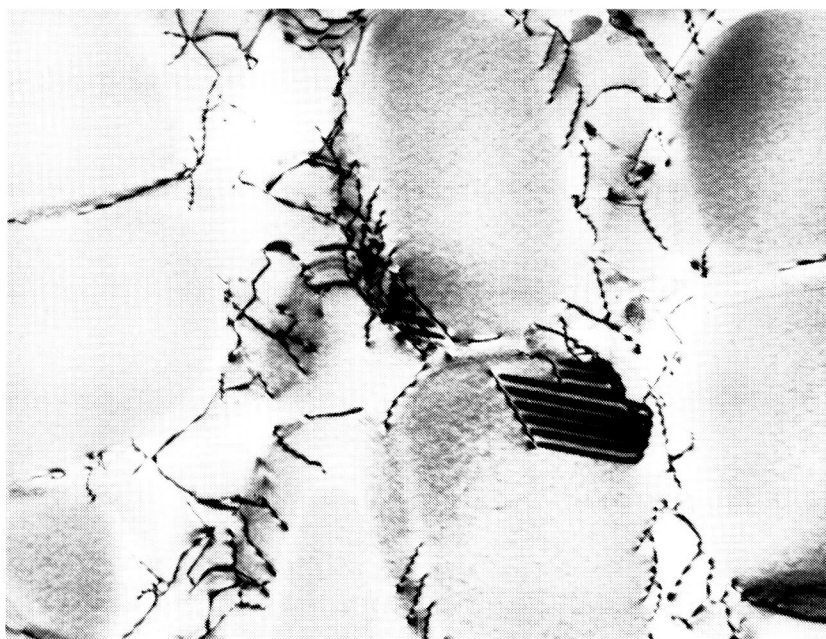


Fig 39. Shearing by $a/3\langle 112 \rangle$ dislocations, leaving S-ISF's behind. T14, $\langle 123 \rangle$, 927°C , 50%/min, interrupted tensile test, $\gamma_p = 0.12\%$, $g = \langle 200 \rangle$.

0.2 μm

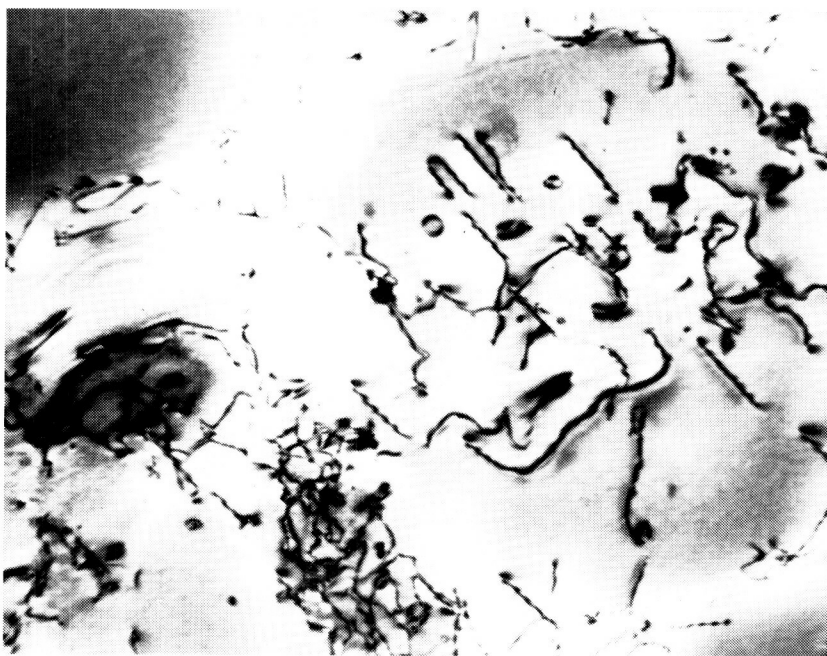


Fig 40. Typical substructure after deformation of $\langle 123 \rangle$ crystals at 705°C . F11, 50%/min, $\Delta\gamma_p = 0.03\%$, $N = 900$, $g = \langle 200 \rangle$.

ORIGINAL PAGE IS
OF POOR QUALITY

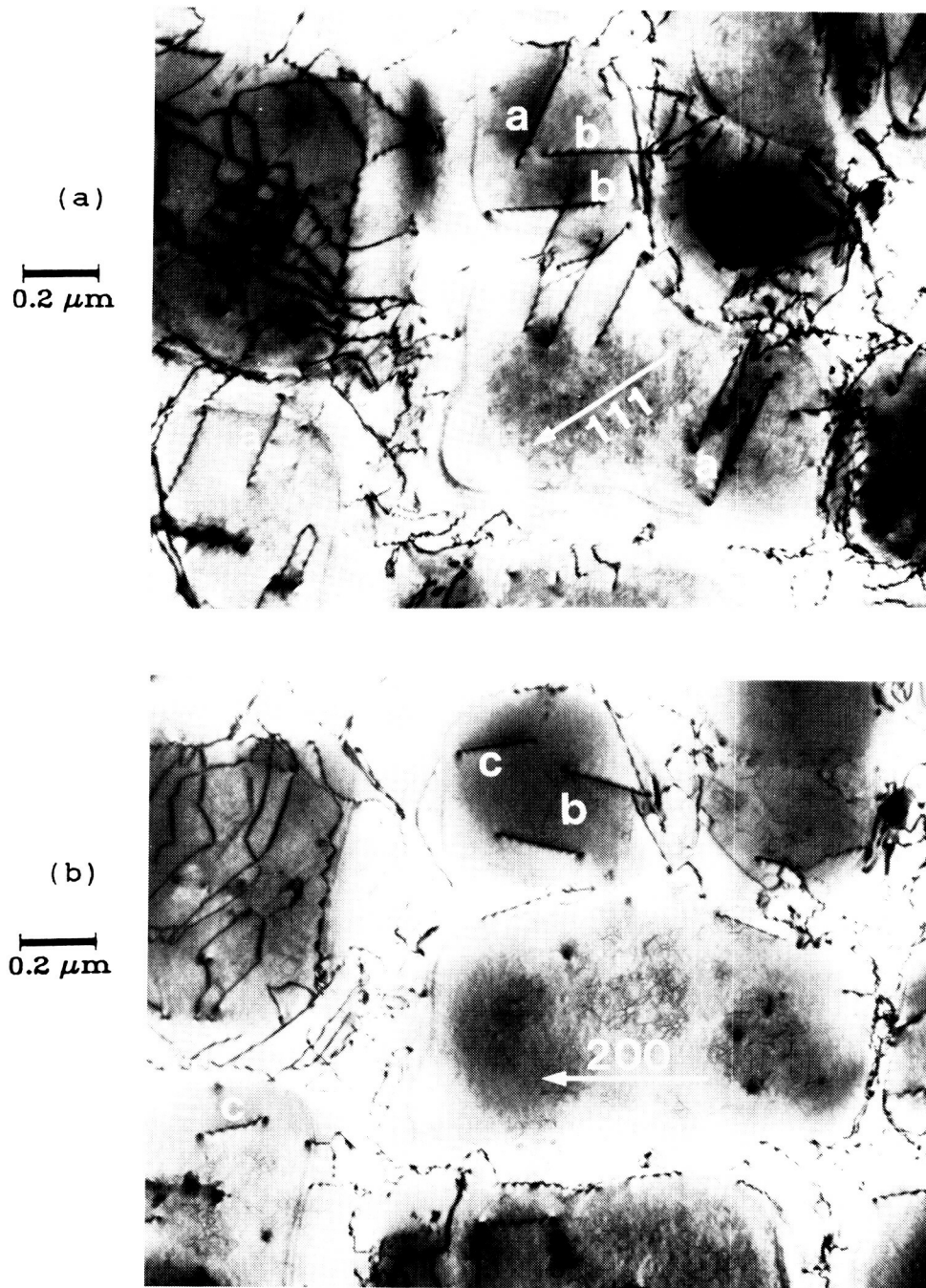


Fig 41. Screw dislocations trapped in the γ' after LCF at 705°C . $b_a = [011]$, $b_b = [101]$, $b_c = [\bar{1}01]$. F100-3, $\langle 001 \rangle$, 50%/min, $\Delta\gamma_p = 0.06\%$, $N = 180$. (a) $g = [111]$. (b) Same area, $g = [200]$.

(a)

0.1 μm



(b)

0.2 μm

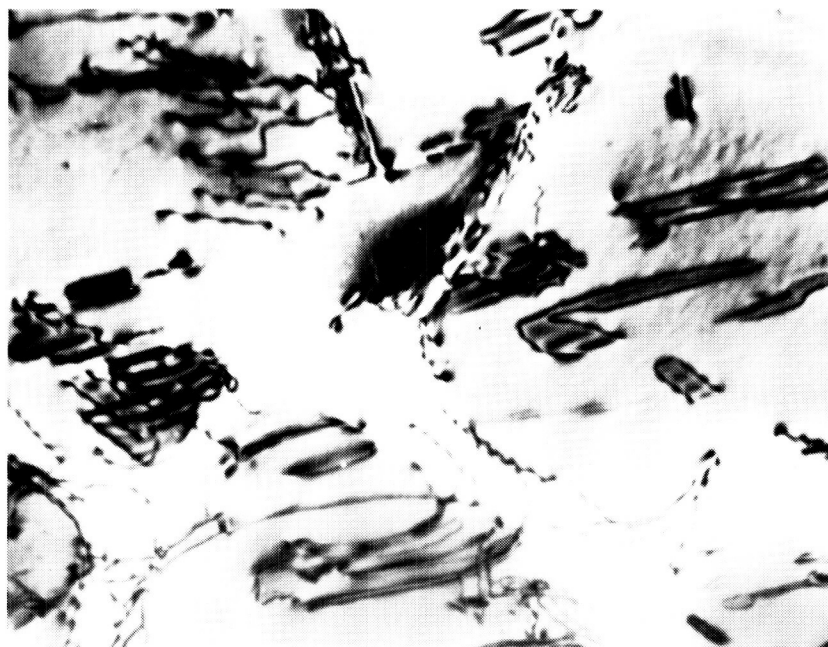


Fig 42. Typical substructures after deformation at 20°C.
 (a) T1, $\langle 123 \rangle$, 0.5%/min, interrupted tensile test, $\gamma_p = 0.11\%$, $g = \langle 200 \rangle$. (b) F70-1, $\langle 001 \rangle$, 50%/min, $\Delta\gamma_p = 0.12\%$, $N = 6$, $g = \langle 200 \rangle$. Both figures show evidence of partial dislocation shearing and loops.

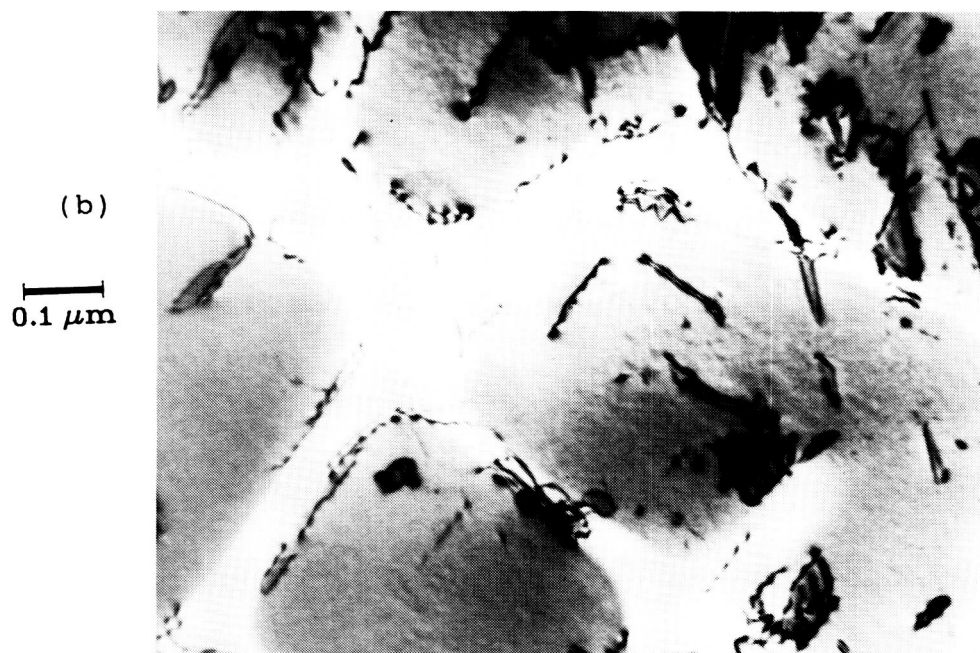
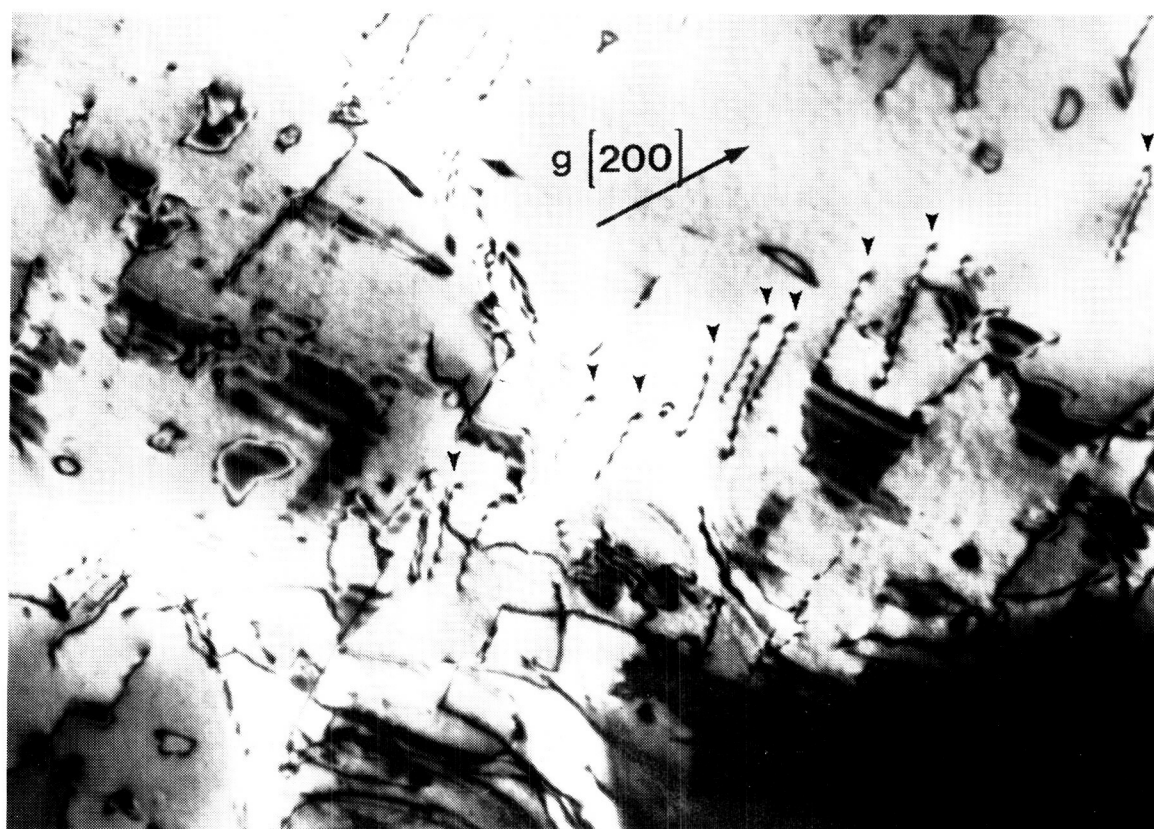
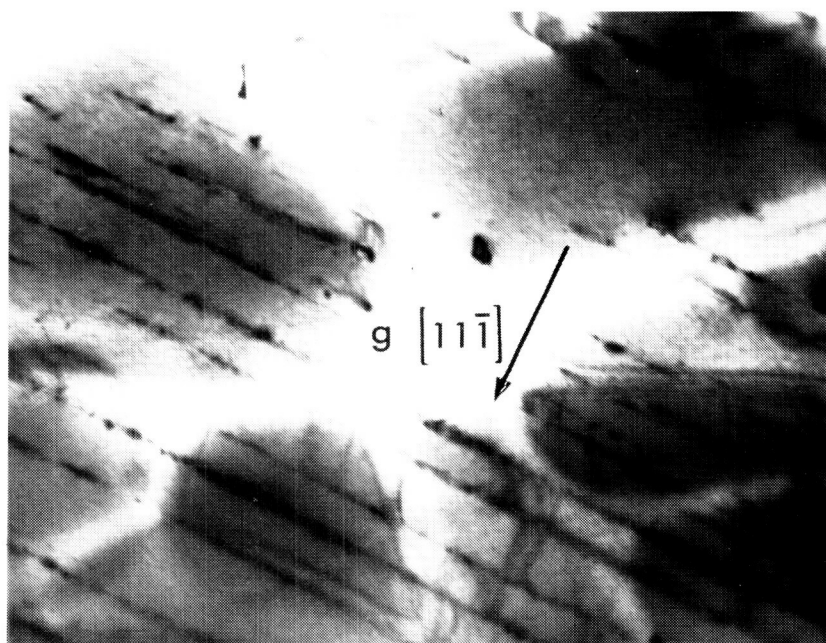


Fig 43. Micrographs of the area in Fig. 42(b). (a) Low magnification photo showing high fault density. (b) Photo showing unit dislocation pairs (as well as partial dislocations) in the interface and γ' .



0.1 μm

(a)



(b)

0.2 μm

Fig 44. Substructure developed during LCF at 20°C. F70-1, $\langle 001 \rangle$, 50%/min, $\Delta\gamma_p = 0.11\%$, $N = 6$. (a) $g = [200]$. Arrows indicate matrix unit dislocations in the same slip bands that contain S-ISF-s in the γ' . (b) $g = [111]$. Slip bands are edge-on.

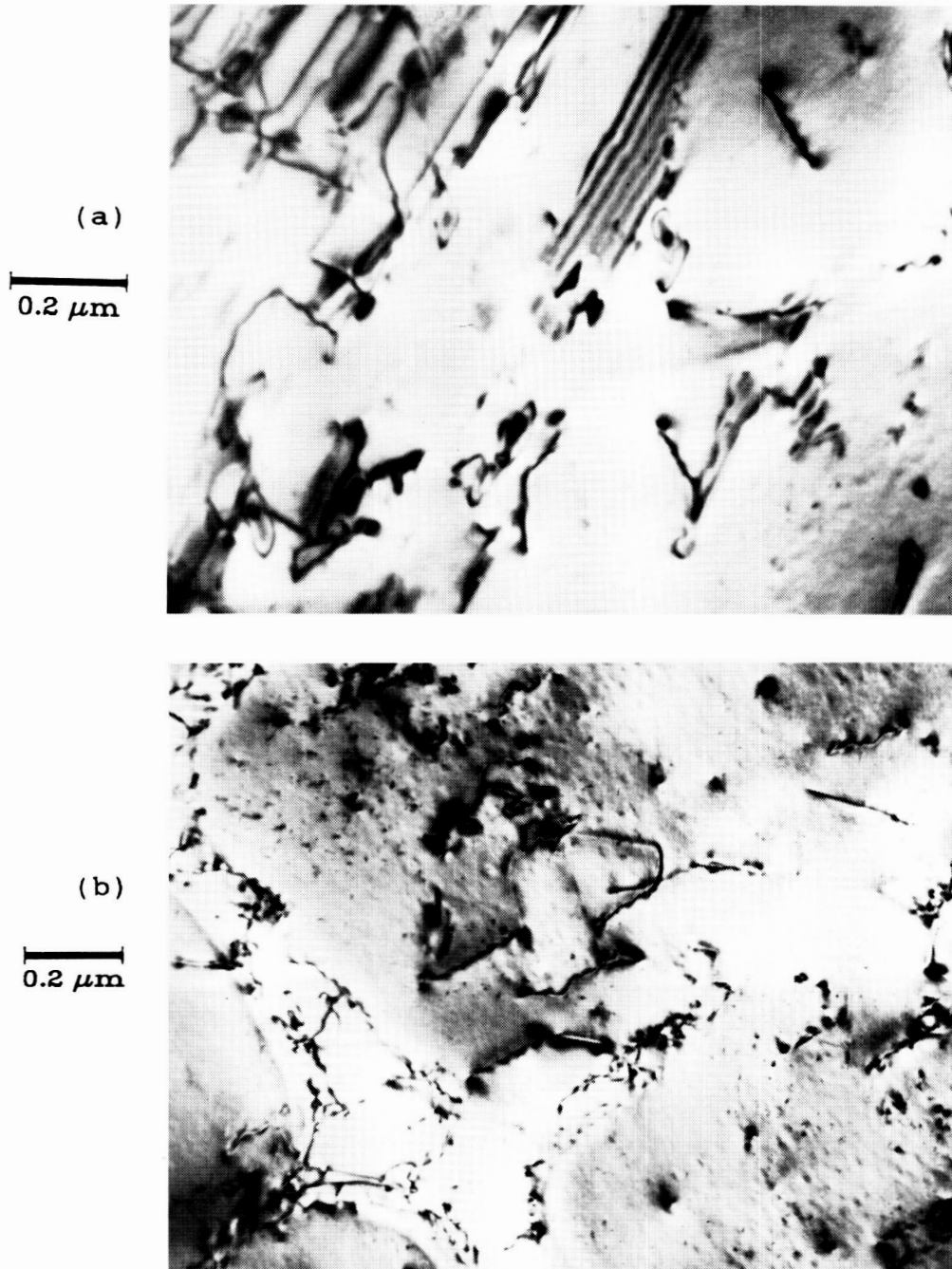


Fig 45. Substructures developed during LCF of $\langle 001 \rangle$ crystals at 50%/min from 200-600°C. (a) F1-3, 200°C, $\Delta\gamma_p = 0.06\%$, $N = 20$, $g = \langle 200 \rangle$. (b) F40-2, 400°C, $\Delta\gamma_p = 0.05\%$, $N = 52$, $g = \langle 200 \rangle$. (c) F40-3, 600°C, $\Delta\gamma_p = 0.04\%$, $N = 150$, $\langle 001 \rangle$ zone axis multi-beam.

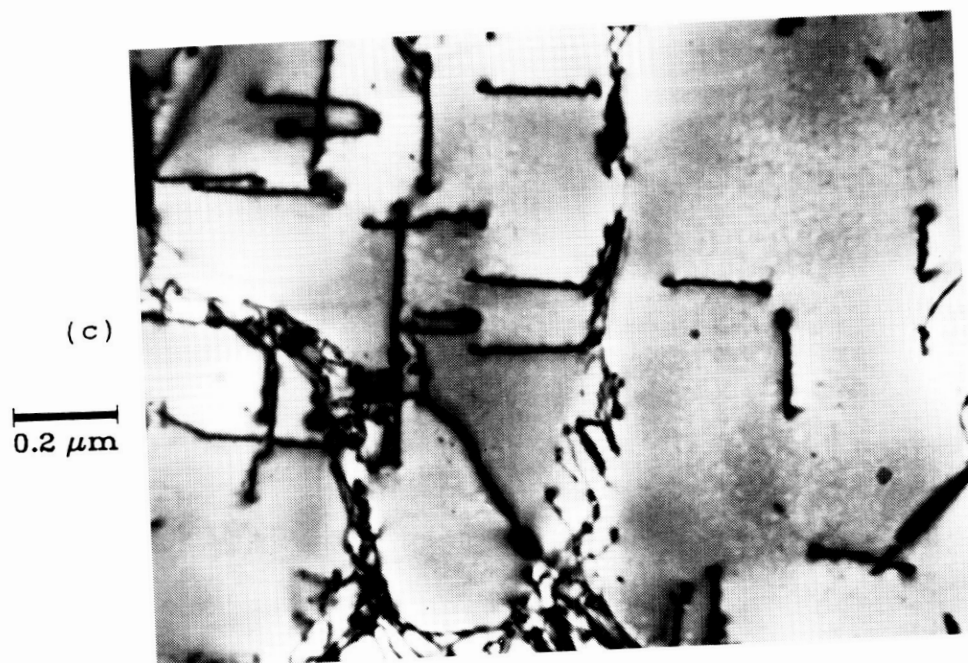


Fig. 45 (Continued)

ORIGINAL PAGE IS
OF POOR QUALITY

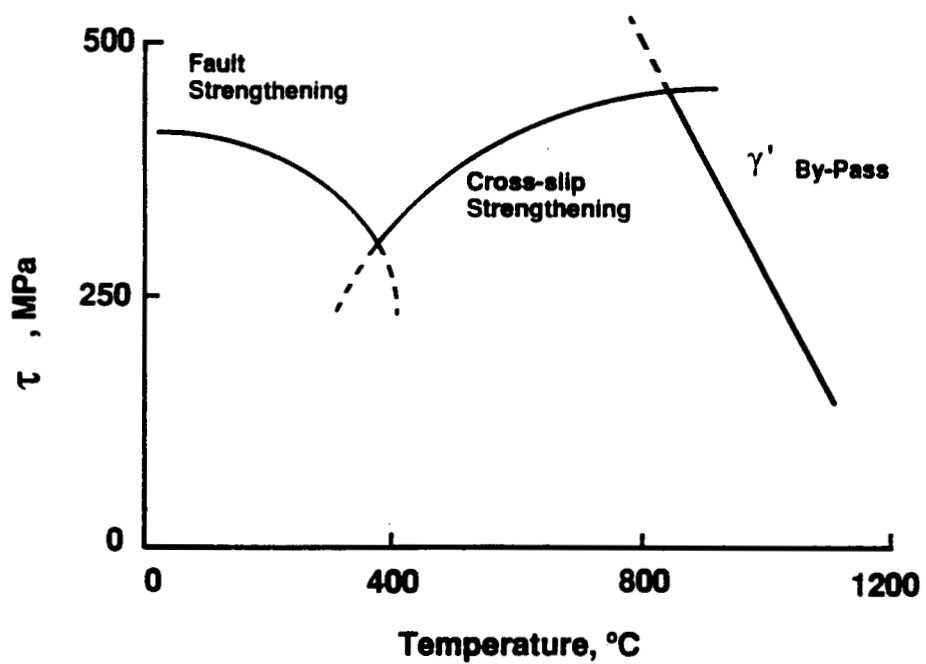


Fig 46. Model of the dominant strengthening mechanism vs temperature.

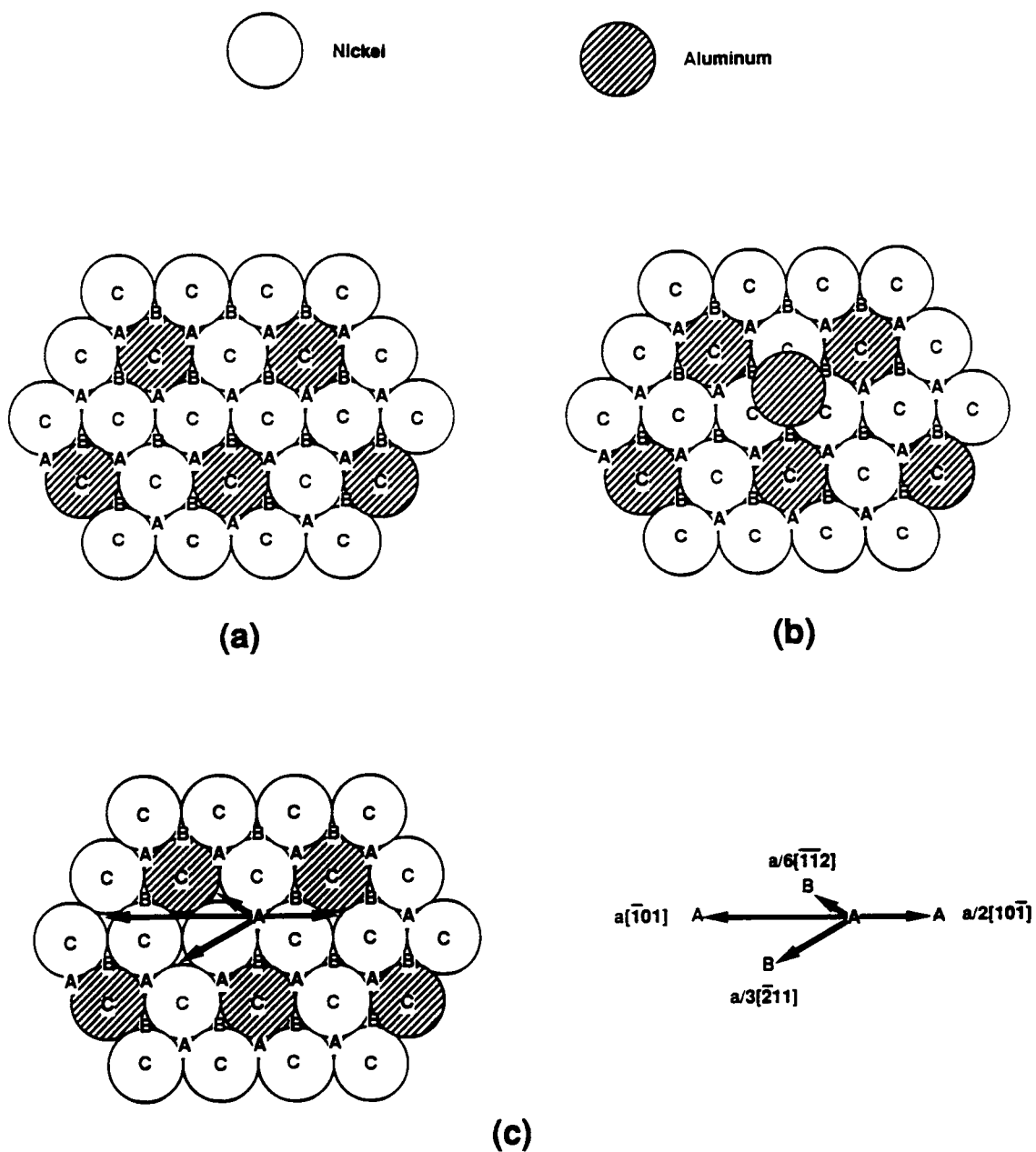


Fig 47. Slip vectors in the $L1_2$ lattice. (a) Top view of the $\{111\}$ plane. The "B" plane is below, the "A" plane is above. (b) Al positions in the "A" plane. (c) Four fundamental slip vectors from the reference of the "A" Al site. See text for details.

ORIGINAL PAGE IS
OF POOR QUALITY

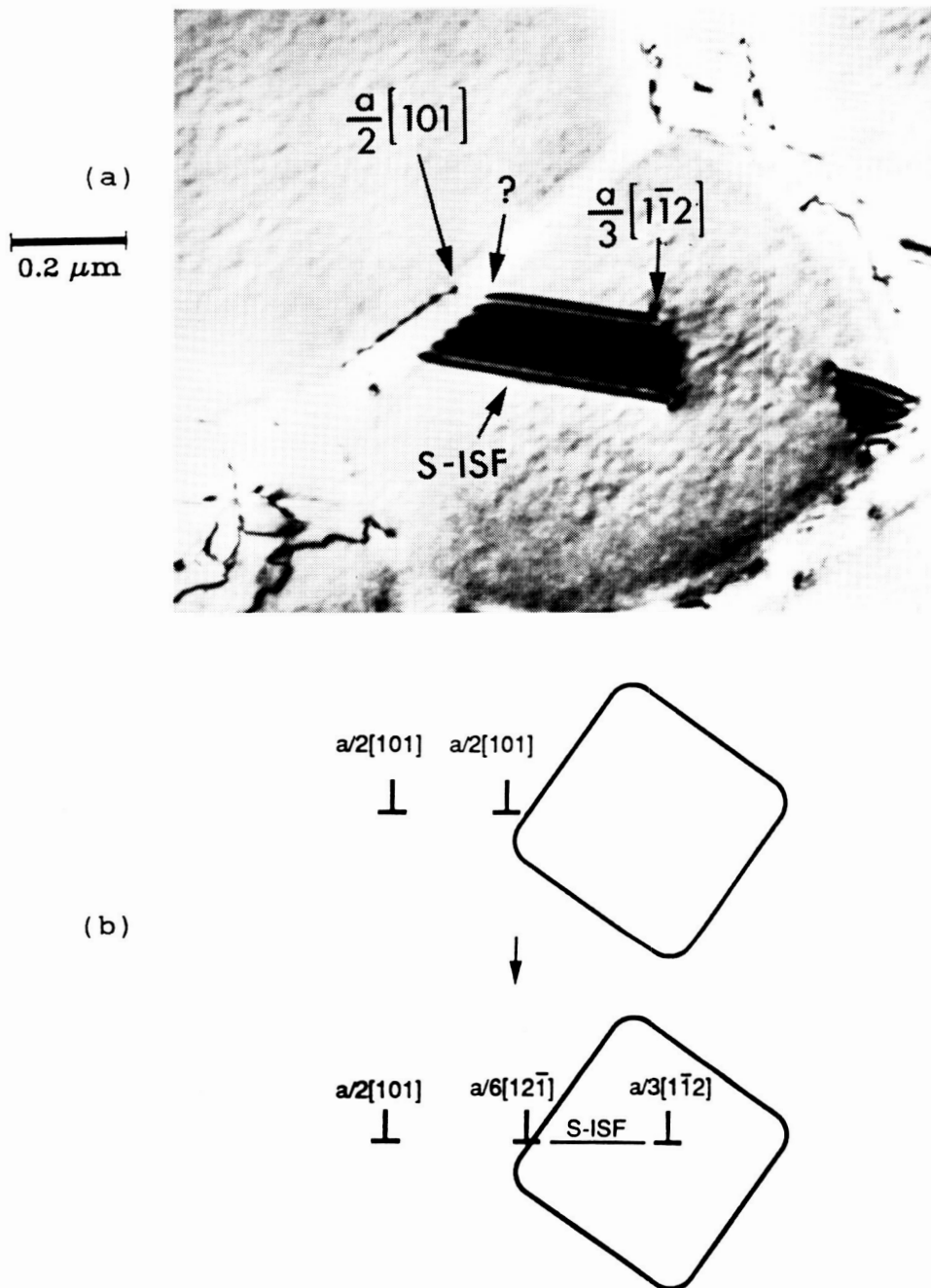


Fig 48. High temperature faults, T44-2, $\langle 001 \rangle$, 760°C , $0.5\%/min$, interrupted tensile test, $\gamma_p = 0.11\%$, $g = [200]$. (a) Only the interfacial dislocation was not identified. (b) Dislocation reaction which is compatible with the structure in (a).

(a)
0.1 μm



(b)
0.2 μm

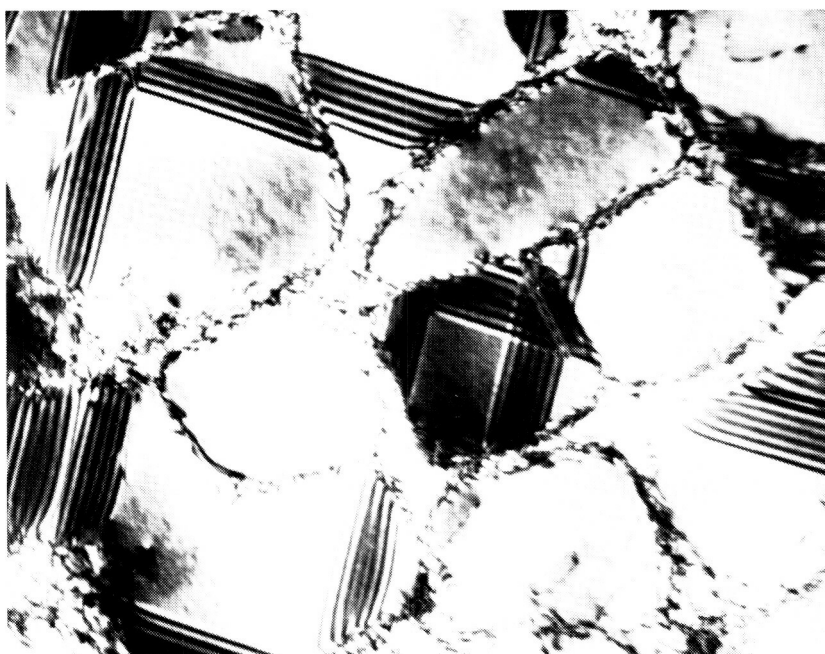


Fig 49. High temperature faults. (a) F14, $\langle 123 \rangle$, 927°C , 50%/min, $\Delta\gamma_p = 0.12\%$, $N = 12$, $g = \langle 200 \rangle$. The faults appear to have been formed by the decomposition of the single $a/2\langle 110 \rangle$ interfacial dislocations. (b) JA34, $\langle 001 \rangle$, 760°C , failed tensile test, $\gamma_p = 5.3\%$, $g = \langle 200 \rangle$, $w = 0$.

ORIGINAL PAGE IS
OF POOR QUALITY

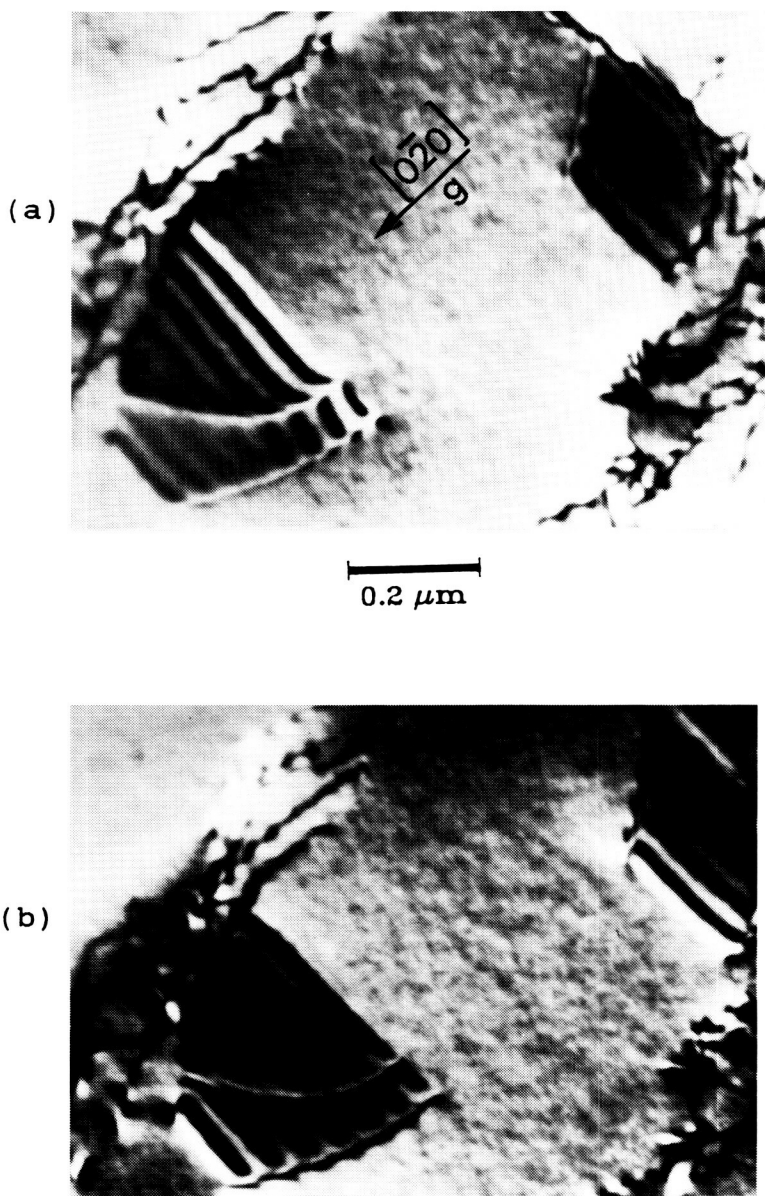


Fig 50. [020] darkfield photos of overlapping faults in foil described in Fig 49(a). Both photos are under the same diffraction condition, with a slight difference in tilt to clarify the contrast in this slightly bent foil.

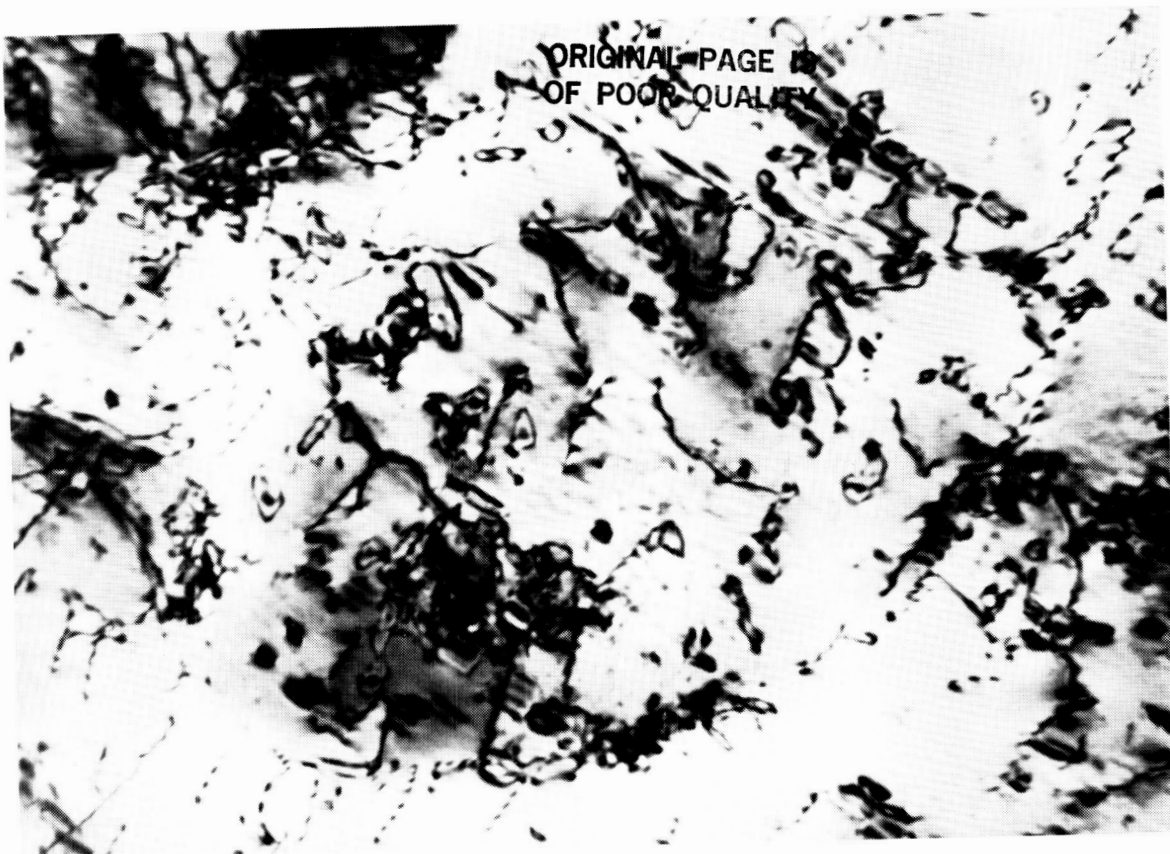


Fig 51. High fault density after deformation at 20°C. F4,
 $\langle 123 \rangle$, 50%/min, $\Delta\gamma_p = 0.06\%$, $N = 300$, $g = \langle 200 \rangle$.

ORIGINAL PAGE IS
OF POOR QUALITY

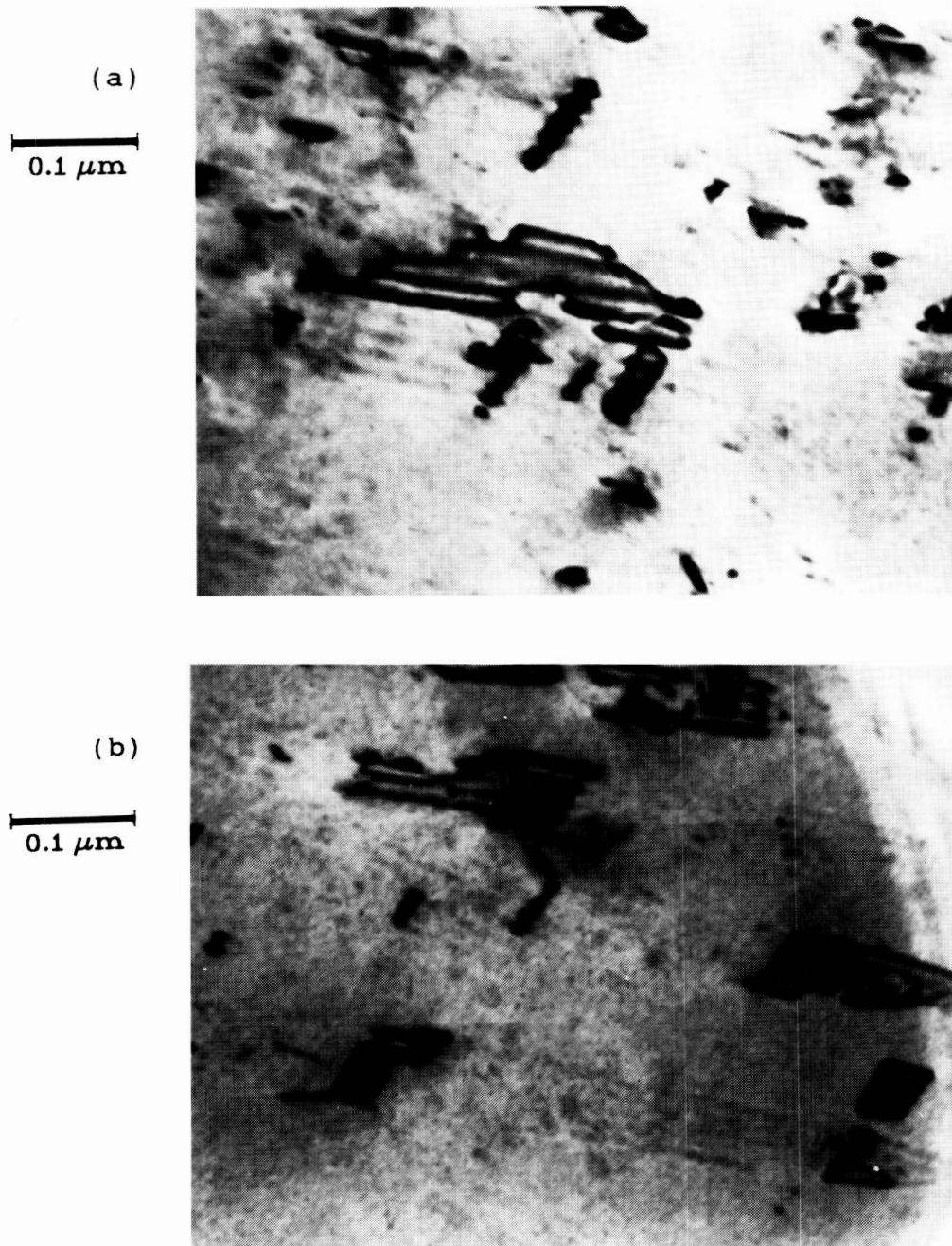


Fig 52. Residual fringe contrast due to overlapping faults.
F4, described in Fig 51. $g = \langle 111 \rangle$.

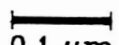

0.1 μm



Fig 53. Partial dislocation pairs bounding superlattice stacking faults. F4, described in Fig 51.

ORIGINAL PAGE IS
OF POOR QUALITY

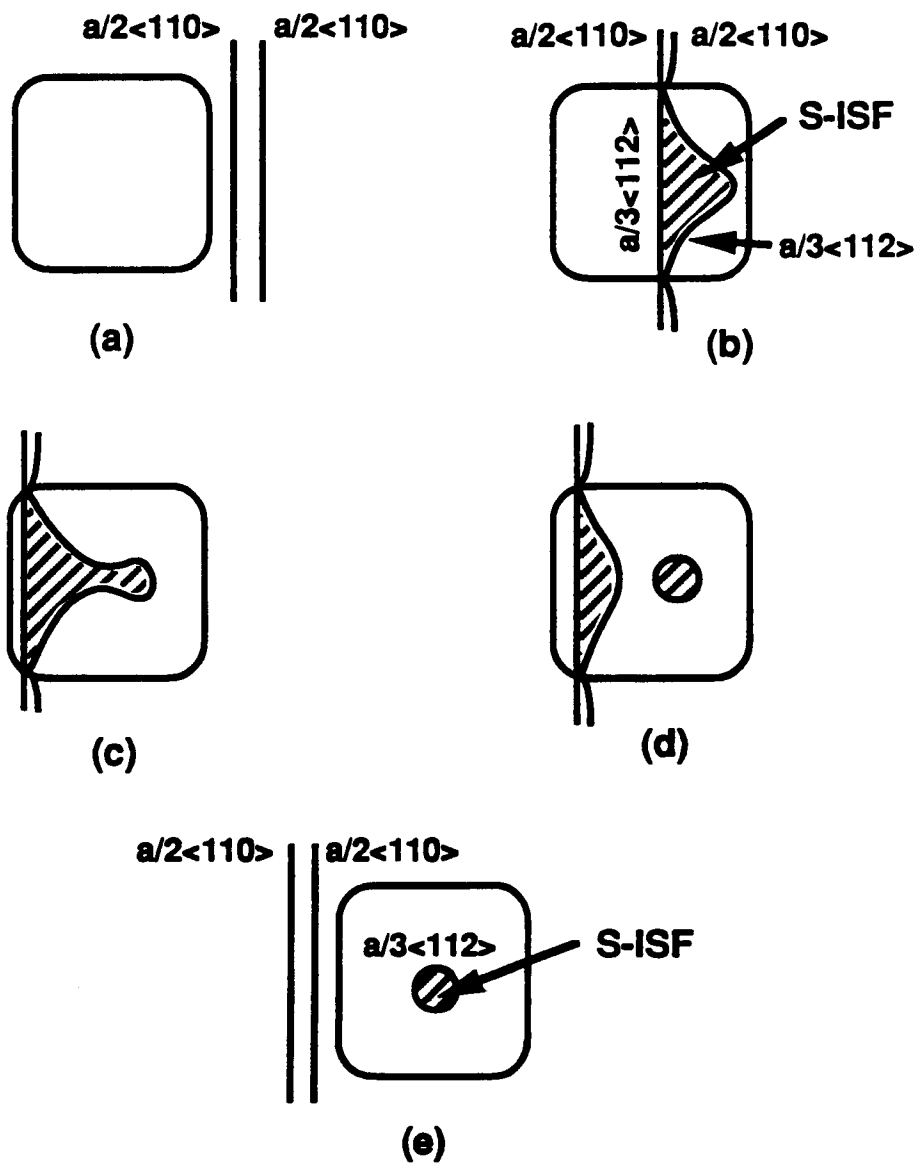


Fig 54. A possible mechanism for the formation of S-ISF loops within the γ' . (Similar to Orowan looping).

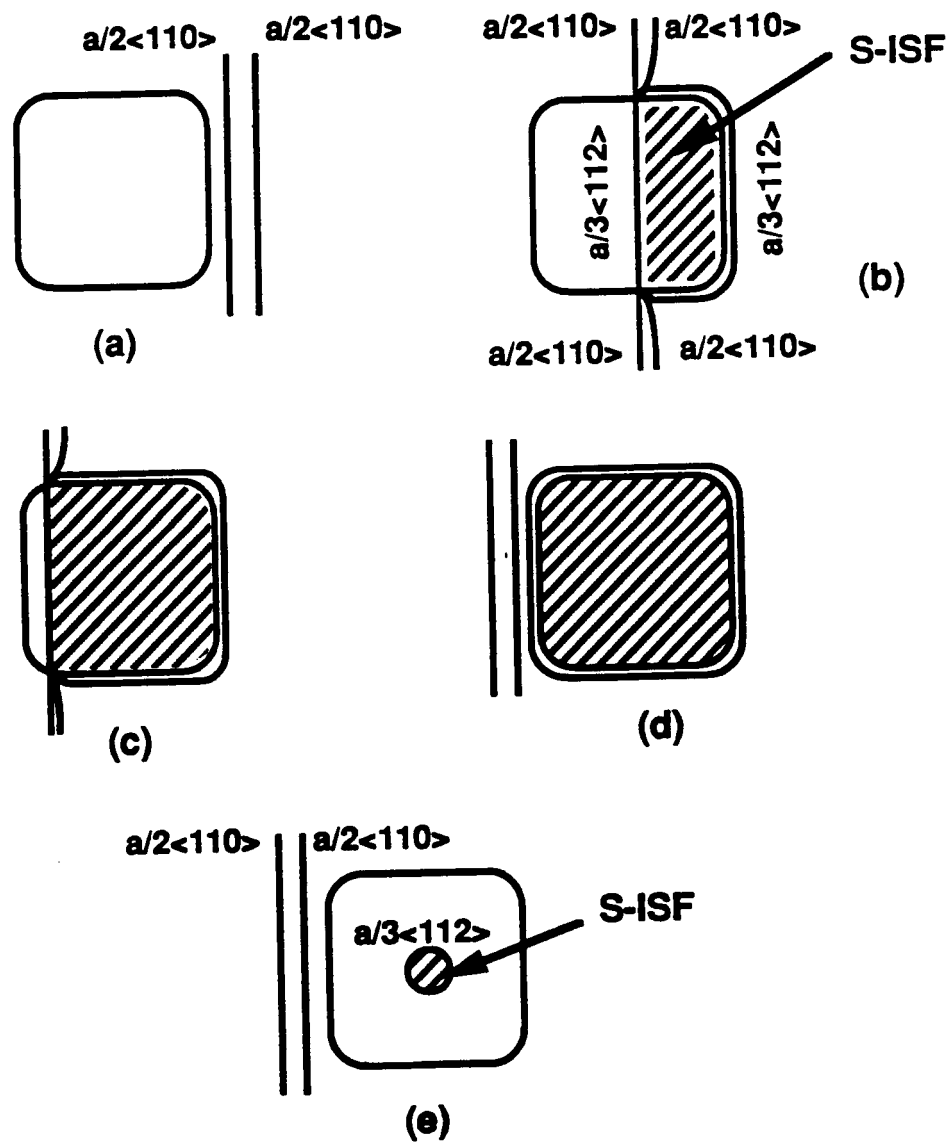


Fig 55. Another possible mechanism for S-ISF loop formation. In this case, the event does not occur within the γ' ; the loop collapses after enclosing the precipitate.

ORIGINAL PAGE IS
OF POOR QUALITY

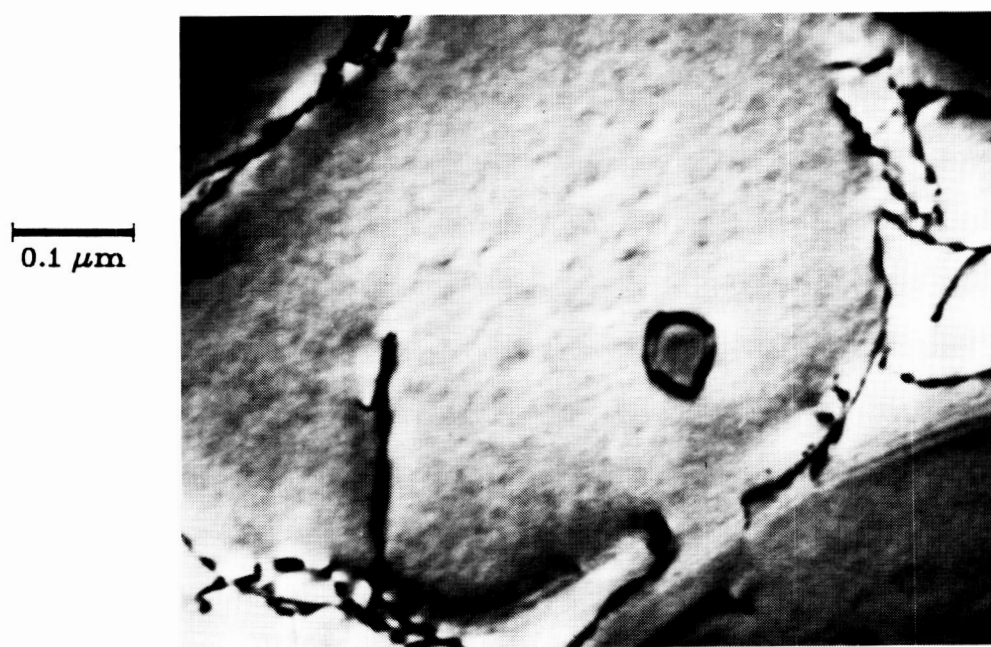


Fig 56. $a\langle 110 \rangle$ dislocation loop found after LCF. F11, $\langle 123 \rangle$, 705°C , 50%/min, $\Delta\gamma_p = 0.03\%$, $n = 760$, $g = \langle 020 \rangle$.

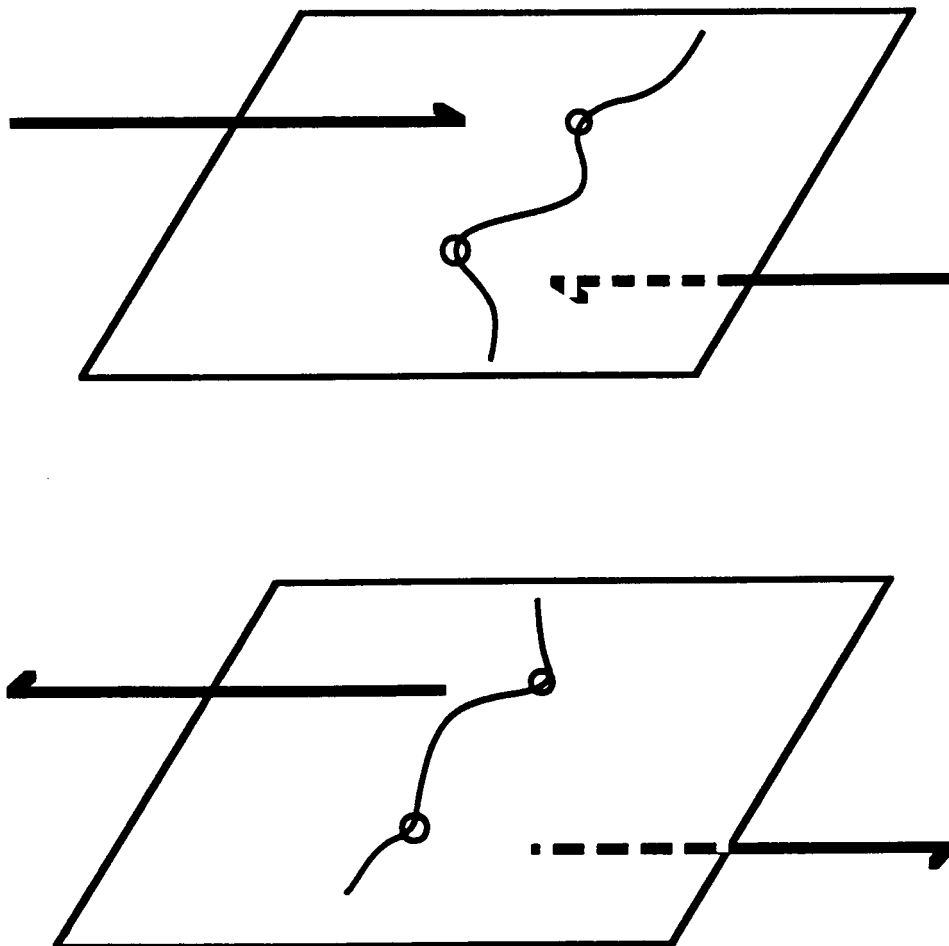


Fig 57. Schematic of screw dislocation pinning mechanism, assuming irreversible cross-slip. (a) Screw segments cross-slip and become pinned in tension at the indicated points. (b) after stress reversal, these points remain pinned. The force necessary to move the dislocation will be the same in tension and compression.

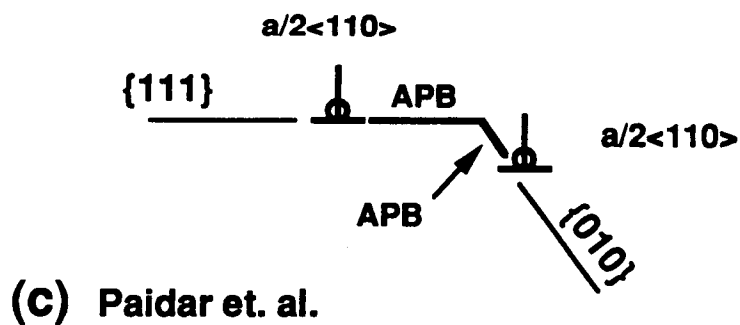
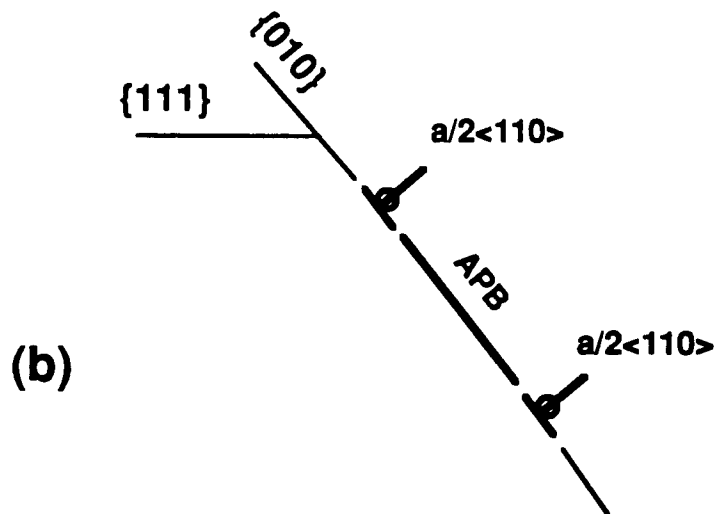
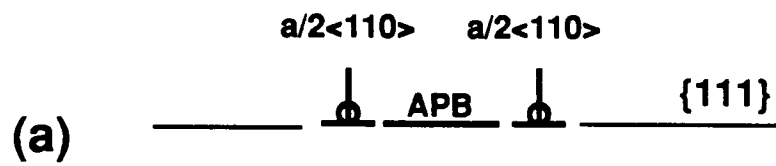


Fig 58. Possible dissociation schemes for $a\langle 110 \rangle$ superdislocations. (a) Octahedral plane. (b) Cube plane. (c) Bi-planar cross-slipped configuration.

$$\Delta E = \frac{\mu b^2}{2\pi} \left(1 - \frac{\Gamma_c}{\Gamma_c + \tau b} + \ln \left[\frac{\Gamma_o}{\Gamma_c + \tau b} \right] \right)$$

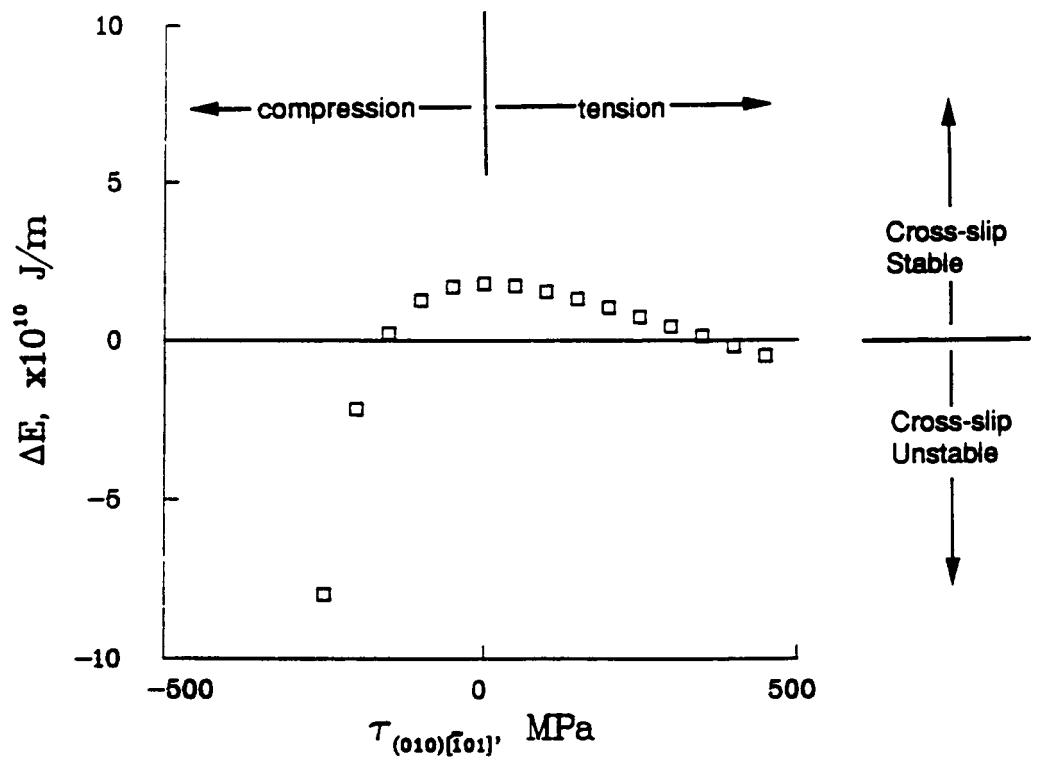
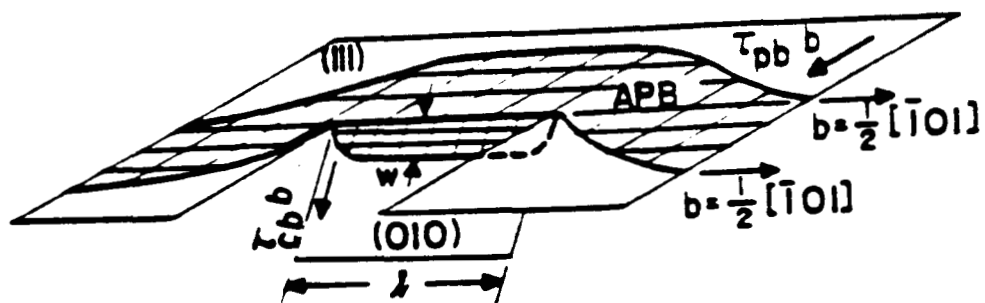
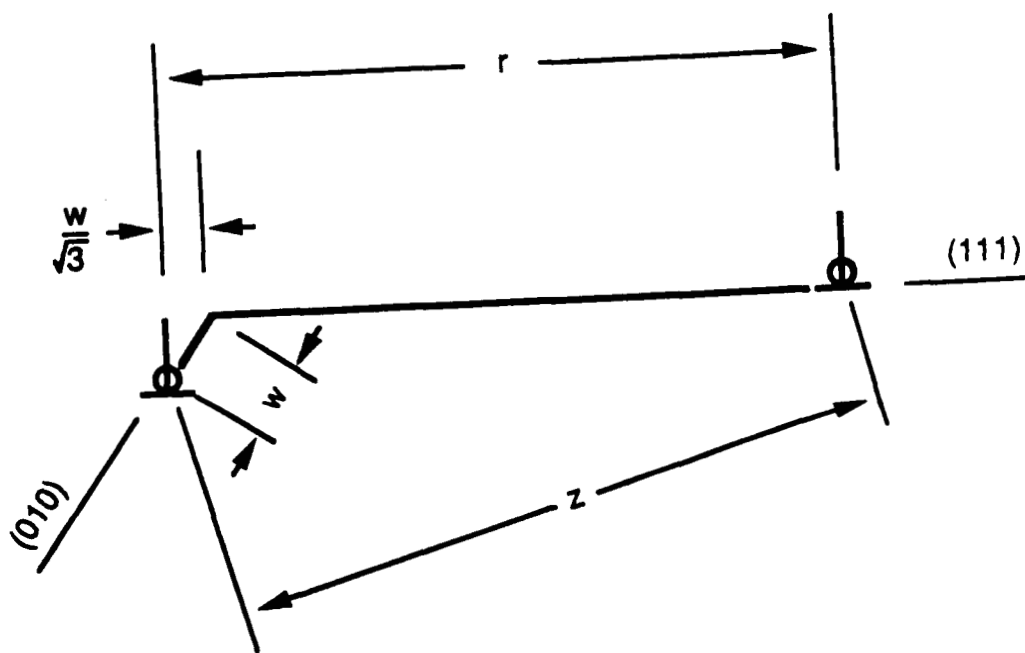


Fig 59. Difference in energy per unit length of a screw superdislocation dissociated on either the octahedral plane or the cube plane, as a function of cube plane glide stress. Plot of Equation 8-7, assuming the leading superpartial is pinned during tensile loading.



(a)



(b)

Fig 60. Proposed PPV cross-slip configuration. (a) Double kink of length l and width w acts as a pinning point. [17] (b) Cross-sectional view.

$$\Delta E = \left[\frac{\Gamma_0}{\sqrt{3}} - \Gamma_c \right] b + \frac{\mu b^2}{2\pi} \left(\frac{\tau b}{\Gamma_0 + \tau b} + \ln \left[\frac{\Gamma_0}{\Gamma_0 + \tau b} \right] \right)$$

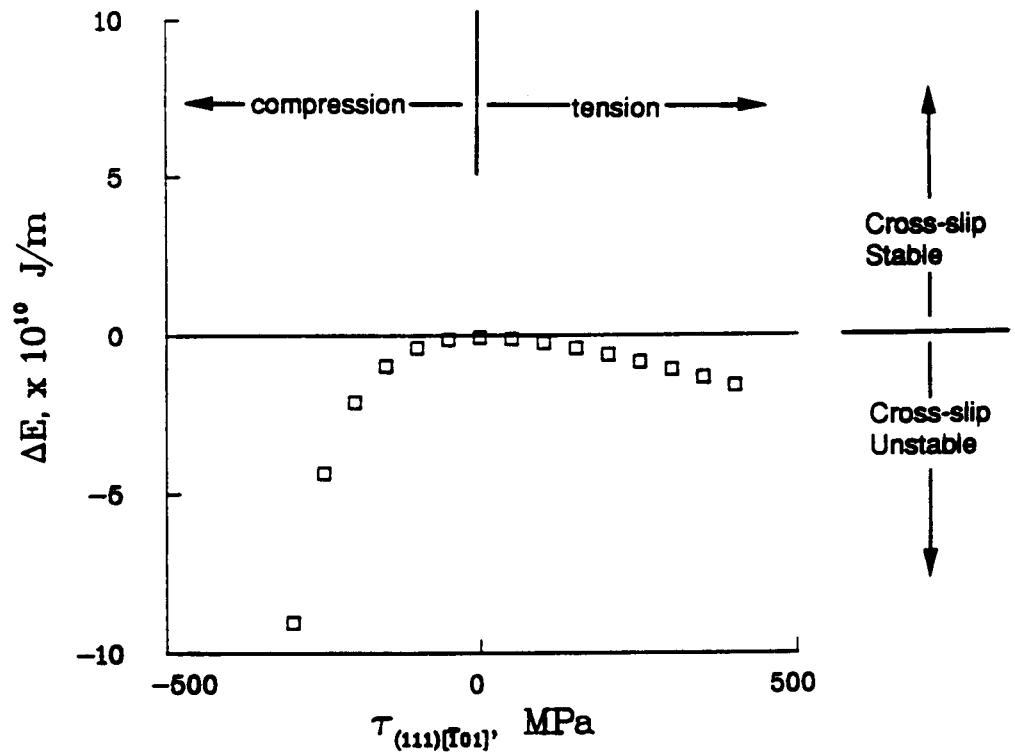


Fig 61. Difference in energy between the reference octahedral dissociation and the PPV lock shown in Figure 60, as a function of octahedral plane glide stress. Plot of Equation 8-15, assuming the leading superpartial is pinned during tensile loading.

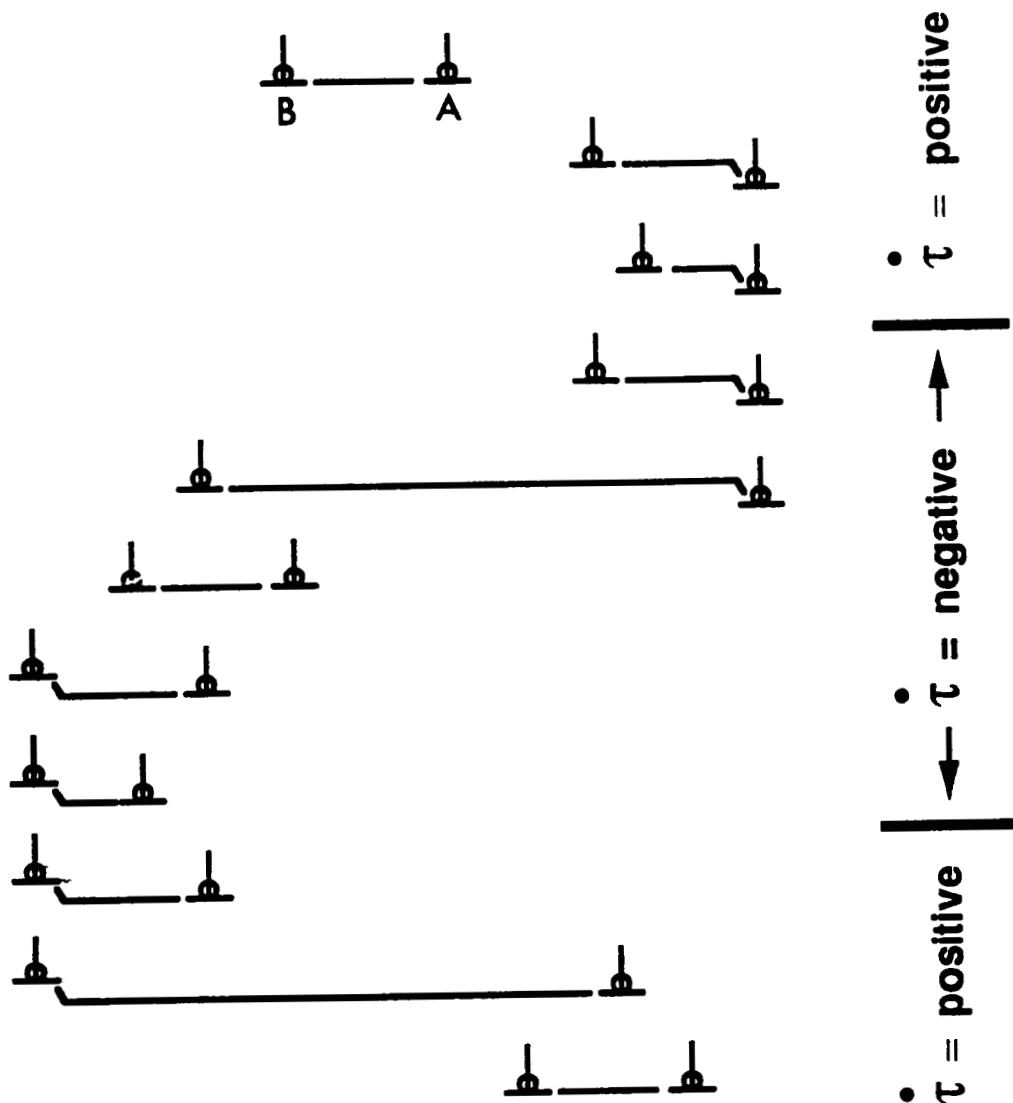
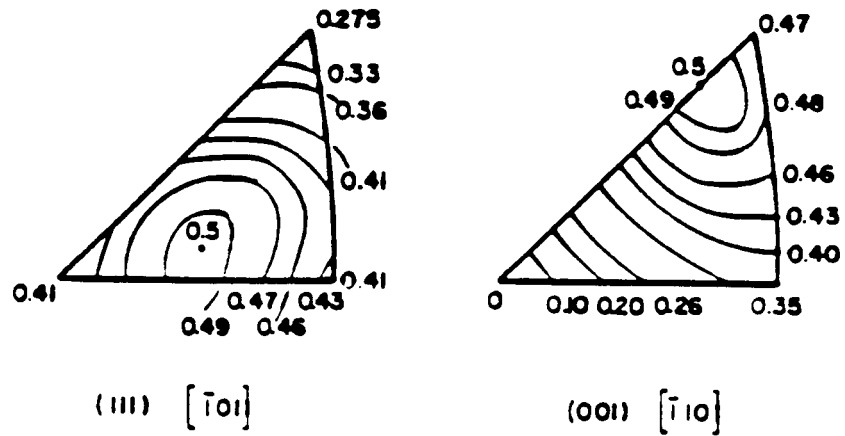
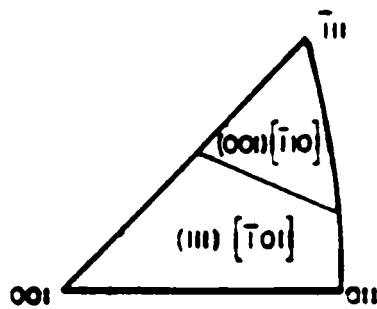


Fig 62. Sequence of events during reversible cross-slip, leading to reversible tension-compression asymmetry. Oversimplified (2-dimensional) diagram which ignores the observation that different points along the dislocation line should become pinned at different times.

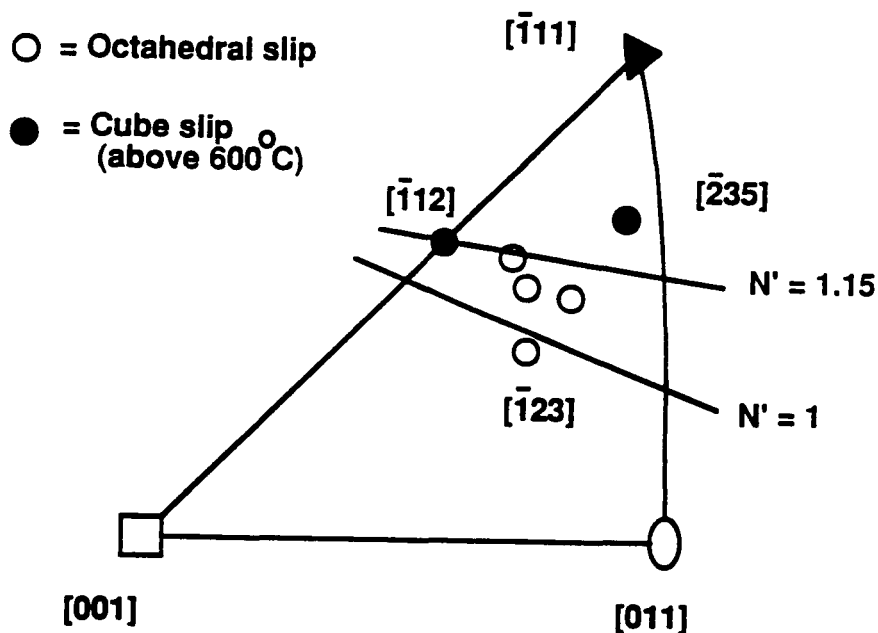


(a)



(b)

Fig 63. (a) Schmid factors for primary cube slip and primary octahedral slip [14]. (b) Great circle representing equal values of Schmid factors for cube and octahedral slip [14].



$\langle 001 \rangle$; Octahedral slip at all temperatures; PWA 1480 [present study] and Rene N4 [25]; $N' = 0$.

$\langle 011 \rangle$; Octahedral slip at all temperatures; Rene N4 [25]; $N' = 0.86$.

$\langle 111 \rangle$; Octahedral slip at 20°C , cube slip at 760 and 980°C ; Rene N4 [25]; $N' = 1.73$.

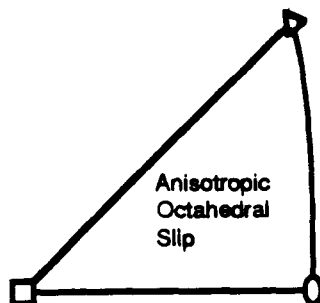
$\langle 112 \rangle$; Same as C, but $N' = 1.15$.

Near- $\langle 235 \rangle$; Cube slip during fatigue at 650°C ; PWA 1480 [28]; $N' = 1.22$

Near- $\langle 123 \rangle$; Octahedral slip at all temperatures; PWA 1480 [present study]; $N' = 1.13$.

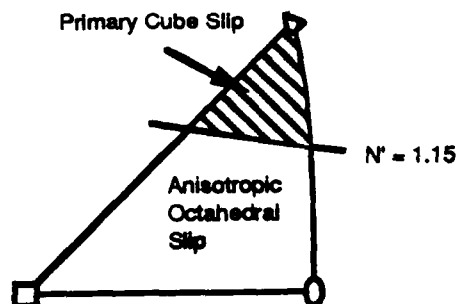
Fig 64. PWA 1480 and Rene N4 crystals which have exhibited octahedral slip (open symbols) or cube slip (closed symbols) above 600°C .

Below 600°C



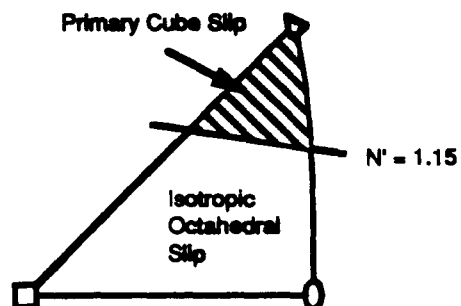
Simplified
Equations 9-25 to 9-28

Between 600 and 820 - 950°C, depending on $\dot{\epsilon}$



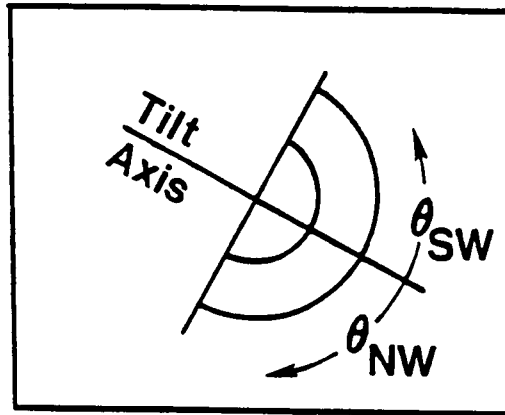
Fully Anisotropic
Equations 9-5, 9-14,
9-16, 9-17 to 9-19

Above 820 - 950°C, depending on $\dot{\epsilon}$

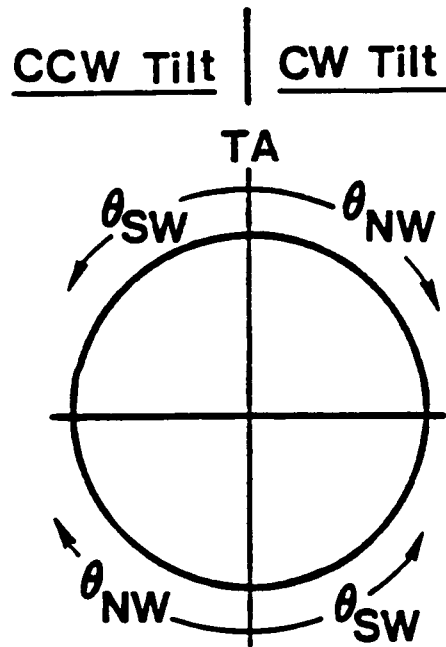


Simplified
Equations 9-29 to 9-35

Fig 65. Proposed regimes of deformation behavior for PWA 1480 under isothermal, uniaxial loading.



(a)



(b)

Fig 66. (a) TEM screen with tilt axis labeled. (b) Wulff net set-up relative to TEM screen.

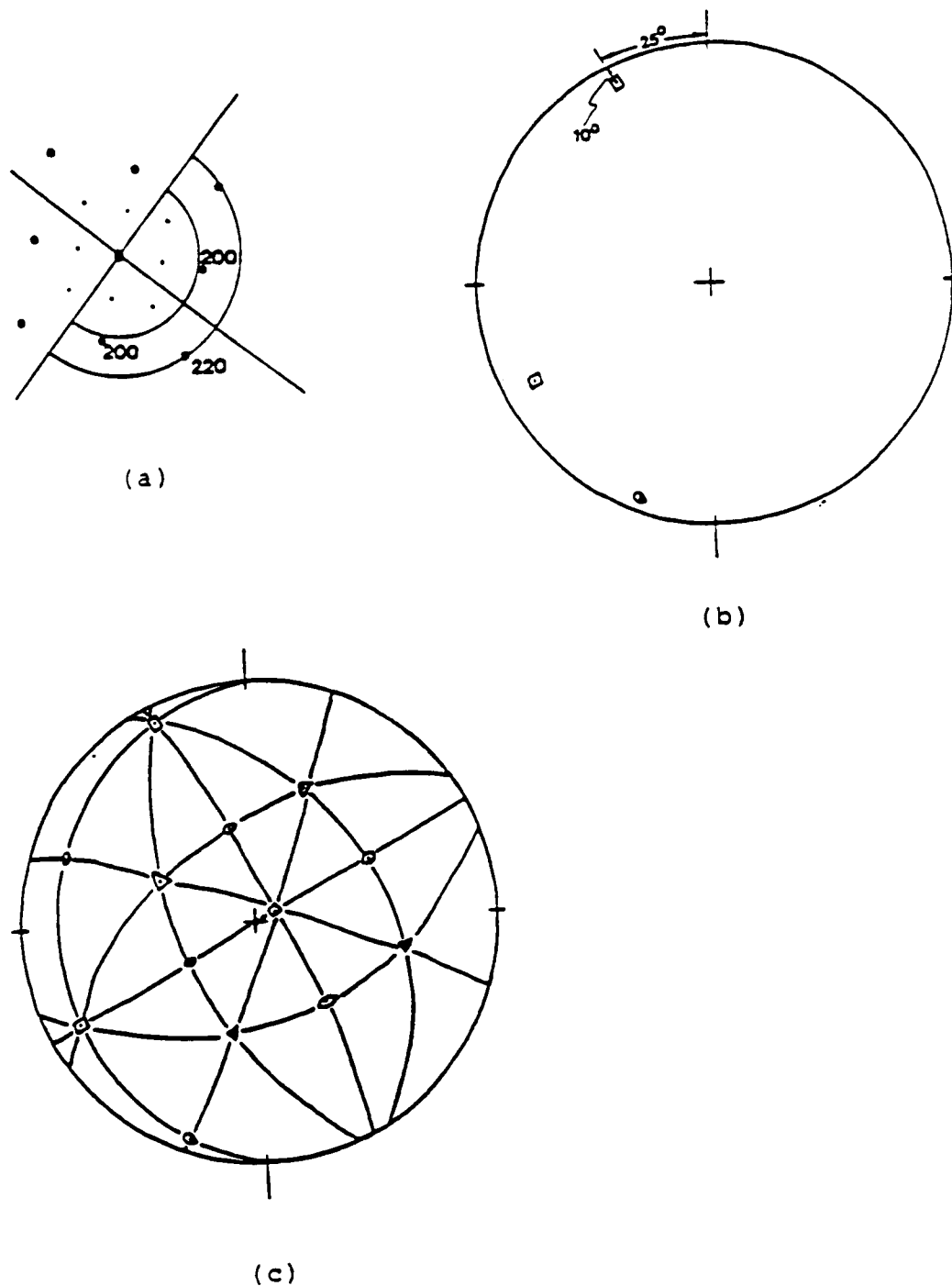


Fig 67. Determination of the crystal orientation in the TEM (See Appendix A). (a) Diffraction pattern. (b) Plotting the first $\langle 200 \rangle$ pole. (c) Finished stereographic projection.

ORIGINAL PAGE IS
OF POOR QUALITY

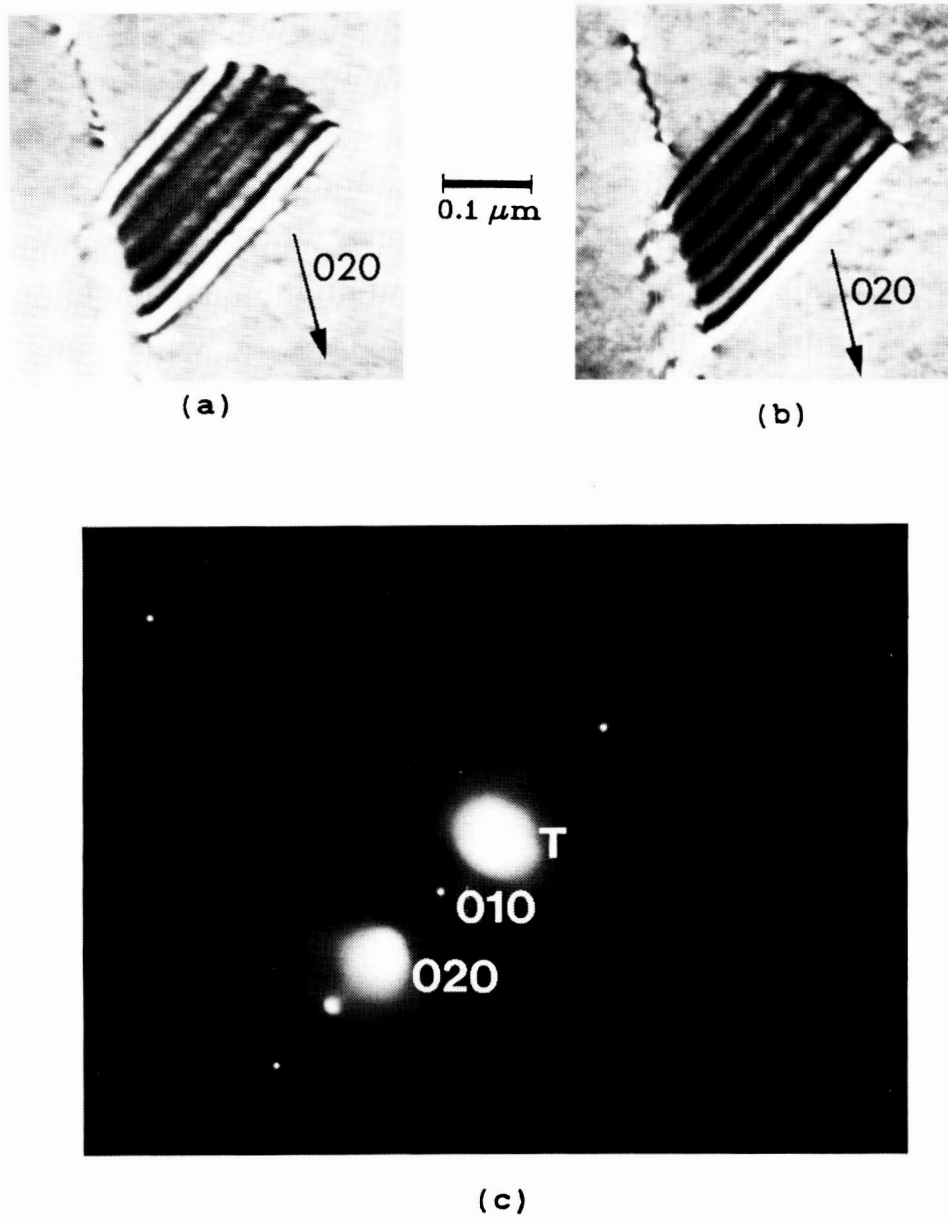
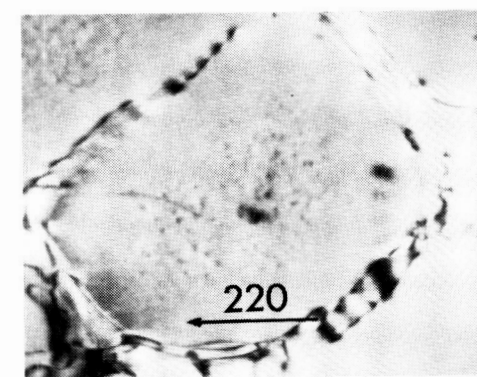
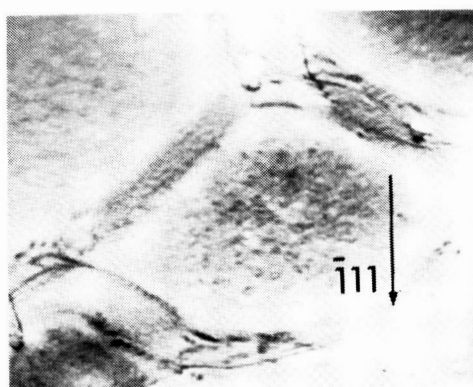
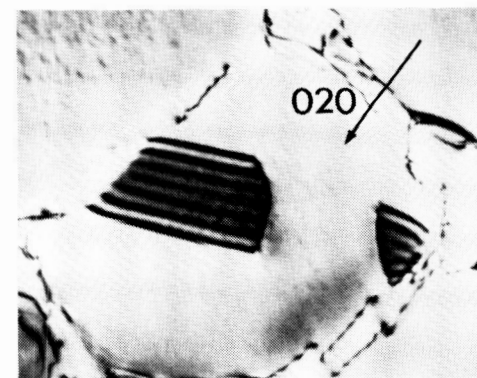
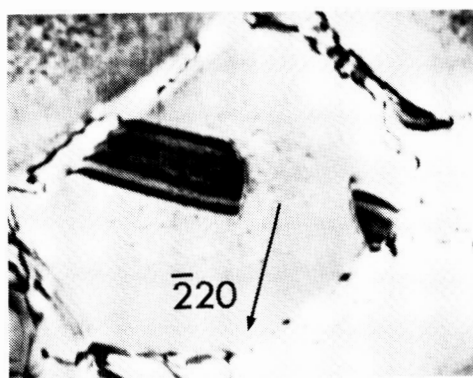
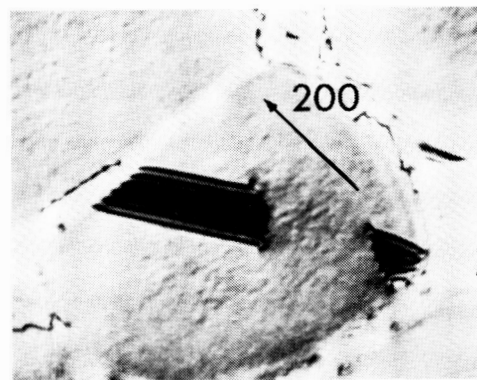
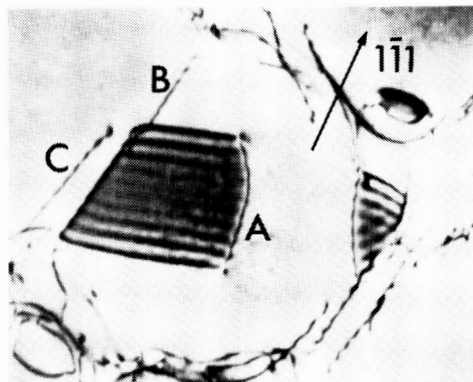
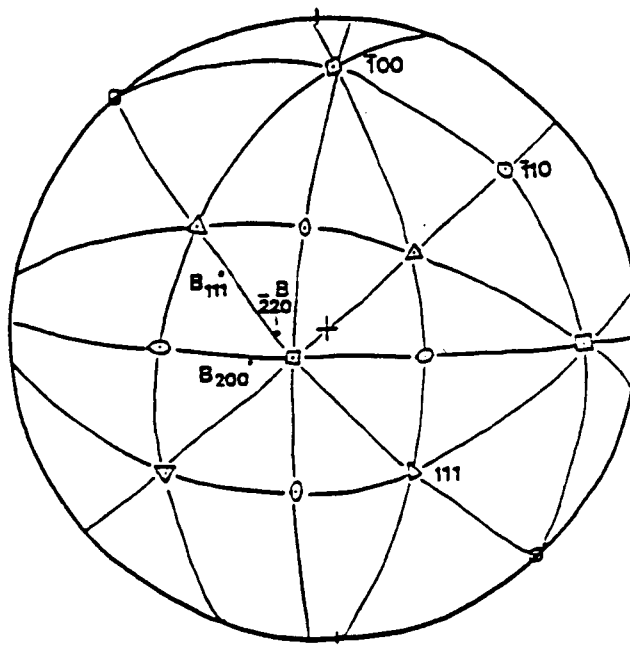


Fig 68. (a) Brightfield micrographs of a stacking fault at $g = [020]$ and $w = 0$. (b) Darkfield micrograph at $g = [020]$ and $w = 0$. (c) Selected area diffraction pattern.

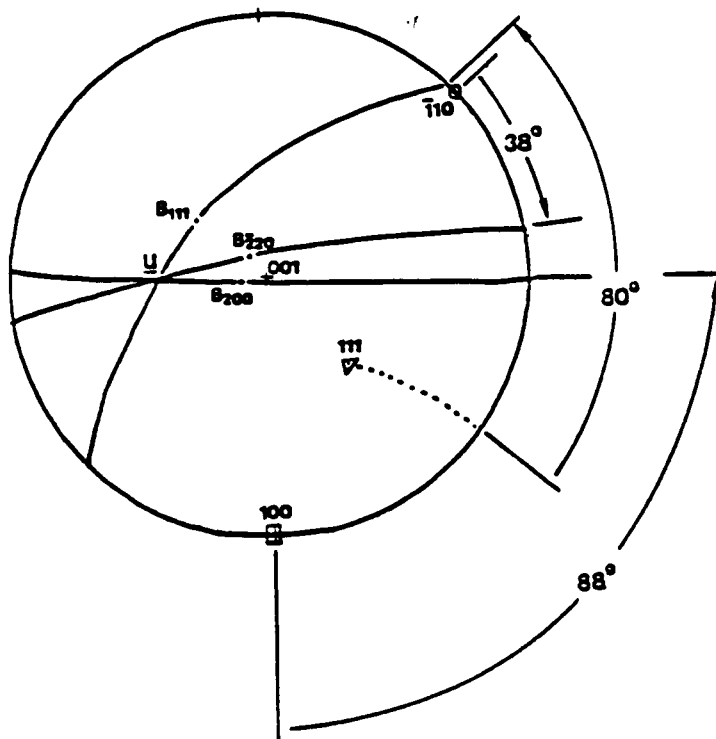


0.2 μm

Fig 69. Dislocation and fault analysis (Appendix B).



(a)



(b)

Fig 70. Line direction determination (Appendix B).

APPENDIX A
DETERMINATION OF CRYSTAL
ORIENTATION IN THE TEM

The crystallographic orientation of a crystal can be determined in-situ in the TEM, thus facilitating diffraction experiments and dislocation analysis. The steps necessary to determine the orientation are outlined briefly below, then each step is discussed individually.

1. Determine the holder tilt axis on the TEM screen.

2. Tilt the crystal until a low index spot appears.

Center the Kikuchi band directly over the transmitted beam spot.

3. Determine the Miller indices of the spot.

4. Measure the angle between the g -vector and the tilt axis. Record this angle, as well as the amount of tilt and sense of the tilt.

5. Plot the g -vector on a Wulff net.

6. Repeat steps 2-5 two to three times.

7. Construct the stereographic projection for the crystal from the poles plotted in Step 5.

Each step is now discussed in detail.

Step 1

The tilt axis was determined prior to this research, and is inscribed in the TEM viewing screen. This was done by measuring the trajectory of the Kikuchi lines during tilting of a crystal, and noting that the tilt axis is perpendicular to this trajectory. Figure 66 shows the screen schematically. Two quadrants are named (NW and SW) to facilitate record keeping.

Step 2

It is essential that the Kikuchi band be centered on the transmitted spot, thus ensuring that the diffracting planes are exactly parallel to the beam.

Step 3

The d-spacing of the diffracting planes can be determined from the spacing between the transmitted and diffracted beams by the following equation [88]:

$$\lambda_e L = R d \quad (A-1)$$

where λ_e = Electron wavelength,

L = Camera length,

R = Spot spacing,

d = Interplanar spacing.

The g-vector can be determined from the d-spacing by the following equation (for cubic crystals):

$$1/d^2 = (h^2 + k^2 + l^2)/a^2 \quad (A-2)$$

where a = Lattice parameter,

$[hkl]$ = Miller indices.

The viewing screen had two semicircles inscribed whose radii corresponded to the R values for $\langle 111 \rangle$ and $\langle 220 \rangle$ g -vectors in nickel, thus allowing visual determination of g .

Step 4

The angle between the tilt axis and the g -vector is recorded, as well as the quadrant in which g lies.

Steps 5-7

The Wulff net is set up as follows (Figure 66(b)): The tilt axis is the North/South great circle; the beam direction is the center of the Wulff net; a clockwise rotation of the tilting stage tilts the crystal from West to East on the Wulff net. Thus, if diffraction occurs when the holder is tilted clockwise, the pole was in the Eastern half of the Wulff net at zero tilt, and vice-versa.

The poles are plotted in the following way. Assume that a $\langle 200 \rangle$ g lies in the NW quadrant after a clockwise tilt of θ degrees, and the angle between the tilt axis and g was measured to be ϕ degrees. Starting at the North pole, travel clockwise around the perimeter of the Wulff net for ϕ degrees. Now, travel inward along a small circle for θ degrees. The pole is plotted at that point. Figure 67

illustrates this procedure, and an example is given in the next section.

At least three low-index poles should be plotted, after which the stereographic projection is constructed. This projection represents the orientation of the crystal when looking down along the electron beam at zero degrees tilt.

Example

A $\langle 001 \rangle$ zone appeared when a crystal was tilted 10° counter-clockwise. The following data were measured (Figure 67(a)):

g	θ	ϕ	Quadrant
$\langle 200 \rangle$	10°CCW	25°	SW
$\langle 220 \rangle$	"	20°	NW
$\langle 200 \rangle$	"	65°	NW

The first $\langle 200 \rangle$ pole is plotted by travelling 25° CCW from the North pole, then travelling 10° inward, Figure 67(b). The other two poles are plotted in a similar manner, and the projection is constructed, Figure 67(c).

APPENDIX B

DISLOCATION AND STACKING FAULT ANALYSIS

Dislocations Burgers vectors, line directions, and slip planes may be determined by a series of diffraction experiments in the TEM. The character and displacement vector of a stacking fault, as well as its habit plane can also be determined. These procedures are summarized below. Hirsch et. al. [88] present a thorough treatment for the interested reader.

Determination of the g-Vector

Due to the electromagnetic nature of the lenses, the brightfield image is rotated with respect to the diffraction pattern, and this rotation is a function of magnification. The rotation is calibrated, so directions which are measured in diffraction mode may be transferred to brightfield micrographs. An example is given in Figure 68. The original magnification was 66,000X, and the camera length in diffraction mode was 76 cm. From the pre-determined rotation calibration, the diffraction pattern was rotated 48° CW with respect to the micrograph. The g-vector direction seen in the diffraction pattern was then rotated 48° CCW and placed on the micrograph.

Determination of Displacement Vectors

Under two-beam conditions, dislocation contrast will result unless the displacement field of the defect lies solely within the diffracting plane. This occurs when:

$$\underline{g} \cdot (\underline{b} \times \underline{u}) = 0 \quad (\text{B-1})$$

where \underline{u} is the line direction of the dislocation. Only residual contrast will occur if

$$\underline{g} \cdot \underline{b} = 0 \quad (\text{B-2})$$

Therefore, the Burgers vector of a dislocation can be determined when two two-beam conditions are found which satisfy Equations (B-1) or (B-2). The Burgers vector will be the cross-product of the two \underline{g} -vectors.

Similarly, the displacement vector of a stacking fault can be determined by finding two two-beam conditions where the following criterion is satisfied:

$$\underline{g} \cdot \underline{R}_f = 0 \quad (\text{B-3})$$

where \underline{R}_f is the fault displacement vector. Additionally, a stacking fault can be nearly invisible when it is viewed edge-on.

For example, consider the dislocations labeled A, B, and C in Figure 69. Dislocation A disappears when $\underline{g} = [\bar{1}11]$ and $[220]$, so the Burgers vector is parallel to $[\bar{1}1\bar{2}]$:

$$\underline{b}_A = [\bar{1}11] \times [220] = [\bar{1}1\bar{2}] \quad (\text{B-4})$$

Similarly,

$$\underline{b}_B = [200] \times [\bar{1}11] = [0\bar{1}1] \quad (\text{B-5})$$

and

$$\underline{b}_C = [020] \times [\bar{1}11] = [101] \quad (\text{B-5})$$

The stacking fault seen in Figure 69 was found to have $\underline{R}_f = [\bar{1}11]$, because the fault was edge-on when $\underline{g} = [\bar{1}11]$. This is also consistent with the observed invisibility of the fault when $\underline{g} = [220]$, because $\underline{g} \cdot \underline{R}_f = 0$.

Determination of Line Directions

The true line direction, \underline{u} , always lies in the plane defined by the beam direction, \underline{B} , and the projected line direction, \underline{u}_p . Therefore, a dislocation line direction can always be determined by finding two or more conditions where \underline{B} and \underline{u}_p are known:

$$\underline{u} = (\underline{u}_p^1 \times \underline{B}^1) \times (\underline{u}_p^2 \times \underline{B}^2) \quad (\text{B-7})$$

This procedure is easier to conduct using the stereographic projection than by using Equation (B-7). The procedure is:

1. Determine the crystal orientation.
2. Tilt the crystal until a two-beam condition occurs where the dislocation is in contrast. Record the tilt settings in order to determine \underline{B} .
3. Measure the angle between \underline{g} and \underline{u}_p .
4. On a standard $\langle 001 \rangle$ projection, plot \underline{B} and \underline{u}_p . Draw

a great circle between the two.

5. Repeat Steps 2-4 for at least 2 more g-vectors.

6. The intersection of the great circles is \underline{u} .

For example, consider Dislocation C in Figure 69. The three g-vectors used were $[200]$, $[\bar{2}20]$, and $[111]$, although the $[111]$ micrograph is not shown in Figure 69. The crystal orientation was determined, and is shown in Figure 70. The following data were recorded from the double-tilt stage:

\underline{g}	Tilt 1	Tilt 2
$[200]$	24° W to E	9° S to N
$[\bar{2}20]$	18° W to E	0
$[111]$	37° W to E	18° N to S

From this data, the \underline{B} 's are plotted on the stereographic projection, Figure 70(a). The following data were measured from the prints, where θ is the angle between \underline{g} and \underline{u}_p :

\underline{g}	θ	Sense of θ
$[200]$	88°	CCW
$[\bar{2}20]$	38°	CW
$[111]$	80°	CCW

A standard $\langle 001 \rangle$ projection is constructed, and the \underline{B} 's are plotted on it. Next, the \underline{u}_p 's are plotted from the data in the above table. The great circles are drawn, and it is seen from Figure 70(b) that the intersection of the great

circles is $[011]$, so $\underline{u} = [0\bar{1}1]$.

Determination of the Slip Plane

The slip plane is defined as the plane that contains both the line direction and the Burgers vector, so the slip plane normal for dislocation C (in this cubic crystal) is

$$[101] \times [0\bar{1}1] = [\bar{1}11] \quad (\text{B-8})$$

Therefore, the dislocation is in the $(\bar{1}11)[101]$ slip system.

Determination of the Fault Character

The easiest way to distinguish between extrinsic and intrinsic faults in the FCC lattice is to take a darkfield image at a deviation parameter, w , equal to zero. The g -vector which was used to obtain the darkfield image is then placed on the print. For $\langle 200 \rangle$, $\langle 222 \rangle$, or $\langle 440 \rangle$ g -vectors, the g -vector points towards the light fringe for intrinsic faults. For $\langle 111 \rangle$ or $\langle 220 \rangle$ g -vectors, the g -vector points away from the light fringe for intrinsic faults. Thus, the fault seen in Figure 69 is intrinsic, since the $[200]$ g -vector points towards the light fringe.

(Note again that these rules were stated backwards in an earlier report [5]. The analysis was done correctly, but an error was made in the preparation of the figures and the statement of the rules).

Appendix C

CRSS Data

The points which are plotted in the Figures in the body of the thesis are average values taken from the Tables listed below. CRSS values were taken only from virgin specimens, either by tensile testing or by measuring the CRSS during the first quarter-cycle of an LCF test. Specimens identified by a "T" or "C" preceding the specimen number were monotonic tests, while those preceded by an "F" were LCF tests.

The number of tests available for measuring the CRSS at 20 and 705°C was smaller than at 927°C. This occurred for two different reasons. At 20°C, the strain rate sensitivity was low, so tensile tests were run only at 0.5%/min, while LCF tests were run only at 50%.min. At 705°C, the plastic strain ranges which were used to study cyclic deformation were so small that the CRSS at 0.05% offset could not always be measured.

The CRSS values were obtained by measuring the normal stress at 0.05 and 0.2% plastic normal strain, then calculating the resolved shear stress.

TABLE C-1

Tensile CRSS Data, <001>

#	T, C	$\dot{\epsilon}$, %/min	$M^{(1)}$	$\tau(0.05\%)$, MPa	$\tau(0.2\%)$, MPa
T37-2	20	0.5	0.43	432	443
T61-2			0.44	444	-
F70-1		50	0.44	419	-
F108-3			0.45	452	-
F1-3 ⁽²⁾	200	0.5	0.45	401	405
F40-2 ⁽²⁾	400	0.5	0.42	378	407
F40-3 ⁽²⁾	600	0.5	0.42	368	401
T35-2	705	0.5	0.44	440	492
T70-1			0.42	416	-
T35-1		50	0.44	417	453
T70-2			0.42	407	-
F100-2			0.42	365	407
F100-3			0.42	382	407
F40-1			0.42	395	419
T42-1	927	0.5	0.43	159	-
T39-1			0.44	172	200
F104-1			0.43	150	-
F104-2			0.43	150	-
T42-2		50	0.43	274	-
T39-2			0.44	296	337
F12-1			0.42	259	-
F12-2			0.42	282	-
F12-3			0.42	281	-
F24-3			0.46	291	-

(1) M = Schmid factor, $\cos\phi\cos\theta$

(2) CRSS measured at 0.5%/min, subsequent LCF test conducted at 50%/min.

Table C-2
Tensile CRSS Data, <123>

#	T, C	$\dot{\epsilon}$, %/min	M	$\tau(0.05\%)$, MPa	$\tau(0.2\%)$, MPa
T1	20	0.5	0.43	381	382
F4		50	0.43	404	-
T6	705	0.5	0.42	315	320
T10			0.42	320	-
F8			0.42	330	-
T7		50	0.42	340	342
F11			0.42	315	-
T16	927	0.5	0.44	166	183
F13			0.44	165	-
T14		50	0.44	232	294
F17			0.44	235	-

Table C-3
Compressive CRSS Data
(All tests at 0.5%/minute strain rate)

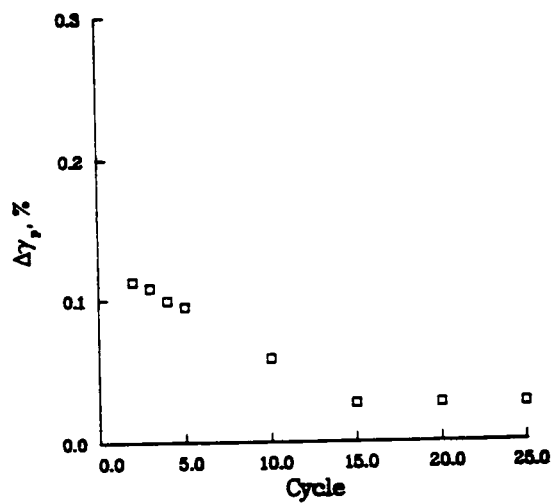
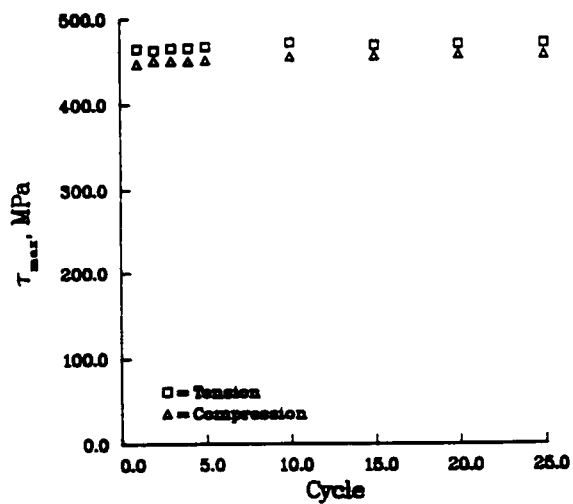
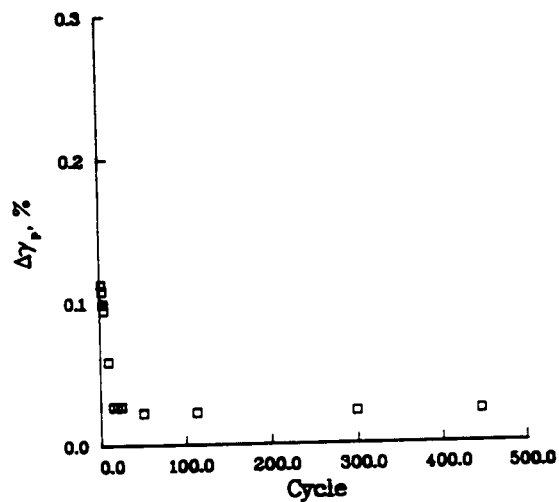
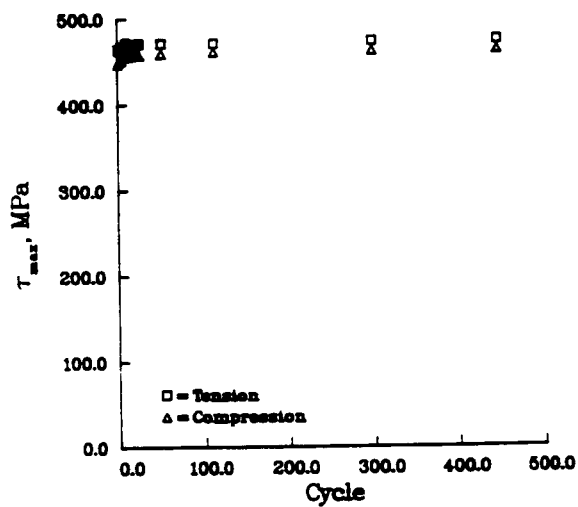
#	T, C	Orientation	M	$\tau(0.05\%)$, MPa	$\tau(.02\%)$, MPa
C7-3	20	<001>	0.44	387	390
C7-2			0.44	383	383
C12		<123>	0.44	400	400
C2			0.42	400	400
C7-1	705	<001>	0.44	372	383
C70-2			0.44	370	385
C13		<123>	0.44	376	380
C5			0.43	356	356

APPENDIX D
CYCLIC DEFORMATION DATA

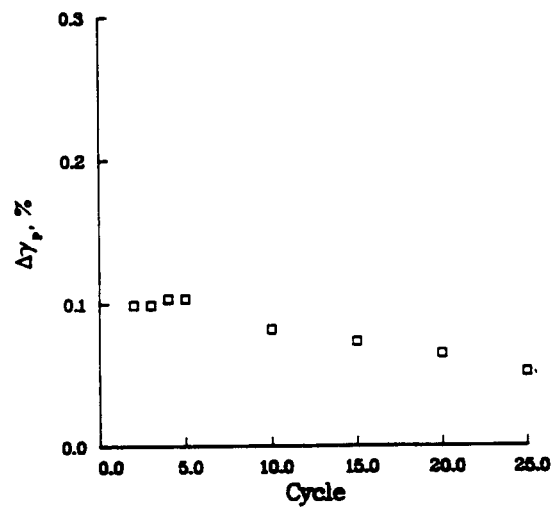
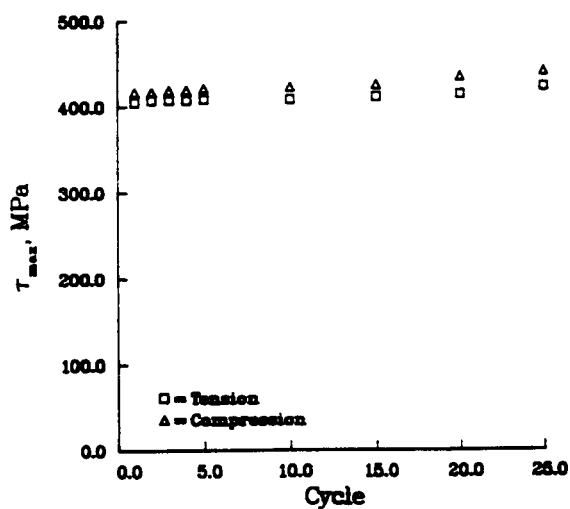
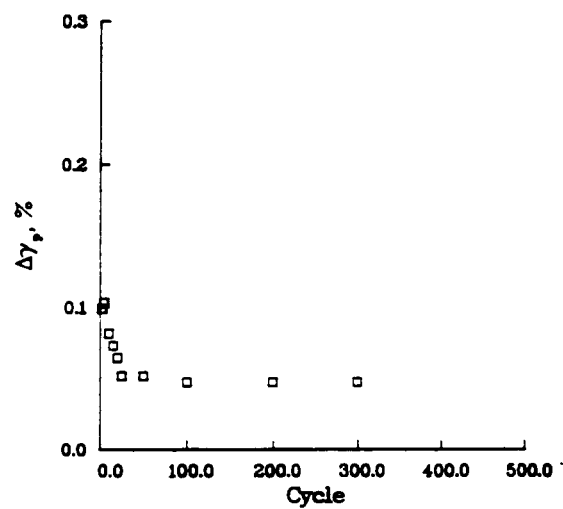
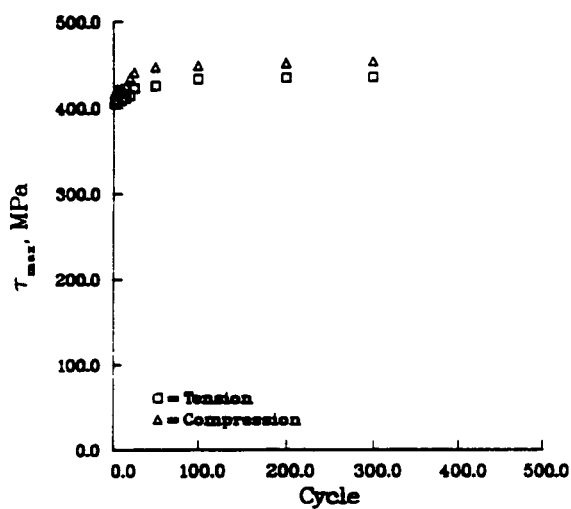
This Appendix contains a complete set of tests from 20°C to 927°C which all saturated to a reasonably similar value of $\Delta\gamma_p$. All but two tests exhibited $\Delta\gamma_p$ between 0.04% and 0.08%, and those two exhibited $\Delta\gamma_p$ values of 0.03% and 0.10%, respectively.

This Appendix contains data for $\langle 001 \rangle$ and $\langle 123 \rangle$ crystals at both 0.5 and 50%/minute strain rates. The only exception is that only $\langle 001 \rangle$ crystals were fatigued at 200-600°C.

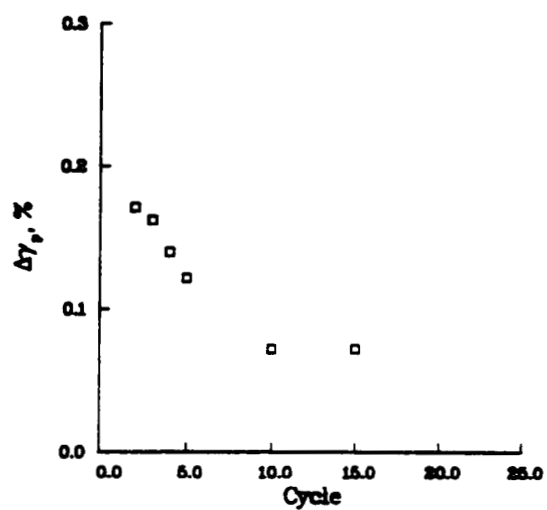
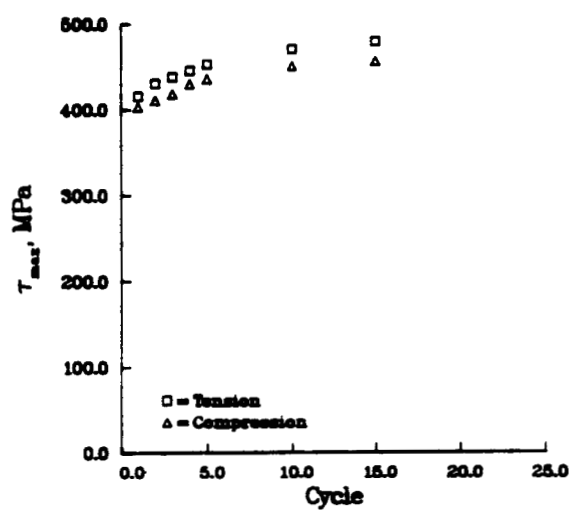
Duplicate tests and tests at different $\Delta\gamma_p$'s are contained in Appendix E.



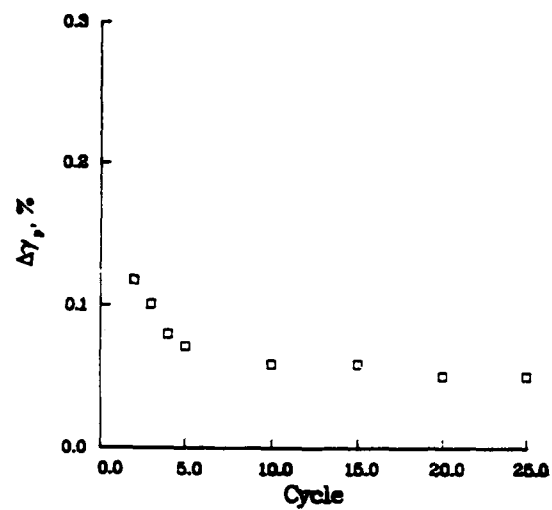
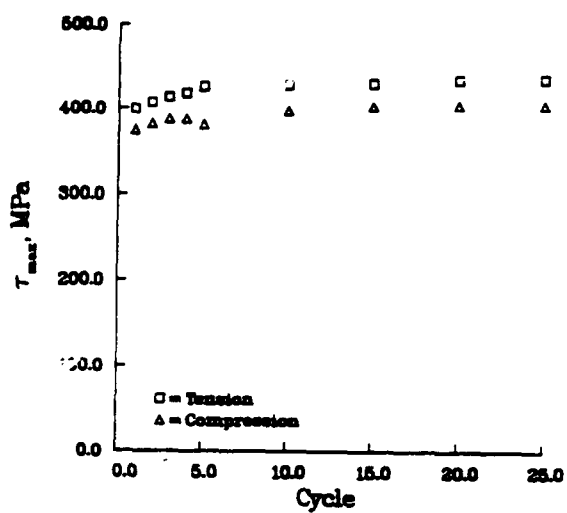
F108-3, <001>, 20°C, 50%/min, $\Delta\epsilon_t = 1.9\%$, $M = 0.45$



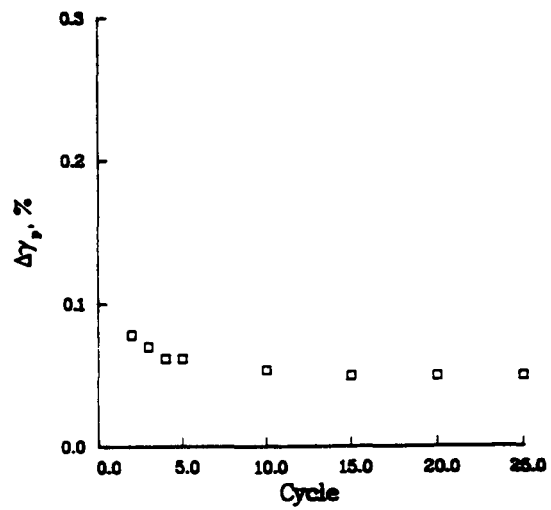
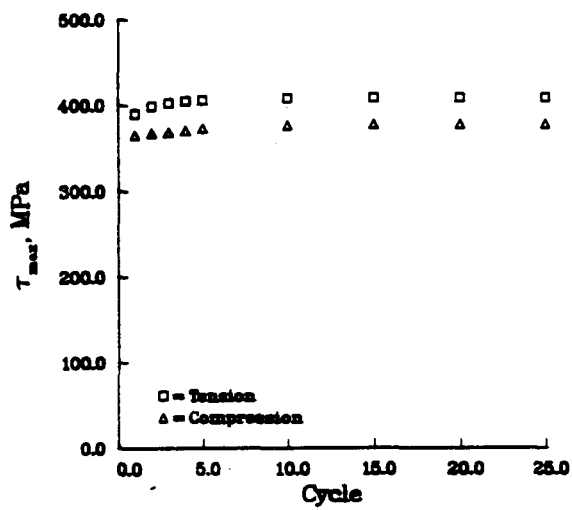
F4, <123>, 20°C, 50%/min, $\Delta\epsilon_t = 1.05\%$, $M = 0.43$



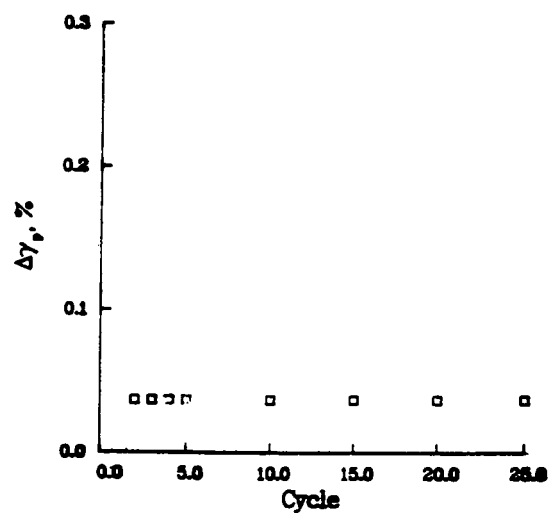
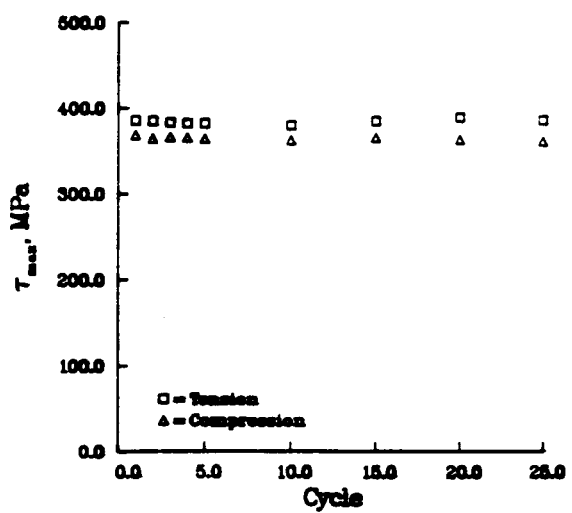
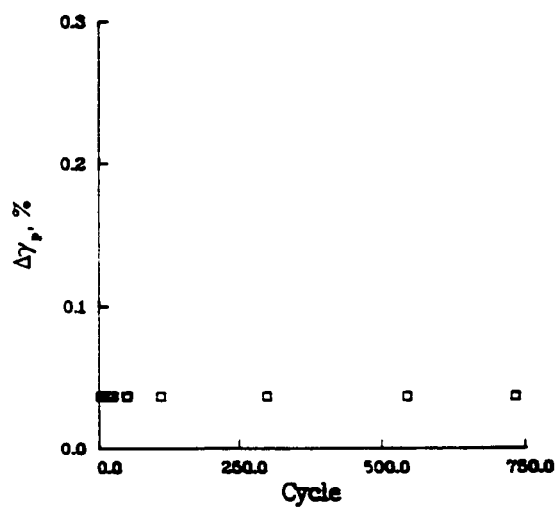
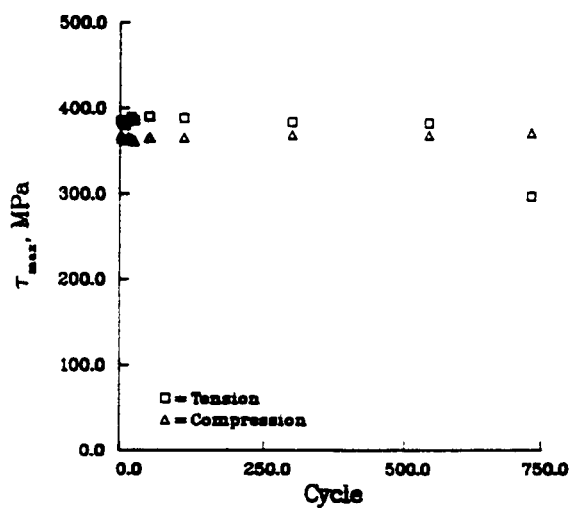
F1-3, <001>, 200°C, 50%/min, $\Delta\epsilon_t = 1.9\%$, $M = 0.45$



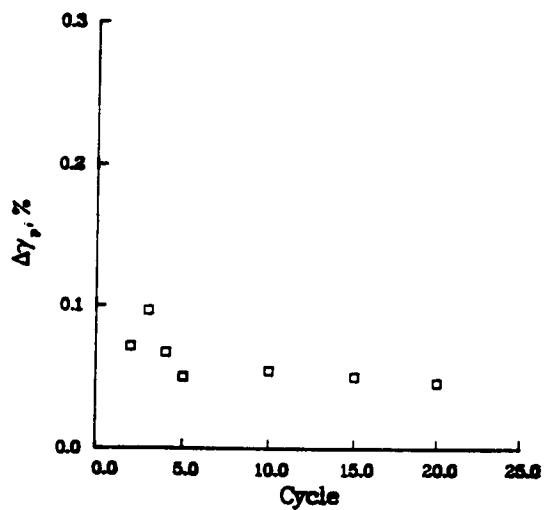
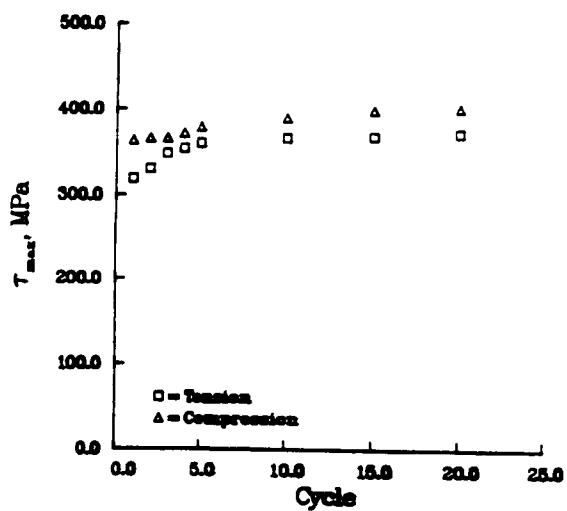
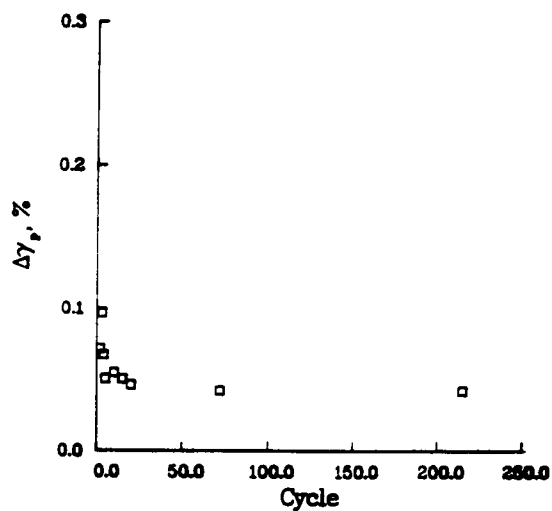
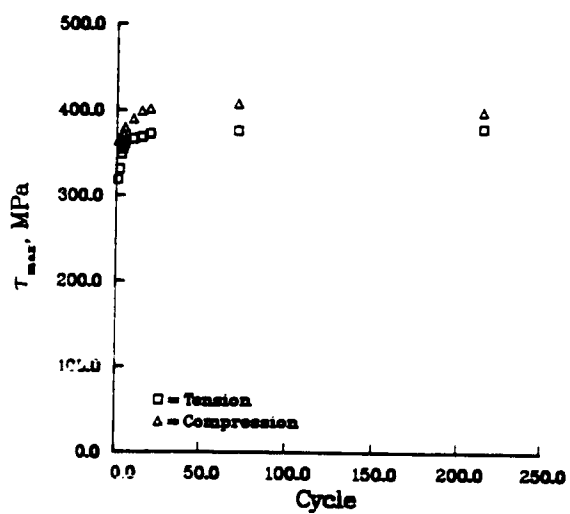
F40-2, <001>, 400°C, 50%/min, $\Delta\epsilon_t = 1.9\%$, $M = 0.42$



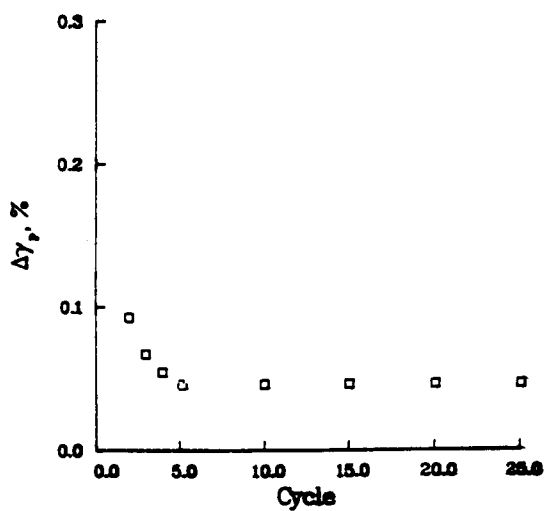
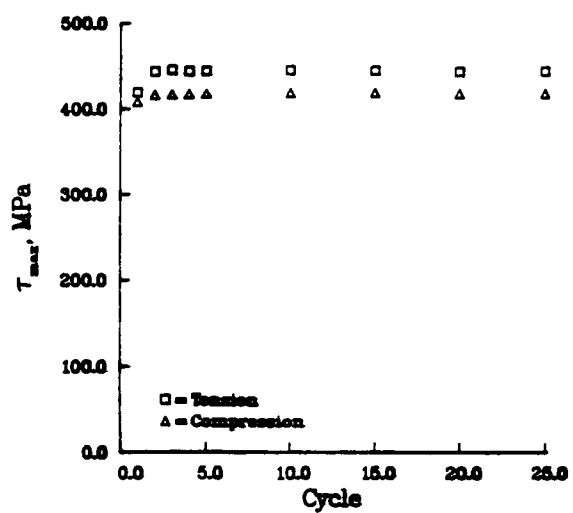
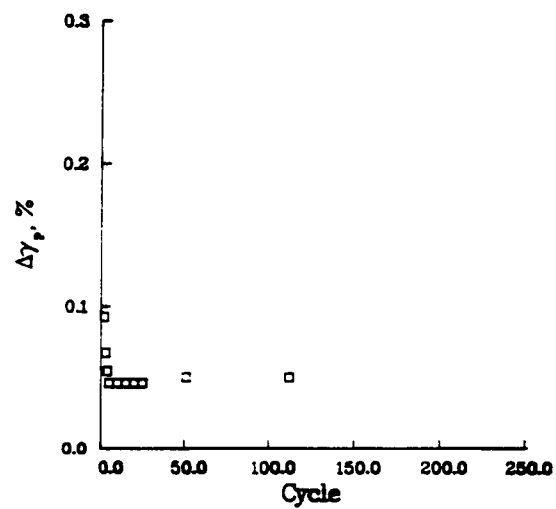
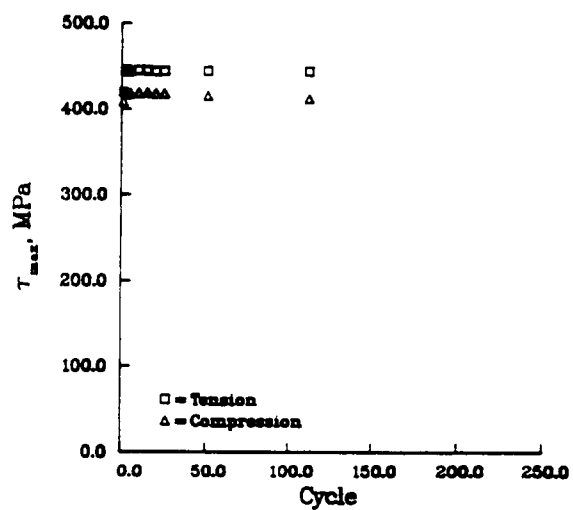
F40-3, <001>, 600°C, 50%/min, $\Delta\epsilon_t = 1.9\%$, $M = 0.42$



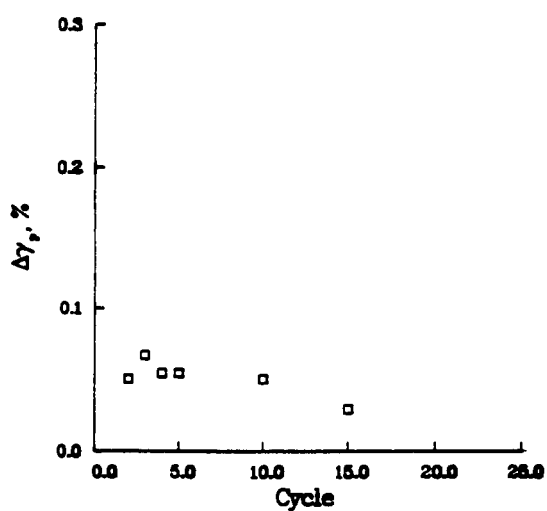
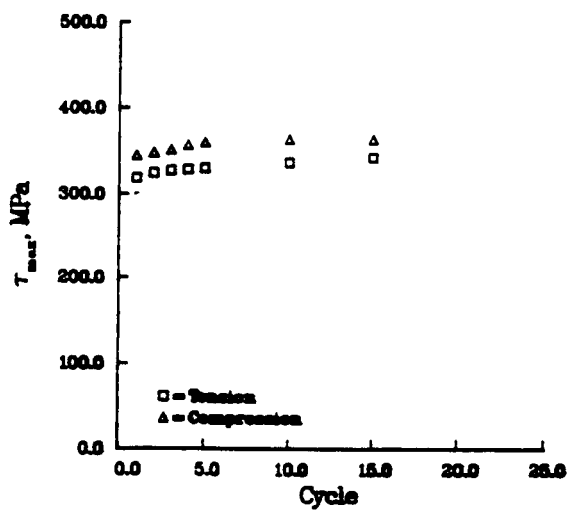
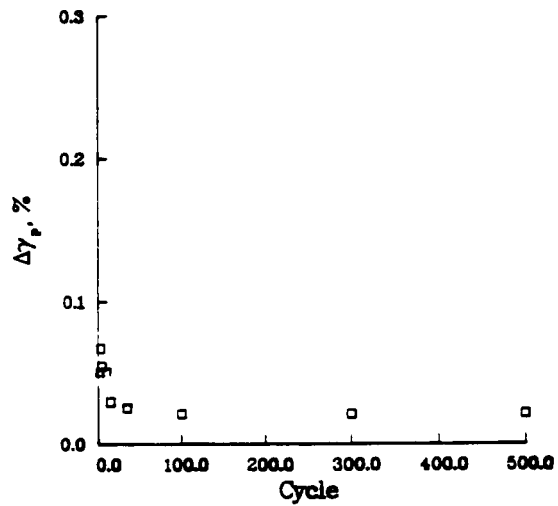
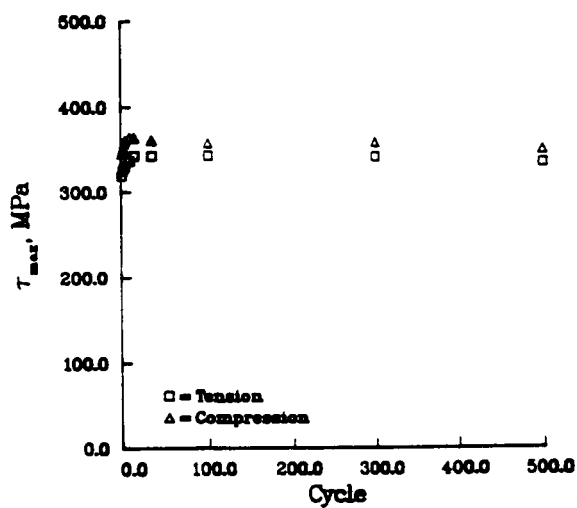
F144-1, <001>, 705°C, 0.5%/min, $\Delta\epsilon_t = 1.8\%$, $M = 0.46$



F8, <123>, 705°C, 0.5%/min, $\Delta\epsilon_t = 1.05\%$, $M = 0.42$

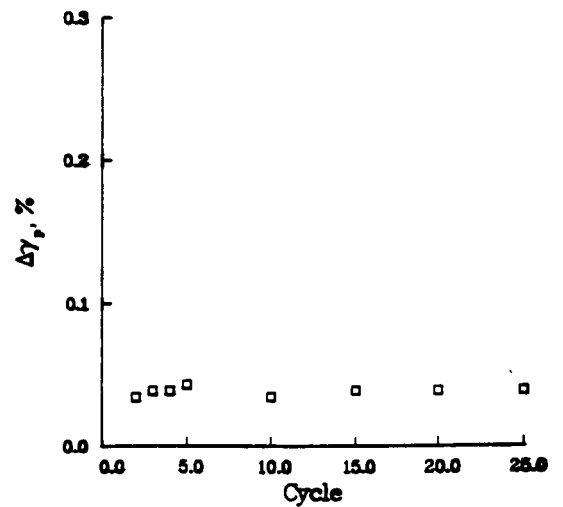
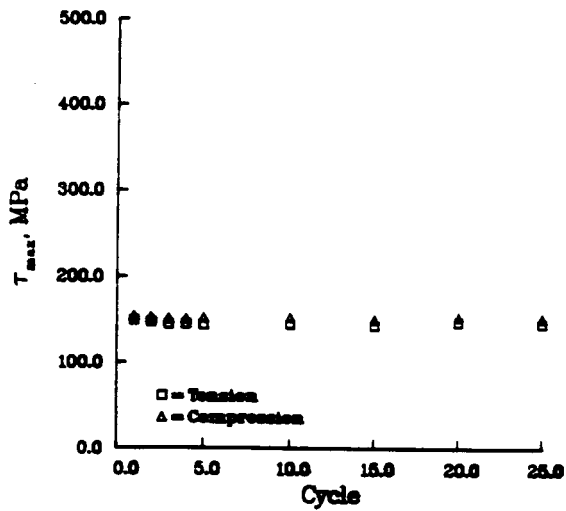
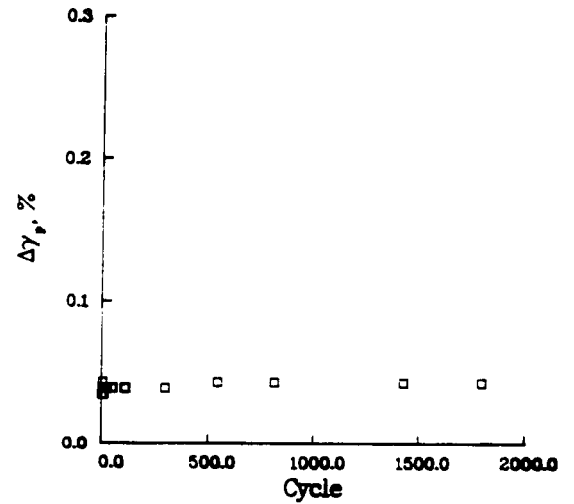
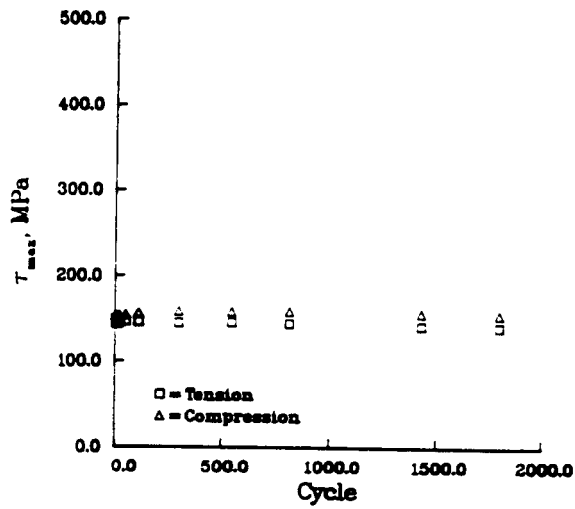


F40-1, <001>, 705°C, 50%/min, $\Delta\epsilon_t = 2.4\%$, $M = 0.42$



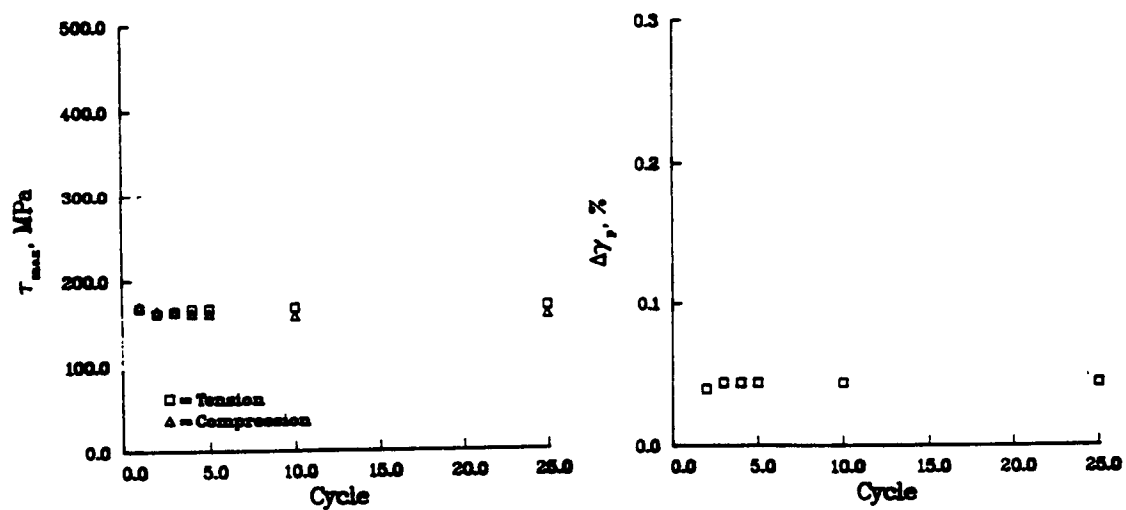
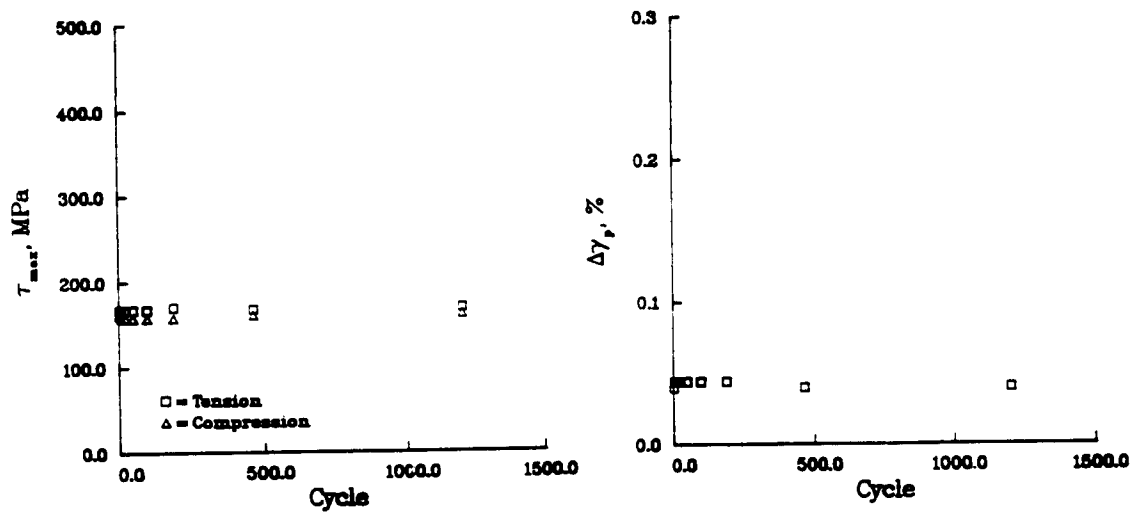
F11, <123>, 705°C, 50%/min, Δε_t = 0.9%, M = 0.42

ORIGINAL PAGE IS
OF POOR QUALITY

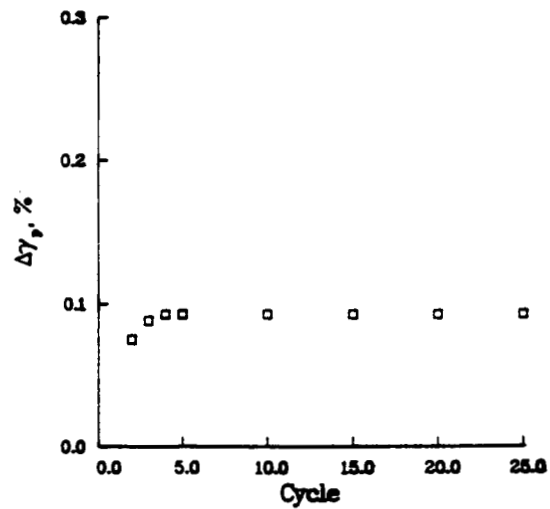
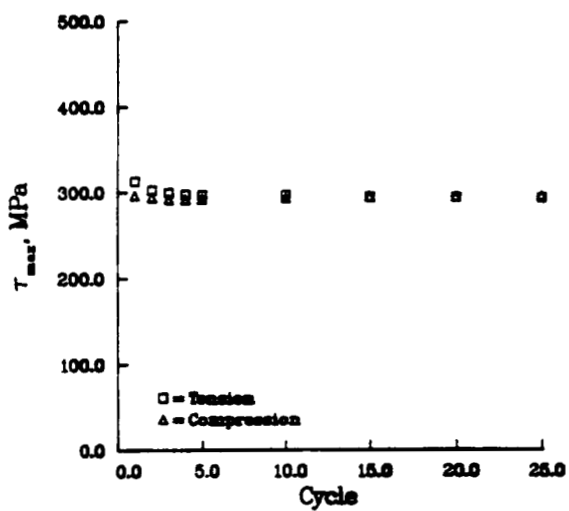
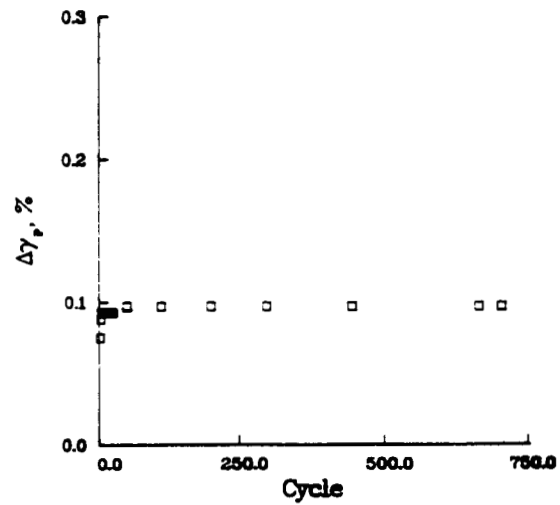
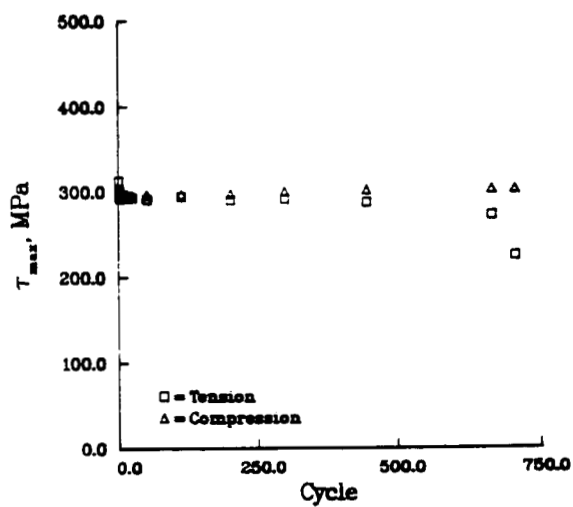


F104-1, <001>, 927°C, 0.5%/min, $\Delta\epsilon_t = 1.0\%$, $M = 0.43$

ORIGINAL PAGE IS
OF POOR QUALITY

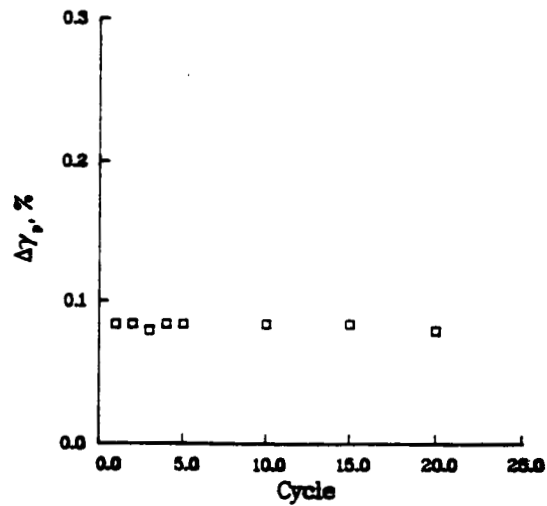
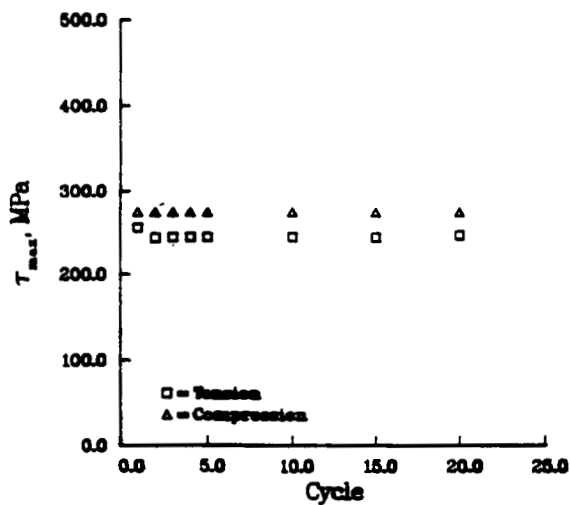
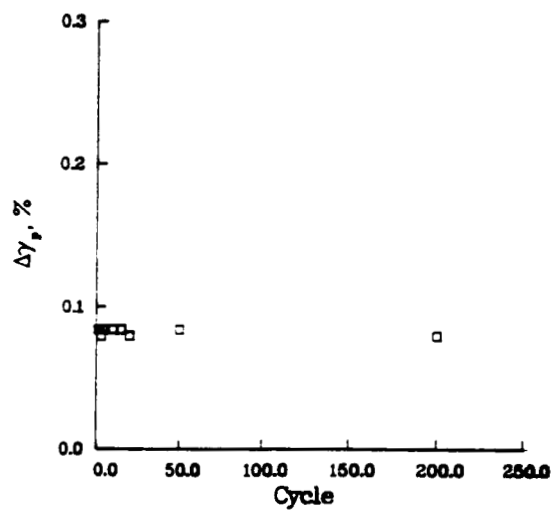
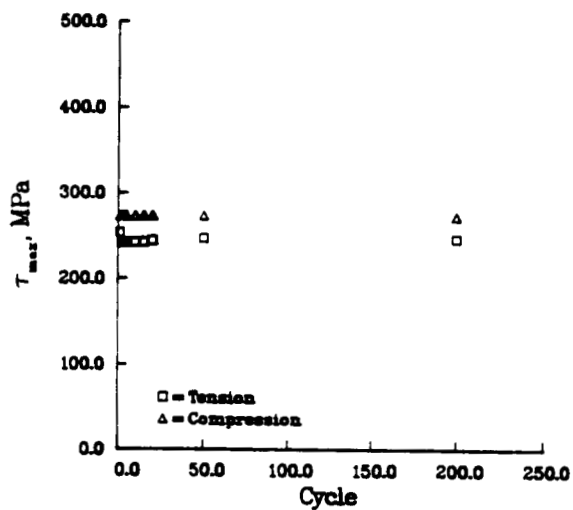


F13, <123>, 927°C, 0.5%/min, $\Delta\epsilon_t = 0.6\%$, $M = 0.44$



F12-2, $\langle 001 \rangle$, 927°C, 50%/min, $\Delta\epsilon_t = 1.9\%$, $M = 0.42$

ORIGINAL PAGE IS
OF POOR QUALITY



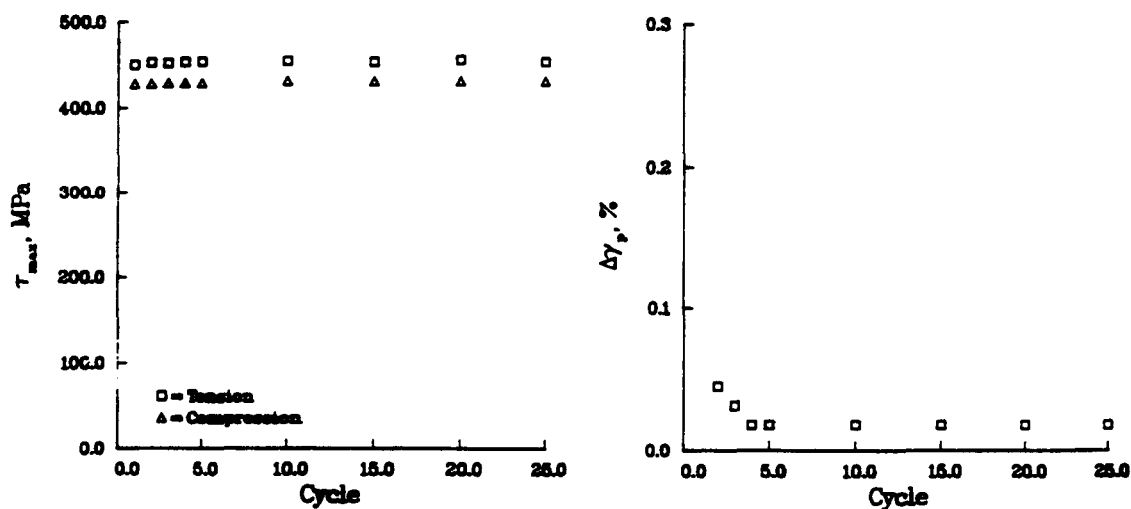
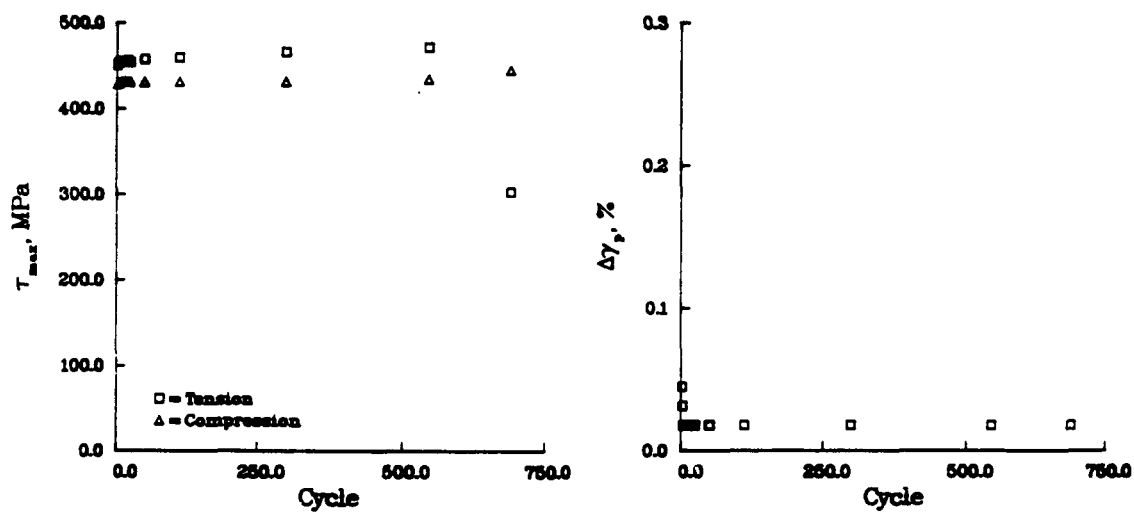
F17, <123>, 927°C, 50%/min, $\Delta\epsilon_t = 1.0\%$, $M = 0.44$

APPENDIX E
ADDITIONAL CYCLIC DEFORMATION DATA

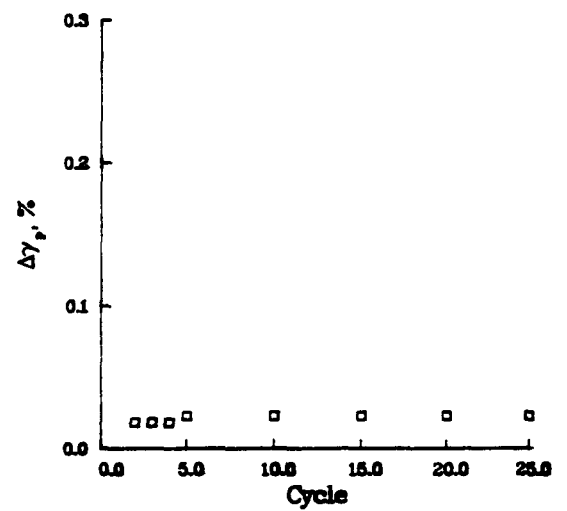
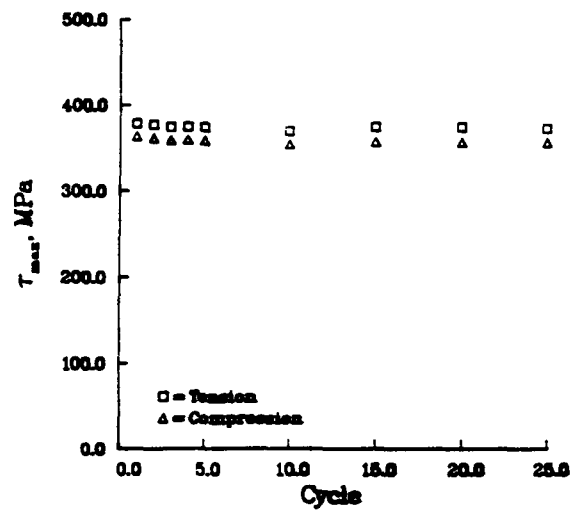
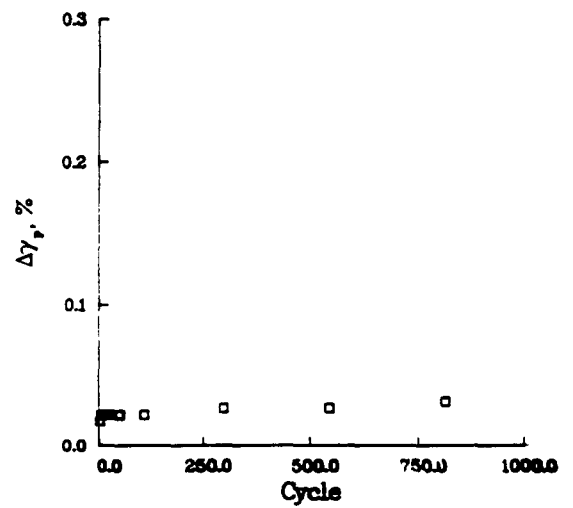
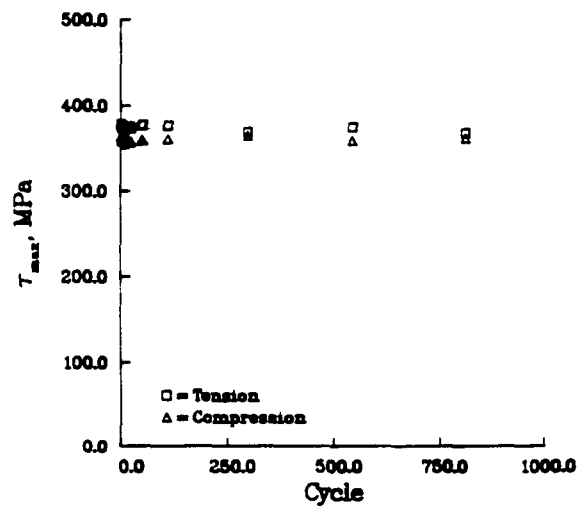
This Appendix contains data from tests which were run either as duplicates at the same conditions as those in Appendix D, or which were run at different $\Delta\gamma_p$ values. Only $\langle 001 \rangle$ crystals are included in this Appendix.

Interrupted tests are not included.

ORIGINAL PAGE IS
OF POOR QUALITY

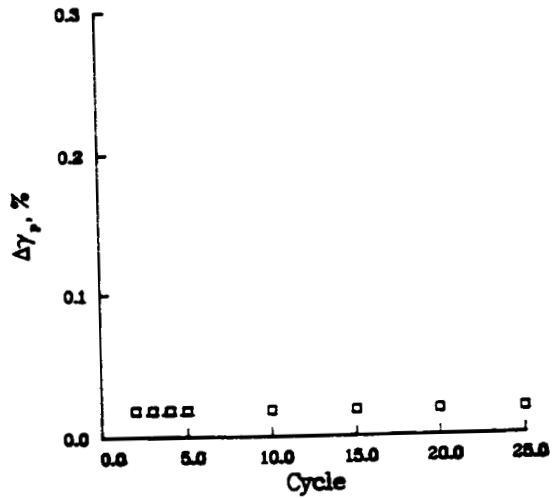
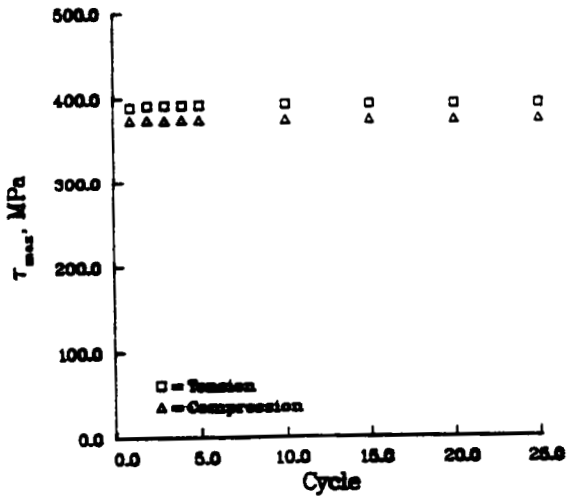
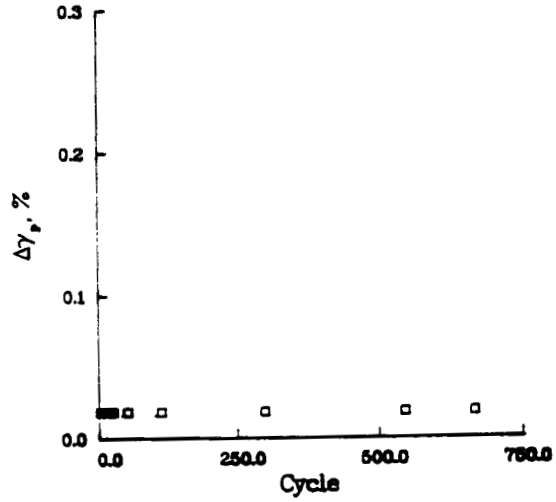
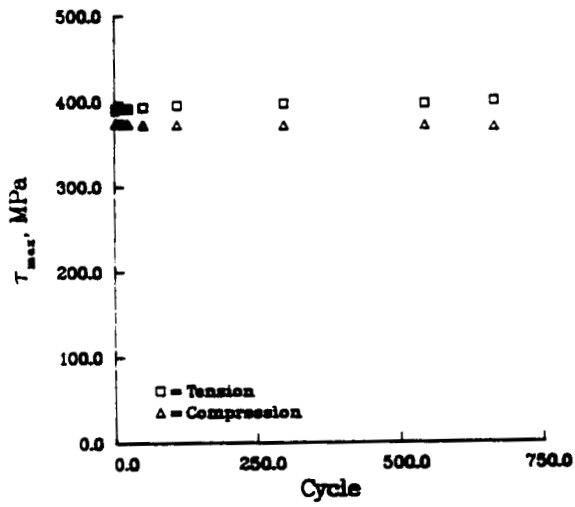


F108-2, <001>, 20°C, 50%/min, $\Delta\epsilon_t = 1.7\%$, $M = .45$.



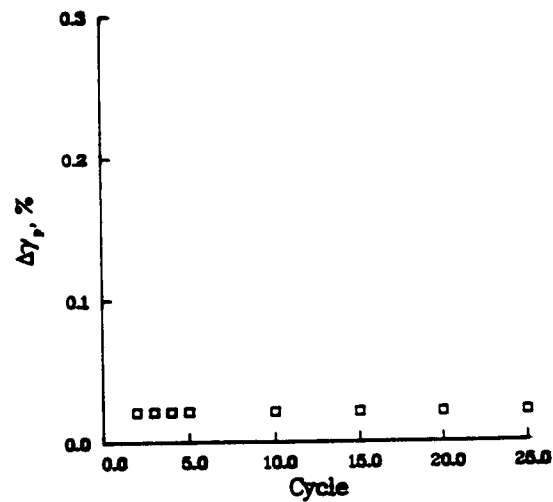
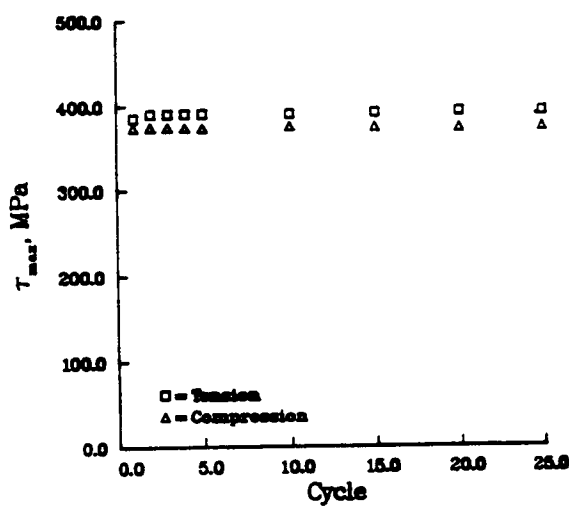
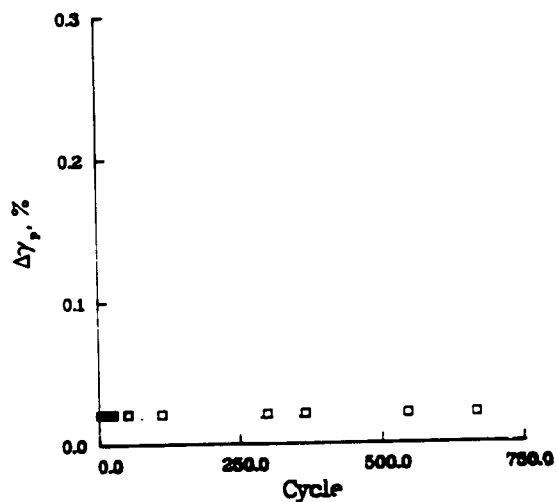
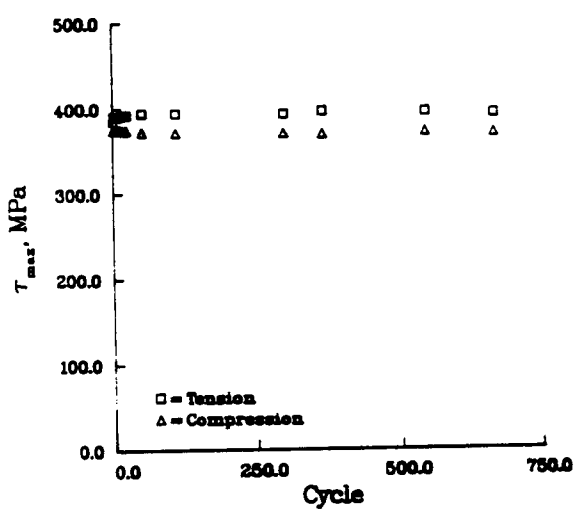
F144-2, <001>, 705°C, 0.5%/min, $\Delta\epsilon_t = 1.8\%$, $M = .46$

ORIGINAL PAGE IS
OF POOR QUALITY

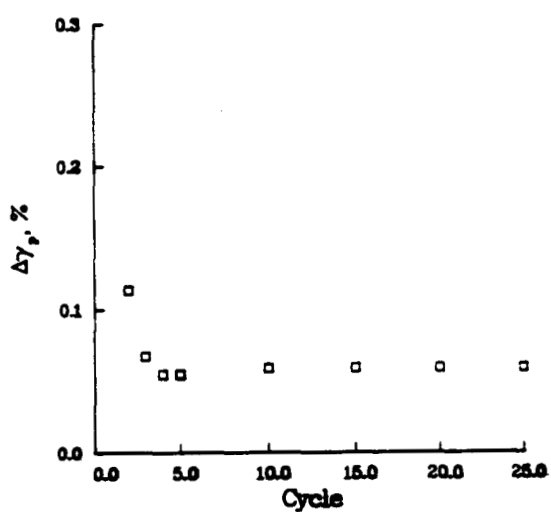
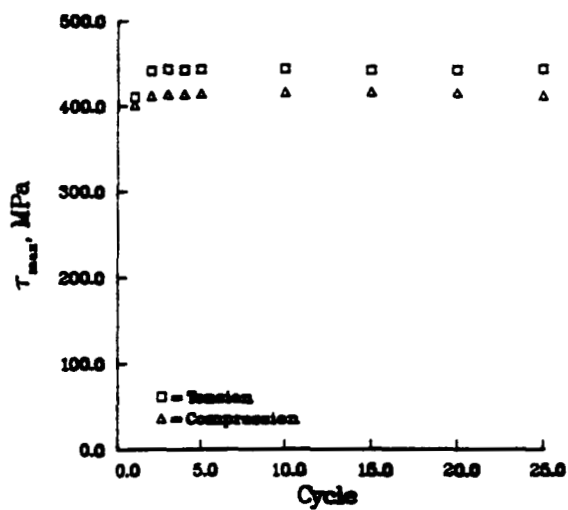
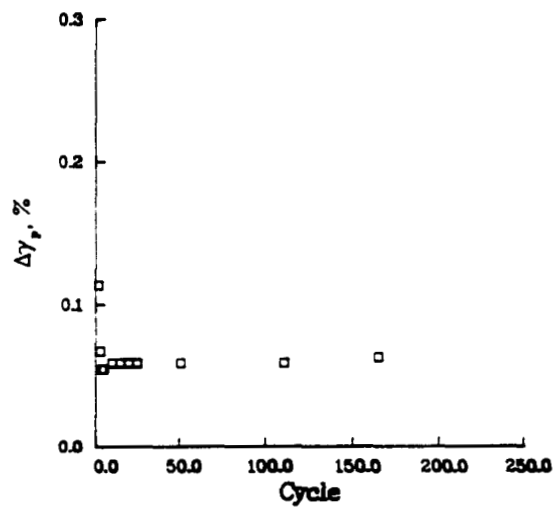
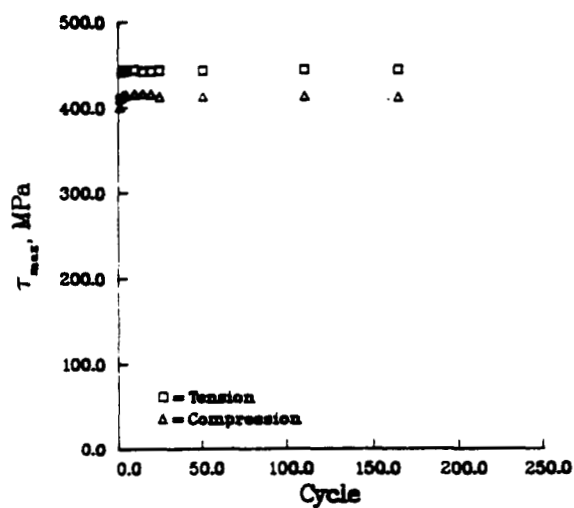


F63-2, <001>, 705°C, 50%/min, $\Delta\epsilon_t = 1.85\%$, $M = .46$

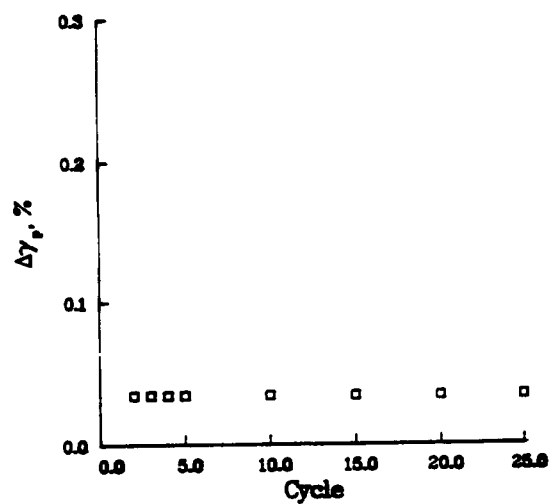
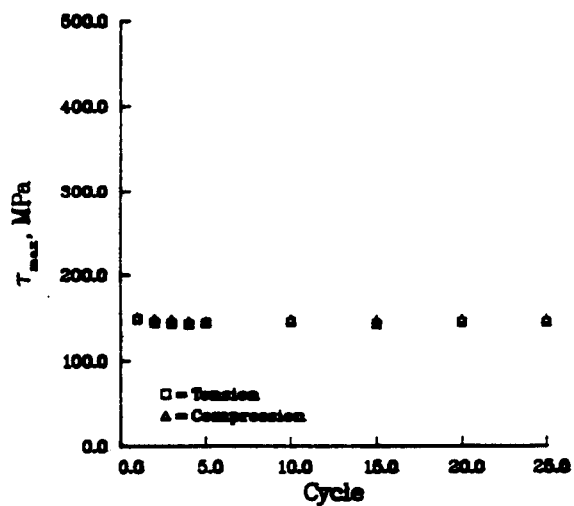
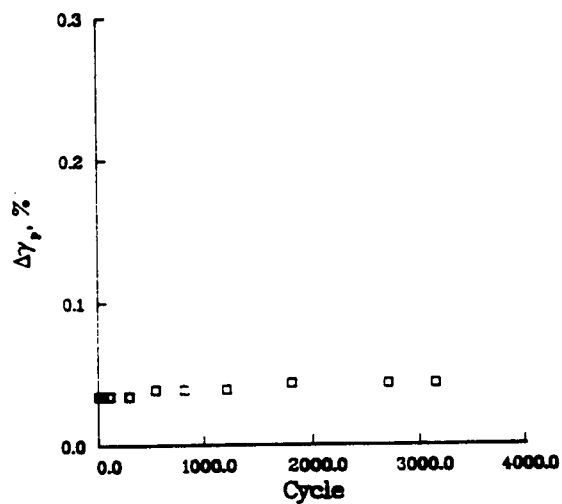
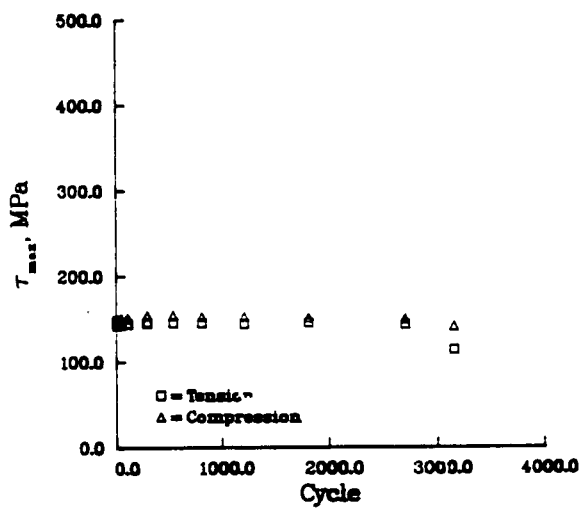
ORIGINAL PAGE IS
OF POOR QUALITY



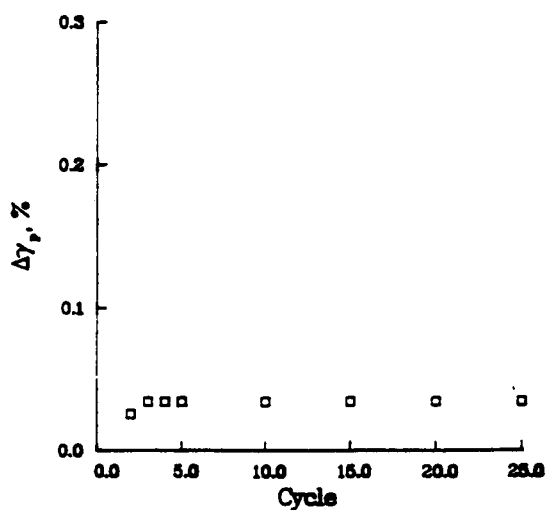
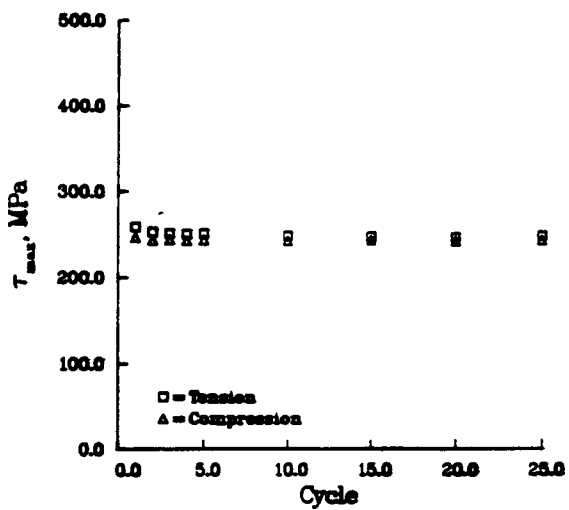
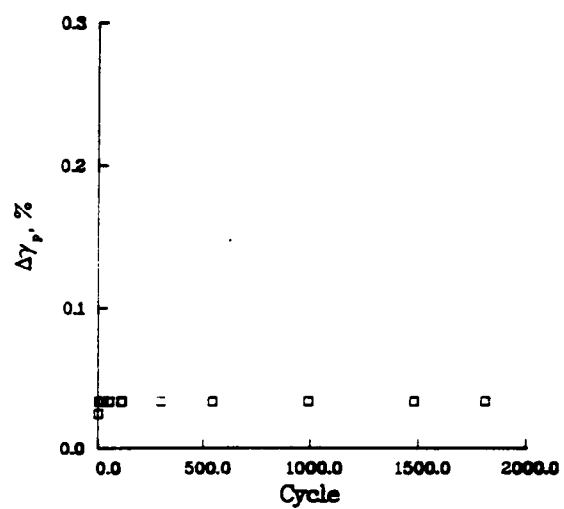
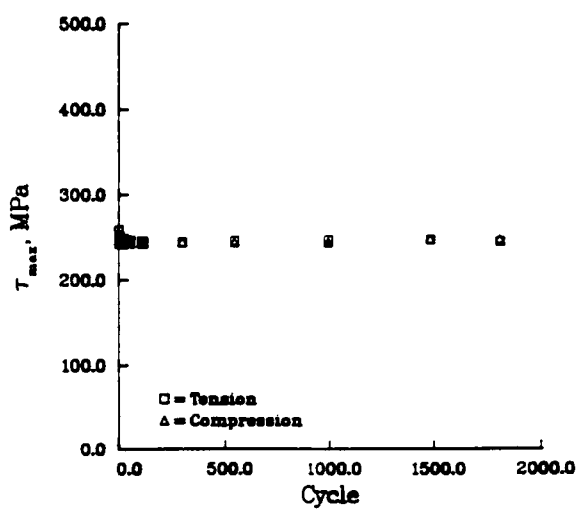
F100-1, <001>, 705°C, 50%/min, $\Delta\epsilon_t = 2.05\%$, $M = .42$



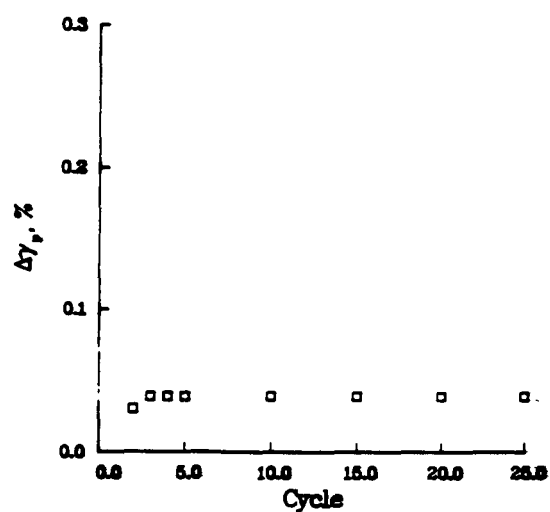
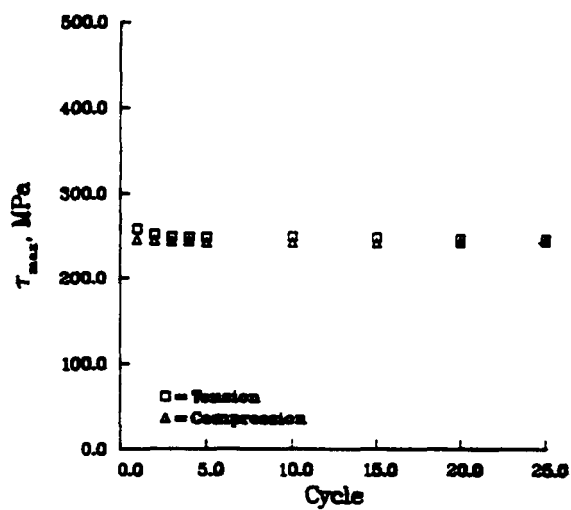
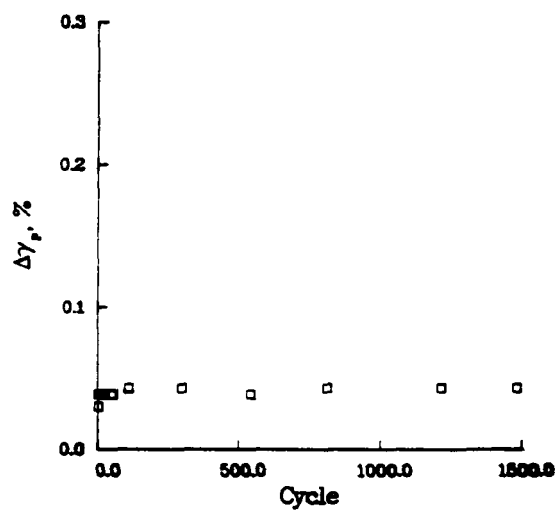
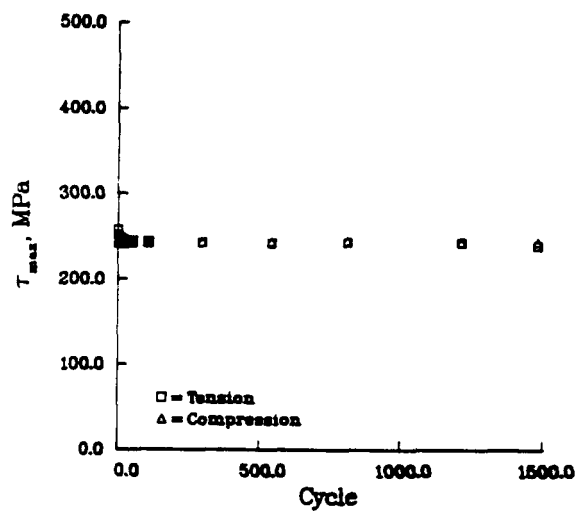
F100-3, <001>, 705°C, 50%/min, $\Delta\epsilon_t = 2.4\%$, $M = .42$



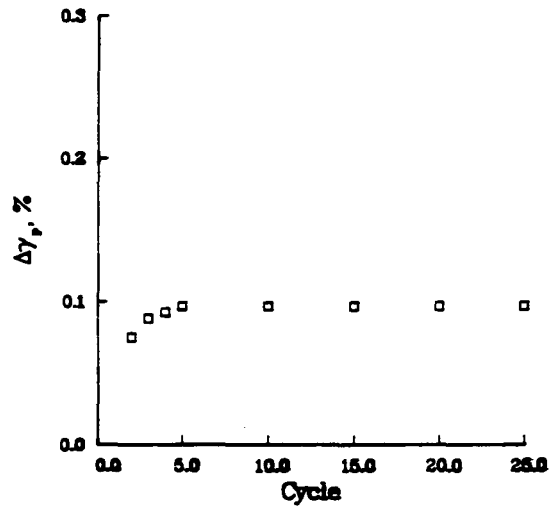
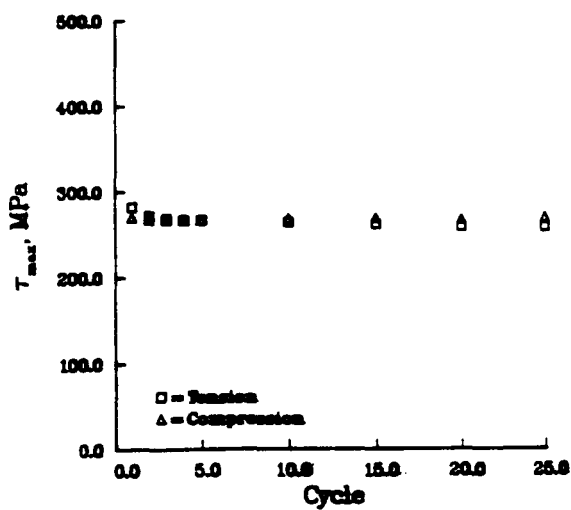
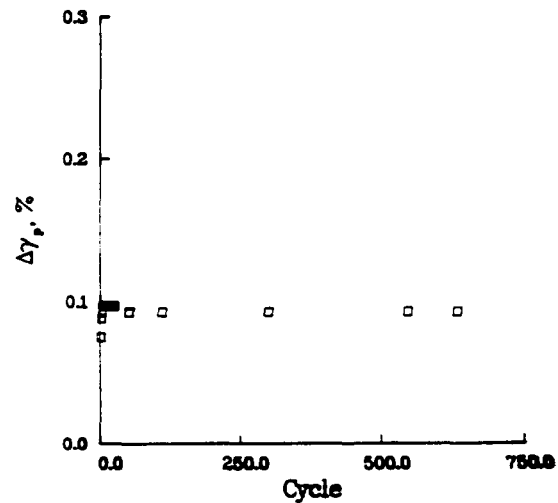
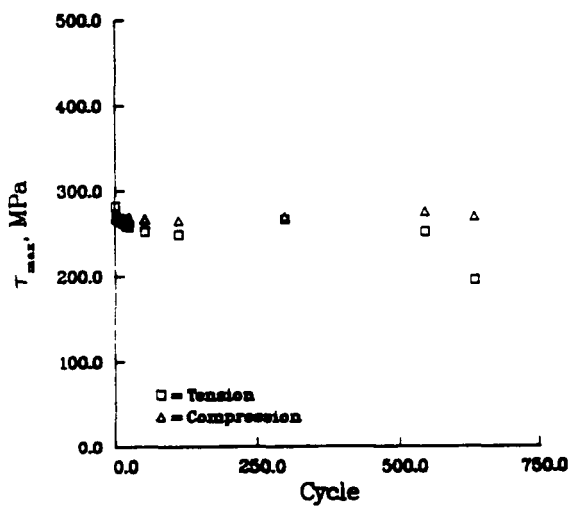
F104-2, <001>, 927°C, 0.5%/min, $\Delta\epsilon_t = 1.0\%$, $M = .43$



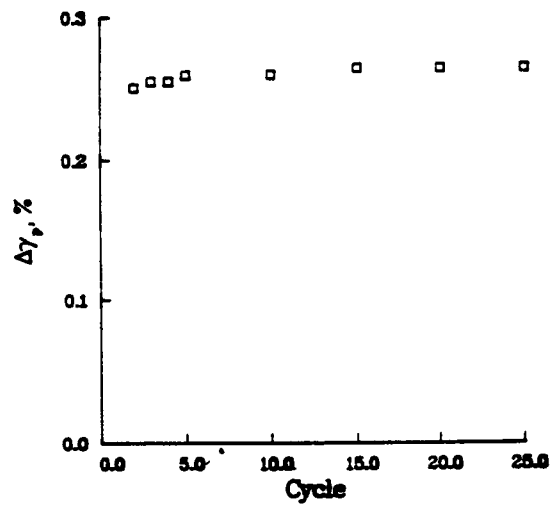
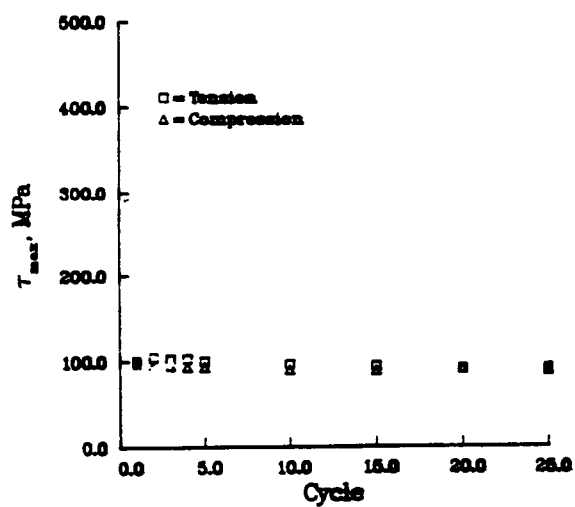
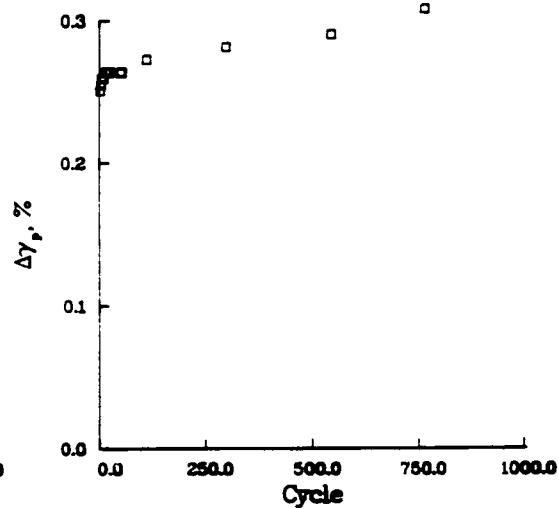
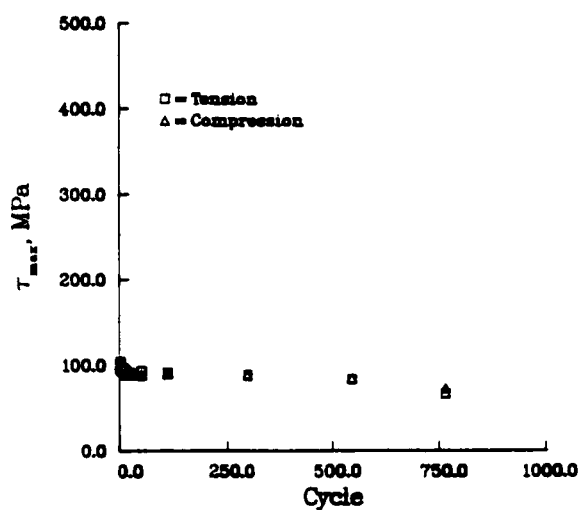
F113-2, <001>, 927°C, 50%/min, $\Delta\epsilon_t = 1.45\%$, $M = .43$



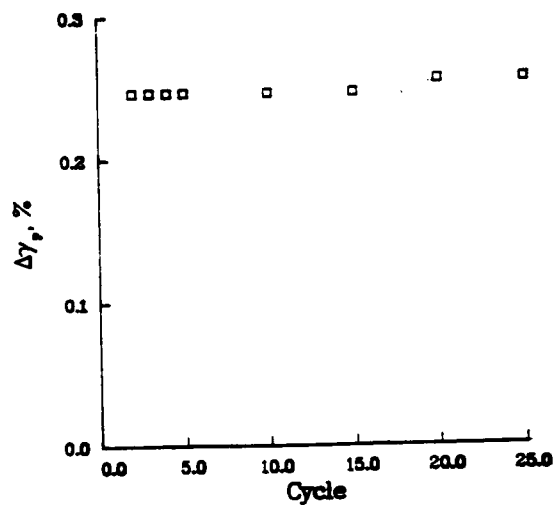
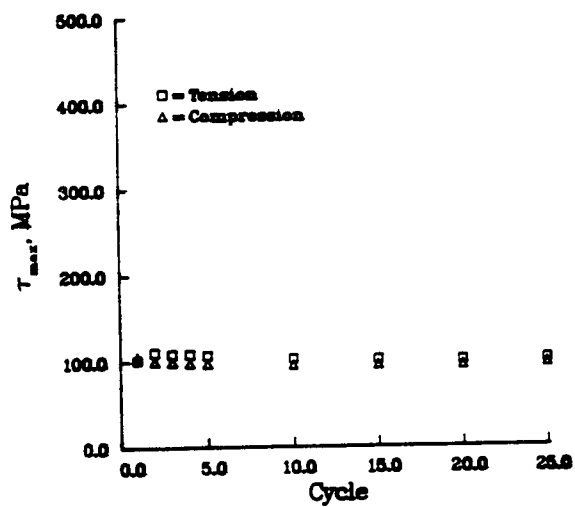
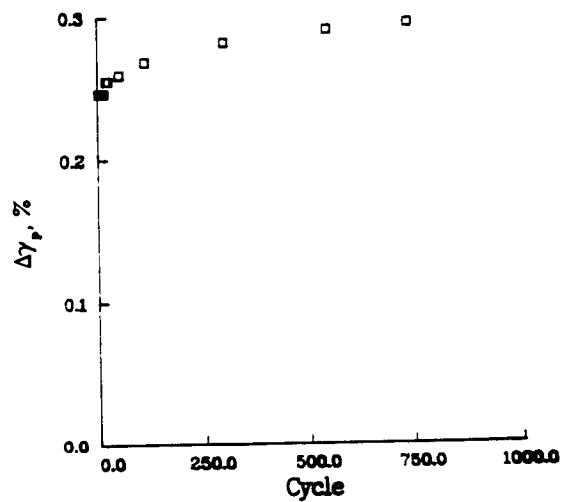
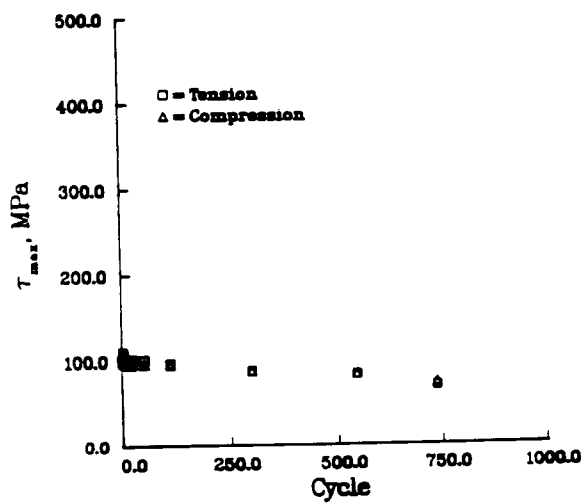
F113-1, <001>, 927°C, 50%/min, $\Delta\epsilon_t = 1.45\%$, $M = .43$



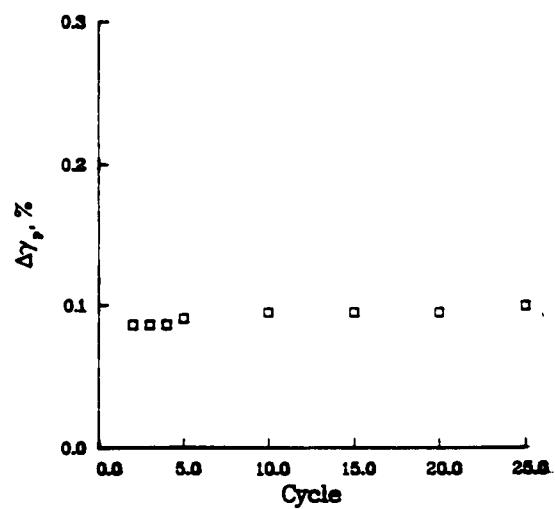
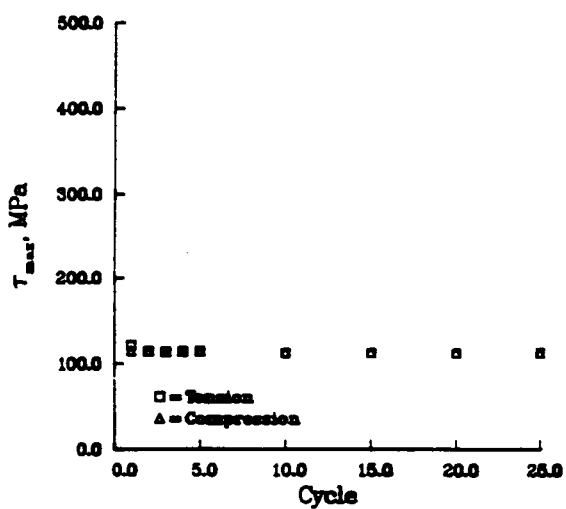
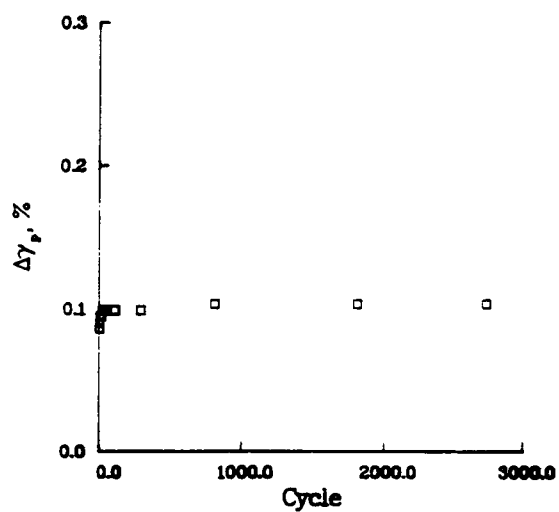
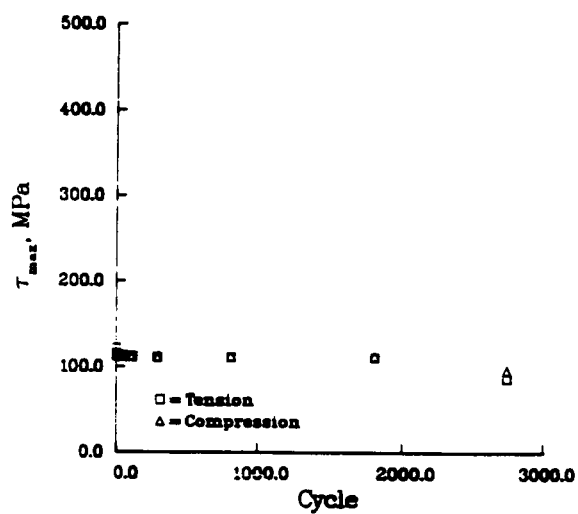
F12-1, $\langle 001 \rangle$, 927°C, 50%/min, $\Delta\epsilon_t = 1.9\%$, $M = .42$



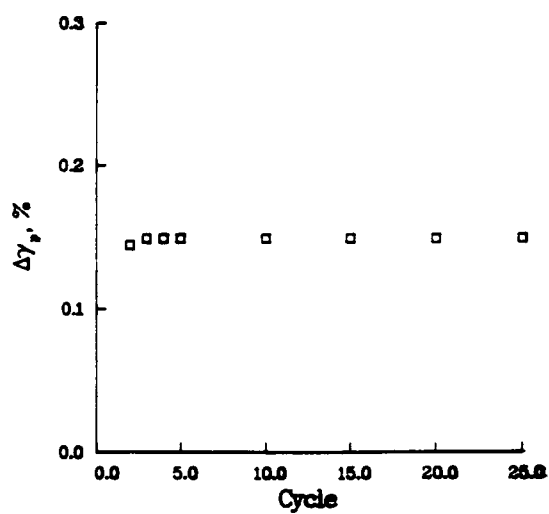
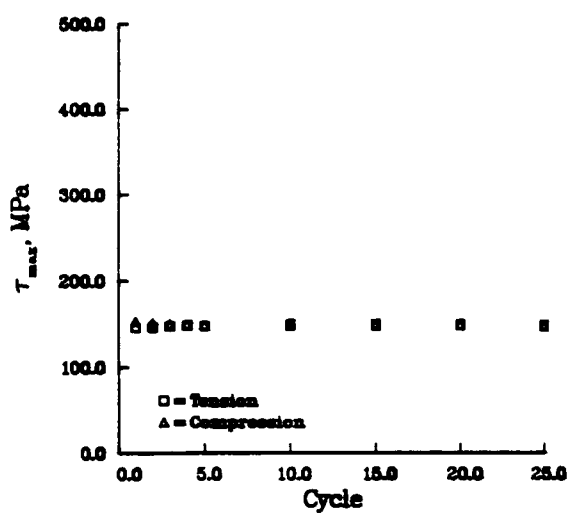
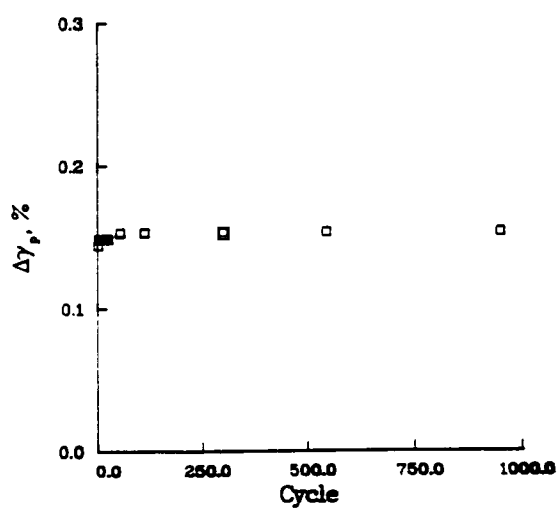
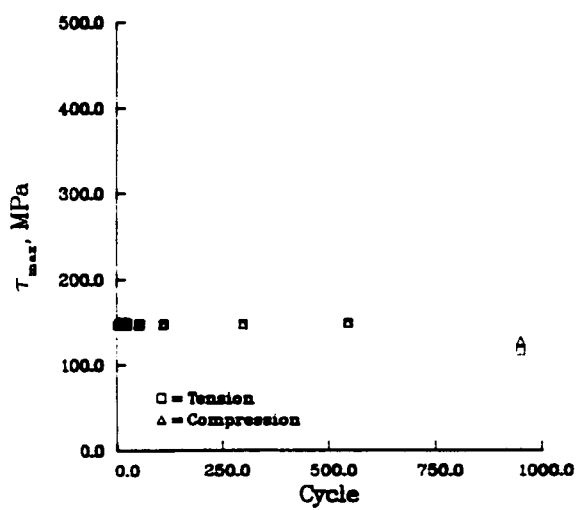
F29-2, <001>, 1093°C, 0.5%/min, $\Delta\epsilon_t = 1.3\%$, $M = .44$



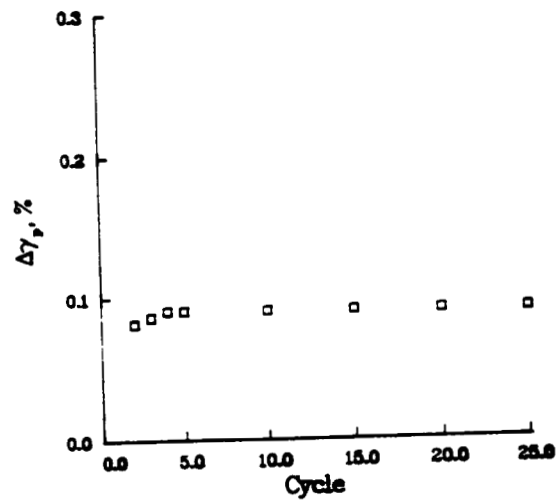
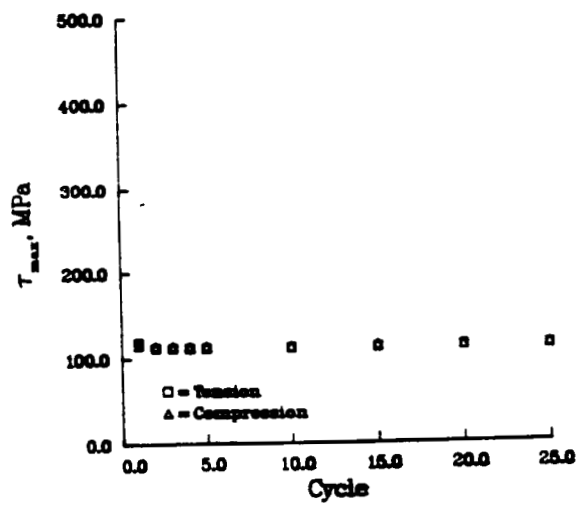
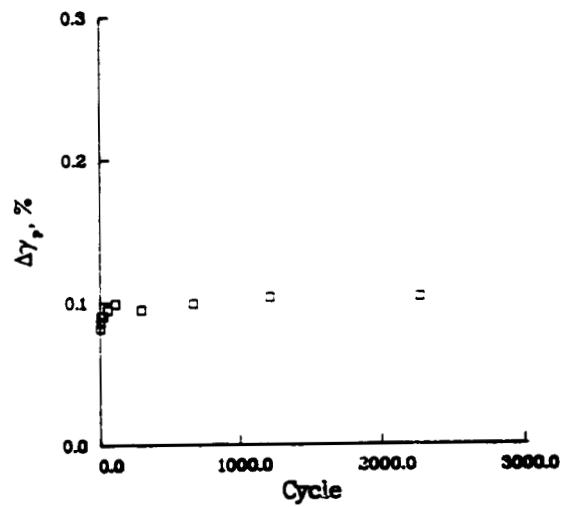
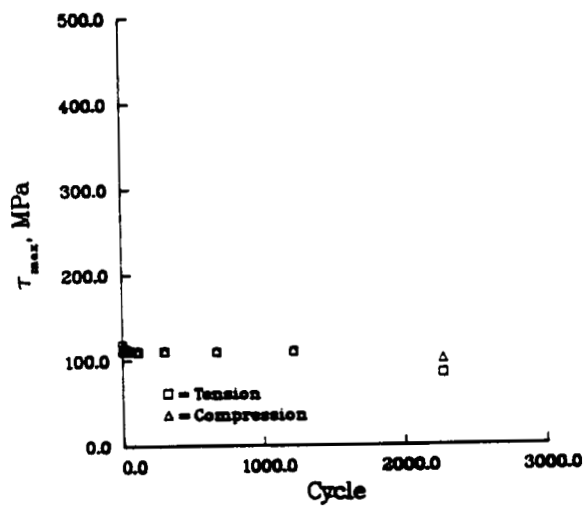
F29-3, <001>, 1093°C, 0.5%/min, $\Delta\epsilon_t = 1.3\%$, $M = .44$



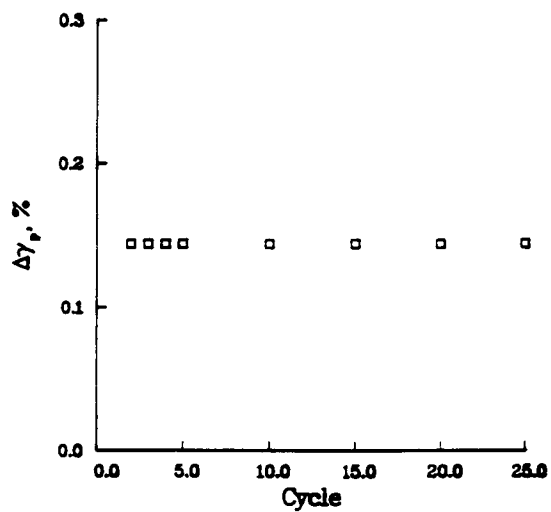
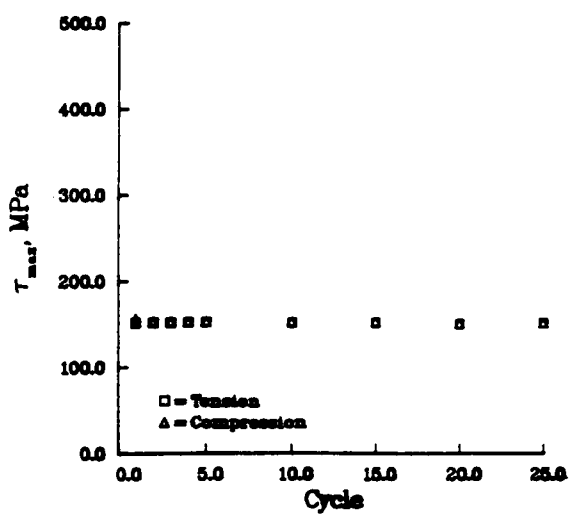
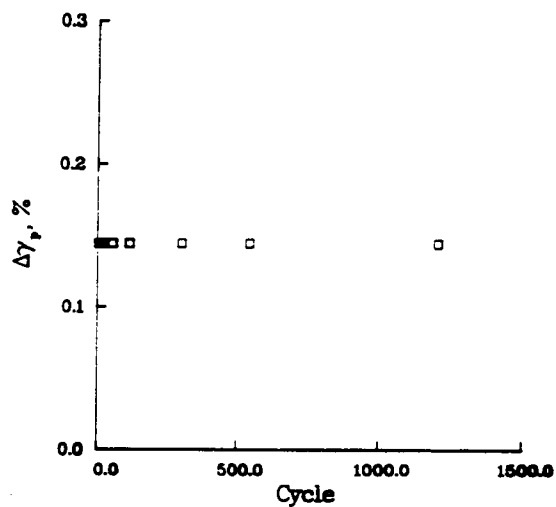
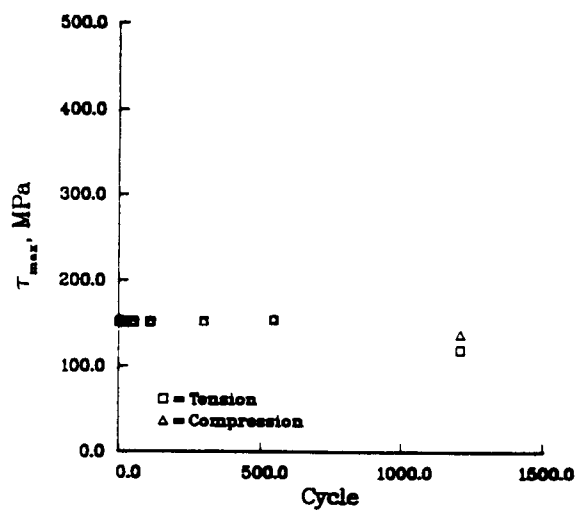
F53-1, <001>, 1093°C, 50%/min, Δε_t = 1.0%, M = .43



F1-1, <001>, 1093°C, 50%/min, $\Delta\epsilon_t = 1.3\%$, $M = .45$



F53-2, <001>, 1093°C, 50%/min, $\Delta\epsilon_t = 1.0\%$, $M = .43$



F1-2, <001>, 1093°C, 50%/min, $\Delta\epsilon_t = 1.3\%$, $M = .45$

REFERENCES

1. R.F. Decker and C.T. Sims: "The Metallurgy of Nickel-Base Alloys", in The Superalloys, C.T. Sims and W.C. Hagel, eds., Wiley, NY, 1972, p 33.
2. R.F. Decker: "Strengthening Mechanisms in Nickel-Base Alloys", International Nickel Co., NY, 1970.
3. B.J. Pearcey, B.H. Kear, and R.W. Smashey: "Correlation of Structure with Properties in a Directionally Solidified Nickel-Base Superalloy", Trans. ASM, 60, 1967, p. 634.
4. W.W. Milligan and S.D. Antolovich: "Yielding and Deformation Behavior of the Single Crystal Superalloy PWA 1480", Met. Trans. A, 18A, 1987, p. 85
5. W.W. Milligan: M.S. Thesis, GA Tech, 1986 and NASA CR-175100, 1986.
6. D. Hull and D.J. Bacon: "Introduction to Dislocations" 3rd Ed., Pergamon, NY, 1984.
7. D.M. Shah and D.N. Duhl: " The Effect of Orientation, Temperature, and γ' Size on the Yield Strength of Single Crystal Nickel-Base Superalloy", in Superalloys 1984, proc., 6th Int'l Symposium on Superalloys, M. Gell et al, eds., AIME, Warrendale, PA, 1984, p. 105.
8. G.A. Swanson et al: "Life Prediction and Constitutive Models for Engine Hot Section Anisotropic Materials Program" , NASA CR-174952, 1986.
9. D.P. DeLuca and B.A. Cowles: "Fatigue and Fracture of Advanced Blade Materials", AFWAL TR-84-4167, 1984.
10. S.M. Copley and B.H. Kear: "A Dynamic Theory of Precipitation Hardening with Application to Nickel Base Superalloys", Trans. TMS-AIME, 239, 1967, p. 984.
11. L.M. Brown and R.K. Ham: "Dislocation - Particle Interactions", in Strengthening Methods in Crystals, A. Kelly and R.B. Nicholson, eds, Wiley, NY, 1971, p. 9.
12. D.P. Pope and S.S. Ezz: "Mechanical Properties of Ni_3Al and Nickel-Base Alloy with High Volume Fractions of γ' ", International Metals Reviews, 29, 1984, p. 136.

13. P.A. Flinn: "Theory of Deformation in Superlattices", Trans. TMS-AIME, 218, 1960, p. 145.
14. S.M. Copley and B.H. Kear: "Temperature and Orientation of the Flow Stress in Off-Stoichiometric Ni_3Al (γ' Phase)", Trans. TMS-AIME, 239, 1967, p. 977.
15. S. Takeuchi and E. Kuramoto: "Temperature and Orientation Dependence of the Yield Stress in Ni_3Ga Single Crystals", Acta Met., 21, 1973, p. 415.
16. C. Lall, S. Chin and D.P. Pope: "The Orientation and Temperature Dependence of the Yield Stress of $\text{Ni}_3(\text{Al},\text{Nb})$ Single Crystals", Met. Trans. A, 10A, 1979, p. 1323.
17. V. Paidar, D.P. Pope and V. Vitek: "A Theory of the Anomalous Yield Behavior in L1_2 Ordered Alloys", Acta Met., 32, 1984, p. 435.
18. P. Veyssi re, J. Douin and P. Beauchamp: "On the Presence of Superlattice Intrinsic Stacking Faults in Plastically Deformed Ni_3Al ", Phil. Mag. A, 51, 1985, p. 469.
19. P. Veyssi re, D.L. Guan, J. Rabier: "Weak-Beam Observation of Dissociated Dislocations in an L1_2 Ordered Alloy Deformed at the Temperature of Strength Anomaly", Phil. Mag. A, 49, 1984, p. 45.
20. P. Veyssi re: "Weak-Beam Study of Dislocations Moving on $\{100\}$ Planes at 800°C in Ni_3Al ", Phil. Mag. A, 50, 1984, p. 189.
21. J.K. Tien, S. Eng, and J.M. Sanchez: "An Overview of the Temperature Dependence of the Strength of the Ni_3Al System", Mat. Res. Soc. Proc., 81, 1987, p. 183.
22. B.H. Kear and B.J. Piarcey: "Tensile and Creep Properties of Single Crystals of the Nickel-Base Superalloy Mar-M 200", Trans. TMS-AIME, 239, 1967, p. 1209.
23. S.M. Copley, B.H. Kear and G.M. Rowe: "The Temperature and Orientation Dependence of Yielding in Mar-M 200 Single Crystals", Mater. Sci. Eng., 10, 1972, p. 87.
24. A.F. Giamei: "Deformation and Fracture of Advanced Anisotropic Superalloys", AFOSR FR-12637, 1979.

25. R.V. Miner, R.C. Voigt, J. Gayda and T.P. Gabb: "Orientation and Temperature Dependence of Some Mechanical Properties of the Single Crystal Nickel-Base Superalloy Rene N4: Part I. Tensile Behavior", Met. Trans. A, 17A, 1986, p. 491.
26. T.P. Gabb, J. Gayda, and R.V. Miner: "Orientation and Temperature Dependence of Some Mechanical Properties of the Single Crystal Nickel-Base Superalloy Rene N4: Part II. Low Cycle Fatigue", Met Trans. A, 17A, 1986, p. 497.
27. R.V. Miner, T.P. Gabb, J. Gayda, and K.J. Hemker: "Orientation and Temperature Dependence of Some Mechanical Properties of the Single Crystal Nickel-Base Superalloy Rene N4: Part III. Tension-Compression Anisotropy", Met. Trans. A, 17A, 1986, p. 507.
28. T.P. Gabb and G.E. Welsch: "The Cyclic Stress-Strain Behavior of a Nickel-Base Superalloy at 650°C", Scripta Met., 20, 1986, p. 1049
29. F.E. Heredia and D.P. Pope: "The Tension - Compression Flow Anisotropy in a High Volume Fraction Nickel-Base Alloy", Acta Met., 34, 1986, p. 279.
30. G.R. Leverant, B.H. Kear and J.M. Oblak: "Creep of Precipitation Hardened Nickel-Base Alloy Single Crystals at High Temperatures", Met. Trans., 4, 1973, p. 355.
31. G.R. Leverant and B.H. Kear: "The Mechanism of Creep in Gamma Prime Precipitation Hardened Nickel-Base Alloys at Intermediate Temperature", Met. Trans., 1, 1970, p. 491.
32. R.A. MacKay and R.D. Maier: "The Influence of Orientation on the Stress Rupture Properties of Nickel-Base Superalloy Single Crystals", Met. Trans. A, 13A, 1982. p. 1747.
33. J.K. Tien and S.M. Copley: "The Effects of Uniaxial Stress in the Periodic Morphology of Coherent Gamma Prime Precipitates Nickel-Base Superalloy Crystals", Met. Trans., 2, 1971, p. 215.
34. D.D. Pearson, F.D. Lemkey and B.H. Kear: "Stress Coarsening of γ' and Its Influence on Creep Properties of a Single Crystal Superalloy", in Superalloys 1980, Proc. 6th Int'l Symposium on Superalloys, J. Tien et. al., eds., ASM, Metals Park, O., 1980, p. 513.

35. R.A. MacKay and L.J. Ebert: "The Development of Directional Coarsening of the γ' Precipitate in Superalloy Single Crystals", Scripta Met., 17, 1983, p. 1217.
36. M.V. Nathal and L.J. Ebert: "Elevated Temperature Creep-Rupture Behavior of the Single Crystal Superalloy NASAIR 100", Met. Trans. A, 16A, 1985, p. 427.
37. D.L. Anton: "Low Cycle Fatigue Characteristics of $\langle 001 \rangle$ and Randomly Aligned Superalloy Single Crystals", Acta Met., 32, 1984, p. 1669.
38. P.K. Wright and A.F. Anderson: "The Influence of Orientation on the Fatigue of Directionally Solidified Superalloys", in Superalloys 1980, Tien et al, eds, ASM, Metals Park, Ohio, 1980, p. 689.
39. W.W. Milligan, N. Jayaraman and R. C. Bill: "Low Cycle Fatigue of Mar-M 200 Single Crystals with a Bimodal γ' Distribution at 760 and 870°C", Mater. Sci. Eng., 82, 1986, p. 127.
40. I.S. Sokolnikoff: Mathematical Theory of Elasticity, Krieger, Malabar, FL, 1986.
41. U.F. Kocks: "Constitutive Relations for Slip", in Constitutive Equations in Plasticity, A. Argon, ed, MIT Press, Cambridge, Mass., 1975, p. 81.
42. J.J. Gilman: "A Unified View of Flow Mechanisms in Materials", in The Physics of Strength and Plasticity, A. Argon. ed, MIT Press, Cambridge, Mass., 1969, p. 3.
43. U.F. Kocks, A.S. Argon and M.F. Ashby: "The Thermodynamics and Kinetics of Slip", in Progress in Materials Science, 19, B. Chalmers et al., eds, Pergamon, NY, 1975.
44. J. Weertman: "Stress Dependence of the Velocity of a Dislocation Moving in a Viscously Damped Slip Plane", in The Physics of Strength and Plasticity, A. Argon, ed, MIT Press, Cambridge, Mass., 1969, p. 75.
45. J.J. Gilman: "Dislocation Mobility in Crystals", J. Appl. Phys., 36, 1965, p. 3195.
46. T. Suzuki and T. Ishi: "Dynamic Yielding of Metals and Alloys" in The Physics of Strength and Plasticity, A. Argon, ed, MIT Press, Cambridge, Mass., 1969, p. 159.

47. D. Kuhlmann-Wilsdorf: "Theory of Work Hardening 1934-1984", Met. Trans. A, 16A, 1985, p. 2091.
48. F. Garafolo: Fundamentals of Creep and Creep-Rupture in Metals, McMillan, NY, 1965.
49. A.K. Mukherjee, J.E. Bird and J.E. Dorn: "Experimental Correlations for High Temperature Creep", Trans. ASM, 62, 1969, p. 155.
50. J. Weertman: "Dislocation Climb Theory of Steady-State Creep", Trans. ASM, 61, 1968, p. 681.
51. W.D. Nix and B. Ilchner: "Mechanisms Controlling Creep of Single Phase Metals and Alloys", in Proc. 5th Intl. Conference on the Strength of Metals and Alloys, Aachen, FRG, Haasen et al, eds, Pergamon, NY, 1979, p. 1503.
52. A.A. Solomon and W.D. Nix: "Interpretation of High Temperature Plastic Deformation in Terms of Measured Effective Stresses", Acta Met., 18, 1970, p. 863
53. C.N. Ahlquist and W.D. Nix: "The Measurement of Internal Stress During Creep of Al and Al-Mg Alloys", Acta Met., 19, 1971, p. 373.
54. M. McClean: "Friction Stress and Recovery During High Temperature Creep: Interpretation of Creep Transients Following a Stress Reduction", Proc. Roy. Soc. A, 371, 1980, p. 279.
55. J.H. Hausselt and W.D. Nix: "A Model for High Temperature Deformation of Dispersion Strengthened Metals Based on Substructural Observations in Ni-20Cr-2ThO₂", Acta Met., 25, 1977, p. 1491.
56. P.J. Henderson and M. McClean: "Microstructural Contributions to Friction Stress and Recovery Kinetics During Creep of the Nickel-Base Superalloy In713LC", Acta Met., 31, 1983, p. 1203.
57. W.J. Evans and G.F. Harrison: "The Development of a Universal Equation for Secondary Creep Rates in Pure Metals and Engineering Alloys", Met. Sci., 1976, p. 307.
58. R.A. Stevens and P.E. Flewitt: "The Dependence of Creep Rate on Microstructure in a γ' Strengthened Superalloy", Acta Met., 29, 1981, p. 867.
59. G.S. Ansell and J. Weertman: "Creep of a Dispersion Hardened Aluminum Alloy", Trans. TMS-AIME, 215, 1959, p. 838.

60. J.D. Eshelby: "Elastic Inclusions and Inhomogeneities", in Progress in Solid Mechanics, I. Snedden and R. Hill, eds, Interscience, NY, 1961.
61. L.M. Brown: "Back Stresses, Image Stresses and Work Hardening", Acta Met., 21, 1973, p. 879.
62. S. Purushothaman and J.K. Tien: "Role of Back Stress in the Creep Behavior of Particle Strengthened Alloys", Acta Met., 26, 1978, p. 519.
63. T.E. Howson, J.E. Stulga and J.K. Tien: "Creep and Stress Rupture of Oxide-Dispersion Strengthened Mechanically Alloyed Inconel Alloy MA754", Met. Trans. A, 11A, 1980, p. 1599.
64. T.E. Howson, D.A. Mervyn and J.K. Tien: "Creep and Stress Rupture of a Mechanically Alloyed Oxide Dispersion and Precipitation Strengthened Nickel-Base Superalloys", Met. Trans. A, 11A, 1980, p. 1609.
65. O. Ajaja, T.E. Howson, S. Purushothaman and J.K. Tien: "The Role of Alloy Matrix in the Creep Behavior of Particle Strengthened Alloys", Mater. Sci. Eng., 44, 1980, p. 165.
66. J.R. Rice: "Continuum Mechanics and Thermodynamics of Plasticity in Relation to Microscale Deformation Mechanisms", in Constitutive Equations in Plasticity, A. Argon, ed, MIT Press, Cambridge, Mass., 1975, p. 23.
67. E.W. Billington and J. Tate: Physics of Deformation and Flow, McGraw Hill, NY, 1980.
68. A.E. Green and R.S. Rivlin: "The Mechanics of Non-Linear Materials with Memory", Arch. Rat. Mech. Anal., 1, 1957, p.1.
69. R. Hill: Mathematical Theory of Plasticity, University Press, Oxford, 1950.
70. L.M. Kachanov: Fundamentals of the Theory of Plasticity, MIR, Moscow, 1974.
71. E.W. Hart: "A Phenomological Theory for Plastic Deformation of Polycrystalline Metals", Acta Met., 18, 1970, p. 599.
72. E.W. Hart et al: "Phenomological Theory: A Guide to Constitutive Relations and Fundamental Deformation Properties", in Constitutive Equations in Plasticity, A. Argon, ed, MIT, Cambridge, Mass., 1975, p. 149.

73. K.P. Walker: "Research and Development Program for Non-Linear Structural Modeling with Advanced Time-Temperature Dependent Constitutive Relationships", NASA CR-165533, 1981.
74. V.G. Ramaswamy, R.H. VanStone, L.T. Dame and J.H. Laflen: "Constitutive Modeling for Isotropic Materials" NASA, CR-175004, 1985.
75. R. Thompson, ed: "Non-Linear Constitutive Relations for High Temperature Applications - 1984" NASA, CP-2369, 1984.
76. R. Thompson, ed: "Non-Linear Constitutive Relations for High Temperature Applications - 1986" NASA, CP-10010, 1986.
77. S.R. Bodner, I. Partom, Y. Partom: "Uniaxial Cyclic Loading of Elastic-Viscoplastic Materials", J. Appl. Mech, 46, 1979, p. 805.
78. D.C. Stouffer and S.R. Bodner: "A Constitutive Model for the Deformation Induced Anisotropic Plastic Flow of Metals", Int'l. J. Eng. Sci., 17, 1979, p. 757.
79. G.A. Swanson et al: "Life Prediction and Constitutive Models for Engine Hot Section Anisotropic Materials Program", NASA CR-179594, 1987.
80. K.P. Walker and E.H. Jordan: "Biaxial Constitutive Modeling and Testing of a Single Crystal Superalloy at Elevated Temperature", Int'l. J. of Fatigue of Eng. Materials and Structures, in press.
81. L.T. Dame: Ph.D. Thesis, University of Cincinnati, 1985.
82. J. Bishop: "A Theoretical Examination of the Plastic Deformation of Crystals by Glide", Phil. Mag., 43, 1952, p. 51.
83. M. Dollar and I. M. Bernstein: "The Effect of Temperature on the Deformation Structure of Single Crystal Nickel-Base Superalloy", in Superalloys 1988, Proc 6th, Int'l Symposium on Superalloys, D. Duhal et al, eds, AIME, Warrendale, PA, 1988, p. 275.
84. U.F. Kocks: "The Kinetics of Solution Hardening", Met. Trans. A, 16A, 1984, p. 2109.
85. A.J. Ardell: "Precipitation Hardening", Met. Trans. A, 16A, 1984, p. 2131.

86. M. Yamaguchi, V. Paidar, D.P. Pope and V. Vitek: "Dissociation and Core Structures of $\langle 110 \rangle$ Screw Dislocations in $L1_2$ Ordered Alloys: I. Core Structure in an Unstressed Crystal", Phil. Mag., 45, 1982, p. 867.
87. V. Paidar, M. Yamaguchi, D.P. Pope, and V. Vitek: "Dissociation and Core Structures of $\langle 110 \rangle$ Screw Dislocations in $L1_2$ Ordered Alloys: II. Effects of an Applied Shear Stress", Phil. Mag., 45, 1982, p. 883.
88. P. Hirsch et al: Electron Microscopy of Thin Crystals, 2nd Ed, Krieger, Malabar, FL, 1977.
89. A.F. Giamei, J.M. Oblak, B.H. Kear, and W.H. Rand: "The Formation of Crystallographically Aligned $a/3\langle 112 \rangle$ Dislocations in Ni_3Al ", Proc 29th Meeting EMSA, 1971, p. 112.
90. I. Baker and E.M. Schulson: "On Intrinsic Stacking Faults in Polycrystalline Ni_3Al ", Phys. Stat. Sol. A, 85, 1984, p. 481.
91. S. Takeuchi, E. Kuramoto, T. Yamamoto and T. Taoko: "The Nature of Stacking Faults and Partial Dislocations in Deformed Ni_3Ga Single Crystals", Jap. J. Appl. Phys., 12, 1973, p. 1486.
92. H-R. Pak, T. Saburi and S. Nenno: "The Formation Mechanism of Superlattice Intrinsic Stacking Faults in Ni_3Ga ", Scripta Met., 10, 1976, p. 1081.
93. D.M. Wee, D.P. Pope and V. Vitek: "Plastic Flow of Pt_3Al Single Crystal", Acta Met., 32, 1984, p. 829.
94. C.M. Howe, M. Rainville and E.M. Schulson: "Transmission Electron Microscopy Investigations of Ordered Zr_3Al ", J. Nucl. Matl., 50, 1974, p. 139.
95. P. Holdway and A.E. Staton-Bevan: "Dislocation Structures in Zr_3Al Based Alloys", J. Mat. Sci., 21, 1986, p. 2843.
96. K. Suzuki, M. Ichihara and S. Takeuchi: "Dissociated Structure of Superlattice Dislocations in Ni_3Ga with the $L1_2$ Structure", Acta Met., 27, 1979, p. 193.
97. M.H. Yoo: "Stability of Superdislocations and Shear Faults in $L1_2$ Ordered Alloys", Acta Met., 35, 1987, p. 1559.
98. G. Vanderschaave: "Determination of Fault Energies in $L1_2$ Alloys", Phil. Mag. A, 56, 1987, p. 689.

99. J. Douin, P. Veyssi re and P. Beauchamp: "Dislocation Line Stability in Ni_3Al ", Phil. Mag. A, 54, 1986, p. 375.
100. V. Vitek: "Interatomic Forces in Relation to the Theory of Dislocations", Phil. Mag. A, 58, 1988, p. 193.
101. L. Remy, B. Thomas and A. Pineau: "Temperature Dependence of Stacking Fault Energy in Close-Packed Metals and Alloys", Mater. Sci. Eng., 36, 1978, p. 47.
102. P.C.J. Gallagher: "The Influence of Alloying, Temperature and Related Effects on the Stacking Fault Energy", Met. Trans., 1, 1970, p. 2429.
103. J.M. Sanchez, S. Eng, Y.P. Wu and J.K. Tien: "Modeling of Antiphase Boundaries in L1_2 Structures", Mat. Res. Soc. Symposium Proc., 81, 1987, p. 57.
104. N.R. Bonda, D.P. Pope and C. Laird: "Cyclic Deformation of $\text{Ni}_3(\text{Al},\text{Nb})$ Single Crystal at Ambient and Elevated Temperatures", Acta Met., 35, 1987, p. 2371.
105. S. Ezz and D.P. Pope: "The Asymmetry of Cyclic Hardening in $\text{Ni}_3(\text{Al},\text{Nb})$ Single Crystals", Scripta Met., 19, 1985, p. 741.
106. Y. Umakoshi, D.P. Pope and V. Vitek: "The Asymmetry of the Flow Stress in $\text{Ni}_3(\text{Al},\text{Ta})$ Single Crystals", Acta Met., 32, 1984, p. 449.
107. P. Veyssi re, J.A. Horton, M.H. Yoo and C.T. Liu: "APB Dragging in Ni_3Al Deformed at Intermediate Temperatures", Phil. Mag. Letters, 57, 1988, p. 17.
108. M.H. Yoo: "On the Theory of Anomalous Yield Behavior of Ni_3Al - Effects of Elastic Anisotropy", Script Met., 20, 1986, p. 915.
109. P. Caron, Y. Ohta, Y.G. Nakagawa, and T. Khan: "Creep Deformation Anisotropy in Single Crystal Superalloys", in Superalloys 1988, Proc 6th, Int'l Symposium on Superalloys, D. Duhl et al, eds, AIME, Warrendale, PA, 1988, p. 215.
110. J.W. Hutchinson: "Elastic-Plastic Behavior of Polycrystalline Metals and Composites", Proc. Roy. Soc. A, 319, 1970, p. 247.
111. R.J. Asaro: "Crystal Plasticity", J. Appl. Mech., 50, 1983, p. 921.

112. U.F. Kocks: "The Relation Between Polycrystal Deformation and Single Crystal Deformation", Met. Trans., 1, 1970, p. 1121.
113. M.Y. Sheh and D.C. Stouffer: "Anisotropic Constitutive Modeling for Nickel-Base Single Crystal Superalloys Using a Crystallographic Approach", Submitted to J. Appl. Mech.. Also M.Y. Sheh: Ph.D. Dissertation, University of Cincinnati, 1988.
114. G. Cailletaud, D. Nouailhas, and P. Poubanne: "Modeling of Viscoplastic Anisotropic Behavior of Single Crystals", Proceedings of the MECAMAT Conference at Besancon, France, G. Cailletaud et. al, eds., 1988, p. 257.
115. E.H. Jordan: "A Review of Single Crystal Plastic and Viscoplastic Behavior", Proceedings of the MECAMAT Conference at Besancon, France, G. Cailletaud et al, eds, 1988, p. 239.

Report Documentation Page

1. Report No. NASA CR-4215		2. Government Accession No.		3. Recipient's Catalog No.	
4. Title and Subtitle Deformation Modeling and Constitutive Modeling for Anisotropic Superalloys				5. Report Date February 1989	
				6. Performing Organization Code	
7. Author(s) Walter W. Milligan and Stephen D. Antolovich				8. Performing Organization Report No. None (E-4543)	
				10. Work Unit No. 505-63-1B	
9. Performing Organization Name and Address Georgia Institute of Technology School of Materials Engineering Atlanta, Georgia 30332-0245				11. Contract or Grant No. NAG3-503	
				13. Type of Report and Period Covered Contractor Report Final	
12. Sponsoring Agency Name and Address National Aeronautics and Space Administration Lewis Research Center Cleveland, Ohio 44135-3191				14. Sponsoring Agency Code	
15. Supplementary Notes Project Manager, Michael J. Verrilli, Structures Division, NASA Lewis Research Center.					
16. Abstract A study of deformation mechanisms in the single crystal superalloy PWA 1480 has been conducted. Monotonic and cyclic tests were conducted from 20 to 1093 °C. Both <001> and near-<123> crystals were tested, at strain rates of 0.5 and 50%/minute. The deformation behavior could be grouped into two temperature regimes: low temperatures, below 760 °C; and high temperatures, above 820-950 °C depending on the strain rate. At low temperatures, the mechanical behavior was very anisotropic. An orientation dependent CRSS, a tension-compression asymmetry, and anisotropic strain hardening were all observed. The material deformed by planar octahedral slip. The anisotropic properties were correlated with the ease of cube cross-slip, as well as the number of active slip systems. At high temperatures, the material was isotropic, and deformed by homogeneous γ by-pass. It was found that the temperature dependence of the formation of superlattice-intrinsic stacking faults was responsible for the local minimum in the CRSS of this alloy at 400 °C. It was proposed that the cube cross-slip process must be reversible. This was used to explain the reversible tension-compression asymmetry, and was used to study models of cross-slip. As a result of this study, the cross-slip model proposed by Paidar, Pope and Vitek was found to be consistent with the proposed slip reversibility. The results of this study were related to anisotropic viscoplastic constitutive models. The model proposed by Walker and Jordan was found to be capable of modeling all aspects of the material anisotropy. Temperature and strain rate boundaries for the model were proposed, and guidelines for numerical experiments were proposed.					
17. Key Words (Suggested by Author(s)) High temperature deformation; Nickel-base superalloys; Single crystals; Dislocations; Tension-compression asymmetry; Constitutive modeling			18. Distribution Statement Unclassified - Unlimited Subject Category 39		
19. Security Classif. (of this report) Unclassified		20. Security Classif. (of this page) Unclassified		21. No of pages 296	
				22. Price* A13	